Investigation of Multiferroic Properties of Graphene and Oxide Multiferroic Systems for Spintronic Applications

Thesis submitted by,

TANIA CHATTERJEE

Index No.:131/19/Phys./26

Doctor of Philosophy (Science)

Advanced Material and Chemical

Characterization Division

CSIR-Central Glass and Ceramic Research Institute

Kolkata, India

2023

CERTIFICATE FROM THE SUPERVISOR(S)

This is to certify that the thesis entitled "**Investigation of multiferroic properties of graphene and oxide multiferroic systems for spintronic applications**" submitted by Smt. **Tania Chatterjee** who got her name registered on 13th **November, 2019** for the award of Ph. D. (Science) degree of Jadavpur University, is absolutely based upon her own work under the supervision of **Dr. Dipten Bhattacharya and Dr. Arnab Mukherjee** and that neither this thesis nor any part of it has been submitted for any degree / diploma or any other academic award anywhere before.

Dr. Dipten Bhattacharya
Principal Scientist
Central Glass & Ceramic Research Institute
(A Constituent National Laboratory of CSIR, Govt. of India)
Kolkata 700032, INDIA

Bhattacharya 22/06/2023

डॉ॰ अर्णब मुखार्जी / Dr. Arnab Mukherjee
वैज्ञानिक / Scientist
केन्द्रीय काँच एवं सिरामिक अनुसंधान संस्थान
CENTRAL GLASS & CERAMIC RESEARCH INSTITUTE
196 राजा एस. सी. मल्लिक रोड /RAJA S.C. MULLICK ROAD
कोलकाता / KOLKATA- 700 032

Arnab Mukherjee 22/6/23

(Signature of the Supervisor(s) date with official seal)

[i]

Dedicated to,

My Family

Who never let me to fall apart

Acknowledgements

A long 5 years journey, from a mere neophyte student to achieve a title of Doctorate, would never be possible without the direct and indirect help of many persons, whom to acknowledge within some pages is a tough job.

Above all, I am deeply indebted to my research advisor Dr. Dipten Bhattacharya, Sr. Pr. Scientist, AMCCD, CSIR-CGCRI. I must convey my deepest gratitude to him for introducing me to this new genre of research field, and also enriching me with the depth of his knowledge. Before 5 years I was just a M.Sc pass out student novice about research methodologies but his guidance has procreated a researcher in me. His liberal attitude always has given us full freedom to chalk out our own work strategy. He used to maintain a positive environment open for any type of discussion which helps us in nourishing our nature as a human being also. He is always empathetic towards any situation and I got unstinting support from him whenever needed. My continuous efforts were to achieve 50% of his perseverance in learning Physics. I owe him more as a finest human being than my advisor.

Secondly, I would like to express my gratefulness to my co-supervisor Dr. Arnab Mukherjee, Sr. Scientist, FMDD, CSIR-CGCRI. He is also a great chemist. He even being a scientist gave me hands on training in material synthesis. He has mended a material researcher in me who was totally tenderfoot towards chemical lab. I have found him always approachable for any type of discussion any time.

I would also like to express my sincere thanks to Dr. Chandan Kumar Ghosh, Associate Professor, School of Material Science, Jadavpur University, Chair person of my Research Advisory Committee (RAC). He has always been available for any sort of guidance.

I would like to acknowledge financial support from DST-INSPIRE in the form of INSPIRE fellowship. I am also obliged towards the former Director Dr. K. Muraleedharan and also the present Director Dr. Suman Kumari Mishra, of CSIR-CGCRI, for allowing me to pursue my project work in CSIR-CGCRI.

I am also thankful towards some persons whose name deserves a special mention here. I owe my gratitude to Dr. Pranab Choudhury, Prof. Tapas Kumar Ballabh, Dr. Prabir Pal and dr. Avijit Ghosh for their valuable advices whenever needed.

I am extremely grateful to my senior colleagues Sudipta di, Partha Da, Ujjal da, Shubhankar Da and Aditi. I got privilege of working with them which in turn boost my fundamental and experimental knowledge also. My fellow research mates Koyel, Ganga, Prarthana, Debal and Saibal, have also helped and taught me many lessons in their own way. I am thankful for their heart and soul efforts whenever needed.

I would like to recognise the assistances from all the technical staffs of CGCRI especially from XRD lab, FESEM lab, TEM lab, XPS lab, RAMAN and centralized testing facility lab. They have always extended their support. A special mention must goes for the members of Financial, HR and Computer sections for their kind cooperation.

I can't conclude without appreciating all the members of Room No 228, my seating place. We laughed together; we enjoyed together, which transforms our tiring environment more breathable. I must specially mention some names like Epsita di, Puja, Shewli, Gourav and Sourav. We have carried a close bonding with each other more than just a colleagues or research mates. Some scholars have left the room in previous years like Arindam Da, Hasan Da, Anurag Da, Sarani di, Santanu Da and Sumita Di. But they still needed a special credit here for always extending their hands towards me.

Generous cooperation has been showed by The Head, Dept of Physics Jadavpur University and all the members of Ph.D Science cell.

Now it's time to mention those names that are my continuous pillar of support since childhood, my MAA and BABA. They never pushed me to opt for any career options they just tell me one thing, "You can do anything whatever you will opt for we know that." This "we know that" phrase never let me to fade out under any situation.

Finally I must thank my husband, my childhood companion and my backbone. I have married in the first year of my PhD and without his continuous support I could not be able to complete my PhD journey. His ceaseless moral support for me by telling me "I know you can do it", has always boosted me up under any adverse situations and never let me to QUIT personally or professionally. I am blessed with such a family that family responsibilities or any issues never blocked my career path. They all have nurtured a strong woman within me to be able to stand against any odds in life.

Tania Chatterjee 22/06/2023

Tania Chatterjee
CSIR-CGCRI, Kolkata

Preface

With the advent of multiferroic materials a new vista of Condensed matter Physics was opened in front of theoretical as well as experimental scientists. Intense research in this field found multifarious applications of these materials which not only adds value to Condensed Matter Physics but also enriches other field of Science. Among them a special branch of materials which possesses both magnetism (M) and polarization (P) and a coupling between them are known as Magnetoelectric (ME) materials. The technologies based on ME materials found pace in last two decades after losing momentum in 70's. The coexistence of magnetism and polarization provides additional degree of freedom in the development of next generation magnetic field sensing, communication systems, spintronics devices, non-volatile memory applications and so on.

In the last century, ME materials have become popular in Spintronics just because they utilize the control over electron's intrinsic spins and its associated magnetic moment by external electric field. One of the notable milestones in the field of spintronics is control of exchange bias in $La_{0.7}Sr_{0.3}MnO_3/BiFeO_3$ heterostructure by electric field. $BiFeO_3$ has carved its own foundation as a single phase room temperature ME material with multifunctional properties. But $BiFeO_3$ as a single material solely would not fulfil all the demands of Spintronics. We want to explore a new type of material and its properties by combining $BiFeO_3$ with graphene, another superior choice of material in Spintronics. Zanolli's research on $BaMnO_3$/Graphene interface with C-Mn bonding intrigued us in exploring Graphene/BiFeO3 interface rigorously. However there are ambiguities or missing links that were not addressed in previous reports.

We mainly aimed to study the influence of Graphene or its derivatives [e.g. reduced Graphene oxide (rGO)] upon the structural, magnetic and ferroelectric properties of $BiFeO_3$. We have opted for two types of systems- (i) nanocomposite of rGO and $BiFeO_3$; and (ii) hybrid structure of rGO and $BiFeO_3$ thin films. In the first we have successfully synthesized two nanocomposite samples via soft chemical route- (i) one with 'Fe-C' covalent bonding and (ii) another with only Van der Waals (vdW) attachment at the interface; and compared their properties.

The covalent bonded composite is found to exhibit sharp change in the magnetic as well as ferroelectric properties in rGO/BiFeO3 nanocomposite compared to vdW bonded composite. The bonding features in both composites are dependent on rGO wt%s. The magnetoelectric study in covalently bonded composite has proved to usher a new domain in spintronics or

[v]

straintronics because it shows magnetic striction mediated nonmonotonic magnetic field dependence of ferroelectric polarization.

The hybrid structure of $BiFeO_3$ and rGO in homogeneous thin film form (85nm thickness), synthesized using inexpensive chemical solution deposition method, has also been found to manifest changes in magnetic as well as ferroelectric properties compared to the properties of $BiFeO_3$ thin film because of the influence of the interface.

We have also explored the issue of making $BiFeO_3$/rGO nanocomposite or $BiFeO_3$/graphene heterostructure biocompatible for a variety of possible biomedical applications. It has been observed earlier that nanostructure require capping by silver or gold for enhanced biocompatibility. We, therefore, synthesized $BiFeO_3$/Ag nanocomposite, as well to find out its efficacy. We introduced a new chemical route to incorporate Silver (highly biocompatible) in $BiFeO_3$ matrix. The $BiFeO_3$/Ag nanocomposite a new type of self-assembled structure of $BiFeO_3$ nanochains wrapped with silver, exhibits an enormous rise in ferromagnetism (about 20 times compared to $BiFeO_3$ nanoparticles) at room temperature. Then to successfully synthesize ferromagnetic Graphene we have chosen chemical modification of single layer graphene (SLG) instead of adding adsorbates, vacancies or edge defects, because- (i) any additional material could modify the ferroelectricity of $BiFeO_3$ upon being incorporated in the hybrid structure while we wanted to study the influence of magnetic SLG upon $BiFeO_3$; and (ii) we could easily dehydrogenate or demagnetise the hydrogenated Graphene via only chemically oxidation route. We found reversibility in magnetic as well as electrical properties in hydrogenated Graphene and dehydrogenated Graphene.

In this work, we aimed to develop a new genre of magnetoelectric multiferroic materials by integrating rGO and $BiFeO_3$ in various forms (nanocomposites and heterostructures) containing different types of interfaces (bonded and nonbonded) and to probe the physics underlying their novel properties.

Tania Chatterjee 22/06/2023

Tania Chatterjee
CSIR-CGCRI, Kolkata

List of Publications

SCI Journal Publication

1. **Review of Multiferroicity in a Few Promising Nanoscale Systems**, Aditi Sahoo, Shubhankar Mishra, *Tania Chatterjee*, Sudipta Goswami, Dipten Bhattacharya; **Res Dev Material Sci.** 2018, 7, 4.

2. **Chemical dehydrogenation of hydrogenated single layer graphene for reversible electrical conductivity**; Prathana Paul Chowdhury, *Tania Chatterjee*, and Arnab Mukherjee , **Gen. Chem**. 2020, 6, 190034.

3. **Nonmonotonic magnetic field dependence of remanent ferroelectric polarization in reduced-graphene-oxide-BiFeO3 nanocomposite**, *Tania Chatterjee*, Arnab Mukherjee, Prabir Pal, Somdatta Kaushik, Vasudeva Siruguri, Subhankar Mandal, Satyajit Hazra, Swarupananda Bhattacharjee, Chandan Kumar Ghosh, and Dipten Bhattacharya, **Phys. Status Solidi RRL** 2022, 16, 2200077.

4. **Influence of Van der Waals bonds on crystallographic and physical properties of reduced-graphene-oxide/BiFeO₃ nanocomposites**, *Tania Chatterjee*, Arnab Mukherjee, Prabir Pal, and Dipten Bhattacharya, **J. Alloys Compd.** 2023, 944, 169210.

5. **Charge-transfer-driven enhanced room-temperature ferromagnetism in BiFeO3/Ag nanocomposite**, *Tania Chatterjee*, Shubhankar Mishra, Arnab Mukherjee, Prabir Pal, Biswajit Satpati, and Dipten Bhattacharya [submitted]

Conference Papers

1. **ICCFM–2018** held at Biswa Bangla Convention Centre organized by S. N. Bose national Centre for Basic Sciences.

2. **NCRDNN-2019** held at Jadavpur University organized by School of Material Science, Jadavpur University.

3. **2nd Indian Materials conclave and 31st AGM** at Kolkata held at CSIR-CGCRI organized by MRSI Kolkata and Kharagpur Chapter.

4. **SMS-2021** held virtually organized by School of Physical science, NISER, Bhubaneswar.

5. **GLAMICS-2022** held at CSIR-CGCRI organized by Research Scholar society of CGCRI.

Contents

List of Figures

[xiv]

[xvi]

[xvii]

[xviii]

[xix]

[xx]

List of Tables

multiphase analysis

1 Chapter

Introduction and review

1.1 **Multiferroic**

The term 'Ferroic'[1] means a special class of quantum condensed matter. It mainly indicates ferromagnetic (FM), ferroelectric (FE), ferroelastics and ferrotoroidics. These materials exhibit long range order and are dependent on one of the macroscopic order parameters like spin polarization, electric polarization, and strain which can be modulated by conjugate field (magnetic, electric or external stress field)[2] [3].

Example:

(i) Iron, a Ferro-magnet with a spontaneous magnetization that is switchable by an applied magnetic field.

(ii) Lead zirconate titanate (PZT), a Ferroelectric with a spontaneous electric polarization that is switchable by an applied electric field.

(iii) Nitinol (nickel titanium), a Ferro-elastic with a spontaneous deformation that is switchable by an applied stress.

Multiferroic materials, by definition, are the materials with a coexistence of two or more primary ferroic order parameters in the same phase. It was first introduced by Schimd[4] as only single phase material but nowadays it is referred to as the materials that include more than one long range ferroic order (ferroelectric and ferro-, ferri- or anti ferromagnetic and /or ferroeleastic order) in single or even multiphase system. The ferroic phases are coupled to each other as shown in Figure 1.1 by either magnetoelectric, piezoelectric or magneto elastic interactions.
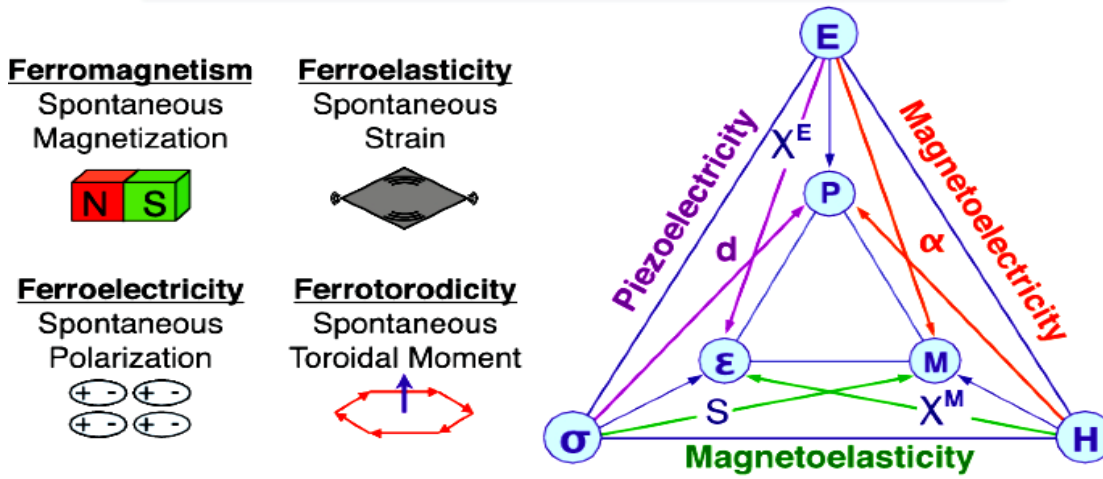
Figure 1.1 The schematic diagram of four ferroic orders and multiferroic material

1.2 **Magnetoelectric multiferroic**

An important type of multiferroic, that include both magnetism and electricity, becomes more appealing because of their magnetoelectric coupling. Here in one material, one can induce magnetic or electric polarization by externally tuning electric field or magnetic field. The discovery of this type of special materials, known as magnetoelectric multiferroic (ME) materials, opens a new domain of potential applications due to electric field control of magnetism. It allows development of next generation ultralow power magnetoelectric devices.

> *Moreover, multiferroic with magnetic and electric order parameters do not always posses linear* magnetoelectric *effect (like YMnO₃) and inversely not all materials that permit linear* magnetoelectric *effect are multiferroic (like Cr₂O₃). Linear* magnetoelectric*s are the materials that posses spontaneous polarization (magnetization) proportionally when magnetic (electric) field induces. Nowadays ME materials are considered to be possesing any type of coupling between magnetic and electric field.*

Because of the coupling between electric and magnetic order parameters it is possible to modify dielectric polarization (P) by external magnetic field (H) and the magnetization (M) by an electric field (E). While the first case, known as direct ME effect (DME), the later is known as Converse ME effect (CME).

The magnetically induced DME effect is defined as:

$$\alpha_H = \frac{\partial P}{\partial H} \cong \varepsilon_0 \varepsilon_r$$

[2]

Where, ε_0 and ε_r are the dielectric permitivity of the vacuum and the relative permitivity of the medium, respectively

The electrically induced CME effect is defined as:

$$\alpha_E = \frac{\partial M}{\partial E}$$

The ME response are mathematically quantified in terms of ME coupling coefficient α_E or α_H which represent the efficiency or strength of ME and are expressed in [s/m] in SI units[5][6].

Now let us assume that $\varepsilon_r \gg 1$

So, $P = \varepsilon_0 \chi E = \varepsilon_0(\varepsilon_r - 1)E \approx \varepsilon_0\varepsilon_r E$ for $\varepsilon_r \gg 1$.

Since, $E = \frac{V}{t}$, where V is the voltage and t is the thickness of the dielectric structure, the following relation for the magnetically induced magnetoelectric effect is obtained:

$$\alpha_H = \frac{\partial P}{\partial H} \cong \varepsilon_0\varepsilon_r \frac{\partial E}{\partial H} = \frac{\varepsilon_0\varepsilon_r}{t}\left(\frac{\partial V}{\partial H}\right)$$

$$\alpha_H^V = \frac{\partial E}{\partial H} = \frac{1}{t}\left(\frac{\partial V}{\partial H}\right)$$

The voltage magnetoelectric coefficient is the main parameter used experimentally. The relationship between the magnetically induced magnetoelectric coupling coefficient and the voltage magnetoelectric coefficient is:

$$\alpha_H = \varepsilon_0\varepsilon_r \, \alpha_H^V.$$

1.3 <u>Historical overview</u>

Maxwell in 19th century first paved the way to combine electricity and magnetism in one common frame which is the foundation of electromagnetism branch in Physics. Though the term magnetoelectric coupling was first originated by Debye in 1926[7] but the concept was first predicted by Curie in 1894 following his research on crystal symmetry considerations[8].

In 1958, Smolenskii and Ioffe[9] developed the idea of introducing magnetic ions in ferroelectric perovskites to bring in magnetic long range orders in the solid without losing the ferroelectricity. This concept was idealized in boracites compound like $Ni_3B_7O_{13}I$, where hysteretic switching of magnetic and ferroelectric domains was observed by magnetic and electric field[10]. The achievements of those days are summarized by H Schmiid in details[11]. An

important development of this field took place in 1959 when Landau and Lifshitz pointed out the topic in a volume of their Course of Theoretical Physics[12]. *Single phase* magnetoelectric effect was first predicted by Dzyaloshinskii [13] in 1959 in an anti- ferromagnetic dielectric Cr_2O_3. This effect was first reported by Astrov [14] which is known nowadays as linear magnetoelectric effect. Similar experimental and theoretical studies were reported by Astrov[14], Folen *et al.*[15], and Rado and Folen[16]. It stimulated more research in this field in the 60s and 70s and were summarized by O'Dell in an article followed by a book[17] in 1970. The substantial developments of the field in those days were because magentoelectric materials were a potential candidate for technological applications as reported by Wood and Austin in 1973 in their review paper on possible applications[18]. A new concept of magnetically driven (improper) ferroelectricity emerged when Newnham and coworkers [19] reported electric polarization in Cr_2BeO_4 which was induced due to the breaking of spatial inversion symmetry due to a special spiral type arrangement of magnetic ions.

The field had lost its momentum because there were few compounds existed and most of them only worked at cryogenic temperature with poor magnetoelectric coupling. This again found pace after a conference on magnetoelectric phenomena, was held at 1993. There a new system was postulated where two types of spontaneous orderings of spin and orbital magnetic moment (ferro-magnetism) and electric dipole moments (ferroelectricity) can coexist even in the absence of external fields. This new genre of materials are known as 'Multiferroic' as named by H. Schmid in 1994. In 2000, Spaldin followed the idea of Smolenskii and Ioffe and explained why the magnetic and ferroelectric orders do not coexist in a persovskite crystal in her paper[20]. The research in this field started taking a new shape after the discovery of magnetoelectric interactions in hexagonal (h-) YMnO3[21], orthorhombic (o-) $TbMnO_3$[22] and $TbMn_2O_5$[23] in the year of 2000-2004. From 1970 to 2000 there were less than 30 articles per year [24] which grew after 2000 till today for industrial demand of novel multifunctional materials. The most notable development in this field was the discovery of multiferroicity in $BiFeO_3$[25][26] which possesses two orders (ferroelectricity and anti-ferromagnetism) at room temperature. The magnetoelectric coupling is weak in bulk $BiFeO_3$ but Ramesh's group[27] in 2003 successfully synthesized epitaxial thin film which exhibited n order of magnitude higher polarization than the bulk. This sets a new horizon in finding multiferroic material globally.

Because of coupling between electric and magnetic order parameters at nanoscale, new vistas have opened up for magnetoelectric multiferroic based nanoelctronic and spintronics devices. The search for new magnetoelectric materials have been facilitated these days by the,

- Availability of modern computational methods such as DFT (density-functional theory) with LDA/GGA (local density approximation/ Generalised Gradient Approximations)

- LSDA+ U (local spin-density approximation+ Coulomb interaction), Berry Phase approaches and many more.

- Advancement in experimental techniques to grow nano scale thin film and to synthesis of complex artificial oxides with atomic level precision.

1.4 <u>Single phase magentoelectric multiferroic materials</u>

Single phase multiferroic materials are chemically isotropic and homogeneous compound in which magnetic moments and electric dipoles coexist with long range ordering to exhibit intrinsic ME coupling. All single-phase multiferroic materials are mostly dielectric oxides.

There are 122 possible crystal structure known as Shubnikov point groups[28], out of which 31 crystallographic point groups permitting electric phase and 31-point groups allowing magnetic phase. Among them only 13 crystallographic point groups are found to be mutually exclusive allowing magnetic and electric order to coexist in same phase as predicted by Shuvalov and Belov[29]. The multiferroic point groups as tabulated by O'Dell[30] and Birss[31] are 1, 2, 20, m, m0, 3, 3m0, 4, 4m0m0, m0m20, m0m020, 6, and 6m0m0. Schmid[32] had published an fascinating article on symmetry aspects in ferroic and multiferroic materials.

According to Maxwell's equation the electric and magnetic field are strictly time variant. But when thermodynamically studied the ferroic components can be also subjected to spatial inversion along with time inversion. Multiferroic materials are determined by crystal symmetry. Magnetic materials break time inversion symmetry and electrically ordered materials break spatial inversion symmetry. This means upon application of time (spatial) inversion symmetry operation, electric polarization (magnetization) remains invariant but magnetization (electric polarization) reverses. Therefore ME multiferroic require simultaneous violation of space and time inversion symmetry.

Some of the example of single phase ME multiferroics as tabulated by M.V Vopson[33] are: Cr_2O_3, $Cr_3B_7O_{13}Cl$, $GaFeO_3$, $LiCoPO_4$, $NdCrTiO_5$, $TbPO_4$, YIG, $BiFeO_3$, $BiMnO_3$, $CdCr_2S_4$, $YMnO_3$, $HoMnO_3$, $TbMnO_3$, $TbMn_2O_5$, $BaMnF_4$, $Ba_{0.5}Sr_{1.5}Zn_2Fe_{12}O_{22}$, $PbFeTiO_3$.

1.4.1 <u>Types of magentoelectric multiferroic materials</u>

The microscopic origin of magnetism depends on the exchange interaction between the localized spin or magnetic moments of partially filled *'d'* of *'f'* shell electrons.

There are several different microscopic origins of ferroelectricity in FE materials. Based on which we can say that there are also different sources of multiferroicity in a single phase ME materials. There are two main groups of multiferroic material denoted as *Type I* and *Type II.*

1.4.1.1 <u>Type-I multiferroics</u>

The materials, where the origin of ferroelectric and magnetic orders is different and the orders develop in different sub lattices, are called *Type I* multiferroics. *Type I* multiferroics are in general good ferroelectrics with large spontaneous polarization of the order of 10-100 $\mu C/cm^2$ the ferroelectricity is typically appear at a higher temperature than magnetism. The main drawback of this type of materials is the poor ME coupling. Here, Ferroelectricity may be driven by electronic lone pairs, geometric effects, charge order or magnetism.

Example:

- $BiFeO_3$ (Ferroelectric Curie Temperature $T_{C,FE}$ ~ 1100K, Neel temperature T_N = 643 K, Polarization P ~ $90\mu C/cm^2$)

- $YMnO_3$ (Ferroelectric Curie Temperature $T_{C,FE}$ ~ 914 K, Neel temperature T_N = 76 K, Polarization P ~ $6\mu C/cm^2$).

1.4.1.1.1 *<u>Lone-pair mechanism</u>*

This mechanism is dependent on unbounded valance electrons which does not involve *sp* hybridization or participate in chemical bonds. These are called lone pair electrons which create local dipoles due to the anisotropic distribution of these electrons around host ion. This mechanism is based on spatial asymmetry created by those lone pairs orderings in one direction.

This mechanism is generally followed by $BiFeO_3$, $BiMno_3$ and $PbVO_3$ having ABO_3 perovskite structure. The A-site valance electrons i.e. in Bi^{3+} and Pb^{2+} ions. There are 2 outer 6s electrons which are lone pairs and create local dipole or dangling bonds. They have high spontaneous polarization.

Robustly used room temperature single phase multiferroic is $BiFeO_3$. It has high polarizability of ~$100\mu C/cm^2$ [34] below Curie Temperature[35] T_c = 1003K and a long range periodic anti-ferromagnetism below Neel temperature[36] T_N = 643 K, thus making it ideal for magnetoelectric coupled material at room temperature.
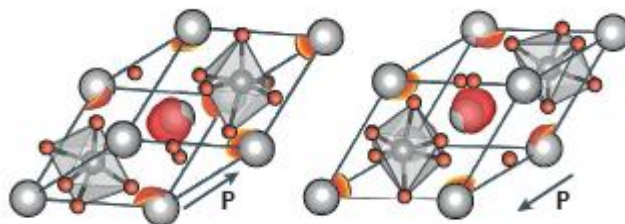
Figure 1.2 Schematic of Lone-pair ferroelectricity in BiFeO$_3$. The lone pair is visualized by the isosurface (red) of the electron localization function of ferroelectric BiFeO$_3$.

1.4.1.1.2 *Geometric ferroelectricity*

Sometimes structural instabilities in some materials can cause shifts in ion positions due to some geometric constraints or space filling effects to make closed packing structures. These ionic shifts can cause polar state which is why it is called Geometric ferroelectricity.

In YMnO$_3$ the magnetic Mn^{3+} ions can cause the tilting of MnO$_5$ block to provide closed packing. This deformation results in shift in Oxygen ions which move closer to Y ions. This formation follows in hexagonal RMnO$_3$ structure (R= Sc, Y, In or Dy-Lu) with polarization of the order of 5.6 μC/cm^2 [37] at T$_C$ ~ 1200K[38 39 40] followed by magnetic ordering at T$_N$ = 120K[41]. In BaNiF$_4$ the asymmetry between Ba^{2+} and F^{-1} sites causes spontaneous polarization of ~0.01μC/cm^2 which couples weak ferromagnetic moment at room temperature[42]. In Ca$_3$Mn$_2$O$_7$ polarization[43] arises from the joint action of 2 non polar lattice modes which couples with canted magnetic moments.
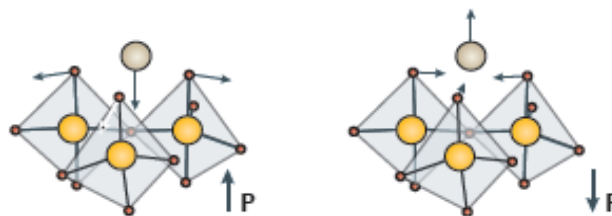
Figure 1.3 Schematic of geometric Ferroetricity in hexagonal (h-) RMnO$_3$ emerges from a tilt and deformation of MnO5 bipyramids, which displace the rare-earth ions as indicated by the arrows, leading to a spontaneous polarization along the [001] axis.

1.4.1.1.3 *Ferroelectricity due to charge ordering*

When a material contains transition metal ions of different valences then these valence electrons can spatially distribute themselves non-uniformly around host ions in such a way that forms a periodic superstructure. This is called charge orderings and usually observed in transitional metal compounds.

In $LuFe_2O_4$ there are transition metal Fe with two valence states Fe^{2+} and Fe^{3+} which form a super lattice with an alternating sequence of Fe^{2+} and Fe^{3+} ions[44][45]. This charge ordered driven polarization also follows in Ca_3CoMnO_6[46], $Pr_{1-x}Ca_xMnO_3$[47][48] and Nickeelates NiO_3. Another possibility is seen in organic ferroelectric $(TMTTF)_2X$ where due to structure there are asymmetry in bonds which is called site centred charge ordering[49]. But even after decade charge order driven ferroelectricity is still remained as an interesting concept with a lot of questions to be answered[50].
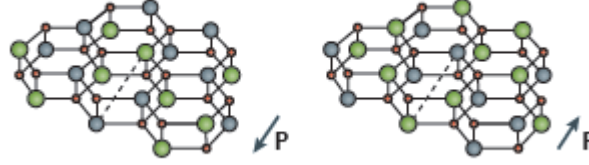
Figure 1.4 Schematic of charge orderings in LuFe₂O₃ creates alternating layers with Fe²⁺/Fe³⁺ ratios of 2:1 and 1:2. This was argued to create a spontaneous polarization between the two layers, which is oriented parallel to the arrow.

1.4.1.2 Type-II multiferroic

When the origin of ferroelectricity is dependent on magnetism i.e. when they occur depending on one another then it is called *Type II* multiferroic. Generally, magnetism causes ferroelectricity. This mechanism is recently discovered[22].

There is strong coupling between magnetism and ferroelectricity but their ferroelectric polarization is much smaller compared to *Type I* of the order of 10^{-2} μC/cm².

In this type of novel materials ferroelectricity only exists in magnetically ordered states and can be divided into 2 groups based on the origin of ferroelectricity. Here ferroelectricity is caused by either magnetic spiral or magnetically collinear structures.

1.4.1.2.1 *Spiral type-II multiferroic*

The microscopic source of this type is generally spin orbit interaction. Ferroelectricity appears due to spiral arrangement of magnetic phases. (Most of the Type II materials are belongs to this group.) Magnetic frustrated system is the source of this type of structure. According to Katsura, *Nagaosa, and Balatsky*[51][51] who used microscopic approach and Mostvoy[52] who applied phenomenological approach we have a equation for polarization P.

$$\vec{P} = \vec{r_{ij}} \times [\vec{S_i} \times \vec{S_j}] \times [\vec{Q} \times \vec{e}]$$

Where,

$\vec{r_{ij}}$ = the vector connecting neighbouring spins S_i and S_j

[8]

$\vec{Q}$= the wave vector describing the spiral

$e\left[\vec{S_i} \times \vec{S_j}\right]$= the spin rotation axis

This type of equation is derived assuming cubic and tetragonal crystal structure. In the case of proper screw i.e. when the spin rotates in the plane normal to the wave vector of spiral then the P would be zero for this particular type of symmetries.

Example: in $TbMnO_3$ the magnetic phase though appear at T_{N1}= 41K but below 28K (T_{N2}), the Mn spins order in such a manner that the tip of spins sweep out a cycloid. The same nature follows for $Ni_3V_2O_6$ and $MnWO_4$.

But in some recent discovered systems as analyzed by Arima[53] it has been seen that there are non-zero polarization exists even forproper screw spiral in some symmetries other than cubic and tetragonal. This type is observed in $RbFe(MoO_4)_3$ [54] and in layered triangular systems such as $CuFeO_2$ and $ACrO_2$ (A= Cu/Ag/Li/Na) [55].
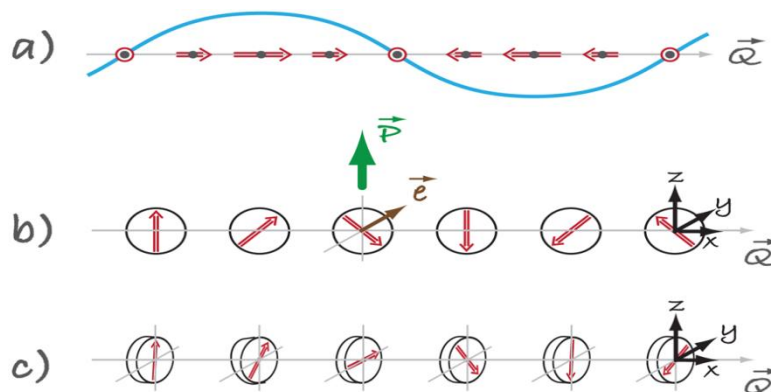
Figure 1.5 Different types of spin structures relevant for type-II multiferroics. (a) Sinusoidal spin density wave, in which spins point along one direction but vary in magnitude. This structure is centro-symmetric and consequently not ferroelectric. (b) The cycloidal spiral with the wave vector Q = Q$_x$ and spins rotating in the (x,z)-plane. It is in this case where one finds nonzero polarization, (c) In a so-called "proper screw" the spins rotate in a plane perpendicular to Q.

1.4.1.2.2 *Type-II multiferroic with collinear magnetic structures*

When the magnetic moments are all aligned along a particular axis i.e. appears as collinear then due to exchange striction polarization appears. Here spin orbit interaction is not necessary but only magnetic striction is needed because here magnetic coupling varies with atomic positions.

In Ca_3CoMnO_6[46], Co^{2+} and Mn^{4+} ions forms a 1D chain of alternating equidistant ions and thus have no polarization. The magnetic spins form a ↑↑↓↓ type magnetic structure which breaks inversion symmetry. Due to exchange stricton there are indifferent distortions in ferro

(↑↑) and anti-ferro (↓↓) bonds, which are the causes of ferroelectricity. Hua *et al..* [56] theoretically predicted this picture.

The same picture can be seen for identical magnetic ions like in $RMnO_3$ where intermediate oxygen plays an important role and exchange striction is dependent on both distance between metal ions and metal-oxygen-metal bond angle.

In $RMnO_3$ the magnetic order of Mn is ↑↑↓↓ type and due to exchange striction oxygen ions shift normal to Mn-Mn bond. Thus produces a polarization along the direction of shift. This was proposed by Sergienko, Sen, and Dagotto [57] and also observed experimentally [58]. Another mechanism involves in this type is electronic ferroelectricity in frustrated magnet [59] where spins are arranged in a triangle and the polarization follows spin correlation function, $\vec{S1}\,(\vec{S2} + \vec{S3}) - 2\vec{S2}\,\vec{S3}$.

Collinear result (frustrated):   Non-collinear result
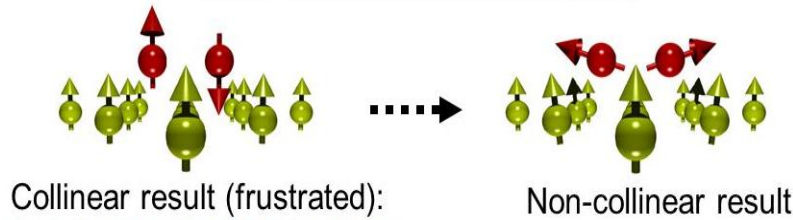
Figure 1.6 Schematic of Non- collinear mechanism in Mn dimer on Ni (001) where magnetic frustrated system transforms into non collinear structure which results from Mn-Ni ferro and Mn-Mn anti-ferro competing interaction

1.5 <u>Direct and indirect magnetoelectric composite</u>

There are generally two groups depending on the magnetoelectric (ME) coupling which are direct and indirect.

Direct: when direct application of magnetic and electric field can change the polarization or magnetization of the system. This effect primarily occurs in single phase multiferroic [60].

Indirect: when application of electric or magnetic field does not directly modulate the magnetization or electric polarization respectively instead they are modified via strain [61]. This effect is found to occur in elasto-magnetoelectric multiferroic or composite multiferroic [6 62].

1.6 <u>Shortcomings of single phase multiferroic</u>

The main challenge of single phase multiferroic is dependence on '3d' or '4f' orbital's valency of metal ions, where there are different preferential need for 2 different ferroics (ferromagnetic and ferroelectric).

Ferromagnetic materials require partially filled '3d' shells or partially filled '4f' shells for transition metals and lanthanides respectively. According to Hund's rule, magnetic coupling

favours parallel electrons in lowest energy levels. This means when electrons are localized then the exchange energy is optimized to have magnetic pair of electrons.

In contrast, ferroelectric materials favour 'd0-ness' or empty 3d shells. In a covalent bonded states after electronic sharing cations and anions shift toward each other to form local dipole which favours polar states. But, when there are additional valence electrons present then the electron clouds overlaps and this again tend to push ions apart which make them non-polar. So, 'd0-ness' is needed for a transition metal ion based compound to be ferroelectric.

In perovskite ABO_3 structure ferroelectric state occurs because of displacive nature. Here electron clouds of neighbouring ions get hybridized which also require empty '3d' shell. So, search of new materials requires non-displacive mechanism of ferroelectricity to be compatible with partially filled '3d' or '4f' shells materials for magnetism to appear simultaneously. Due to this mutually exclusive rule only a few single phase ME materials exist.

Conventional perovskite ME multiferroic[20] have lone pair electron in A-site and B-site respectively which favours magnetism. Lone pair in A-sites move to off-centre of centro-symmetric crystal to make them non-centrosymmetry polarized one. As, in perovskite structure electricity and magnetism are associated with different ions so their coupling are usually weak.

Most of the single phase materials also possess low permittivity and permeability which is also another reason for their weak coupling at room temperature.

Most studied room temperature single phase ME is $BiFeO_3$ but it displays weak ferro-magnetism above room temperature[63] [64]. Moreover, phase pure sample preparation is one of the challenges in $BifeO_3$ because impurities such as Bi_2O_3 and $Bi_2Fe_4O_9$ present in it may cause leakage currents and dielectric loss[65]. Other single phase ME are rare-earth manganites $(RMnO_3)$ [66] which exhibit good multiferroicity. But, their Curie temperature is well below room temperature.

So, despite huge efforts and fascinating properties, single phase ME are not becoming the ideal materials for technological applications at room temperature. Therefore, researchers are in search of alternative ME materials. A different genre of magnetoelectric multiferroic systems which exhibit promise, in this context, has been discussed below.

1.6.1 <u>ME as Composite</u>

In composite materials efforts have been given to synthesize composites of two mixed phases containing magnetic and electric order which are physically separated from each other. Here requirement of 'pure dielectric though magnetic' material is not needed any more. The magnetic phase can be metallic conductor as well whereas electric phase can be dielectric. Most

of them are operable above room temperature. The ME coupling is a few orders of magnitude larger[62] so that it become comparable close to most sensitive magnetic field detectors SQUIID or MFM. Some of the examples are CoFe2O4/BaTiO3, LSMO/PZT, LSMO/BaTiO3, $Tb_{1-x}Dy_xFe_2$/PZT, CoPd/PZT, $NiFe_2O_4$/PZT.

In the composites one observes indirect ME coupling[67] which occurs extrinsically in three different ways by - (i) strain (ii) charge carriers (iii) spin exchange. Since the coupling originates at the interfaces of the constituent systems, it requires structural similarities, lattice matching or chemical compatibilities between the constituent materials[68].

1.6.2 <u>ME as thin films and heterostructures</u>

Technological demand of miniaturization of electronic devices motivates researchers in search for atomically thin low dimensional multiferroic. At first, efforts have been given to reproduce bulk phase thin film with an aim to observe switching under electric field. Then efforts have also been given to grow thin film layer by layer with atomic scale precision which becomes more controlled and more accurate.

This was accomplished in o-TbMnO$_3$, h-RMnO$_3$ and BiFeO$_3$[69] which were grown in large range with more superior properties than bulk crystals. This work has been reviewed in details in Ref [70] [71] [72].

The challenges in thin film are interfacial strain and hetero-epitaxy which widens the development of thin film heterostructure for potential device applications. The interaction between interface materials determines the unique properties of heterostructure which can be divided into three types[73].

0-3 structure	magneto-elastic material embedded in a piezoelectric matrix	CoFe$_2$O$_4$ or CFO nano particles in a Pb(Zr,Ti)O$_3$ or PZT matrix
2-2 structure	multilayer thin films of magneto-strictive and piezoelectric materials	Pb(Zr$_{0.52}$Ti$_{0.48}$)O$_3$ (430 nm)/LSMO (330 nm)
1-3 structure	monolayer self-assembled nanostructures	CFO nano pillars in a BiFeO$_3$ or BFO matrix

1.6.3 <u>ME as 2D multiferroic: A new Genre</u>

The recent discovery of 2D FM[74] [75] [76] [77] provides opportunities to manipulate electric field induced modification of magnetic order, saturation magnetization, coercive field and Curie temperature[78].

Similarly 2D FE materials[79][80][81][82] have certain advantages over perovskite materials like it can effectively avoid negative effect of dangling bonds and quantum tunnelling observed in 3D thin film.

2D ferroelectric materials
- Gr-IV mono-chalcogenides, [83][84][85][86]
- group-V monolayers Atomic-Thick SnTe [79]
- III2−VI3 van der Waals (vdW) materials: In_2Se_3 mono to layered structures[87][88][89][90]
- transition-metal thiophosphate family: layered A-In_2Se_3[91] $CuInP_2S_6$[80] Monolayer $AgBiP_2Se_6$[92] Metal Chalcogen Diphosphates [93]
- oxygen-functionalized scandium carbide MXene (Sc_2CO_2) $CuCrP_2S_6$[94]

  2D ferromagnetic materials
- few-layer $Cr_2Ge_2Te_3$[95]
- CrI_3 [74]
- Fe_3GeTe_2[96]

However, the 2D FM and FE materials also suffer from enhanced thermal fluctuations and depolarization field respectively. O course, the demand for electric field control of magnetization direction[97][98][99] opens the path for search of 2D multiferroic for new generation spintronics[100][101].

A lot of work has already been done in search of 2D multiferroic[102][103][95]. A recent work by Zhang's group[104] predicted multiferroicity in VdW artificial heterostructure where magnetic easy axis of $Cr_2Ge_2Te_3$ can be tuned by the polarization of FE layer.

Tan et al[105] studied 2D multiferroic using first principal DFT. However intrinsic ME coupling has been proposed in these predicted materials.

Some examples of:

- Room temperature multiferroic are- GeS, SnS, GeSe, SnSe.

- VdW materials with coexistence of FM and FE order are-

  (i) Monolayer transition-metal phosphorus chalcogenides -$CuMP_2X_6$ (M = Cr, V; X = S, Se)[103][94]

  (ii) charged (electron doped) $CrBr_3$ monolayer[102]

  (iii) vanadium oxide dihalides ($VOCl_2$) [106]

  (iv) chemically functionalized phosphorene[107]

[13]

(v) MXene $Hf_2VC_2F_2$ monolayer[108]

- <u>VdW materials with magnetoelectric coupling are-</u>

(i) FM $Cr_2Ge_2Te_6$/ FE In_2Se_3: first principal DFT calculations showed that by reversing polarization magneto-crystalline anisotropy can be changed between easy axis and easy plane. Moreover, In_2Se_3 became magnetic ferroelectrics where spin switches according to its own electric polarization[104].

(ii) FM bilayer CrI_3/FE monolayer Se_2CO_2: Switching in electronic polarization in Sc_2CO_2 layers altered energy band alignement of heterostructure from Type II to Type III and the charge transfer in TypeIII between CrI_3 and Sc_2CO_2 converts interlayer magnetic coupling of CrI_3 bilayer from AFM to FM[109].

(iii) FE $Sc_2P_2Se_6$ monolayer/2D multiferroic $ScCrP_2Se_6$: Monolayer shows distinct magnetoelectric coupling[110].

1.6.3.1 <u>Mechanism of 2D materials with ferromagnetic and ferroelectric coupling</u>

Different methods have been utilized to induce spin or electric polarization in 2D Vdw materials in order to achieve 2D multiferroic with coexistence of FM and FE order.

Type I	
Intercalation	halogen-intercalated phosphorene bilayer[107] - C_6N_8H 2D organic[107].
doping	$CrBr_3$[102] - monolayer metal tri-halides[111] - 2D FM CrI_3
The Ruddlesden-Popper (RP) phase	Zhang *et al.*[99] studied the designing of the two-dimensional multiferroics with the coupling of polarization and magnetization by taking a double perovskite (DP) bilayer Ca_3FeOsO_6 where Ca is at A-site Fe and osmium (Os) are at B-site and X is an anion as per RP phase. The transition metal ions at the B-site have the rock-salt structure[112].
Heterostructures by simply bringing FM and FE layers together.	Ferromagnetic $Ti_{0.8}Co_{0.2}O_2$ nanosheets and dielectric $Ca_2Nb_3O_{10}$ nanosheets [113]
Magnetic transition metal is introduced into the intrinsic 2D ferroelectrics	CIPS monolayer - transition-metal phosphorus chalcogenides $CuMP_2X_6$ (M = Cr,V; X = S, Se) monolayers[94,103] - 2D CrN and CrB_2 monolayers[114]
TypeII	
Ferroelectricity originates directly from its magnetism	- MXene $Hf_2VC_2F_2$ monolayer[108]

1.7 <u>Possible applications of multiferroics</u>

Multiferroic materials simultaneously own different ferroic orders and have the ability to tune one ferroic order by others. Among them magnetoelectric (ME) materials have the features of manipulating magnetism with electric field or voltage and vice-versa. So, this voltage controlling capability makes them ideal for device applications because of miniaturization, high speed, low energy & heat consumption and high signal to noise properties[115]. It also has an additional integrity of ME coupling. Some of their applications are briefly discussed as follows. ME materials are precious for satellite, radar, portable electronic devices where low volume, low mass and energy consumption are highly needed. Beside these ME materials also influences other remote research areas such as complex magnetism and ferroelectricity and cosmology.

1.7.1 <u>Multiferroic in sensing applications</u>

Magnetic sensors are known to be a device to detect creation or variation of environmental magnetic field. Now-a-days Magnetoelectric (ME) coupling based multi-ferroic materials are becoming alternative of traditional conventional Hall sensors and Giant Magneto-resistance (GMR) devices. ME based sensors utilize magnetically induced ME effect, where, voltage is induced proportional to the amplitude of external magnetic field which is to be sensed.

AC Sensor: Almost all magnetic field sensors are basically bi or tri-lyer composite materials which can sense AC magnetic field but not DC. The sensitivity lies- $10^{-13} < H_{ac} < 10^{-3}$ T [116 117 118].

DC Sensor: DC magnetic field response can be possible when a composite multiferroic performs linear response in M-H or strain-field curves. Currently, AC magnetic field senors are based on self biased multiferroic composites following Enno *et al.* [119] who first experimentally proved this concept.

Example: PMN-PT/Terfenol-D layers (136 pT/$\sqrt{Hz}$)[116], Metglas/PMNT laminate (4.2 pT/$\sqrt{Hz}$ [120]), Metglas/Mn-PMNT (0.87 pT/$\sqrt{Hz}$ [121]), $Fe_{0.7}Ga_{0.3}$/ PZT/ Si thin film (23 nT/$\sqrt{Hz}$ [122]), SiO2/Ti/Pt/AlN/Cr/FeCoSiB (100pT/$\sqrt{Hz}$ [123]), PZT/Terfenol-D thin films (1 pT/$\sqrt{Hz}$ [124]).

1.7.2 <u>Multiferroic in microwave devices applications</u>

1.7.2.1 <u>Microwave resonator, phase shifter and delay line</u>

Microwave resonators and phase shifters are elements used in Phased array antenna system in radars, filters. Traditionally used microwave resonators are ferromagnetic (FM) materials (basically soft magnetic materials) which are able to display the phenomenon known as ferromagnetic resonance (FMR) when are subjected to high frequency [125]. Similarly traditional Phase shifters are semiconductor ferroelectric (FE) or ferrite materials which are based on Faraday rotation of electro-magnetic (EM) radiation. Microwave Delay lines are placed across 2 micro-strip microwave transducers. The high frequency EM spin waves propagate from input to output micro-strip via delay lines. Typical delay lines are ferrite materials where signal propagation delay is very high. All of these devices need additional magnetic field to operate and tuning frequency and also have disadvantages like slow operation, high noise level, large power consumption and limitation in miniaturization. To eliminate these possibilities ME materials basically bi-layer ME composites are used and here electrical tuning of devices are also possible. These ME based microwave devices are less noisy, energy & time efficient, compact and light weight.

Example:

- Microwave resonators- YIG/PZT[126], epitaxial nickel ferrite ($NiFe_2O_4$) films (X-band[127]), Y-($Ba_2Zn_2Fe_{12}O_{22}$:ZnY) and Z-type ($Ba_3Co_2Fe_{24}O_{41}$) hexagonal ferrites (10–40 GHz [128]), M-type hexa-ferrites $MFe_{12}O_{19}$ (M = Ba, Sr) (40–75 GHz [129]), Al doped M-type hexa-ferrites (50–110 GHz [130]),bi-layers of single crystal ZnY and polycrystalline PZT or single crystal PMN-PT (8–25 GHz[131]), layered ferroic FeGaB and single crystal, piezoelectric PZN-PT-based resonator[132 133].

- Microwave phase shifter- $Ba_{0.6}Sr_{0.4}TiO_3$/YIG ferrite[134], YIG/PZT[135], Zn2Y/PMN-PT[136].

- Microwave delay lines- Yttrium-Iron-Garnet (YIG) ferrite and Lead- Magnesium-Niobate-Lead-Titanate (PMN-PT) ferroelectric[137 138].

1.7.2.2 <u>Antenna</u>

Rapid advancement in communication system require smaller antenna suitable for lower frequency bands. To achieve smaller antenna with dielectric material is prone to surface wave excitations and lower efficiency. Nearest approach is to use engineered ME composite.

Example: nickel zinc ferrites ($Ni_{1-x}Zn_xFe_2O_4$:NZFO)/BST (100-MHz antenna[139]), helical antennas using Co2Z type hexaferrite and ferrite substrates (195 MHz [140 141]), (Co/Ti) doped BaM substrate (231 to 201 MHz [142]).

1.7.3 **Multiferroic in memory devices applications**

1.7.3.1 **Multiferroic magnetic recording read heads**

Current genre of storing digital data in magnetic hard disk drive opted for perpendicular magnetic recording media (PMRM) where data are stored in tiny regions in magnetically thin film perpendicularly. This digital data can be retrieved using magneto-resistive (MR) [143] read head using anisotropic magneto-resistive (AMR), GMR or TMR effects. New radar technology is based on ME effect of multiferroic material proposed in 2007 [144] and experimentally demonstrated in 2008 based on tri-layer FM/FE/FM ME composite structure. The advantages are multifold, reduced power consumption, improved thermal performance.

Example: BTO-NFO and BTO-CFO bilayered heterostructures [145] , tri-layer ME composite structure and consists of 7 layers, arranged as seed/AFM/FM/FE/FM/AFM/cap[138].

1.7.3.2 **Multiferroic random access memories and multi-state memories**

To overcome the issues of ferroelectric RAM and magneto-resistive RAM, multiferroic material is used and so it is named as MFRAM with multiple memory states. In this multilayer stack 2 binary states could be encoded by FE polarization states and 2 additional binary states are encoded by magento-resistive states. MFRAM's main advantage is electrically read/write four state memories RAM which offers less power consumption, more memory density and non-volatility simultaneously.

Another memory device utilized ME coupling of multiferroic material with interfacial exchange bias between FE layer and AFM layer known as MeRAM device[146].

Example: epitaxial $La_{0.1}Bi_{0.9}MnO_3$ (four-resistance-state memory system [147]), nano epitaxial $BaTiO_3$ thin films deposited on $SrRuO_3$ (non-volatile four-state memory RAM[148]), ($CoFe/BiFeO_3$) heterostructures[149], NiFe/NiCoO/glass/PZN-PT heterostructure[150].

1.7.3.3 **Magnetic data storage based on multiferroic**

Multiferroic data storage medium lead to increase in data storage areal density and replacement of heat assisted magnetic recording (HAMR) technology [151] . Kim et al [152] demonstrated this concept of controlling super para-magnetism via magnetoelectric effect in multiferroic.

Example: Ni magnetic nano particles strain coupled to a piezo-electric $[Pb(Mg_{1/3}Nb_{2/3})O_3]_{(1-x)}$-$[PbTiO_3]_x$.

1.7.4 <u>Multiferroic in energy harvesting</u>

1.7.4.1 <u>Photovoltaic energy harvesting</u>

Solar is the most suitable as a renewable energy source. Photovoltaic effect is based on generation of electron-hole pairs by photons. Standard solar cells are p-n semiconductor junction. Here, the requirement is small band gap with highest conversion efficiency. E-e magnetic interaction and intrinsic strain coupling would lower the band gap to a certain useful level so that it is photo-voltaic in a wider solar spectrum. Here multiferroic materials display multiple order parameters. Research in this field promotes photo-strictive effect also.

Example: for $BiFeO_3$ multiferroic perovskites (2.6–2.7 eV)[153 154 155], Cr doped BiFeO3 multiferroic (Bi_2CrFeO_6) thin films (1.4–2 eV).

1.7.4.2 <u>Magnetic energy harvesting</u>

Ambient environmental is filled with magnetic noise of 50-60 Hz. Harvesting this low frequency magnetic noise and convert it to electricity is always a challenge. Magneto-mechanic-electric (MME) mechanism is useful to convert AC magnetic field to electric field with an in direct piezo-electric effect. Similarly, piezo energy harvesting and magneto-strictive energy harvesting of mechanical vibration within single device is known as vibrational energy harvester.

Example: Metglas/Pb(Zr,Ti)O3 laminate (16 µW/Oe [156], 420 µW/Oe [157]), piezoelectric $Pb(Mg_{1/3}Nb_{2/3})O_3$–$PbTiO_3$ (PMN–PT) single crystal fiber composite (SFC).

1.7.5 <u>Multiferroic as electrical elements</u>

1.7.5.1 <u>Multiferroic Gyrators</u>

In 1948, Bernard D.H. Tellegen proposed[158] a hypothetical fifth linear element and proposed the following equations,

$$\mathbf{D} = \epsilon\mathbf{E} + \gamma\mathbf{H} \text{ and } \mathbf{B} = \gamma\mathbf{E} + \mu\mathbf{H}$$

(ϵ is the dielectric permittivity and µ is the magnetic permeability)

This was named after Tellegen as Tellegen's equation and the linear element is known as Gyrator. Gyrator is known as linear, passive, lossless, 2 port electrical element and have the property that it can invert current-voltage characteristics. In the equation γ is known as linear ME coupling coefficient of multiferroic and he also proposed the relationship between the magnetoelectric coupling and the magnetic (χ^m) and electric susceptibilities (χ^e), as,

$$\frac{\gamma^2}{\epsilon\mu} \leq \frac{\gamma^2}{\chi^e\chi^m} \leq 1.133$$

[18]

The tri-layer composite ME materials are used as Gyrator.

Example: a Terfenol-D/PZT/Terfenol-D structure (resonance frequency 86 kHz), Metglas/PZT/Metglas (resonance frequency 64 kHz), Nickel/PZT/Nickel composite multiferroic (resonance frequency 15 kHz)

1.7.5.2 High voltage gain multiferroic amplifier

Strain mediated magnetically induced ME effect is useful for the generation of AC magnetic field when voltage is fed in the input. Dong *et al..* realized this in tr-layer multiferroic composite resulted in large voltage gain of 300 operable at frequency 21.3 kHz under dc bias 300Oe.

Example: Terfenol-D/PZT/Terfenol-D shaped in an elongated bar geometry.

1.7.5.3 Multiferroic magnetic gradiometer

Magnetic field gradient is measured through frequency shift and output voltage by realizing bi-layer multiferroic composite. This was designed by Baedekar *et al.*

Example: Terfenol-D and PZT were used and the device had a working resonance frequency of 91–94 kHz[159].

1.7.5.4 Multiferroic inductor

Tunable inductor is widely used in various applications such as communication system and power electronics. They are magnetically tuned by electro-magnets which are bulky, noisy and energy consuming. To develop electrically tunable inductors ME composites are used to overcome these factors.

Example: PZT/MnZn/PZT composite inductor[160], a ring inductor using insulating single phase $Bi_{0.7}Dy_{0.3}FeO_3$ multiferroic material[161].

1.7.6 Multiferroic in biomedical applications

The recent advancement of biomedical applications offers magnetic bio sensing, magnetic separation of labelled cells, therapeutic drug delivery, hyperthermic treatment for malignant cells, contrast enhancement agents for magnetic resonance imaging (MRI) [162 163 164]. The quest of finding ideal magnetic nano particles (MNPs) or their clusters with relatively small size and high magnetic moment is still a subject of intense research. ME composite have been also utilized in biomedical applications such as wireless endoscopy, minimally invasive surgical tools, and stimulation of functions of living cells[165]. ME nano particles (MENs) are used as carriers in drug delivery with high specificity to cancerous tumor cells[166]. MENs are

also modelled as by Yue *et al.*[167] to non-invasively stimulate the neural network in brain and also has been used to treat various diseases like Parkinson's disease[168].

1.8 <u>Spintronics</u>

In the last century, multiferroic materials have been very popular in spintronics[169]. Usually spin stands for spin of a single electron 's' which is either '$\frac{1}{2}$' or '$-\frac{1}{2}$' and it is associated with magnetic moment '$-g\mu_B s$' (where μ_B is the Bohr magneton and g is the electron g factor). The spin control means either the control over the population of spins or control over the phase of spins of an ensemble or particle. It can also be termed as coherent spin manipulation of a single or few spin system i.e. ensemble of spins. In the era of Information storage and logic devices Spintronics[170] opens a new door utilizing the control over electron's intrinsic spin and its associated magnetic moment by manipulating external electric field. Spin channel solid state materials must have high Spin orbit coupling (SOC) along with long spin diffusion length[171]. The commercial application of spintronics is based on giant magneto-resistive (GMR) effect, for which the Nobel Prize in Physics was awarded in 2007 to Albert Fert and Peter Gru¨ nberg. They have made a spin valve with a layered structure like FM/non FM metal spacer/FM layer where valve is open/close when magnetization of two FM layers are parallel/anti-parallel.

Fundamentally spintronics studies include spin transport, spin dynamics and spin relaxation in electronic materials. Traditionally, optical techniques were used to create non-equilibrium spin population i.e. spin polarization by transferring angular moment from photons to electrons. Now-a-days it has been utilized using electrical spin injection. This rate of spin accumulation depends on spin relaxation time and length which are solely material's properties. Spintronics applications can be utilized via- magnetic field control, electric field control, spin polarized current controlled and photonic field control. We are interested in the electric field control of magnetic moments as shown in Figure 1.7 .

There are 2ways by which electric field has control over magnetic moments or electronic spins-

- To manipulate magnetic anisotropy of ultrathin Fe based systems

- In multiferroic system where magnetic and electric fields are coupled[172].

We are interested in studying interface of multiferroic and graphene composite or hybrid structure for spintronics applications. WHY? Those points are discussed as follows.
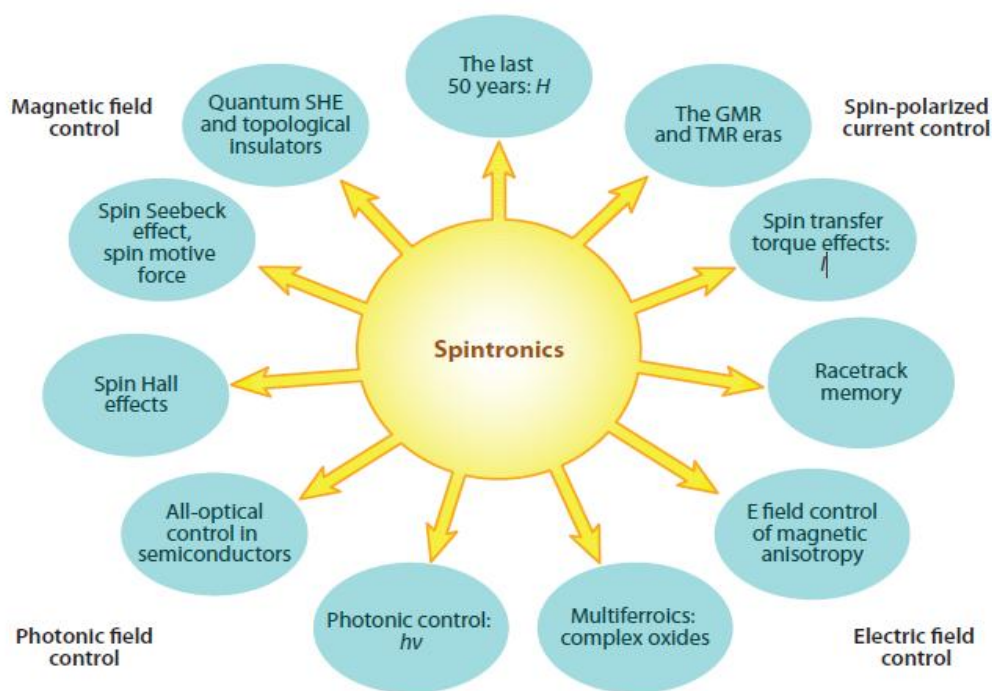
Figure 1.7 Overview of different mechanism of Spintronics

1.8.1 <u>Graphene as a spintronics material</u>

graphene, a superior choice for room temperature spin transport material, is 2D allotropic form of sp^2 hybridized carbon network joined covalently (σ-σ) to form honeycomb planer lattice. graphene produces weak spin orbit coupling but longer spin relaxation time[173] with long spin diffusion lengths of several micrometres[174] [175] [176] at room temperature which made it a choice for spintronics applications. The spin lifetime lies in the range 0.5ns-2ns that is much larger than 45ps of Aluminium metal and 1.3ns of highly doped semiconductor[171]. Along with it has room temperature spin diffusion length of 3-12μm[174] which is also higher than 0.4μm of Aluminium metal and 0.5μm of highly doped Silicon[175] [176]. Transport of spin polarized carriers(with carrier mobility as high as ~17000 $cm^2V^{-1}1s^{-1}$) injected by ferromagnetic electrodes - deposited on single or multilayer graphene either in local or nonlocal configuration - as well as manipulations such as introduction of large spin-orbit coupling(SOC), zigzag and/or edge states turn out to be extremely useful or spin logic gate devices. Moreover, other unique properties of graphene include high thermal conductivity (5000 W $(m\ K)^{-1}$, superior electrical conductivity (6000 S/cm), and also high mechanical stiffness[177] and gate-tuneable carrier concentration[178].
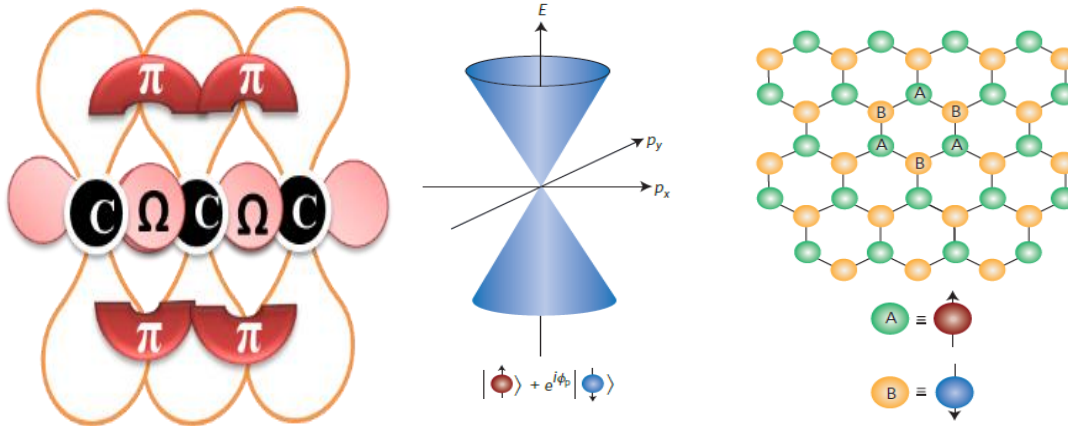
Figure 1.8 The structure of graphene

graphene is electronically half field in bipartite lattice system[179]. The Fermi levels of isolated graphene touches each other at Dirac points and produces null band gap which therefore limits the spin orbit coupling[180]. Moire heterostructure of h-BH/graphene/h-BN has shown an interesting FE behaviour. Bi-layer graphene shows hysteresis behaviour as a function of applied electric field when top and bottom h-BN layer have a particular orientation[181]. 2D FE-FET made of α-In2Se/graphene can be switched over 10^5 cycles randomly[182].

Isolated graphene is not optimal choice for spintronics application as it must have high Spin orbit coupling (SOC) along with long spin diffusion length which manipulates electron's intrinsic spin via external electric field. Some efforts have been made to introduce SOC via introducing magnetization in graphene by creating defect[183] or vacancy[184] or by edge[185] or via hydrogenation[186]. Therefore, functionalized graphene along with composites based on graphene seem to usher a new domain of systems for future electronic, optoelectronic, and spintronics devices. Our work is based on functionalize graphene by hydrogenation and make multiferroic composite to manipulate properties for the advancement in magnetoelectric domain for further applications in spintronics.

1.8.2 BiFeO$_3$ as a spintronics material

Bismuth ferrite (BFO) [BiFeO$_3$] is one of few single multiferroic materials where we can couple AFM and FE properties at room temperature whereas most of the ME materials can't meet this need. BFO have FE phase transition Curie temperature T$_c$ at 1103K and G type AFM phase transition Neel temperature (T$_N$) at 643K[187].

In BFO Bi^{3+} and Fe^{3+} ions are mainly accountable for ferroelectric polarization and magnetization respectively. BFO was first synthesized at 1957, but it is still a challenge to synthesize pure phase BFO because of volatility of Bi^{3+} ions and oxygen vacancies, which can

lead to appearance of secondary phases. Moreover fluctuations of valency of Fe ion (from Fe^{3+} to Fe^{2+}) along with oxygen vacancies may cause high leakage current which can diminish high FE polarization. BFO can be synthesized in different form bulk, nano materials or thin film. There are impacts of size and morphologies of BFO nano structure upon magnetic properties. Magnetization increases with decrease in particle size and dramatically increases below 62nm. Similarly BFO nano wires are found to exhibit higher magnetization than nano rods and nano tubes[188][189]. High quality BFO film was first fabricated by Wang et al[190] with Pr ~ 55µC/cm2 at room temperature. The structure of BFO is dependent on thickness and epitaxial strain of substrate.

➤ <u>**Crystal structure and origin of ferroelectricity and magnetism:**</u>

BFO ceramic usually belong to rhombohedral (R-phase) symmetry with $R3c$ space group, lattice constant $a = 5.63\overset{\circ}{A}$ and angle $\alpha = 89.45°$ at room temperature[191]. Phase transition from Rhombohedral (R-phase) to orthorhombic (o-phase) can take place by adding dopants in Bi-site**Error! Bookmark not defined.**[192] or Fe-site[193][194] or when tensile strain is applied. Large strain can produce transition from R-phase to tetragonal phase (T- phase) also[72]. BFO films are grown usually in T-phase but when thickness dominates then they become purely R-like.

2 perovskite pseudo-cubic cells are connected along [111] direction to form rhombohedral cell. Each pseudo-cubic cell contains $Fe - O6$ octahedra in cetre and Bi3+ ions in each corner. The $Fe - O6$ octahedra are rotated around [111] axis by $11° - 14°$[195]. This octahedral rotation distorts oxygen octahedral also due to change in $Fe - O - Fe$ bond angle and is also the reason of orbital overlap or hybridization.

The hybridization between Bi^{3+} lone pair (6s orbitals) and O^{2-} (2p orbital) leads to displacement of Bi^{3+} ions (breaking inversion symmetry) from centro-symmetric position. This forms the localized dipoles result in FE polarization along [111] direction.

The spins of FE^{3+} are oriented anti-ferromagnetically along every faces except [110]. Each $3 \uparrow$ up- spins are surrounded by $6 \downarrow$ anti-parallel spins. Due to distortion the surrounding spins are not properly anti-parallel that means spins are canted. The spins are spatially modulated to form a spin cycloid with a period of 62nm[196]. BFO consists of anti-ferromagnetic plane (G-type normal to ferro electric direction[197]. The incomplete spin cycloid permits FM below 673K which is Neel temperature. Curie and Neel temperature both depend on particle size and morphology.

There were numerous experiments done to improve polarization from 6 µC/cm^2, first obtained at 1970, in BFO bulk to 55µC/cm^2 in BFO film at 2003[190]. The main drawback was large leakage current which can be overcome by ion substitution or making composite with other ABO_3 perovskite structure. The highest reported remanent polarization was observed by Ramesh's group with 100 µC/cm^2. Now with increasing strain phase transition occurs that is stated in previous paragraph. This phase transition is responsible for change in FE polarization direction from [110] to [001] to [010] when phase changes from orthorhombic to tetragonal M_A

to tetragonal M_C phases respectively[198][199]. The highest polarization was reported in tetragonal phase to be 150 $\mu C/cm^2$ theoretically[200], and 130 $\mu C/cm^2$ experimentally[201]. The spontaneous polarization is also proportional to strain in tetragonal phase.
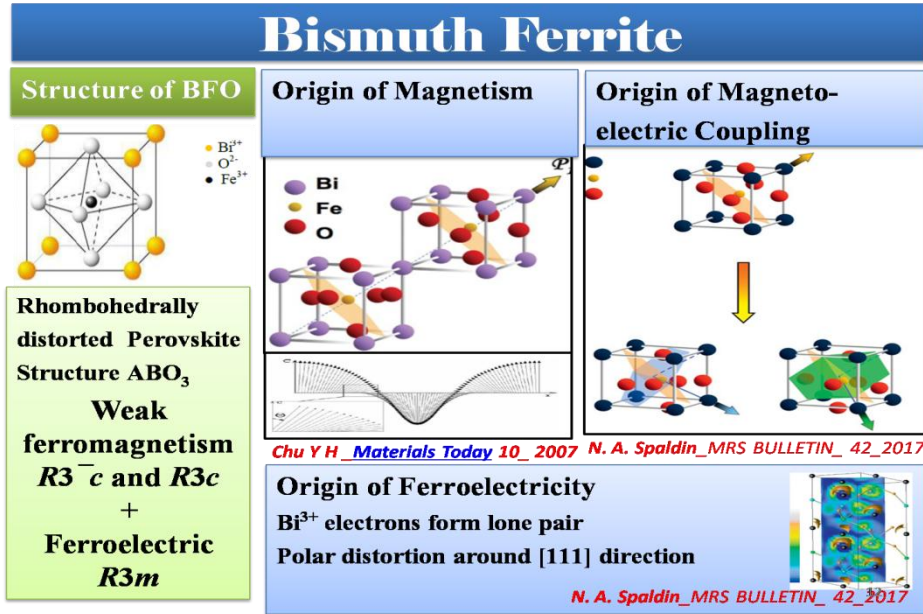
Figure 1.9 The crystal structure and origin of magnetism, ferroelectricity and magnet-electric coupling in BiFeO$_3$

As stated earlier, morphology and size can largely tune the magnetic properties along with doping at Fe-site also. There is also huge impact of epitaxial strain in modulating magnetic properties because strain causes additional anisotropy. Bulk like spiral modulated spin structure persists in BFO thin film under low strain[202]. When strain is increased then this cycloidal spin structure changes to pseudo-collinear anti-ferromagnetic structure and low energy magnon modes are also suppressed so that magnetic response gets changed. According to Chen et al[203] high strain changes average spin angle from in-plane [1$\bar{1}$0] direction to out of plane direction [110]. Whereas, strain can change the polarization direction from [111] to [110] by an angle ~15° only. Thus large strain can deviate the perpendicular relationship between magnetization and FE polarization. The strain can be engineered to modify magnetic orientation and also exchange bias which is *useful for Spintronics device applications*.

From the first observation of electrical control of AFM domain by Zhao *et al.*, numerous research activities were focused to couple magnetic and electrical order parameters[204]. The spontaneous polarization which is along [111] direction can only switches to either ~71° or 109° where AFM plane is perpendicular to polarization direction. There are only 2 plausible directions where coupling between AFM domain and FE domain exists. To achieve large ME

coupling FM/AFM heterostructures are found to be befitted because there exist magnetic anisotropy, at the interface, which can be modulated with epitaxial strain engineering. In this context oxide FM and transitional metal FM layers are mostly used in making heterostructure with BFO where LSMO[205] is used as oxide FM and $Co_{0.9}Fe_{0.1}$ [206] or Co[207] as transitional metal FM. In transitional metal/BFO heterostructures magnetic film of BFO film are reoriented with switching of external electric field. Maniputrani *et al.*[208] observed control of uni-directional anisotropy by external voltage in CoFe/BFO heterostructure. LSMO/BFO structure enables researchers to tune electrically control magnetic exchange bias and a useful step *towards spintronics applications*.

Allibe[209] first introduces GMR with the help of BFO based nano materials where exchange bias was regulated by applied voltage. Strain can be engineered to modify exchange bias, magnetic orientation and GMR response. Epitaxial strain can help in modulating anisotropy in interface of FM/AFM heterostructure. Lastly, electric field control over exchange bias in LSMO/BFO by Wu *et al.*[205] becomes the milestone for spintronics.

For spintronics application we cannot use single phase BFO we previous reports indicate towards heterostructure or composite of BFO.

1.8.3 <u>Literature review- graphene and BiFeO$_3$ hybrid structure</u>

1.8.3.1 <u>Proximity effect of magnetism on graphene</u>

Pristine graphene possess no SOC; it can be achieved by depositing 3d transition metal atoms on graphene[210] but metal adatoms tend to nucleate into cluster on graphene [211,212]. Now the focus made on graphene Hybrid Structures and their possibilities to spin orbit coupling. Y. Zhang *et al.* [213]first observed magneto-transport in a high-mobility single layer of graphene by adjusting the chemical potential with the use of the electric field effect and observed an unusual half integer quantum Hall effect for both electron and hole carriers in graphene. The relevance of Berry's phase to these experiments is confirmed by magneto-oscillations. The existence of a non-zero Berry's phase (a geometric quantum phase) of the electron wave function--a consequence of the exceptional topology of the graphene band structure is confirmed theoretically. Haugen et al[214] observed that interaction between electrons in graphene and the localized magnetic moments in the ferromagnetic insulator will give rise to a proximity-induced exchange splitting and he had used EuS as gate upon graphene. Dirac cone structure has 3DOFs; Spin, sub-lattice and valley; breaking AB sub lattice symmetry could open an energy band gap at Dirac point which promotes Valley contrasting Hall Magnetic and Optical property. Now Rashba SOC breaks the symmetry of graphene plane. There are two types of Spin Hall Effect Quantum Spin Hall effect (QSHE) and Quantum Anomalous Hall Effect (QAHE).

QSHE is too weak to demonstrate experimentally and need strong magnetic field and intrinsic SOC. Whereas QAHE can be realized by introducing Rashba SOC and an exchange field along with breaking of time reversal symmetry.Z. Quio *et al..* group[215] first indicated that Iron (Fe) adsorbed on graphene Led to strong hybridization between C and Fe 3d shell led to macroscopic exchange field. Other than adsorbates QAHE can be realized when the substrate satisfies the following criteria; (i) it is insulating so that graphene provides the only transport channel. (ii) Its orbital hybridize with those of graphene sufficiently to induce sizable exchange and spin-orbit coupling fields. (iii) Its dipolar magnetic field is sufficiently weak that the quantum anomalous Hall signature is not obscured by normal quantum Hall effect. In this quest to explore the possibility of depositing graphene on a proper magnetic substrate, which can induce both a time-reversal symmetry breaking exchange field and Rashba spin-orbit coupling due to broken inversion symmetrythe same group theoretically proved that graphene π bands spin split on a $BiFeO_3$ thin film substrate as seen in Figure 1.10.
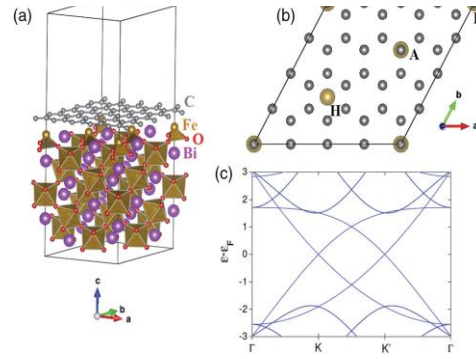
Figure 1.10 How the band spin splits in the graphene/BiFeO$_3$interface [18]

Small band gap (δ) opens near the graphene K and K_0 Dirac points which are located inside the bulk band gap Δ of the BiFeO3 thin film substrate. Berry curvature analysis confirmed that the resulting band gap is topologically nontrivial, yielding a two-dimensional quantum anomalous Hall phase. They also showed that δ can be increased to a value that is large enough for high temperature operation by reducing the separation between graphene and the thin film substrate[216]. They also confirmed that the two top sites (Fe) belong todifferent sublattices of graphene, the surface structure helps suppress induced staggered sublattice potentials, which favor valley-Hall-effect gap in graphene and are detrimental to QAHE. It can be clearly stated that Two-dimensional (2D) materials such as graphene are predicted to experience strong exchange field in hybrid heterostructures with magnetic materials and its electronic structure can be significantly modulated by proximity effect. Exchange proximity interaction with magnetic insulator with substantial exchange field was theroretically established using Ferromagnetic material[217,218], Anti ferromagnetic material[216], Topological material [219] , Magnetoelectric material [220] , Multiferroic material[252]. The experimental

[26]

demostration was done by some groups making heterostructure of graphene/YIG[221,222,223,224], graphene/EuS[225] and graphene/ BiFeO$_3$[226,227]. QAHE and Zeeman Spin Hall Effect with strong exchange field in graphene was observed by Wei P et al[225] and Wang et al[221]using YIG and EuS substrate.Now, Both the groups of Yan Fei Wu[226] and Hua Ding Song[227]had opted the configuration shown in FigFigure 1.11 and took BiFeO$_3$ single crystal on Single layer graphene and performed magneto trasport measurements in Hall bar configuration to directly correlate the zeeman splitting and QAHE with hall measurements.
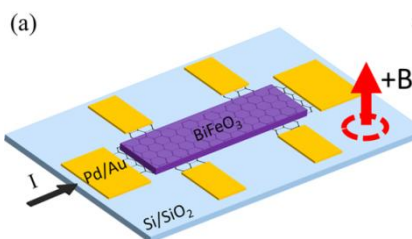
Figure 1.11 Configurations of graphene/BiFeO$_3$ hybrid structure for magneto transport measurement.

Quio et al[216]theoretically calculated the exchage splitting to be 70meV because of strong exchange interaction between 4d orbitals and graphene π orbitals and the 3d orbitals of the Fe layer; the experimental result showed that with increasing external perpendicular magnetic field, the $N = 0$ Landau level of graphene transforms from a ferromagnetic state to a canted anti-ferromagnetic state above 10T and a substantial exchange field observed up to 19.8-287.9 T. Hua Song Di *et al..* [227]showed similar observation with the variations that exchange field is larger in positive Magnetic field than negative. They have shown Spin splitting in Landau level at -6T which is the direct evidence of B$_{exc}$; this spin splitting was not observed at positive magnetic field. The net understanding is that electronic hybridization with proximity material can modulate the band structure of graphene. Inversion symmetry cannot lift the valley degeneracy [eigen state for one valley have the precise distribution of residing on only one sublattice A or B]. Peirls instability induced by B(Normal) give rise to sublattice ditortion in graphene- Breaks Mirror symmetry which inturn breaks inversion symmetry of A/B sublattice.Interfacial exchange splitting originates from the overlapping between wave function of localized moments and itinerant electrons at G/BFO interface: Breaks mirror symmetry results exchange spilitting and QAHE. The confirmed result state that Positive and negative fields have assymetric influence on net magnetic moment of Fe atoms. External magnetic field helps to align the magnetic moments of Fe atoms and enhance the magnetic proximity effect.

Strong exchange coupling at G/BFO interface can enhanceinterfacial magnetization as feed back effect.

1.8.3.2 **Proximity effect of ferroelectricity on graphene**

The traditional heterostructures with covalent bonding at the interface has possibilities of the interfacial issues, such as lattice mismatch or atomic diffusion.The passivated surface without dangling bonds interacts with one another via weak vdWs force.Unlike The electronic properties of atomically thin 2D materials are quite sensitive to external stimulus like especially electric field or charge accumulation/ depletion of underlying layer and accumulation ofsurface charges from 2D materials enhances possibilities of Ferroelectric polarization[228]. graphene or (TMD) as 2D material with PVDF-TrFE and $Pb(Zr_{0.2}Ti_{0.8})O_3$ was taken by H Lu et al[229] and they had shown that Ferroelectric material acted as a gate dielectric to modulate the in plane electric behaviour (conductivity or carrier mobility) of the channel (2D materials) and the out-of plane electrical transport of 2D/FE hetero-junctions is induced by ferroelectric polarization.Gruverman's group [230] had taken graphene as an electrode to study the out-of-plane transport behaviour in ferroelectric tunnel junctions, and found the significant enhancement of tunneling electroresistance (TER) . MoS_2–$BaTiO_3$ heterostructure had taken by T Li et al[231] where MoS_2 as 2D material and reported ferroelectric polarization induced reversible accumulation/depletion of carriers in MoS_2. Controllable p-n Junc in graphene depending on the polarized ferro substrate was studied by C. Bauemer et al[232] and J. H. Hinnerfield[233] group but Yang Li et al[228]first reported experimentally that modulation of the contact barriers and depletion width at the hetero-interface induced by the ferroelectric polarization in graphene/$BiFeO_3$ and MoS_2/ $BiFeO_3$ heterojunctions. Their group showed graphene as electrode does not affect the Ferroelectric behavior of $BiFeO_3$ but with different bias field the G/BFO/NSTO structure showed different diode behavior as seen in Figure 1.12.
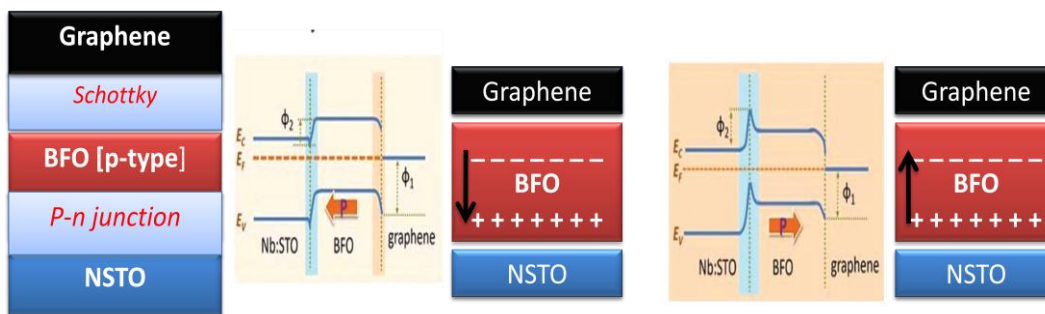
Figure 1.12 forward and reverse diode behaviour with Up and Down polarization in BiFeO₃

Here $BiFeO_3$ behaves as p type with respect to NSTO substrate and formed a Schottky junction at the graphene interface. With the downward polarization in $BiFeO_3$ layer positive bound charges accumulate; Electrons (majority) from NSTO attracted towards $BiFeO_3$ layer

and flow of electrons reduces. In contrast electrons at $BiFeO_3$ /G region inturn increases E_F in graphenewhich showed positive diode like behavior. The opposite is the case forupward polarization which shows reverse diode like behavior. The resistance On/Off ratio is inversly proportinal to the no of layer inc. Here it has shown that work function of graphene can be easily tuned by external stimuli like electric field.

Electrostatic Charge doping in graphene by ferroelectric polarization could be achieved in graphene Hybrid structures combined with functional materials such as ferroelectric oxides[234,235,236,237]and ferroelectric perovskites [238,239,240,241]; where high dielectric constants constant of ferroelectric perovskites facilitate higher carrier density and mobility by electric field gating of graphene as compared to other dielectrics. W. Jie et al[242] and B. E. Song[243] *et al..* group studied switchable spontaneous polarization of Ferroelectric substrates ; non volatile resistance hysterisis in graphene/ ferroelectric hybrid structure. Jian-Qing Dai[244] theorectically studied how influencial the surface termination of $BiFeO_3$ is on the graphene/$BiFeO_3$ hybrid structure via 1st principal calculations. They have took trilayer of $BiFeO_3$ negatively terminated at graphene region with the (001) plane inclination and attached via VanderWalls bonding. The ferroelectric polarization of the underlying substrate is responsible for electrostatic charge doping on graphene by inducing spin polarized Dirac Fermions on graphene. Doping type & carrier density is not proportional to polarization direction but proportional to electro negativity difference between graphene and $BiFeO_3$.Intrinsic resistance change in graphene on ferroelectric substrate can show proper hysteresis or anti-hysteresis behavior depending on surface terminations. Moreover Different surface termination means different electrostatic potential graphene (High electrostatic potential : large electron affinity) and different electrostatic charge doping on graphene. Here, Π bonds of C $2p_z$ orbital loose electon & O^{3-} orbitals gain electron and according to Pauling's the electronegativity difference of Bi [2.02] & C [2.55] is responsible for electron transfer (Bi termination).
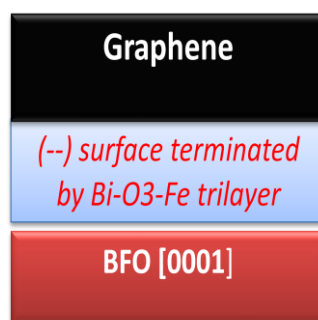
Figure 1.13 Configuration taken by Jian-Quing Dai group

They indicates that if Fe-O_3 termination ocuurs then O-C electronegativity dfference will be larger and electron will transfer from graphene to BFO [p type charge doping in graphene].graphene is adsorbed on BFO by weak vDW bond thus absence of bond attractor in G/BFO interface implies unshared electrons feature of coupling between G & BFO surface. Without bonding this feauture also promotes coupling between them.

1.8.3.3 **Magnetoelectric control effect on graphene**

The new genre of magnetoelectric coupling was achieved in functionalized graphene conciliated by charge carriers on the surface. Acording to previous literature the functinalization was done by using adatoms [245] [246] and Nitrophenyl diazonium molecule (NPD)[247248,249]. Magnetism was induced by aryl radicals covalently attached on top graphene layer. These Radicals are sensitive to external electric field which coupled to interlayer charge imbalance; yields strong magnetoelectric coupling. This Interplay lead to fully polarized spin state (half metalicity) efficiency nearly to 100% spin polarization is observed at low electric bias. Here selection of spin conductive channel is determined by field polarization. Elton J. G. Santos[250] studied the NPD functinalized graphene attached on the top layer of graphene and address that the magnetoelectric coefficient is dependent on no of layers of graphene; higher the no of layers the coefficient would be comparable to perovskite.

He calculated magnetoelectric coefficient α= (6.03- 32.2)E-14 G cm^2 /V in single layer and for 176 Layers α= 2E-12 G cm^2 /V via 1st Principal calculations. He further showed radicals (NPD concentration 3.1% to 0.8%) generate strong spin charge coupling which induces Magnetoelectric coupling [comparable in magnitude to those found in thin films based on 3d transition metals (Fe, Co, and Ni), perovskite interfaces, and half-metals]. According to their report Electric field generates polarization charge density $\Delta\rho$ localized at NPD molecules and bottom G layer which creates dipole moment in slab [protects Electric field over screening length of layers]. Main contribution for this spin polarization does come from 1st C neighbour to the adsorption site.For single layer, adsorbates induced dispersion less defect state which appeared at E_F . $2p_z$ contribution from 3C atoms near to adsorbtion site had more contribution than this defect states. Half filled character of this $2p_z$ defect band combined with its dispersionless behavior induces spin splitting between Up & DN state. When another Layer introduced then another Dirac Cone created at K point that couples with $2p_z$ defect band at E_F. At E=0 negligible charge transfer between molecule at C plane maintain defect level at similar point. Now the coupling between $2p_z$ defect band and Dirac Cone of 2nd Layer in electrically sensitive and can be drawn by bias. Dirac Cone shift Up or Downward depending on defect states which promotes interlayer charge transfer and inturn changes spin polarization induced by adsorbate.
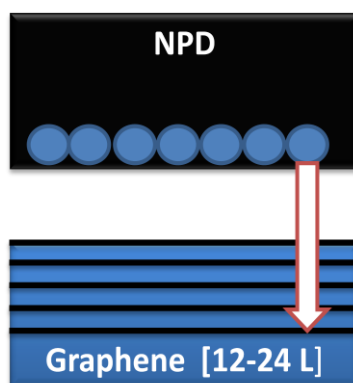
Figure 1.14 configuration of NPD on graphene layers [56]
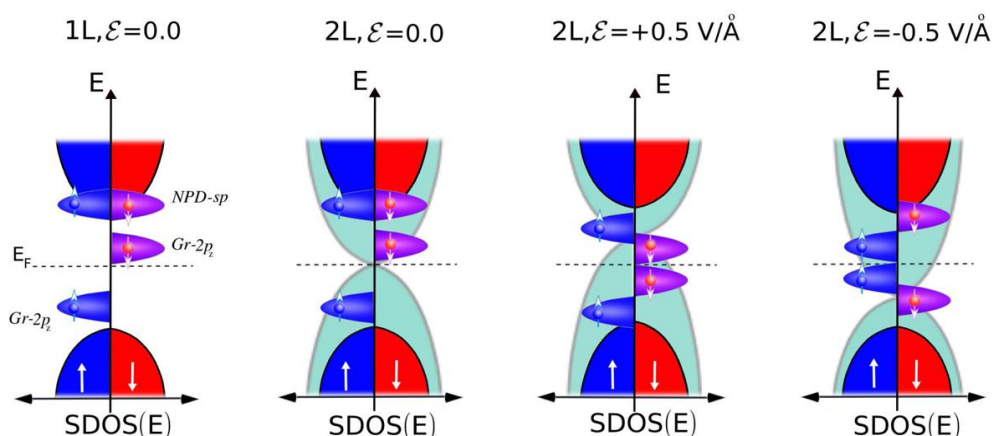
Figure 1.15 Change in Density of states in NPD attached graphene

There is less work done on this field and ferroelectric control of magnetic proximity is not yet achieved experimentally but theoretically has done by F. Ibrahim[251] group. They have performed 1st principal calculation on graphene/BiFeO₃/ graphene heterostructure where 3layers of BiFeO₃sandwiched between two graphene layers with Fe termination and (111) inclination as seen in Figure 1.16. Spin dependent electronic structure of graphene is highly influenced not only by Magnetic order but also by ferroelectric polarization in underlying BFO. Fe and Bi have z displacement from their centro-symmetric position per atomic layer but two surfaces of BFO/G have different values of atomic displacements. Both the surfaces are polar with net charge but no charge lies inside slab; Negative charge accumulated in graphene side screens positive charges.

[31]
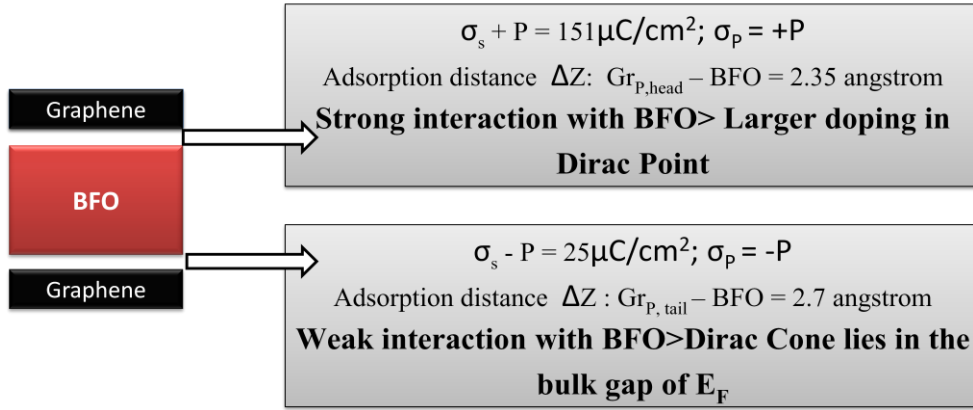
Figure 1.16 Schematic of graphene/BFO/graphene

Proximity of BFO induces modification in linear dispersion of graphene band structure opening a band gap at Dirac Point. This degenaracy at Dirac Point is spin dependent. An additional band opened with the impact of SOC.This genre need more impact in future.

1.9 <u>Motivation of our work</u>

Following the literature there are few ambiguities which need detail investigations. They are as follows,

- Single atomic layer provides stronger hybridization with the substrate than few layers but multi-layer graphene generate strong spin charge coupling

- In Bonded structure there is strong electronic hybridization with proximity material which produces Dirac splitting but bonding also arise lattice mismatch or atomic diffusion. Absence of bond implies unshared electron features

- Modulation of graphene Properties by introducing multiferroic (either bonded or non bonded) was reported but modulation of Multiferroic properties with the introduction of graphene is not reported yet.

Zanoli[252] theoretically studied graphene/$BaMnO_3$ composite interface and figured out the role of C-Mn bonding in inducing magnetism and spin splitting of Dirac cones up to 300meV. Based on these ambiguities there are few questions raised in our mind that is which structure is ideal for enhancement of properties?

(i) graphene Multiferroic Nano composite or graphene/ Multiferroic hybrid structure?

(ii) SLG or Multi layer graphene?

(iii) Covalent interaction or Van der Waals Interaction between graphene and multiferroic in composite?

This attracts our attention to perovskite-graphene composites where Bismuth Ferrite (BFO) as a choice of perovskite. According to the literature the magnetoelectric coupling between graphene composites are also not addressed yet and our focus is on that. Our work is based on functionalize graphene and make composite with BFO to manipulate properties for the advancement in magnetoelectric domain for further applications in spintronics. BFO, a Magnetoelectric multiferroic enable us to witness enormous applications in spintronics are already discussed in section 1.8.2. The schematic of our research work is shown in Figure 1.17.

Figure 1.17 The schematic of Research outline
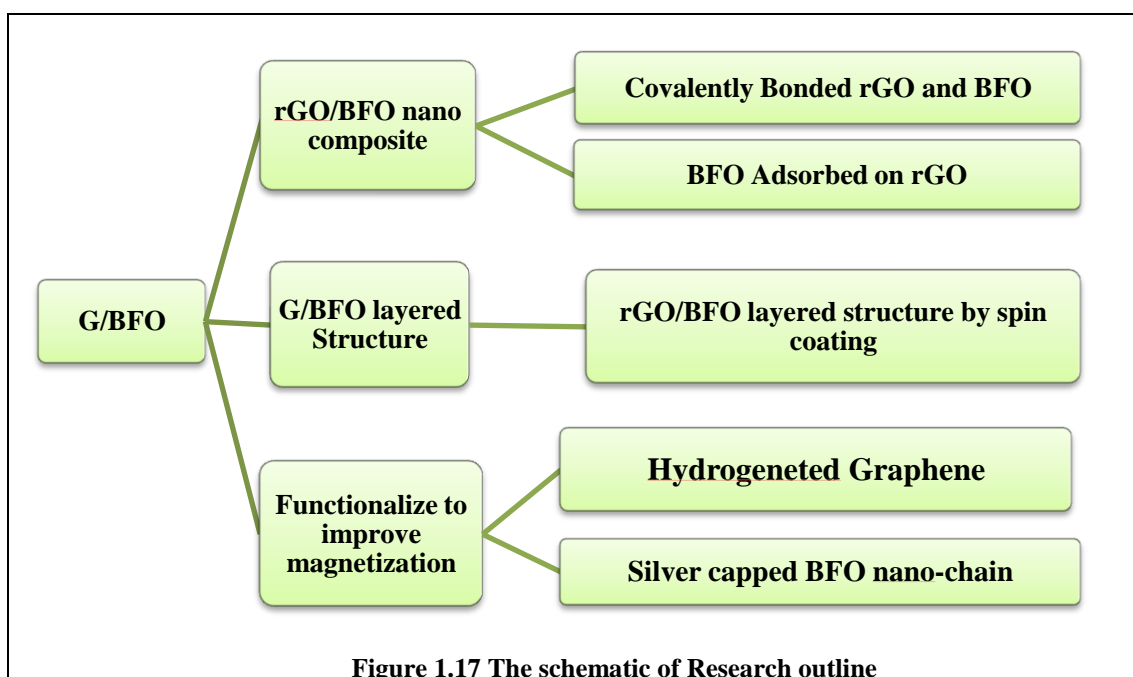
We have used reduced graphene oxide as one of the graphene derivates or multi layer graphene. Reduced graphene oxide can be synthesized in various ways one of them is electrochemical routes using the starting material Graphite which is honeycomb stacking of 2D graphene. Graphite can be oxidized using Modified Hummers Method and via exfoliation we have reduced graphene Oxide (rGO) is multilayer stacking of graphene.

> ➤ *Literature review- rGO/BFO* **nano** *composite:*
> Reduced graphene oxide (rGO) and Bismuth Ferrite (BFO) composite is well studied in past decades for its enhanced optical properties[253 254] with superior band gap energy which is necessary for high SOC. Some studies are reported with a little change in magnetization in composite than pure phase $BiFeO_3$ with an ambiguity in the source of magnetization. Tie Li reported the change in magnetization ~0.003 emu/g in composite than pure phase $BiFeO_3$ but no precise origination is justified[255] D.Moitra group showed that with the variation of graphene loading the magnetization decreases than pure phase $BiFeO_3$[256] Jalil *et al.* pointed on the

suppression of spin cycloid structure in composite for increase in magnetization but more magnetization was reported for selenite phase $Bi_{25}FeO_{40}$ [257]. G.Volonakis reported that ferroelectric distortion can be induced in graphene- $MaPbI_3$ structure through charge rearrangement at graphene–perovskite interstitial region [258]. D.Moitra *et al.* through DFT calculation suggests that there is a possibility of having Ferro electricity in this composite structure. Apart from other novel functionalities possible in graphene-multiferroic composites, the question; whether magnetoelectric multiferroicity itself- i.e., ferroelectric and magnetic order and their cross-coupling -can enhance dramatically in such composites is still an open one.

In our first approach we aim to introduce hybrid organic material- reduced graphene oxide (rGO) and Bismuth Ferrite (BFO) nano composite in two different routes one is in-situ hydrothermal and another is sono-chemical mixing in order to investigate via thorough comparative characterization that how the bonding between rGO and BFO manipulates the properties indifferently in covalent bonded one and non bonded one. In literature there shows indifferent properties like with covalent attachment the magnetic property enhances but opposite is the case while manipulating the charge state with ferroelectric polarization. There is only Vander walls attraction needed to manipulate the properties. Our sole aim is to investigate if the property though enhances then what would be the reason behind the improvement of the properties. Does bonding with magnetic ions and carbon atoms is necessary or only Vander-Walls bond play the key role? These bonding have a huge impact on the properties which need to be explored in our work.

In our second approach we want justification of the question that which would be beneficial in tuning magnetic and ferroelectric properties of BFO when rGO is introduced as a composite or hybrid structure? For this reason we aim to make hybrid heterostructure of BFO and rGO in order to study the magnetic and ferroelectric properties with a simplest and cheapest spin coating technique and compare the results with bonded and non-bonded composites as well.

In our third approach we turn our focus to functionalize both graphene and $BiFeO_3$ in order to improve their magnetization independently and to make heterostructure or composite of highly magnetic graphene and $BiFeO_3$ in near future.

Though researchers have made different types of BFO nano particles for over a century but it is still a challenge to overcome agglomeration of BFO when its size comes below 100nm. There were numerous efforts have been made to make highly magnetic BFO but we want to make BFO with high saturation magnetization comparable to nano scale alloys $Fe_{65}Co_{35}$ (~240emu/g), $Fe_{100-x}Co_x$, or iron oxide (~70-80emu/g) nano particles So that to enhance the magnetic properties we will introduce Silver, as a promising antimicrobial agent, in-spite of using surfactants. We aim to make a proper array of BFO nano chains wrapped in silver matrix which may also have high bio-compatibility.

In our whole work we will work with rGO as a derivative of graphene. Now we will approach towards working with Single Layer graphene fabricated using Chemical vapour Deposition Technique (CVD). Single layer graphene (SLG) is diamagnetic in nature but there were efforts made to make it magnetic like adding adatoms, vacancies, adsorbates or inducing edges or defects. But when we have an aim to make heterostructure of magnetic SLG with BFO then we must not consider the approaches that may be detrimental to ferroelectric properties of BFO. So that we want easier lab based and more cheaper approaches to make SLG magnetic. So we want to modify SLG chemically to introduce magnetism in it and for that we will opt for hydrogenation reaction. The hydrogenation of SLG and reversible de-hydrogenation of SLG chemically able us to notice subtle change in magnetic ordering as well as band gap tuning.

1.10 <u>Thesis organization</u>

In this present chapter we have discussed from the origin of multiferroicity and different art of mechanisms to their discrepancies in single phase system and discussed the new genres and their advancement in various device applications. From there we have pointed out why Spintronics application allures our attention and have also discussed how our interest generates in the branch of graphene/BiFeO$_3$ multiferroic composite/hybrid structure following a thorough literature review in those systems.

Excluding the first one this Thesis includes following chapters,

Chapter 2 describes different synthesis techniques we have opted for in our sample preparation and in-detail summary of synthesis procedures of all materials. This chapter also includes brief description of all experimental set up and instruments that we have used to characterize the samples and to study various properties.

In *Chapter 3* we have discussed comparative study of magnetic and ferroelectric properties rGO/BFO nano composite of bonded and non-bonded one. This chapter also presents the origin of structural dissimilarities in both composites and their impact on magnetic and ferroelectric properties.

In *Chapter 4* we have discussed a new research finding: the non-monotonic magnetic field dependence of ferroelectric polarization in covalently bonded nano composite. It was studied from both direct experimental approach and from Neutrons diffraction study.

In *Chapter 5* we have discussed the simplest technique to make BFO and rGO hybrid heterostructure using spin-coating techniques. Various spin coating parameters are controlled and their effects on film making were discussed in this chapter. Then we finally arrive to discuss the study of magnetic and ferroelectric properties.

In ***Chapter 6*** we have discussed another new finding of 20 times enhancement of magnetisation in silver wrapped self assembly of BiFeO₃ nano chain. The details methodology and magnetic studies are enclosed in this chapter.

In ***Chapter 7*** we have discussed the functionalization of single layer graphene to enhance its magnetic property to ferromagnetism via hydrogenetation. The chemical reversible process of de-hydrogenetion was also included.

Chapter 8 is the final chapter to summarize important findings of all research works done related to this thesis. The chapter also concludes to give new exposure in this field and interpret new direction for future applications.

1.11 <u>Bibliography</u>

[1] Wadhawan, V., 2000. *Introduction to ferroic materials*. CRC press.

[2] Aizu, K., 1970. Possible species of ferromagnetic, ferroelectric, and ferroelastic crystals. *Physical Review B*, *2*(3), p.754.

[3] Litvin, D.B., 2008. Ferroic classifications extended to ferrotoroidic crystals. *Acta Crystallographica Section A: Foundations of Crystallography*, *64*(2), pp.316-320.

[4] Schmid, H., 1994. Multi-ferroic magnetoelectrics. Ferroelectric*s*, *162*(1), pp.317-338.

[5] Rivera, J.P., 1994. On definitions, units, measurements, tensor forms of the linear magnetoelectric effect and on a new dynamic method applied to Cr-Cl boracite. Ferroelectric*s*, *161*(1), pp.165-180.

[6] Srinivasan, G., 2010. Magnetoelectric composites. *Annual Review of Materials Research*, *40*, pp.153-178.

[7] Debye, P., 1926. Bemerkung zu einigen neuen Versuchen über einen magneto-elektrischen Richteffekt. *Zeitschrift für Physik*, *36*(4), pp.300-301.

[8] Curie, P., 1894. Sur la symétrie dans les phénomènes physiques, symétrie d'un champ électrique et d'un champ magnétique. *Journal de physique théorique et appliquée*, *3*(1), pp.393-415.

[9] Smolenskiĭ, G.A. and Chupis, I.E.E., 1982. Ferroelectromagnets. *Soviet Physics Uspekhi*, *25*(7), p.475.

[10] Ascher, E., Rieder, H., Schmid, H. and Stössel, H., 1966. Some properties of ferromagnetoelectric nickel-iodine boracite, Ni3B7O13I. *Journal of Applied Physics*, *37*(3), pp.1404-1405.

[11] Schmid, H., 2012. The dice-Stone der Würfelstein: Some personal souvenirs around the discovery of the first ferromagnetic ferroelectric. Ferroelectric*s*, *427*(1), pp.1-33.

[12] Landau, L.D., Bell, J.S., Kearsley, M.J., Pitaevskii, L.P., Lifshitz, E.M. and Sykes, J.B., 2013. *Electrodynamics of continuous media* (Vol. 8). elsevier.

[13] Dzyaloshinskii, I.E., 1960. On the magnetoelectrical effects in antiferromagnets. *Soviet Physics JETP*, *10*, pp.628-629.

[14] Astrov, D.N., 1960. The magnetoelectric effect in antiferromagnetics. *Sov. Phys. JETP*, *11*(3), pp.708-709.

[15] Folen, V.J., Rado, G.T. and Stalder, E.W., 1961. Anisotropy of the magnetoelectric effect in Cr 2 O 3. *Physical Review Letters*, *6*(11), p.607.

[16] Rado, G.T. and Folen, V.J., 1961. Observation of the magnetically induced magnetoelectric effect and evidence for antiferromagnetic domains. *Physical review letters*, *7*(8), p.310.

[17] O'Dell, T.H., 1962. The electrodynamics of magnetoelectric media. *Philosophical Magazine*, *7*(82), pp.1653-1669.

[18] Wood, V.E. and AE, A., 1974. Possible applications for magnetoelectric materials.

[19] Newnham, R.E., Kramer, J.J., Schulze, W.A. and Cross, L.E., 1978. Magnetoferroelectricity in Cr2BeO4. *Journal of Applied Physics*, *49*(12), pp.6088-6091.

[20] Hill, N.A., 2000. Why are there so few magnetic ferroelectrics?. *The journal of physical chemistry B*, *104*(29), pp.6694-6709.

[21] Fiebig, M., Lottermoser, T., Fröhlich, D., Goltsev, A.V. and Pisarev, R.V., 2002. Observation of coupled magnetic and electric domains. *Nature*, *419*(6909), pp.818-820.

[22] Kimura, T., Goto, T., Shintani, H., Ishizaka, K., Arima, T.H. and Tokura, Y., 2003. Magnetic control of ferroelectric polarization. *nature*, *426*(6962), pp.55-58.

[23] Hur, N., Park, S., Sharma, P.A., Ahn, J.S., Guha, S. and Cheong, S.W., 2004. Electric polarization reversal and memory in a multiferroic material induced by magnetic fields. *Nature*, *429*(6990), pp.392-395.

[24] Fiebig, M., 2005. Revival of the magnetoelectric effect. *Journal of physics D: applied physics*, *38*(8), p.R123.

[25] Teague, J.R., Gerson, R. and James, W.J., 1970. Dielectric hysteresis in single crystal BiFeO3. *Solid State Communications*, *8*(13), pp.1073-1074.

[26] Fischer, P., Polomska, M., Sosnowska, I. and Szymanski, M., 1980. Temperature dependence of the crystal and magnetic structures of BiFeO3. *Journal of Physics C: Solid State Physics*, *13*(10), p.1931.

[27] Wang, J.B.N.J., Neaton, J.B., Zheng, H., Nagarajan, V., Ogale, S.B., Liu, B., Viehland, D., Vaithyanathan, V., Schlom, D.G., Waghmare, U.V. and Spaldin, N.A., 2003. Epitaxial BiFeO3 multiferroic thin film heterostructures. *science*, *299*(5613), pp.1719-1722.

[28] Shubnikov, A.V., 1951. Symmetry and antisymmetry of finite figures, Moscow: USSR Acad.

[29] Shuvalov LA and NV Belov 1962. *Sov. Phys. Crystallogr*, *7*, p.150.

[30] O'Dell, T.H., 1970. *The electrodynamics of* magnetoelectric *media* (Vol. 11). North-Holland Publishing Company.

[31] Birss, R.R., 1966. Symmetry and Magnetism North-Holland.

[32] Schmid, H., 2008. Some symmetry aspects of ferroics and single phase multiferroics. *Journal of Physics: Condensed Matter*, *20*(43), p.434201.

[33] Vopson, M.M., 2015. Fundamentals of multiferroic materials and their possible applications. *Critical Reviews in Solid State and Materials Sciences*, *40*(4), pp.223-250.

[34] Wang, J.B.N.J., Neaton, J.B., Zheng, H., Nagarajan, V., Ogale, S.B., Liu, B., Viehland, D., Vaithyanathan, V., Schlom, D.G., Waghmare, U.V. and Spaldin, N.A., 2003. Epitaxial BiFeO3 multiferroic thin film heterostructures. *science*, *299*(5613), pp.1719-1722.

[35] Fedulov, S.A., 1961. Determination of Curie temperature for the BiFeO_3 ferroelectric. In *Doklady Akademii Nauk* (Vol. 139, No. 6, pp. 1345-1346). Russian Academy of Sciences.

[36] Kiselev, S.V., Ozerov, R.P. and Zhdanov, G.S., 1963, February. Detection of magnetic order in ferroelectric BiFeO 3 by neutron diffraction. In *Soviet Physics Doklady* (Vol. 7, p. 742).

[37] Coeuré, P., Guinet, P., Peuzin, J.C., Buisson, G. and Bertaut, E.F., 1966. Ferroelectric properties of hexagonal orthomanganites of yttrium and rare earths. In *Proceedings of the International Meeting on* Ferroelectri*city* (Vol. 1, p. 332). Institute of Physics of the Czechoslovak Academy of Sciences, Prague.

[38] Van Aken, B.B., Palstra, T.T., Filippetti, A. and Spaldin, N.A., 2004. The origin of ferroelectricity in magnetoelectric YMnO3. *Nature materials*, *3*(3), pp.164-170.

[39] Fennie, C.J. and Rabe, K.M., 2005. Ferroelectric transition in Y Mn O 3 from first principles. *Physical Review B*, *72*(10), p.100103.

[40] Lilienblum, M., Lottermoser, T., Manz, S., Selbach, S.M., Cano, A. and Fiebig, M., 2015. Ferroelectricity in the multiferroic hexagonal manganites. *Nature Physics*, *11*(12), pp.1070-1073.

[41] Fiebig, M., Fröhlich, D., Kohn, K., Lottermoser, T., Pavlov, V.V. and Pisarev, R.V., 2000. Determination of the magnetic symmetry of hexagonal manganites by second harmonic generation. *Physical review letters*, *84*(24), p.5620.

[42] Eibschütz, M., Guggenheim, H.J., Wemple, S.H., Camlibel, I. and DiDomenico Jr, M., 1969. Ferroelectricity in BaM2+ F4. *Physics Letters A*, *29*(7), pp.409-410.

[43] Benedek, N.A. and Fennie, C.J., 2011. Hybrid improper ferroelectricity: a mechanism for controllable polarization-magnetization coupling. *Physical review letters*, *106*(10), p.107204.

[44] Ikeda, N., Ohsumi, H., Ohwada, K., Ishii, K., Inami, T., Kakurai, K., Murakami, Y., Yoshii, K., Mori, S., Horibe, Y. and Kitô, H., 2005. Ferroelectricity from iron valence ordering in the charge-frustrated system LuFe2O4. *Nature*, *436*(7054), pp.1136-1138.

[45] Van Den Brink, J. and Khomskii, D.I., 2008. Multiferroicity due to charge ordering. *Journal of Physics: Condensed Matter*, *20*(43), p.434217.

[46] Choi, Y.J., Yi, H.T., Lee, S., Huang, Q., Kiryukhin, V. and Cheong, S.W., 2008. Ferroelectricity in an Ising chain magnet. *Physical review letters*, *100*(4), p.047601.

[47] Jooss, C., Wu, L., Beetz, T., Klie, R.F., Beleggia, M., Schofield, M.A., Schramm, S., Hoffmann, J. and Zhu, Y., 2007. Polaron melting and ordering as key mechanisms for colossal resistance effects in manganites. *Proceedings of the National Academy of Sciences*, *104*(34), pp.13597-13602.

[48] Cheong, S.W. and Mostovoy, M., 2007. Multiferroics: a magnetic twist for ferroelectricity. *Nature materials*, *6*(1), pp.13-20.

[49] Monceau, P., Nad, F.Y. and Brazovskii, S., 2001. Ferroelectric Mott-Hubbard phase of organic (TMTTF) 2 X conductors. *Physical Review Letters*, *86*(18), p.4080.

[50] de Groot, J.D., Mueller, T., Rosenberg, R.A., Keavney, D.J., Islam, Z., Kim, J.W. and Angst, M., 2012. Charge order in LuFe 2 O 4: an unlikely route to ferroelectricity. *Physical review letters*, *108*(18), p.187601.

[51] Katsura, H., Nagaosa, N. and Balatsky, A.V., 2005. Spin current and magnetoelectric effect in noncollinear magnets. *Physical review letters*, *95*(5), p.057205.

[52] Mostovoy, M., 2006. Ferroelectricity in spiral magnets. *Physical review letters*, *96*(6), p.067601.

[53] Arima, T.H., 2007. Ferroelectricity induced by proper-screw type magnetic order. *Journal of the Physical Society of Japan*, *76*(7), pp.073702-073702.

[54] Kenzelmann, M., Lawes, G., Harris, A.B., Gasparovic, G., Broholm, C., Ramirez, A.P., Jorge, G.A., Jaime, M., Park, S., Huang, Q. and Shapiro, A.Y., 2007. Direct transition from a disordered to a multiferroic phase on a triangular lattice. *Physical review letters*, *98*(26), p.267205.

[55] Kimura, T., Lashley, J.C. and Ramirez, A.P., 2006. Inversion-symmetry breaking in the noncollinear magnetic phase of the triangular-lattice antiferromagnet Cu Fe O 2. *Physical Review B*, *73*(22), p.220401.

a. Seki, S., Onose, Y. and Tokura, Y., 2008. Spin-driven ferroelectricity in triangular lattice antiferromagnets A CrO 2 (A= Cu, Ag, Li, or Na). *Physical review letters*, *101*(6), p.067204.

b. Kimura, K., Nakamura, H., Ohgushi, K. and Kimura, T., 2008. Magnetoelectric control of spin-chiral ferroelectric domains in a triangular lattice antiferromagnet. *Physical Review B*, *78*(14), p.140401.

[56] Wu, H., Burnus, T., Hu, Z., Martin, C., Maignan, A., Cezar, J.C., Tanaka, A., Brookes, N.B., Khomskii, D.I. and Tjeng, L.H., 2009. Ising magnetism and ferroelectricity in Ca 3 CoMnO 6. *Physical review letters*, *102*(2), p.026404.

[57] Sergienko, I.A., Şen, C. and Dagotto, E., 2006. Ferroelectricity in the magnetic E-phase of orthorhombic perovskites. *Physical review letters*, *97*(22), p.227204.

[58] Lorenz, B., Wang, Y.Q. and Chu, C.W., 2007. Ferroelectricity in perovskite Ho Mn O 3 and Y Mn O 3. *Physical Review B*, *76*(10), p.104405.

[59] Bulaevskii, L.N., Batista, C.D., Mostovoy, M.V. and Khomskii, D.I., 2008. Electronic orbital currents and polarization in Mott insulators. *Physical Review B*, *78*(2), p.024402.

[60] Prellier, W., Singh, M.P. and Murugavel, P., 2005. The single-phase multiferroic oxides: from bulk to thin film. *Journal of Physics: Condensed Matter*, *17*(30), p.R803.

[61] Vopsaroiu, M., Stewart, M., Hegarty, T., Muniz-Piniella, A., McCartney, N., Cain, M. and Srinivasan, G., 2008. Experimental determination of the magnetoelectric coupling coefficient via piezoelectric measurements. *Measurement Science and Technology*, *19*(4), p.045106.

[62] Nan, C.W., Bichurin, M.I., Dong, S., Viehland, D. and Srinivasan, G., 2008. Multiferroic magnetoelectric composites: Historical perspective, status, and future directions. *Journal of applied physics*, *103*(3), p.1.

[63] Ederer, C. and Spaldin, N.A., 2005. Weak ferromagnetism and magnetoelectric coupling in bismuth ferrite. *Physical Review B*, *71*(6), p.060401.

[64] Priya, S., Islam, R., Dong, S. and Viehland, D., 2007. Recent advancements in magnetoelectric particulate and laminate composites. *Journal of Electroceramics*, *19*, pp.149-166.

[65] Suastiyanti, D., Ismojo, M.W. and Wijaya, M., 2017. Magnetic Properties of Magnesium Doped Bismuth Ferrite as Multiferroic Material Produced by Sol-Gel Method at Low Temperature. *International Journal of Advanced Research*, *5*(5), pp.1954-1963.

[66] Song, S., Han, H., Jang, H.M., Kim, Y.T., Lee, N.S., Park, C.G., Kim, J.R., Noh, T.W. and Scott, J.F., 2016. Implementing Room-Temperature Multiferroism by

Exploiting Hexagonal-Orthorhombic Morphotropic Phase Coexistence in LuFeO3 Thin Films. *Advanced Materials*, *28*(34), pp.7430-7435.

[67]   Vopsaroiu, M., Stewart, M., Hegarty, T., Muniz-Piniella, A., McCartney, N., Cain, M. and Srinivasan, G., 2008. Experimental determination of the magnetoelectric coupling coefficient via piezoelectric measurements. *Measurement Science and Technology*, *19*(4), p.045106.

[68]   Zheng, H., Wang, J., Lofland, S.E., Ma, Z., Mohaddes-Ardabili, L., Zhao, T., Salamanca-Riba, L., Shinde, S.R., Ogale, S.B., Bai, F. and Viehland, D., 2004. Multiferroic batio3-cofe2o4 nanostructures. *Science*, *303*(5658), pp.661-663.

[69]   Wang, J.B.N.J., Neaton, J.B., Zheng, H., Nagarajan, V., Ogale, S.B., Liu, B., Viehland, D., Vaithyanathan, V., Schlom, D.G., Waghmare, U.V. and Spaldin, N.A., 2003. Epitaxial BiFeO3 multiferroic thin film heterostructures. *science*, *299*(5613), pp.1719-1722.

[70]   Yang, Y., Infante, I.C., Dkhil, B. and Bellaiche, L., 2015. Strain effects on multiferroic BiFeO3 films. *Comptes Rendus Physique*, *16*(2), pp.193-203.

[71]   Heron, J.T., Schlom, D.G. and Ramesh, R., 2014. Electric field control of magnetism using BiFeO3-based heterostructures. *Applied Physics Reviews*, *1*(2), p.021303.

[72]   Sando, D., Barthélémy, A. and Bibes, M., 2014. BiFeO3 epitaxial thin films and devices: past, present and future. *Journal of Physics: Condensed Matter*, *26*(47), p.473201.

[73]   Yan, L., Yang, Y., Wang, Z., Xing, Z., Li, J. and Viehland, D., 2009. Review of magnetoelectric perovskite–spinel self-assembled nano composite thin films. *Journal of Materials Science*, *44*, pp.5080-5094.

[74]   Gong, C., Li, L., Li, Z., Ji, H., Stern, A., Xia, Y., Cao, T., Bao, W., Wang, C., Wang, Y. and Qiu, Z.Q., 2017. Discovery of intrinsic ferromagnetism in two-dimensional van der Waals crystals. *Nature*, *546*(7657), pp.265-269.

[75]   Huang, B., Clark, G., Navarro-Moratalla, E., Klein, D.R., Cheng, R., Seyler, K.L., Zhong, D., Schmidgall, E., McGuire, M.A., Cobden, D.H. and Yao, W., 2017. Layer-dependent ferromagnetism in a van der Waals crystal down to the monolayer limit. *Nature*, *546*(7657), pp.270-273.

[76]   Deng, Y., Yu, Y., Song, Y., Zhang, J., Wang, N.Z., Sun, Z., Yi, Y., Wu, Y.Z., Wu, S., Zhu, J. and Wang, J., 2018. Gate-tunable room-temperature ferromagnetism in two-dimensional Fe3GeTe2. *Nature*, *563*(7729), pp.94-99.

[77]   Bonilla, M., Kolekar, S., Ma, Y., Diaz, H.C., Kalappattil, V., Das, R., Eggers, T., Gutierrez, H.R., Phan, M.H. and Batzill, M., 2018. Strong room-temperature

ferromagnetism in VSe2 monolayers on van der Waals substrates. *Nature nanotechnology*, *13*(4), pp.289-293.

[78] Jiang, S., Shan, J. and Mak, K.F., 2018. Electric-field switching of two-dimensional van der Waals magnets. *Nature materials*, *17*(5), pp.406-410.

[79] Chang, K., Liu, J., Lin, H., Wang, N., Zhao, K., Zhang, A., Jin, F., Zhong, Y., Hu, X., Duan, W. and Zhang, Q., 2016. Discovery of robust in-plane ferroelectricity in atomic-thick SnTe. *Science*, *353*(6296), pp.274-278.

[80] Liu, F., You, L., Seyler, K.L., Li, X., Yu, P., Lin, J., Wang, X., Zhou, J., Wang, H., He, H. and Pantelides, S.T., 2016. Room-temperature ferroelectricity in CuInP2S6 ultrathin flakes. *Nature communications*, *7*(1), pp.1-6.

[81] Zhou, Y., Wu, D., Zhu, Y., Cho, Y., He, Q., Yang, X., Herrera, K., Chu, Z., Han, Y., Downer, M.C. and Peng, H., 2017. Out-of-plane piezoelectricity and ferroelectricity in layered α-In2Se3 nanoflakes. Nano *letters*, *17*(9), pp.5508-5513.

[82] Fei, Z., Zhao, W., Palomaki, T.A., Sun, B., Miller, M.K., Zhao, Z., Yan, J., Xu, X. and Cobden, D.H., 2018. Ferroelectric switching of a two-dimensional metal. *Nature*, *560*(7718), pp.336-339.

[83] Wu, M. and Zeng, X.C., 2016. Intrinsic ferroelasticity and/or multiferroicity in two-dimensional phosphorene and phosphorene analogues. Nano *letters*, *16*(5), pp.3236-3241.

[84] Hanakata, P.Z., Carvalho, A., Campbell, D.K. and Park, H.S., 2016. Polarization and valley switching in monolayer group-IV monochalcogenides. *Physical Review B*, *94*(3), p.035304.

[85] Fei, R., Kang, W. and Yang, L., 2016. Ferroelectricity and phase transitions in monolayer group-IV monochalcogenides. *Physical review letters*, *117*(9), p.097601.

[86] Mehboudi, M., Fregoso, B.M., Yang, Y., Zhu, W., Van Der Zande, A., Ferrer, J., Bellaiche, L., Kumar, P. and Barraza-Lopez, S., 2016. Structural phase transition and material properties of few-layer monochalcogenides. *Physical review letters*, *117*(24), p.246802.

[87] Xiao, C., Wang, F., Yang, S.A., Lu, Y., Feng, Y. and Zhang, S., 2018. Elemental ferroelectricity and antiferroelectricity in Group-V monolayer. *Advanced Functional Materials*, *28*(17), p.1707383.

[88] Ding, W., Zhu, J., Wang, Z., Gao, Y., Xiao, D., Gu, Y., Zhang, Z. and Zhu, W., 2017. Prediction of intrinsic two-dimensional ferroelectrics in In2Se3 and other III2-VI3 van der Waals materials. *Nature communications*, *8*(1), p.14956.

[89] Zheng, C., Yu, L., Zhu, L., Collins, J.L., Kim, D., Lou, Y., Xu, C., Li, M., Wei, Z., Zhang, Y. and Edmonds, M.T., 2018. Room temperature in-plane ferroelectricity in van der Waals In2Se3. *Science advances*, *4*(7), p.eaar7720.

[90]   Cui, C., Hu, W.J., Yan, X., Addiego, C., Gao, W., Wang, Y., Wang, Z., Li, L., Cheng, Y., Li, P. and Zhang, X., 2018. Intercorrelated in-plane and out-of-plane ferroelectricity in ultrathin two-dimensional layered semiconductor In2Se3. Nano *letters*, *18*(2), pp.1253-1258.

[91]   Xue, F., Hu, W., Lee, K.C., Lu, L.S., Zhang, J., Tang, H.L., Han, A., Hsu, W.T., Tu, S., Chang, W.H. and Lien, C.H., 2018. Room-temperature ferroelectricity in hexagonally layered α-In2Se3 nanoflakes down to the monolayer limit. *Advanced Functional Materials*, *28*(50), p.1803738.

[92]   Xu, B., Xiang, H., Xia, Y., Jiang, K., Wan, X., He, J., Yin, J. and Liu, Z., 2017. Monolayer AgBiP 2 Se 6: An atomically thin ferroelectric semiconductor with out-plane polarization. Nano*scale*, *9*(24), pp.8427-8434.

[93]   Song, W., Fei, R. and Yang, L., 2017. Off-plane polarization ordering in metal chalcogen diphosphates from bulk to monolayer. *Physical Review B*, *96*(23), p.235420.

[94]   Lai, Y., Song, Z., Wan, Y., Xue, M., Wang, C., Ye, Y., Dai, L., Zhang, Z., Yang, W., Du, H. and Yang, J., 2019. Two-dimensional ferromagnetism and driven ferroelectricity in van der Waals CuCrP 2 S 6. Nano*scale*, *11*(12), pp.5163-5170.

[95]   Hu, T. and Kan, E., 2019. Progress and prospects in low-dimensional multiferroic materials. *Wiley Interdisciplinary Reviews: Computational Molecular Science*, *9*(5), p.e1409.

[96]   Huang, B., Clark, G., Navarro-Moratalla, E., Klein, D.R., Cheng, R., Seyler, K.L., Zhong, D., Schmidgall, E., McGuire, M.A., Cobden, D.H. and Yao, W., 2017. Layer-dependent ferromagnetism in a van der Waals crystal down to the monolayer limit. *Nature*, *546*(7657), pp.270-273.

[97]   Chen, L., Xu, C., Tian, H., Xiang, H., Íñiguez, J., Yang, Y. and Bellaiche, L., 2019. Electric-field control of magnetization, jahn-teller distortion, and orbital ordering in ferroelectric ferromagnets. *Physical Review Letters*, *122*(24), p.247701.

[98]   Spaldin, N.A. and Ramesh, R., 2019. Advances in magnetoelectric multiferroics. *Nature materials*, *18*(3), pp.203-212.

[99]   Zhang, J., Shen, X., Wang, Y., Ji, C., Zhou, Y., Wang, J., Huang, F. and Lu, X., 2020. Design of two-dimensional multiferroics with direct polarization-magnetization coupling. *Physical Review Letters*, *125*(1), p.017601.

[100] Matsukura, F., Tokura, Y. and Ohno, H., 2015. Control of magnetism by electric fields. *Nature* nano*technology*, *10*(3), pp.209-220.

[101] Garcia-Castro, A.C., Ibarra-Hernandez, W., Bousquet, E. and Romero, A.H., 2018. Direct magnetization-polarization coupling in BaCuF 4. *Physical Review Letters*, *121*(11), p.117601.

[102] Huang, C., Du, Y., Wu, H., Xiang, H., Deng, K. and Kan, E., 2018. Prediction of intrinsic ferromagnetic ferroelectricity in a transition-metal halide monolayer. *Physical review letters*, *120*(14), p.147601.

[103] Qi, J., Wang, H., Chen, X. and Qian, X., 2018. Two-dimensional multiferroic semiconductors with coexisting ferroelectricity and ferromagnetism. *Applied Physics Letters*, *113*(4), p.043102.

[104] Gong, C., Kim, E.M., Wang, Y., Lee, G. and Zhang, X., 2019. Multiferroicity in atomic van der Waals heterostructures. *Nature communications*, *10*(1), p.2657.

[105] Tan, H., Li, M., Liu, H., Liu, Z., Li, Y. and Duan, W., 2019. Two-dimensional ferromagnetic-ferroelectric multiferroics in violation of the d 0 rule. *Physical review B*, *99*(19), p.195434.

[106] Ai, H., Song, X., Qi, S., Li, W. and Zhao, M., 2019. Intrinsic multiferroicity in two-dimensional VOCl 2 monolayers. Nano*scale*, *11*(3), pp.1103-1110.

[107] Yang, Q., Xiong, W., Zhu, L., Gao, G. and Wu, M., 2017. Chemically functionalized phosphorene: two-dimensional multiferroics with vertical polarization and mobile magnetism. *Journal of the American Chemical Society*, *139*(33), pp.11506-11512.

[108] Zhang, J.J., Lin, L., Zhang, Y., Wu, M., Yakobson, B.I. and Dong, S., 2018. Type-II multiferroic Hf2VC2F2 MXene monolayer with high transition temperature. *Journal of the American Chemical Society*, *140*(30), pp.9768-9773.

[109] Lu, Y., Fei, R., Lu, X., Zhu, L., Wang, L. and Yang, L., 2020. Artificial multiferroics and enhanced magnetoelectric effect in van der Waals heterostructures. *ACS applied materials & interfaces*, *12*(5), pp.6243-6249.

[110] Feng, X., Liu, J., Ma, X. and Zhao, M., 2020. Ferroelectricity and multiferroicity in two-dimensional Sc 2 P 2 Se 6 and ScCrP 2 Se 6 monolayers. *Physical Chemistry Chemical Physics*, *22*(14), pp.7489-7496.

[111] Zhao, Y., Lin, L., Zhou, Q., Li, Y., Yuan, S., Chen, Q., Dong, S. and Wang, J., 2018. Surface vacancy-induced switchable electric polarization and enhanced ferromagnetism in monolayer metal trihalides. Nano *Letters*, *18*(5), pp.2943-2949.

[112] Oh, Y.S., Luo, X., Huang, F.T., Wang, Y. and Cheong, S.W., 2015. Experimental demonstration of hybrid improper ferroelectricity and the presence of abundant charged walls in (Ca, Sr) 3 Ti 2 O 7 crystals. *Nature materials*, *14*(4), pp.407-413.

[113] Li, B.W., Osada, M., Ebina, Y., Ueda, S. and Sasaki, T., 2016. Coexistence of magnetic order and ferroelectricity at 2D nanosheet interfaces. *Journal of the American Chemical Society*, *138*(24), pp.7621-7625.

[114] Luo, W., Xu, K. and Xiang, H., 2017. Two-dimensional hyperferroelectric metals: A different route to ferromagnetic-ferroelectric multiferroics. *Physical Review B*, *96*(23), p.235415.

[115] Zhou, Z., Yang, Q., Liu, M., Zhang, Z., Zhang, X., Sun, D., Nan, T., Sun, N. and Chen, X., 2015, March. Antiferroelectric materials, applications and recent progress on multiferroic heterostructures. In *Spin* (Vol. 5, No. 01, p. 1530001). World Scientific Publishing Company.

[116] Dong, S., Zhai, J., Bai, F., Li, J.F. and Viehland, D., 2005. Push-pull mode magnetostrictive/piezoelectric laminate composite with an enhanced magnetoelectric voltage coefficient. *Applied Physics Letters*, *87*(6), p.062502.

[117] Laletsin, U., Padubnaya, N., Srinivasan, G. and Devreugd, C.P., 2004. Frequency dependence of magnetoelectric interactions in layered structures of ferromagnetic alloys and piezoelectric oxides. *Applied Physics A*, *78*, pp.33-36.

[118] Dong, S., Li, J.F., Viehland, D., Cheng, J. and Cross, L.E., 2004. A strong magnetoelectric voltage gain effect in magnetostrictive-piezoelectric composite. *Applied Physics Letters*, *85*(16), pp.3534-3536.

[119] Lage, E., Kirchhof, C., Hrkac, V., Kienle, L., Jahns, R. and Kn, R., 2012. ochel, E. Quandt, and D. Meyners. *Nat. Mater*, *11*(6), pp.523-529.

[120] Wang, Y., Gray, D., Berry, D., Gao, J., Li, M., Li, J. and Viehland, D., 2011. An extremely low equivalent magnetic noise magnetoelectric sensor. *Advanced materials*, *23*(35), pp.4111-4114.

[121] Fang, C., Jiao, J., Ma, J., Lin, D., Xu, H., Zhao, X. and Luo, H., 2015. Significant reduction of equivalent magnetic noise by in-plane series connection in magnetoelectric Metglas/Mn-doped Pb (Mg1/3Nb2/3) O3-PbTiO3 laminate composites. *Journal of Physics D: Applied Physics*, *48*(46), p.465002.

[122] Zhao, P., Zhao, Z., Hunter, D., Suchoski, R., Gao, C., Mathews, S., Wuttig, M. and Takeuchi, I., 2009. Fabrication and characterization of all-thin-film magnetoelectric sensors. *Applied Physics Letters*, *94*(24), p.243507.

[123] Marauska, S., Jahns, R., Greve, H., Quandt, E., Knöchel, R. and Wagner, B., 2012. MEMS magnetic field sensor based on magnetoelectric composites. *Journal of Micromechanics and Microengineering*, *22*(6), p.065024.

[124] Gun Lee, D., Man Kim, S., Kyung Yoo, Y., Hyun Han, J., Won Chun, D., Kim, Y.C., Kim, J., Seon Hwang, K., Song Kim, T., Woo Jo, W. and Kim, H., 2012. Ultra-sensitive magnetoelectric microcantilever at a low frequency. *Applied Physics Letters*, *101*(18), p.182902.

[125] Kittel, C., 1948. On the theory of ferromagnetic resonance absorption. *Physical review*, *73*(2), p.155.

[126] Fetisov, Y.K. and Srinivasan, G., 2006. Electric field tuning characteristics of a ferrite-piezoelectric microwave resonator. *Applied physics letters*, *88*(14), p.143503.

[127] Li, N., Liu, M., Zhou, Z., Sun, N.X., Murthy, D.V.B., Srinivasan, G., Klein, T.M., Petrov, V.M. and Gupta, A., 2011. Electrostatic tuning of ferromagnetic resonance and magnetoelectric interactions in ferrite-piezoelectric heterostructures grown by chemical vapor deposition. *Applied Physics Letters*, *99*(19), p.192502.

[128] Srinivasan, G., 2015. Microwave and millimeter-wave multiferroic devices. *Composite* Magnetoelectric*s; Srinivasan, G., Priya, S., Sun, NX, Eds*, pp.241-264.

[129] Wang, S.G., Yoon, S.D. and Vittoria, C., 2002. Microwave and magnetic properties of double-sided hexaferrite films on (111) magnesium oxide substrates. *Journal of applied physics*, *92*(11), pp.6728-6732.

[130] Ustinov, A.B., Tatarenko, A.S., Srinivasan, G. and Balbashov, A.M., 2009. Al substituted Ba-hexaferrite single-crystal films for millimeter-wave devices. *Journal of Applied Physics*, *105*(2), p.023908.

[131] Tatarenko, A.S., Murthy, D.V.B. and Srinivasan, G., 2012. Hexagonal ferrite-piezoelectric composites for dual magnetic and electric field tunable 8–25 GHz microstripline resonators and phase shifters. *Microwave and Optical Technology Letters*, *54*(5), pp.1215-1218.

[132] Lou, J., Reed, D., Pettiford, C., Liu, M., Han, P., Dong, S. and Sun, N.X., 2008. Giant microwave tunability in FeGaB/lead magnesium niobate-lead titanate multiferroic composites. *Applied Physics Letters*, *92*(26), p.262502.

[133] Lou, J., Liu, M., Reed, D., Ren, Y. and Sun, N.X., 2009. Giant electric field tuning of magnetism in novel multiferroic FeGaB/Lead Zinc Niobate–Lead Titanate (PZN-PT) heterostructures. *Advanced Materials*, *21*(46), pp.4711-4715.

[134] Ustinov, A.B., Srinivasan, G. and Kalinikos, B.A., 2007. Ferrite-ferroelectric hybrid wave phase shifters. *Applied physics letters*, *90*(3), p.031913.

[135] Fetisov, Y.K. and Srinivasan, G., 2005. Ferrite/piezoelectric microwave phase shifter: studies on electric field tunability. *Electronics Letters*, *41*(19), p.1.

[136] Tatarenko, A.S. and Srinivasan, G., 2011. A strain engineered voltage tunable millimeter-wave ferrite phase shifter. *Microwave and Optical Technology Letters*, *53*(2), pp.261-264.

[137] Fetisov, Y.K. and Srinivasan, G., 2005. Electrically tunable ferrite-ferroelectric microwave delay lines. *Applied Physics Letters*, *87*(10), p.103502.

[138] Vopsaroiu, M., Blackburn, J., Muniz-Piniella, A. and Cain, M.G., 2008. Multiferroic magnetic recording read head technology for 1 Tbit∕ in. 2 and beyond. *Journal of Applied Physics*, *103*(7), p.07F506.

[139] Petrov, R.V., Tatarenko, A.S., Pandey, S., Srinivasan, G., Mantese, J.V. and Azadegan, R., 2008. Miniature antenna based on magnetoelectric composites. *Electronics Letters*, *44*(8), pp.506-508.

[140] Bae, S., Hong, Y.K., Lee, J.J., Jalli, J., Abo, G.S., Lyle, A., Seong, W.M. and Kum, J.S., 2009. Low loss Z-type barium ferrite (Co 2 Z) for terrestrial digital multimedia broadcasting antenna application. *Journal of Applied Physics*, *105*(7), p.07A515.

[141] Bae, S., Hong, Y.K., Lee, J.J., Seong, W.M., Kum, J.S., Ahn, W.K., Park, S.H., Abo, G.S., Jalli, J. and Park, J.H., 2010. Miniaturized broadband ferrite T-DMB antenna for mobile-phone applications. *IEEE Transactions on Magnetics*, *46*(6), pp.2361-2364.

[142] Lee, J., Hong, Y.K., Lee, W., Abo, G.S., Park, J., Neveu, N., Seong, W.M., Park, S.H. and Ahn, W.K., 2012. Soft M-type hexaferrite for very high frequency miniature antenna applications. *Journal of Applied Physics*, *111*(7), p.07A520.

[143] Thompson, S.M., 2008. The discovery, development and future of GMR: The Nobel Prize 2007. *Journal of Physics D: Applied Physics*, *41*(9), p.093001.

[144] Vopsaroiu, M., Blackburn, J. and Cain, M.G., 2007. A new magnetic recording read head technology based on the magnetoelectric effect. *Journal of Physics D: Applied Physics*, *40*(17), p.5027.

[145] Zhang, Y., Li, Z., Deng, C., Ma, J., Lin, Y. and Nan, C.W., 2008. Demonstration of magnetoelectric read head of multiferroic heterostructures. *Applied Physics Letters*, *92*(15), p.152510.

[146] Bibes, M. and Barthélémy, A., 2008. Towards a magnetoelectric memory. *Nature materials*, *7*(6), pp.425-426.

[147] Gajek, M., Bibes, M., Fusil, S. and Bouzehouane, K., 2007. J. Fon tcuberta, A. Barthélémy, and A. Fert. *Nat. Mater*, *6*, p.296.

[148] Gruverman, A., Wu, D., Lu, H., Wang, Y., Jang, H.W., Folkman, C.M., Zhuravlev, M.Y., Felker, D., Rzchowski, M., Eom, C.B. and Tsymbal, E.Y., 2009. Tunneling electroresistance effect in ferroelectric tunnel junctions at the nanoscale. *Nano letters*, *9*(10), pp.3539-3543.

[149] Fridkin, V.M., 1984. Review of recent work on the bulk photovoltaic effect in ferro and piezoelectrics. Ferroelectric*s*, *53*(1), pp.169-187.

[150] Han, J., Hu, J., Wang, S.X. and He, J., 2014. Magnetic energy harvesting properties of piezofiber bimorph/NdFeB composites. *Applied Physics Letters*, *104*(9), p.093901.

[151] Vopson, M.M., Zemaityte, E., Spreitzer, M. and Namvar, E., 2014. Multiferroic composites for magnetic data storage beyond the super-paramagnetic limit. *Journal of Applied Physics*, *116*(11), p.113910.

[152] Kim, H.K., Schelhas, L.T., Keller, S., Hockel, J.L., Tolbert, S.H. and Carman, G.P., 2013. Magnetoelectric control of superparamagnetism. Nano *letters*, *13*(3), pp.884-888.

[153] Basu, S.R., Martin, L.W., Chu, Y.H., Gajek, M., Ramesh, R., Rai, R.C., Xu, X. and Musfeldt, J.L., 2008. Photoconductivity in Bi Fe O 3 thin films. *Applied Physics Letters*, *92*(9), p.091905.

[154] Hauser, A.J., Zhang, J., Mier, L., Ricciardo, R.A., Woodward, P.M., Gustafson, T.L., Brillson, L.J. and Yang, F.Y., 2008. Characterization of electronic structure and defect states of thin epitaxial Bi Fe O 3 films by UV-visible absorption and cathodoluminescence spectroscopies. *Applied Physics Letters*, *92*(22), p.222901.

[155] Choi, T., Lee, S., Choi, Y.J., Kiryukhin, V. and Cheong, S.W., 2009. Switchable ferroelectric diode and photovoltaic effect in BiFeO3. *Science*, *324*(5923), pp.63-66.

[156] Gao, J., Hasanyan, D., Shen, Y., Wang, Y., Li, J. and Viehland, D., 2012. Giant resonant magnetoelectric effect in bi-layered Metglas/Pb (Zr, Ti) O3 composites. *Journal of Applied Physics*, *112*(10), p.104101.

[157] Dong, S., Zhai, J., Li, J.F., Viehland, D. and Priya, S., 2008. Multimodal system for harvesting magnetic and mechanical energy. *Applied Physics Letters*, *93*(10), p.103511.

[158] Tellegen, B.D., 1948. The gyrator, a new electric network element. *Philips Res. Rep*, *3*(2), pp.81-101.

[159] Bedekar, V., Islam, R.A., Kim, H., Bichurin, M.I., Ivanov, S.N., Pukinski, Y.J. and Priya, S., 2009. Magnetoelectric gradiometer. *The European Physical Journal B*, *71*, pp.387-392.

[160] Fang, X., Zhang, N. and Wang, Z.L., 2008. Converse magnetoelectric effects on heterotype electrostrain-piezopermeability composites. *Applied physics letters*, *93*(10), p.102503.

[161] Mandal, M., Duttagupta, S.P. and Palkar, V.R., 2013. Study of multiferroic Bi0. 7Dy0. 3FeO3 based tunable ring inductor. *Journal of Physics D: Applied Physics*, *46*(32), p.325001.

[162] Berry, C.C. and Curtis, A.S., 2003. Functionalisation of magnetic nanoparticles for applications in biomedicine. *Journal of physics D: Applied physics*, *36*(13), p.R198.

[163] Pankhurst, Q.A., Connolly, J., Jones, S.K. and Dobson, J., 2003. Applications of magnetic nanoparticles in biomedicine. *Journal of physics D: Applied physics*, *36*(13), p.R167.

[164] Tartaj, P., del Puerto Morales, M., Veintemillas-Verdaguer, S., Gonzalez-Carreno, T. and Serna, C.J., 2003. The preparation of magnetic nanoparticles for applications in biomedicine. *Journal of physics D: Applied physics*, *36*(13), p.R182.

[165] Paluszek, M., Avirovik, D., Zhou, Y., Kundu, S., Chopra, A., Montague, R. and Priya, S., 2015. Magnetoelectric composites for medical application. *Composite* Magnetoelectric*s; Srinivasan, G., Priya, S., Sun, NX, Eds*, pp.297-327.

[166] Guduru, R., Liang, P., Runowicz, C., Nair, M., Atluri, V. and Khizroev, S., 2013. Magnetoelectric nanoparticles to enable field-controlled high-specificity drug delivery to eradicate ovarian cancer cells. *Scientific reports*, *3*(1), p.2953.

[167] Yue, K., Guduru, R., Hong, J., Liang, P., Nair, M. and Khizroev, S., 2012. Magnetoelectric nano particles for non-invasive brain stimulation. *PLOS ONE*, *7*(9), p.e44040.

[168] Kargol, A., Malkinski, L. and Caruntu, G., 2012. Biomedical applications of multiferroic nanoparticles. *Advanced magnetic materials*, pp.89-118.

[169] Liu, M., Obi, O., Lou, J., Chen, Y., Cai, Z., Stoute, S., Espanol, M., Lew, M., Situ, X., Ziemer, K.S. and Harris, V.G., 2009. Giant electric field tuning of magnetic properties in multiferroic ferrite/ferroelectric heterostructures. *Advanced Functional Materials*, *19*(11), pp.1826-1831.

[170] Žutić, I., Fabian, J. and Sarma, S.D., 2004. Spintronics: Fundamentals and applications. *Reviews of modern physics*, *76*(2), p.323.

[171] Han, W., Kawakami, R.K., Gmitra, M. and Fabian, J., 2014. graphene spintronics. *Nature* nano*technology*, *9*(10), pp.794-807.

[172] Bader, S.D. and Parkin, S.S.P., 2010. Spintronics. *Annu. Rev. Condens. Matter Phys.*, *1*(1), pp.71-88.

[173] Fasiku, V., Owonubi, S.J., Mukwevho, E., Aderibigbe, B.A., Lemmer, Y., Neerish, R. and Sadiku, E.R., 2019. graphene-based materials for implants. *Graphene: Biomaterials*, pp.143-175.

[174] Tombros, N., Jozsa, C., Popinciuc, M., Jonkman, H.T. and Van Wees, B.J., 2007. Electronic spin transport and spin precession in single graphene layers at room temperature. *nature*, *448*(7153), pp.571-574.

[175] Han, W., Pi, K., McCreary, K.M., Li, Y., Wong, J.J., Swartz, A.G. and Kawakami, R.K., 2010. Tunneling spin injection into single layer graphene. *Physical review letters*, *105*(16), p.167202.

[176] Yang, T.Y., Balakrishnan, J., Volmer, F., Avsar, A.H.M.E.T., Jaiswal, M., Samm, J., Ali, S.R., Pachoud, A., Zeng, M., Popinciuc, M. and Güntherodt, G., 2011.

Observation of long spin-relaxation times in bilayer graphene at room temperature. *Physical review letters*, *107*(4), p.047206.

[177] Park, S. and Ruoff, R.S., 2009. Chemical methods for the production of graphenes. *Nature* nano*technology*, *4*(4), pp.217-224.

[178] Neto, A.C., Guinea, F., Peres, N.M., Novoselov, K.S. and Geim, A.K., 2009. The electronic properties of graphene. *Reviews of modern physics*, *81*(1), p.109.

[179] Bagani, K., Bhattacharya, A., Kaur, J., Rai Chowdhury, A., Ghosh, B., Sardar, M. and Banerjee, S., 2014. Anomalous behaviour of magnetic coercivity in graphene oxide and reduced graphene oxide. *Journal of Applied Physics*, *115*(2), p.023902.

[180] Dubois, S.M., Zanolli, Z., Declerck, X. and Charlier, J.C., 2009. Electronic properties and quantum transport in graphene-based nanostructures. *The European Physical Journal B*, *72*, pp.1-24.

[181] Zheng, Z., Ma, Q., Bi, Z., de La Barrera, S., Liu, M.H., Mao, N., Zhang, Y., Kiper, N., Watanabe, K., Taniguchi, T. and Kong, J., 2020. Unconventional ferroelectricity in moiré heterostructures. *Nature*, *588*(7836), pp.71-76.

[182] Wan, S., Li, Y., Li, W., Mao, X., Wang, C., Chen, C., Dong, J., Nie, A., Xiang, J., Liu, Z. and Zhu, W., 2019. Nonvolatile ferroelectric memory effect in ultrathin α-In2Se3. *Advanced Functional Materials*, *29*(20), p.1808606.

[183] Bhowmick, S. and Shenoy, V.B., 2008. Edge state magnetism of single layer graphene nanostructures. *The Journal of chemical physics*, *128*(24), p.244717.

[184] Singh, R. and Kroll, P., 2009. Magnetism in graphene due to single-atom defects: dependence on the concentration and packing geometry of defects. *Journal of Physics: Condensed Matter*, *21*(19), p.196002.

[185] Kumazaki, H. and S. Hirashima, D., 2008. Local magnetic moment formation on edges of graphene. *Journal of the Physical Society of Japan*, *77*(4), p.044705.

[186] Zhou, J., Wang, Q., Sun, Q., Chen, X.S., Kawazoe, Y. and Jena, P., 2009. Ferromagnetism in semihydrogenated graphene sheet. Nano *letters*, *9*(11), pp.3867-3870.

[187] Yang, J.C., He, Q., Yu, P. and Chu, Y.H., 2015. BiFeO3 thin films: a playground for exploring electric-field control of multifunctionalities. *Annual Review of Materials Research*, *45*, pp.249-275.

[188] Gao, F., Yuan, Y., Wang, K.F., Chen, X.Y., Chen, F., Liu, J.M. and Ren, Z.F., 2006. Preparation and photoabsorption characterization of Bi Fe O 3 nanowires. *Applied Physics Letters*, *89*(10), p.102506.

[189] Li, S., Lin, Y.H., Zhang, B.P., Wang, Y. and Nan, C.W., 2010. Controlled fabrication of BiFeO3 uniform microcrystals and their magnetic and photocatalytic behaviors. *The Journal of Physical Chemistry C*, *114*(7), pp.2903-2908.

[190] Wang, J.B.N.J., Neaton, J.B., Zheng, H., Nagarajan, V., Ogale, S.B., Liu, B., Viehland, D., Vaithyanathan, V., Schlom, D.G., Waghmare, U.V. and Spaldin, N.A., 2003. Epitaxial BiFeO3 multiferroic thin film heterostructures. *science*, *299*(5613), pp.1719-1722.

[191] Moreau, J.M., Michel, C., Gerson, R. and James, W.J., 1971. Ferroelectric BiFeO3 X-ray and neutron diffraction study. *Journal of Physics and Chemistry of Solids*, *32*(6), pp.1315-1320.

[192] Singh, H. and Yadav, K.L., 2015. Structural, dielectric, vibrational and magnetic properties of Sm doped BiFeO3 multiferroic ceramics prepared by a rapid liquid phase sintering method. *Ceramics International*, *41*(8), pp.9285-9295.

[193] Khan, A.H., Atiq, S., Anwar, M.S., Naseem, S. and Abbas, S.K., 2018. Optimization of magnetodielectric coupling in Mn substituted BiFeO 3 for potential memory devices. *Journal of Materials Science: Materials in Electronics*, *29*, pp.11812-11823.

[194] Kawae, T., Terauchi, Y., Tsuda, H., Kumeda, M. and Morimoto, A., 2009. Improved leakage and ferroelectric properties of Mn and Ti codoped BiFeO 3 thin films. *Applied Physics Letters*, *94*(11), p.112904.

[195] Royen, P. and Swars, K., 1957. Das system Wismutoxyd-Eisenoxyd im Bereich von 0 bis 55 mol% Eisenoxyd. *Angewandte Chemie*, *69*(24), pp.779-779.

[196] Sosnowska, I., Neumaier, T.P. and Steichele, E., 1982. Spiral magnetic ordering in bismuth ferrite. *Journal of Physics C: Solid State Physics*, *15*(23), p.4835.

[197] Kiselev, S.V., Ozerov, R.P. and Zhdanov, G.S., 1962. Detection of magnetic arrangement in the BiFeO_3 ferroelectric by means of neutron diffraction study. In *Doklady Akademii Nauk* (Vol. 145, No. 6, pp. 1255-1258). Russian Academy of Sciences.

[198] Yang, J.C., He, Q., Suresha, S.J., Kuo, C.Y., Peng, C.Y., Haislmaier, R.C., Motyka, M.A., Sheng, G., Adamo, C., Lin, H.J. and Hu, Z., 2012. Orthorhombic BiFeO 3. *Physical review letters*, *109*(24), p.247606.

[199] Jang, H.W., Baek, S.H., Ortiz, D., Folkman, C.M., Das, R.R., Chu, Y.H., Shafer, P., Zhang, J.X., Choudhury, S., Vaithyanathan, V. and Chen, Y.B., 2008. Strain-induced polarization rotation in epitaxial (001) BiFeO 3 thin films. *Physical review letters*, *101*(10), p.107602.

[200] Béa, H., Dupé, B., Fusil, S., Mattana, R., Jacquet, E., Warot-Fonrose, B., Wilhelm, F., Rogalev, A., Petit, S., Cros, V. and Anane, A., 2009. Evidence for room-temperature multiferroicity in a compound with a giant axial ratio. *Physical review letters*, *102*(21), p.217603.

[201] Zhang, J.X., He, Q., Trassin, M., Luo, W., Yi, D., Rossell, M.D., Yu, P., You, L., Wang, C.H., Kuo, C.Y. and Heron, J.T., 2011. Microscopic origin of the giant ferroelectric polarization in tetragonal-like BiFeO 3. *Physical review letters*, *107*(14), p.147602.

[202] Sando, D., Agbelele, A., Rahmedov, D., Liu, J., Rovillain, P., Toulouse, C., Infante, I.C., Pyatakov, A.P., Fusil, S., Jacquet, E. and Carrétéro, C., 2013. Crafting the magnonic and spintronic response of BiFeO3 films by epitaxial strain. *Nature materials*, *12*(7), pp.641-646.

[203] Chen, Z., Chen, Z., Kuo, C.Y., Tang, Y., Dedon, L.R., Li, Q., Zhang, L., Klewe, C., Huang, Y.L., Prasad, B. and Farhan, A., 2018. Complex strain evolution of polar and magnetic order in multiferroic BiFeO3 thin films. *Nature communications*, *9*(1), p.3764.

[204] Zhao, T., Scholl, A., Zavaliche, F., Lee, K., Barry, M., Doran, A., Cruz, M.P., Chu, Y.H., Ederer, C., Spaldin, N.A. and Das, R.R., 2006. Electrical control of antiferromagnetic domains in multiferroic BiFeO3 films at room temperature. *Nature materials*, *5*(10), pp.823-829.

[205] Wu, S.M., Cybart, S.A., Yu, P., Rossell, M.D., Zhang, J.X., Ramesh, R. and Dynes, R.C., 2010. Reversible electric control of exchange bias in a multiferroic field-effect device. *Nature materials*, *9*(9), pp.756-761.

[206] Chu, Y.H., Martin, L.W., Holcomb, M.B., Gajek, M., Han, S.J., He, Q., Balke, N., Yang, C.H., Lee, D., Hu, W. and Zhan, Q., 2008. Electric-field control of local ferromagnetism using a magnetoelectric multiferroic. *Nature materials*, *7*(6), pp.478-482.

[207] Kuo, C.Y., Hu, Z., Yang, J.C., Liao, S.C., Huang, Y.L., Vasudevan, R.K., Okatan, M.B., Jesse, S., Kalinin, S.V., Li, L. and Liu, H.J., 2016. Single-domain multiferroic BiFeO3 films. *Nature communications*, *7*(1), p.12712.

[208] Manipatruni, S., Nikonov, D.E., Lin, C.C., Prasad, B., Huang, Y.L., Damodaran, A.R., Chen, Z., Ramesh, R. and Young, I.A., 2018. Voltage control of unidirectional anisotropy in ferromagnet-multiferroic system. *Science Advances*, *4*(11), p.eaat4229.

[209] Allibe, J., Fusil, S., Bouzehouane, K., Daumont, C., Sando, D., Jacquet, E., Deranlot, C., Bibes, M. and Barthelemy, A., 2012. Room temperature electrical manipulation of giant magnetoresistance in spin valves exchange-biased with BiFeO3. Nano *letters*, *12*(3), pp.1141-1145.

[210] Ding, J., Qiao, Z., Feng, W., Yao, Y. and Niu, Q., 2011. Engineering quantum anomalous/valley Hall states in graphene via metal-atom adsorption: An ab-initio study. *Physical Review B*, *84*(19), p.195444.

[211] Eelbo, T., Waśniowska, M., Thakur, P., Gyamfi, M., Sachs, B., Wehling, T.O., Forti, S., Starke, U., Tieg, C., Lichtenstein, A.I. and Wiesendanger, R., 2013. Adatoms and clusters of 3 d transition metals on graphene: Electronic and magnetic configurations. *Physical review letters*, *110*(13), p.136804.

[212] Chen, H., Niu, Q., Zhang, Z. and MacDonald, A.H., 2013. Gate-tunable exchange coupling between cobalt clusters on graphene. *Physical Review B*, *87*(14), p.144410.

[213] Zhang, Y., Tan, Y.W., Stormer, H.L. and Kim, P., 2005. Experimental observation of the quantum Hall effect and Berry's phase in graphene. *nature*, *438*(7065), pp.201-204.

[214] Haugen, H., Huertas-Hernando, D. and Brataas, A., 2008. Spin transport in proximity-induced ferromagnetic graphene. *Physical Review B*, *77*(11), p.115406.

[215] Qiao, Z., Yang, S.A., Feng, W., Tse, W.K., Ding, J., Yao, Y., Wang, J. and Niu, Q., 2010. Quantum anomalous Hall effect in graphene from Rashba and exchange effects. *Physical Review B*, *82*(16), p.161414.

[216] Qiao, Z., Ren, W., Chen, H., Bellaiche, L., Zhang, Z., MacDonald, A.H. and Niu, Q., 2014. Quantum anomalous Hall effect in graphene proximity coupled to an antiferromagnetic insulator. *Physical review letters*, *112*(11), p.116404.

[217] Yang, H.X., Hallal, A., Terrade, D., Waintal, X., Roche, S. and Chshiev, M., 2013. Proximity effects induced in graphene by magnetic insulators: first-principles calculations on spin filtering and exchange-splitting gaps. *Physical review letters*, *110*(4), p.046603.

[218] Sakai, S., Majumdar, S., Popov, Z.I., Avramov, P.V., Entani, S., Hasegawa, Y., Yamada, Y., Huhtinen, H., Naramoto, H., Sorokin, P.B. and Yamauchi, Y., 2016. Proximity-induced spin polarization of graphene in contact with half-metallic manganite. *ACS* nano, *10*(8), pp.7532-7541.

[219] Vobornik, I., Manju, U., Fujii, J., Borgatti, F., Torelli, P., Krizmancic, D., Hor, Y.S., Cava, R.J. and Panaccione, G., 2011. Magnetic proximity effect as a pathway to spintronic applications of topological insulators. Nano *letters*, *11*(10), pp.4079-4082.

[220] Takenaka, H., Sandhoefner, S., Kovalev, A.A. and Tsymbal, E.Y., 2019. Magnetoelectric control of topological phases in graphene. *Physical Review B*, *100*(12), p.125156.

[221] Wang, Z., Tang, C., Sachs, R., Barlas, Y. and Shi, J., 2015. Proximity-induced ferromagnetism in graphene revealed by the anomalous Hall effect. *Physical review letters*, *114*(1), p.016603.

[222] Leutenantsmeyer, J.C., Kaverzin, A.A., Wojtaszek, M. and Van Wees, B.J., 2016. Proximity induced room temperature ferromagnetism in graphene probed with spin currents. *2D Materials*, *4*(1), p.014001.

[223] Mendes, J.B.S., Santos, O.A., Meireles, L.M., Lacerda, R.G., Vilela-Leão, L.H., Machado, F.L.A., Rodríguez-Suárez, R.L., Azevedo, A. and Rezende, S.M., 2015. Spin-current to charge-current conversion and magnetoresistance in a hybrid structure of graphene and yttrium iron garnet. *Physical review letters*, *115*(22), p.226601.

[224] Evelt, M., Ochoa, H., Dzyapko, O., Demidov, V.E., Yurgens, A., Sun, J., Tserkovnyak, Y., Bessonov, V., Rinkevich, A.B. and Demokritov, S.O., 2017. Chiral charge pumping in graphene deposited on a magnetic insulator. *Physical Review B*, *95*(2), p.024408.

[225] Wei, P., Lee, S., Lemaitre, F., Pinel, L., Cutaia, D., Cha, W., Katmis, F., Zhu, Y., Heiman, D., Hone, J. and Moodera, J.S., 2016. Strong interfacial exchange field in the graphene/EuS heterostructure. *Nature materials*, *15*(7), pp.711-716.

[226] Wu, Y.F., Song, H.D., Zhang, L., Yang, X., Ren, Z., Liu, D., Wu, H.C., Wu, J., Li, J.G., Jia, Z. and Yan, B., 2017. Magnetic proximity effect in graphene coupled to a BiFeO3 nanoplate. *Physical Review B*, *95*(19), p.195426.

[227] Song, H.D., Wu, Y.F., Yang, X., Ren, Z., Ke, X., Kurttepeli, M., Tendeloo, G.V., Liu, D., Wu, H.C., Yan, B. and Wu, X., 2018. Asymmetric modulation on exchange field in a graphene/BiFeO3 heterostructure by external magnetic field. Nano *letters*, *18*(4), pp.2435-2441.

[228] Li, Y., Sun, X.Y., Xu, C.Y., Cao, J., Sun, Z.Y. and Zhen, L., 2018. Ferroelectric resistive switching behavior in two-dimensional materials/BiFeO 3 hetero-junctions. Nano*scale*, *10*(48), pp.23080-23086.

[229] Lu, H., Lipatov, A., Ryu, S., Kim, D.J., Lee, H., Zhuravlev, M.Y., Eom, C.B., Tsymbal, E.Y., Sinitskii, A. and Gruverman, A., 2014. Ferroelectric tunnel junctions with graphene electrodes. *Nature communications*, *5*(1), p.5518.

[230] Lipatov, A., Sharma, P., Gruverman, A. and Sinitskii, A., 2015. Optoelectrical Molybdenum Disulfide (MoS2) Ferroelectric Memories. *ACS* nano, *9*(8), pp.8089-8098.

[231] Li, T., Sharma, P., Lipatov, A., Lee, H., Lee, J.W., Zhuravlev, M.Y., Paudel, T.R., Genenko, Y.A., Eom, C.B., Tsymbal, E.Y. and Sinitskii, A., 2017. Polarization-mediated modulation of electronic and transport properties of hybrid MoS2–BaTiO3–SrRuO3 tunnel junctions. Nano *letters*, *17*(2), pp.922-927.

[232] Baeumer, C., Saldana-Greco, D., Martirez, J.M.P., Rappe, A.M., Shim, M. and Martin, L.W., 2015. Ferroelectrically driven spatial carrier density modulation in graphene. *Nature communications*, *6*(1), p.6136.

[233] Hinnefeld, J.H., Xu, R., Rogers, S., Pandya, S., Shim, M., Martin, L.W. and Mason, N., 2016. Single gate pn junctions in graphene-ferroelectric devices. *Applied Physics Letters*, *108*(20), p.203109.

[234] Jie, W. and Hao, J., 2014. graphene-based hybrid structures combined with functional materials of ferroelectrics and semiconductors. Nano*scale*, *6*(12), pp.6346-6362.

[235] Park, N., Kang, H., Park, J., Lee, Y., Yun, Y., Lee, J.H., Lee, S.G., Lee, Y.H. and Suh, D., 2015. Ferroelectric single-crystal gated graphene/hexagonal-BN/ferroelectric field-effect transistor. *ACS* nano, *9*(11), pp.10729-10736.

[236] Yuan, S., Yang, Z., Xie, C., Yan, F., Dai, J., Lau, S.P., Chan, H.L. and Hao, J., 2016. Ferroelectric-driven performance enhancement of graphene field-effect transistors based on vertical tunneling heterostructures. *Advanced Materials*, *28*(45), pp.10048-10054.

[237] Lipatov, A., Li, T., Vorobeva, N.S., Sinitskii, A. and Gruverman, A., 2019. Nanodomain engineering for programmable ferroelectric devices. Nano *Letters*, *19*(5), pp.3194-3198.

[238] Zheng, Y., Ni, G.X., Toh, C.T., Tan, C.Y., Yao, K. and Özyilmaz, B., 2010. graphene field-effect transistors with ferroelectric gating. *Physical review letters*, *105*(16), p.166602.

[239] Hong, X., Posadas, A., Zou, K., Ahn, C.H. and Zhu, J., 2009. High-mobility few-layer graphene field effect transistors fabricated on epitaxial ferroelectric gate oxides. *Physical review letters*, *102*(13), p.136808.

[240] Zheng, Y., Ni, G.X., Bae, S., Cong, C.X., Kahya, O., Toh, C.T., Kim, H.R., Im, D., Yu, T., Ahn, J.H. and Hong, B.H., 2011. Wafer-scale graphene/ferroelectric hybrid devices for low-voltage electronics. *Europhysics Letters*, *93*(1), p.17002.

[241] Bidmeshkipour, S., Vorobiev, A., Andersson, M.A., Kompany, A. and Stake, J., 2015. Effect of ferroelectric substrate on carrier mobility in graphene field-effect transistors. *Applied Physics Letters*, *107*(17), p.173106.

[242] Jie, W., Hui, Y.Y., Chan, N.Y., Zhang, Y., Lau, S.P. and Hao, J., 2013. Ferroelectric polarization effects on the transport properties of graphene/PMN-PT field effect transistors. *The Journal of Physical Chemistry C*, *117*(26), pp.13747-13752.

[243] Song, E.B., Lian, B., Min Kim, S., Lee, S., Chung, T.K., Wang, M., Zeng, C., Xu, G., Wong, K., Zhou, Y. and Rasool, H.I., 2011. Robust bi-stable memory operation in single-layer graphene ferroelectric memory. *Applied Physics Letters*, *99*(4), p.042109.

[244] Dai, J.Q., Cao, T.F. and Wang, X.W., 2018. Effect of surface termination on charge doping in graphene/BiFeO3 (0001) hybrid structure. *The Journal of Physical Chemistry C*, *122*(30), pp.17250-17260.

[245] McCreary, K.M., Swartz, A.G., Han, W., Fabian, J. and Kawakami, R.K., 2012. Magnetic moment formation in graphene detected by scattering of pure spin currents. *Physical review letters*, *109*(18), p.186604.

[246] Nair, R.R., Sepioni, M., Tsai, I.L., Lehtinen, O., Keinonen, J., Krasheninnikov, A.V., Thomson, T., Geim, A.K. and Grigorieva, I.V., 2012. Spin-half paramagnetism in graphene induced by point defects. *Nature Physics*, *8*(3), pp.199-202.

[247] Hong, J., Bekyarova, E., Liang, P., de Heer, W.A., Haddon, R.C. and Khizroev, S., 2012. Room-temperature magnetic ordering in functionalized graphene. *Scientific reports*, *2*(1), pp.1-6.

[248] Hong, J., Niyogi, S., Bekyarova, E., Itkis, M.E., Ramesh, P., Amos, N., Litvinov, D., Berger, C., De Heer, W.A., Khizroev, S. and Haddon, R.C., 2011. Effect of nitrophenyl functionalization on the magnetic properties of epitaxial graphene. *Small*, *7*(9), pp.1175-1180.

[249] Niyogi, S., Bekyarova, E., Hong, J., Khizroev, S., Berger, C., de Heer, W. and Haddon, R.C., 2011. Covalent chemistry for graphene electronics. *The Journal of Physical Chemistry Letters*, *2*(19), pp.2487-2498.

[250] Santos, E.J., 2013. Carrier-mediated magnetoelectric coupling in functionalized graphene. *ACS* nano, *7*(11), pp.9927-9932.

[251] Ibrahim, F., Hallal, A., Lerma, D.S., Waintal, X., Tsymbal, E.Y. and Chshiev, M., 2019. Unveiling multiferroic proximity effect in graphene. *2D Materials*, *7*(1), p.015020.

[252] Zanolli, Z., 2016. graphene-multiferroic interfaces for spintronics applications. *Scientific reports*, *6*(1), pp.1-6.

[253] Li, Z., Shen, Y., Yang, C., Lei, Y., Guan, Y., Lin, Y., Liu, D. and Nan, C.W., 2013. Significant enhancement in the visible light photocatalytic properties of BiFeO 3– graphene nanohybrids. *Journal of Materials Chemistry A*, *1*(3), pp.823-829.

[254] Zhou, Q., Lin, Y., Zhang, K., Li, M. and Tang, D., 2018. Reduced graphene oxide/BiFeO3 nanohybrids-based signal-on photoelectrochemical sensing system for prostate-specific antigen detection coupling with magnetic microfluidic device. *Biosensors and Bioelectronics*, *101*, pp.146-152.

[255] Li, T., Shen, J., Li, N. and Ye, M., 2013. Hydrothermal preparation, characterization and enhanced properties of reduced graphene-BiFeO3 nanocomposite. *Materials Letters*, *91*, pp.42-44.

[256] Moitra, D., Dhole, S., Ghosh, B.K., Chandel, M., Jani, R.K., Patra, M.K., Vadera, S.R. and Ghosh, N.N., 2017. Synthesis and microwave absorption properties of BiFeO3 nanowire-RGO nanocomposite and first-principles calculations for insight of

electromagnetic properties and electronic structures. *The Journal of Physical Chemistry C*, *121*(39), pp.21290-21304.

[257] Jalil, M.A., Chowdhury, S.S., Alam Sakib, M., Enamul Hoque Yousuf, S.M., Khan Ashik, E., Firoz, S.H. and Basith, M.A., 2017. Temperature-dependent phase transition and comparative investigation on enhanced magnetic and optical properties between sillenite and perovskite bismuth ferrite-rGO nanocomposites. *Journal of Applied Physics*, *122*(8), p.084902.

[258] Volonakis, G. and Giustino, F., 2015. Ferroelectric graphene–perovskite interfaces. *The journal of physical chemistry letters*, *6*(13), pp.2496-2502.

2. Chapter

Experimental details

2.1 <u>Introduction</u>

In this section we will briefly discuss about the different techniques that of sample preparations. We have prepared rGO/BiFeO$_3$ (rGO/BFO) nano composite using two different routes. The rGO/BFO heterostructure was prepared using chemical solution deposition (CSD) derived spin coating techniques. Moreover, single layer graphene (SLG) was prepared using Chemical vapour deposition (CVD) followed by functionalization using Birch reduction. The BFO/Ag composite was prepared using both hydrothermal and sol-gel techniques. In this chapter the various material synthesis processes and their detailed characterization to investigate structure property correlation will be discussed. We have used laboratory X-ray diffraction (XRD) and Neutron diffraction techniques for sample characterization. Further, Rietveld refinement method was utilized to determine lattice structure and structural properties of the sample. The supporting information about phases, chemical states and bonding within the as prepared materials were determined from RAMAN and FTIR spectroscopies. Bonding features and charge state of the samples was determined by using X-ray Photo Electron Spectroscopy (XPS). Electron microscopic techniques- i.e. Field Effect Scanning Electron Microscopy (FESEM) and Transmission Electron Microscopy (TEM) were also used to determine the surface features and sample morphology. Vibrating Sample Magnetometer (VSM) and Superconducting Quantum Interference Device (SQUID) were used to study the magnetic properties of the sample.

2.2 <u>Material synthesis techniques</u>

2.2.1 <u>Synthesis techniques used for the preparation of nano powder</u>

The synthesis procedures of inorganic powder materials primarily include the solid phase, liquid phase, and gas phase methods[1][2]. Amongst these the liquid phase method is the most common and includes precipitation[3], hydrothermal[4][5][6], colloidal[7][8], and sol-gel methods[9]

[10]. The advantages of the liquid phase method are convenient operation, simple synthesis process, and controllable particle size. However, most liquid phase methods consume are energy extensive and costly. Sol–gel and hydrothermal synthesis process being the most common approaches for synthesizing low-dimensional BFO nano materials.

2.2.1.1 **Hydrothermal technique**

The hydrothermal method is a promising liquid phase preparation technology that is developed rapidly in recent years. The hydrothermal method is a type of soft chemical synthesis method developed by simulating the formation process of some ores in nature. The term, hydrothermal, originated from geology, beginning during the mid-19th century when geologists simulated hydrothermal conditions to study the formation of certain minerals and rocks. On this basis, hydrothermal methods began to be applied to single crystal growth; powder preparation using hydrothermal technique had been developing for nearly 200 years.
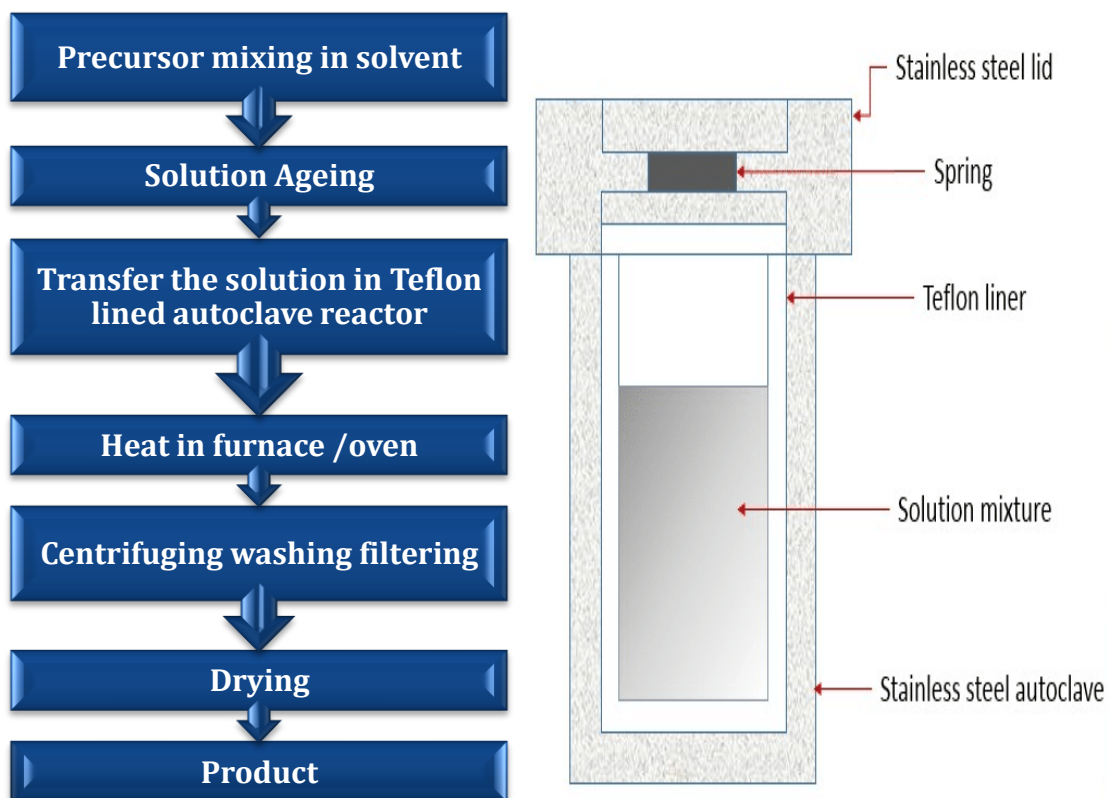
Figure 2.1 Hydrothermal schematic technique (Left) and Teflon lined autoclave (RHS)

It is widely used in many fields, such as the piezoelectric, ferroelectric, ceramic powder, and oxide film preparation. The hydrothermal method has resulted in many new methods during the long-term research process, such as adding other force fields to the hydrothermal condition reaction system. These force fields mainly include direct current, electric, magnetic (autoclaves composed of non-ferroelectric materials), and microwave fields. In addition, the

[59]

crystal size, morphology, and agglomeration of ceramic oxides can be controlled by adjusting the ratio of starting materials, pH of the reaction system, time, and temperature of the reaction medium.

The hydrothermal method refers to the use of an aqueous solution as a reaction system in a special closed reaction vessel (Figure 2.1 (RHS)) to create a high-temperature, high-pressure reaction environment by heating the reaction system and pressurizing it (or the vapour pressure generated by itself). The process dissolves and re-crystallizes a substance that is poorly soluble or insoluble under normal conditions[11][12]. The general preparation steps of the hydrothermal method are shown in Figure 2.1 (LHS).

➢ *Reaction Kinetics and the Crystal Growth Mechanism of the Hydrothermal Method:*

The main steps of crystalline growth under hydrothermal conditions are as follows: First, the reactants are dissolved in a hydrothermal medium and they dissolve in the medium in the form of ions or molecular groups. Second, the ions or molecules are separated by the temperature difference between the upper and lower portions of the kettle. The ions or molecular groups are transported to the low-temperature region, where the seed crystal is grown to form a supersaturated solution. Third, the ions or molecular groups are adsorbed, decomposed, and desorbed at the growth interface. Fourth, the adsorbed material moves to the interface. Finally, the dissolved matter crystallizes. The crystal morphology of crystals under hydrothermal conditions is closely related to the growth conditions[13][14][15]. The same crystals may show different morphologies under different hydrothermal conditions. It is very important to study the crystal morphology to predict the crystal growth mechanism.

➢ *The Role of Water in the Hydrothermal Method:*

Water can participate in the reaction as a chemical component or it can act as a solvent or a puffing accelerator. The properties of water will produce the following changes:

(1) The ionic product increases and the ionic product of water rapidly increase with the increase in pressure and temperature. Under high-temperature and high-pressure hydrothermal conditions, the hydrolysis reaction and ion reaction rates will naturally increase with water as the medium. Therefore, the main reason for the increase in the hydrothermal reaction is that the ionization constant of water increases as the reaction temperature and pressure increase.

(2) The viscosity and surface tension of water decrease as the temperature increases. In hydrothermal systems, the viscosity of water decreases and the mobility of molecules and ions in solution greatly increase, such that crystals grow under hydrothermal conditions more rapidly than under other conditions.

(3) Under hydrothermal conditions, the reaction is mainly affected by temperature and the dielectric constant of water is significantly reduced. This decrease affects the stability.

(4) The density decreases, and properties, such as the viscosity, dielectric constant, and solubility of the material, increase with increasing density while the diffusion coefficient decreases with increasing density.

(5) The vapour pressure increases and accelerates the reaction by increasing the chance of collision among molecules.

➢ *Role of Mineralisers:*

Because of the low solubility of the compounds involved in the hydrothermal method in water, even if the hydrothermal reaction temperature is very high, the solubility of most substances in pure water will not exceed 0.1 to 0.2 wt.%. Therefore, one or several substances are often introduced into the system to increase the solubility during the crystal growth process. These substances are termed as "mineralisers". Mineralisers are generally a class of compounds whose solubility in water continues to increase with increasing temperature, such as some low melting salts, acids, and bases[16] [17]. The addition of a suitable mineralizer not only increases the solubility of the solute in the hydrothermal solution, but also changes its solubility temperature coefficient. Some mineralisers can also form complexes with the crystalline material to accelerate the crystal nucleation rate. In addition, the type of mineralization agent also has a great influence on the quality and growth rate of the crystal.

Hydrothermal synthesis is an effective method to prepare multi-component oxide ceramic powders, including perovskite.

2.2.1.2 Sol–gel process

The sol–gel process is one of the most common and earliest known chemical synthesis methods for metal oxides that can be traced back to the mid-1800s. In the 1990s the sol–gel process received a major boost for the preparation of multicomponent metal oxides such as perovskite materials[18] [19]. Today sol–gel processes are routinely used to prepare 0-D, 1-D and 2-the perovskite materials. Chemical solution deposition (CSD) is a typical chemical deposition method for thin film preparation using the sol–gel solution as the deposition precursor.

Regardless of the desired material structure, the fabrication process often starts from a chemical solution, which acts as the precursor. The typical precursor includes a metal source, a solvent and chelating agent. Under appropriate heating conditions, the precursor solution transforms into a cross-linked polymeric state, called the "gel". Due to the liquid nature of the precursor, the end-product material can be fabricated in a range of morphologies simply by "casting" the precursor into an appropriate template or by using different deposition

approaches. For example, whilst spin-coating is suitable for thin films, pouring into template is employed for nano wires or nano tubes, and electro-spinning is used for nano fibers etc. It follows therefore that understanding what happens to the precursor at each processing step, and how its stoichiometry and physical features are affected, is of prime importance.

➤ *Metal compounds*

In the traditional sol-gel process, aqueous precursors based on metal alkoxides in water are used as the starting materials, which follow a route of hydrolysis-condensation-gelation. However, metal alkoxides are expensive and thus compromise the economic advantage of the CSD method.

➤ *Chelating agent*

Chelating agents such as acetic anhydride, acetic acid, citric acid, or tartaric acid, affect the solution viscosity and oligomeric structures during film formation[20]. Chelation reactions between the chelating agent and the metal source facilitate the gelation process under certain reaction conditions. The molecular structures of the different chelating agents determine the phases and morphologies of the final products.
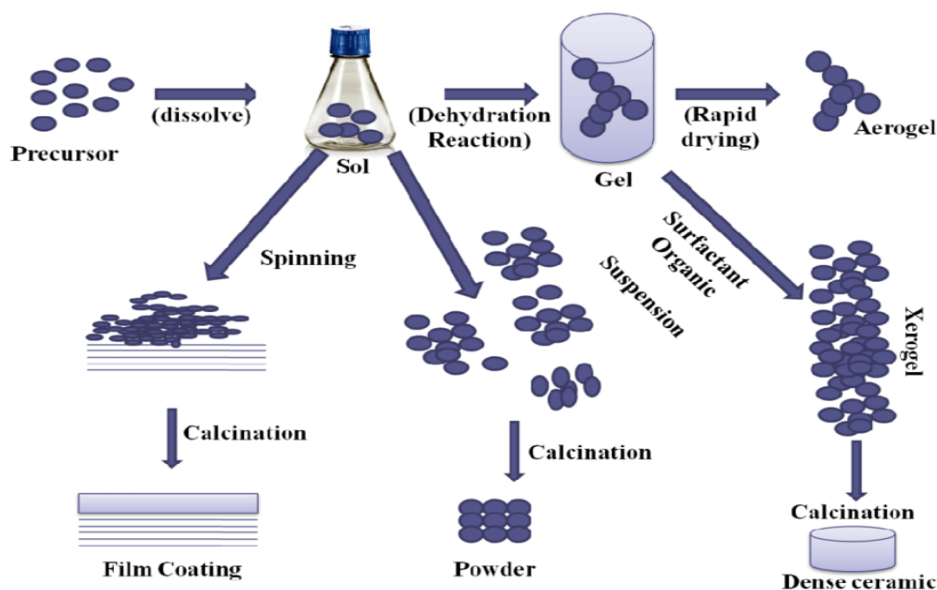
Figure 2.2 Schematic of Sol-Gel process

2.2.2 <u>Synthesis techniques used for the preparation of nano structured film</u>

Producing the highest quality films require quite expensive experimental setup and raw materials. Deposition techniques such as Molecular Beam Epitaxy (MBE), Pulsed Laser Deposition (PLD) or other methods falling under Physical Vapor Deposition (PVD) processes,

are very costly to setup and maintain. Moreover, getting epitaxial, or at least textured, films involve expensive single crystal substrates[21 22 23].

On the other hand, CSD is a cheap and easy method of thin film fabrication. Specific processes falling under CSD include dip coating, spray pyrolysis, spin coating etc[24]. The equipment necessary for CSD processes are generally not that expensive and raw materials are cost effective as well. We are hereby discussing two methods that are used in our work. CVD is used to prepare Single Layer graphene and Spin coating process is used to make BFO and rGO thin film.

2.2.2.1 <u>Chemical vapor deposition (CVD)</u>

Chemical vapor deposition (CVD) is one of the most popular routes to manufacture functional nano materials. It is often used to prepare high quality, high-performance thin films on large area wafers or complex patterned substrates. 1970s when this method was successfully used in semiconductor manufacturing, it has experienced rapid development[25], and now has become a mature process in fabrication of various coatings[26 27]. The key difference from CSD is that instead of solutions as precursors, materials are prepared by CVD via the deposition of gaseous precursor onto the substrate. Thus, it requires high vapour pressure composition as the precursor and often the substrate must be heated to a particular temperature to facilitate the deposition reaction as well as the motion of adatoms[28]. A typical CVD system is shown in Figure 2.3, which includes a vapour pressure, feed system, a CVD reactor (for heating the substrate) and an effluent gas handling system. Vapour precursors are often metal halides but depend on the type of reaction and materials. They are flowed with a reductant (H_2) or non-metal source gas (e.g. oxidant)[28]. The film thickness is heavily controlled by the reaction kinetics and hence the growth time. In the CVD process, the film composition and structure are rather sensitive to the substrate temperature, the precursor delivery ratio and the vaporizer temperature[29]. CVD processes have the advantage of high deposition rate at low deposition temperature. Compared with the CSD process, they offer much better control over the morphology, crystal structure and orientations, and as a result are often used to prepare epitaxial thin films. In addition, CVD is the most popular method to achieve highly conformal coatings on 3-D substrates for various devices. However, it also has disadvantages, such as possible toxic gas released from the reaction; the substrate temperature may cause phase changes or grain growth and diffusion of dopants in microelectronic components; the corrosive gas can lead to poor adhesion between film and substrate and contamination of the film, and the process has a higher cost than CSD.
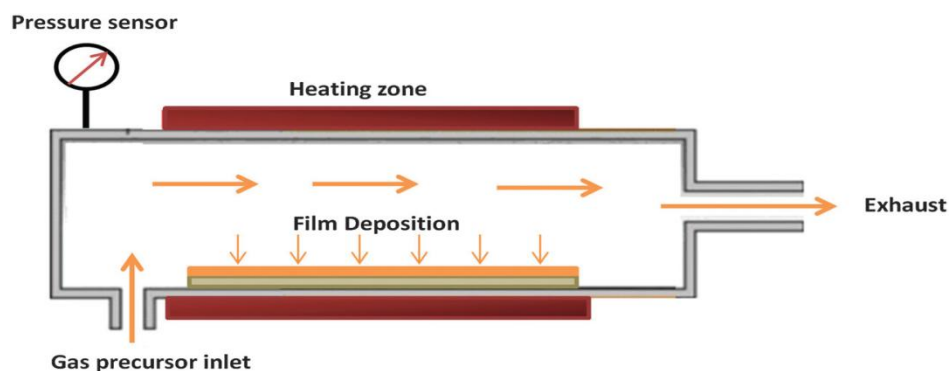
Figure 2.3 Schematic diagram of a chemical vapor deposition (CVD) system.

2.2.2.2 <u>Chemical solution deposition (CSD) derived Spin-coating process</u>

The CSD + Spin coating technique are an overall 3 stages process to obtain highly homogeneous, dense or thin film. In the first stage the precursors are dissolved in a solution, which is deposited in the second stage (using spin coating) following the heat treatment in third stage. It is a low energy consumed process with high morphological control of film. The morphology can be easily tuned by varying the composition, the viscosity, pH or concentration of the solution.

2.2.2.2.1 <u>*First stage- Precursor Preparation*</u>

The first step involves dissolving precursor using soft chemistry routine like sol-gel process. Here we defer the first case of sol-gel process which involves high temperature for gelation to obtain colloidal suspension of alkali or alkaline earth ions[30][31]. We prefer to use solution use alcohols to dissolve metal precursors to form metal alkoxides through hydrolysis and poly condensation reaction. These metal alkoxides are highly reactive in water which is then hydrolyzed by reacting with water and produces M-O-M chain. The hydrolysis and condensation create chain or branched structure i.e. gel[32][33][34]. Most commonly used alcohols are methanol, ethanol, 2-methoxyethanol, and 1,3-propanediol [35][36] and among them 2-metoxyethanol is widely used for the OH group exchange reaction in which there is formation of metal alkoxide that is less prone to hydrolysis, allowing an easy gel formation rather than precipitation[37]. The use of acids or bases as chelating agents[38] are to slow down the excessive tendency of alkoxides to reaction thus chelating agents are acting as catalysts and also they block un-controlled reactions[39].

Both 2-metoxyethanol (2-MOE) and Ethylene Glycol (EG) have a linear molecular structure, which is thought to be easier to form a dense and stable precursor molecule[34]. Moreover, the viscosity and surface tension of 2-MOE and EG are found to be highly suited to the spin-coating deposition process used for thin film fabrication.

[64]

2.2.2.2.2 *Second stage- Spin Coating*

This stage involves deposition of film on the surface by spin coating deposition process. In various processes the formation of film is governed by various forces such as surface tension, inertial force or pressure, viscous resistance and gravitational forces[40]. During spinning the centrifugal force is dominant than the force of gravity, generating a rapid thinning of the layer. The detailed procedure is discussed in later section.

Spin coating is a simple process for rapidly depositing thin coatings onto relatively flat substrates. The substrate to be covered is held by some rotatable fixture (often using vacuum to clamp the substrate in place) and the coating solution is dispensed onto the surface; the action of spinning causes the solution to spread out and leave behind a very uniform coating of the chosen material on the surface of the substrate. The pioneering analysis of spin coating was performed more than fifty years ago by Emil *et al.*.[41] who considered the spreading of a thin axi-symmetric film of Newtonian fluid on a planner substrate rotating with constant angular velocity. Centrifugal force drives the liquid radial outward. The viscous force and surface tension causes a thin residual film to be retained on the flat substrate. The film thins by the combination of outward fluid flow and evaporation[42]. This process has been widely used in the manufacture of integrated circuits[43], optical mirrors, colour television screens and magnetic disk for data storage[44].

➢ *Key stages of spin coating:*

The spin coating can be broken down into several key stages: fluid dispense, spin-up, stable fluid out flow, and finally evaporation dominated drying[45] as seen in Figure 2.4. Stage 3 (flow controlled) and stage 4 (evaporation controlled) are the two stages that have the most impact on final coating thickness. Clearly stage 3 and stage 4 describe the two processes that most be occurring simultaneously throughout all times (viscous flow and evaporation). However, at an engineering level the viscous flow effects dominate early on while the evaporation processes dominate later. Fluid flow on a flat spinning substrate is one of the most important physical processes involved in spin coating[46]. Several processing parameters involved in the spinning process are: dispense volume, final spin speed (w), final film thickness, solution viscosity, solution concentration (c), spin time, etc.

Film thickness is easily changed by changing spin speed, or switching to a different viscosity photo resist. But among the alternative coating techniques, many have multiple coupled parameters, making coating control more complex. Another advantage of spin coating is the ability of the film to get progressively more uniform as it thins, and if the film ever becomes completely uniform during the coating process, it will remain so for the duration of the process. It is low cost and fast operating system.

Typical spin coating processes utilize only 2–5% of the material dispensed onto the substrate, while the remaining 95–98% is flung off in to the coating bowl and disposed.

1. *Deposition :*

During this stage, solution is allowed to fall on rotating substrates from micro syrings and the substrate is accelerated to the desired speed. Spreading of the solution takes place due to centrifugal force and height is reduced to critical height. This is the stage of delivering an excess of the liquid to be coated to the surface of the substrate a portion of which's immediately covered or "wetted". In this stage liquid can be deposited in different ways (a) as a heavy rain that inundates the entire disk; (b) as a bolus at the centre or around the perimeter of hole if the centre has been cut out, the liquid then spreading over the rest of the disk, or (c) as a continuous stream at the centre, or all the way around the inner perimeter, the liquid then flowing outward over the entire disk, or (d) as a continuous stream from an elevated delivery port that moves racially over the disk. No matter what way is used the amount of liquid deposited through excessive is limited and this stage ends when delivery ceases.

The substrate is either not rotating called static deposition or rotating at a low speed called dynamic deposition.

2. *Spin-up :*

The second stage is when the substrate is accelerated up to its final, desired, rotation speed. This stage is usually characterized by aggressive fluid expulsion from the wafer surface by the rotational motion. Because of the initial depth of fluid on the wafer surface, spiral vortices may briefly be present during this stage; these would form as a result of the twisting motion caused by the inertia that the top of the fluid layer exerts while the wafer below rotates faster and faster. Eventually, the fluid is thin enough to be completely co-rotating with the wafer and any evidence of fluid thickness differences is gone. Ultimately, the wafer reaches its desired speed and the fluid is thin enough that the viscous shear drag exactly balances the rotational accelerations.

3. *Stable fluid outflow/spin off :*

The third stage is when the substrate is spinning at a constant rate and fluid viscous forces dominate fluid thinning behavior. This stage is characterized by gradual fluid thinning. Fluid thinning is generally quite uniform, though with solutions containing volatile solvents; it is often possible to see interference colors "spinning off", and doing so progressively more slowly as the coating thickness is reduced. Edge effects are often seen because the fluid flows uniformly outward, but must form droplets at the edge to be flung off. Thus, depending on the surface tension, viscosity, rotation rate, etc., there may be a small bead of coating thickness

[66]

difference around the rim of the final wafer. Mathematical treatments of the flow behavior show that if the liquid exhibits Newtonian viscosity (i.e. is linear) and if the fluid thickness is initially uniform across the wafer (albeit rather thick), then the fluid thickness profile at any following time will also be uniform.

4. *Evaporation:*

When spin-off stage ends the film drying stage begins. During this stage centrifugal out flow stops and further shrinkage is due to solvent loss. This results in the formation of thin film on the substrate. The fourth stage is when the substrate is spinning at a constant rate and solvent evaporation dominates the coating thinning behaviour. In this, the rate of evaporation depends on two factors (a) the difference in partial pressure (actually chemical potential) of each solvent species between the free surface of the liquid layer and the bulk of the gas flowing nearby. During the evaporation stage the suspended or dissolved solids may grow as concentrated at the liquid surface as to form a high viscosity, low diffusivity layer or solid skin.
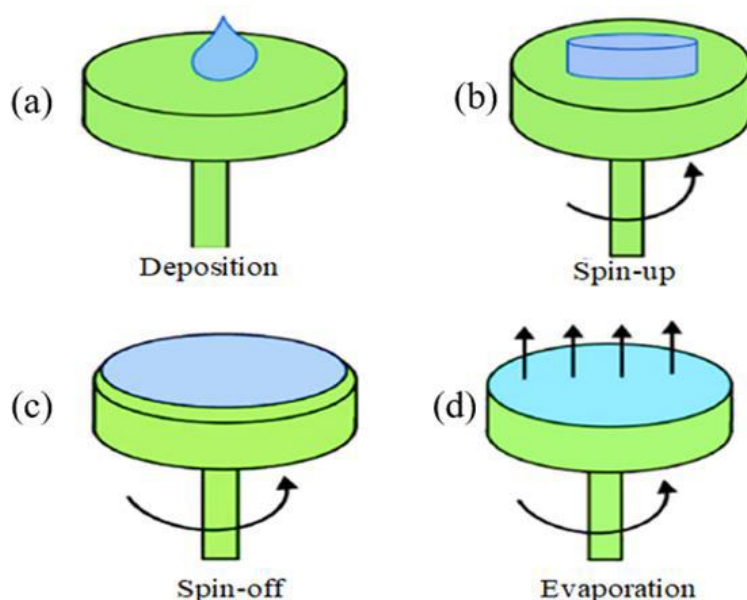
Figure 2.4 Key stages of spin coating

➢ Factors that impact the thickness of the thin film of materials coated on the substrates, are discussed below.

1. *Spin Speed:*

Spin speed can be considered as one of the significant factors in the spin coating system[47] [48]. The speed of spin is measured by rotation per minute (rpm). The speed (rpm) of the substrate impacts the degree of radial (centrifugal) force applied to the liquid resin and the characteristic

as well as velocity of the air directly above it. In this step, comparatively slight differences of ± 50 rpm could produce a change of about 10% of the resulting thickness.

2. Acceleration:

The wafer acceleration across the ending speed could be described as the second important factor which influences the properties of the coated film[49]. Subsequently, the resin starts to dry throughout the first part of the spin series, and it is very essential to precisely control acceleration. In the first few seconds of some process, around 50% of the solvents in the resin will be wasted by evaporation.

3. Rotating Time:

Time can be considered as another important aspect that affects the spin coating procedure and the characteristic of the final film[49 50]. The degree of drying of the liquid resin through the spin method is well- expressed by the nature of the liquid itself (volatility of the solvent systems applied) also by the air that surrounded the sample throughout the spin progress.

Film thickness after deposition strongly depends on the precursor viscosity, precursor density, spin-coating velocity and spin coating time. The relationship between film thickness and above factors can be described as :

$$h(t) = \frac{h_0}{\left(\sqrt{1 + \frac{4\rho\omega^2 h_0^2\, t}{3\eta}}\right)}$$

where, $h(t)$= film thickness at time t

ρ = density of the liquid

η = liquid viscosity

ω = angular velocity

h_0= initial film thickness

2.2.2.2.3 *Third stage- Heat Treatment*

The final thickness is achieved by evaporation after it becomes thin and viscous enough that it does not flow. The subsequent drying and crystallization treatments are then carried out. These heat-treatment processes include drying, pyrolysis and crystallization.

➢ *Drying:*

Drying is a step to remove the solvent by heating. As drying simply works on evaporation, its rate is sensitive to the temperature and vapour pressure[51]. Compared to a bulk

[68]

material, thin films have a comparatively large surface area to volume ratio, so the evaporation process of a thin film is often easier and faster. As discussed above, this process can happen during spin coating and heating. For thin-film samples, gelation often happens during the drying step as well as heating. To obtain a uniform gel film after drying, it is important to ensure that the gelation step is completed before drying, so that no precipitates are formed.

> ➢ *Pyrolysis:*

The drying temperature is often not sufficient to remove all the polymers in the material and a higher temperature pyrolysis process is needed before crystallization to prevent the formation of defects. Films after pyrolysis are amorphous and the nucleation and- growth process will occur in the following annealing/sintering (crystallization) process which takes place at a higher temperature.

> ➢ *Annealing:*

Two different high-temperature heat-treatments are often used for ceramic thin film annealing/sintering. One is the conventional heating process, by which the materials are heated slowly to a target temperature and maintained at this temperature for a specific duration (typically minutes). The other process, called rapid thermal processing, is an increasingly popular manufacturing process which heats films to a high temperature over short timescales of several seconds. For both heat treatments, nucleation of the amorphous thin films starts first during the heating process, followed by the grain growth. The driving force of crystallization is determined by the free energy difference between the amorphous and crystallized material, and the temperature below melting point[52].

During the sintering and densification process, the particles begin to join together and the pores become smaller until elimination due to the diffusion of materials driven by interfacial energy. Nucleation often takes place either in the bulk body or the substrate-film interface of the thin-films. The former is a case of homogeneous nucleation, leading to random oriented grains and polycrystalline thin films. The latter case is heterogeneous nucleation, which often contributes to oriented columnar grain nucleation and growth matched to the substrate lattice structure. Generally, the nucleation barrier for heterogeneous nucleation is lower than that for homogeneous nucleation. A higher heating temperature decreases the driving force, thereby preventing homogenous nucleation. Therefore, rapid heating of the dried film to a high temperature promotes preferred heterogeneous nucleation at the interface thereby promoting textured or epitaxial grain growth[52].

2.3 <u>Material synthesis</u>

In this complete thesis we report the synthesis of rGO/BFO nano composite, rGGO/BFO heterostructure, super ferromagnetic BFO/Ag nano composite and fabricated Single Layer graphene (SLG) followed hydrogenation and dehydrogenation. There are different techniques that we have applied to synthesize the abovementioned materials. We will now discuss those synthesis procedures in details in the next few sections.

2.3.1 <u>Preparation of rGO/BiFeO$_3$ nano composite</u>

The two published procedures namely sono-chemical mixing and in-situ hydrothermal process with a few modifications are followed to synthesize the rGO (multilayer graphene) and BFO composite and it was observed that in-situ hydrothermal process was better suited for enhancement in properties with an insight to bond formation between rGO and BFO which was necessary for Fe-C bond formation.

2.3.1.1 <u>Synthesis of reduced graphene Oxide (rGO)</u>

Graphite is multilayer stacking of 2D graphene. There were numerous approaches to synthesise graphene using Graphite as starting material. We have opted a well-known approach of modified Hummer's route[53] [54].to synthesize graphene Oxide (GO) followed by reduction to obtain the reduced graphene oxide (rGO) or multilayer graphene. Synthetic Graphite powder (particle size ~0.2μm) was used as the precursor material for graphene Oxide (GO) synthesis. At first, adequate amount of Sulphuric Acid (H$_2$SO$_4$) was taken in a round bottom flask in an ice bath to control the temperature of the bath below 20°C. Then, proportionate amount of Graphite powder along with Sodium Nitrate (NaNO$_3$) was added to the acid solvent and stirred for a while. After a while, Potassium Permanganate (KMnO$_4$) was added gradually and stirred vigorously. When, the bath temperature was stable then the ice bath was removed and the sample got slowly heated up to the room temperature and was maintained at that temperature for some time. After that the solution was diluted with 5% hydrogen peroxide (H$_2$O$_2$) solution slowly and the colour of the solution turned to brownish yellow. This confirmed the complete oxidation of graphite. The solution was stirred for some more time to ensure the complete exfoliation of graphite oxide. The final product was graphene oxide GO which was collected by filtration and washing with 1N hydrochloric acid (HCl) solution and de-ionized water several times. Then, the aqueous solution of as prepared GO (1mg/ml) was then mixed with Ascorbic acid (Vitamin C) (10 wt% of GO) followed by ultrasonication was used to obtain reduced graphene Oxide (rGO) solution.
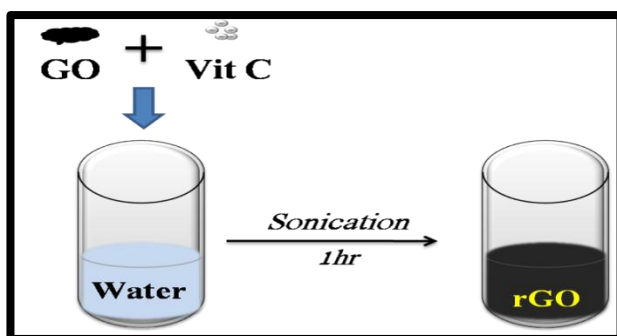
Figure 2.5 schematic of rGO synthesis

2.3.1.2 <u>Synthesis of bismuth ferrite nano powder via hydrothermal technique</u>

In this process, Bismuth Nitrate penta-hydrate [Bi $(NO_3)_3$, $5H_2O$] and Iron Nitrate nona-hydrate [Fe$(NO_3)_3$, $9H_2O$] in equal molar ratio was directly dissolved in 8M potassium hydroxide [KOH] solution. The solution turned into a dark brown homogenous mixture. To this was added 4 volume percent of 5% hydrogen peroxide (H_2O_2, 30% Merck) and stirred well. The whole mixture was transferred in a Teflon lined autoclave and put in hydrothermal heating for 30hr at 180°C. The resulting powder was collected by centrifugation and washed several times with DI water and Ethanol.
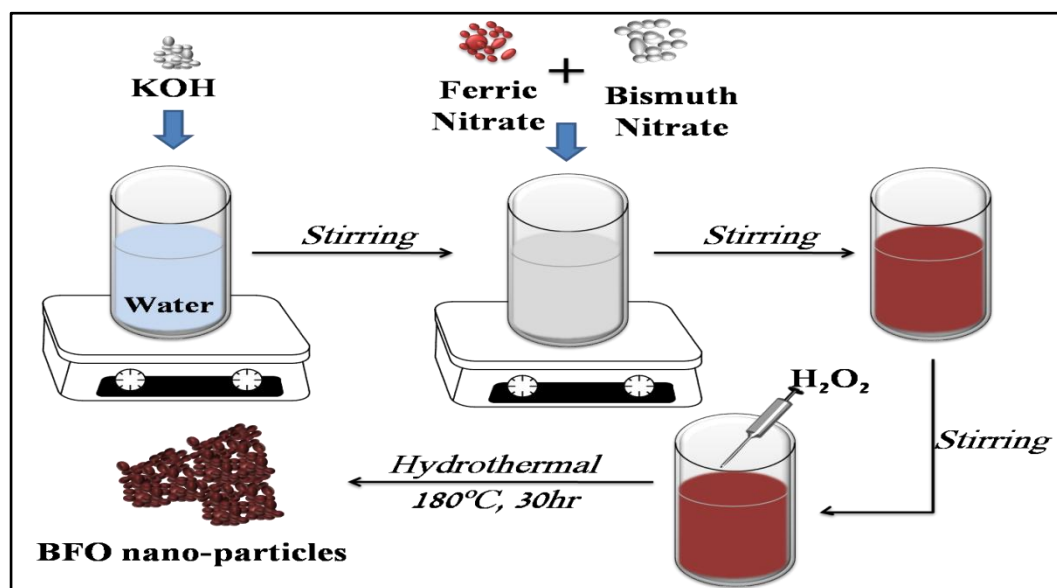
Figure 2.6 Schematic of making BFO nano particles

2.3.1.3 <u>Synthesis of reduced graphene oxide/bismuth ferrite nano composite via hydrothermal technique</u>

In this process Bismuth Ferrite precursors (Bismuth Nitrate penta-hydrate [Bi$(NO_3)_3$,$5H_2O$] and Iron Nitrate nona-hydrate [Fe$(NO_3)_3$, $9H_2O$]) were added to highly molar basic solution of Potassium Hydroxide [KOH] in stotiometric ratio. After a while the mixture became homogeneous, an aqueous solution of of rGO was added to the mixture in a proper

[71]

weight percentage. A small amount of Ammonium Hydroxide [NH$_4$OH] was mixed to stabilize the negatively charged rGO in the bath. After vigorous stirring the solution was transferred to an autoclave and hydrothermally heated at 170°C for 2, 4, 5, 6 hours time frame. After cooling the sample was collected via centrifugation with ethanol and de-ionized water until the pH became neutral. The hydrothermally treated sample for 6hrs gave the best result and a phase pure BFO was obtained. Different weight percentages mainly 0.5wt%, 1.5wt% and 2.5 wt% of rGO was incorporated into the mixture and accordingly the resulting composites were named as Com-H-0.5, Com-H and Com-H-2.5 respectively.

Also, the nano composite Com-H was heated upto 550°C with a ramp of 10 $^\circ$C/min for 20 min and cooled at same rate. This was purposefully done to remove the carbon skeleton from the composite and get the bare BFO which was used for further characterizations as BFO (BFO_H) and comparative analysis.
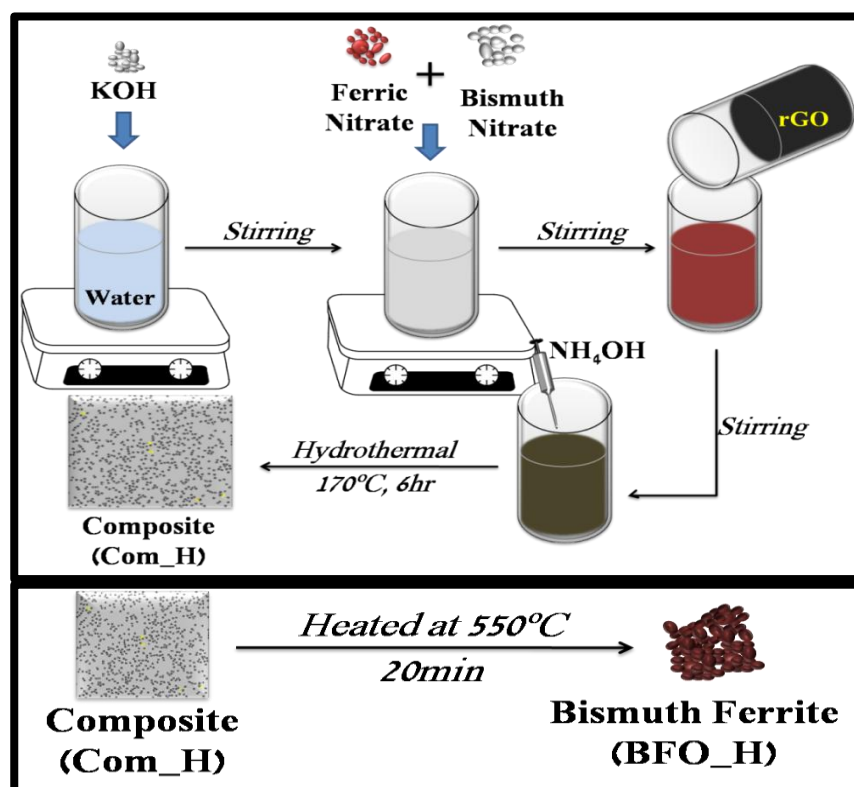
Figure 2.7 Schematic of samples prepared in Hydrothermal route

2.3.1.4 <u>Synthesis of reduced graphene oxide/bismuth ferrite nano composite via sono-chemical mixing</u>

In this procedure, BFO nano powder (following section 2.3.1.2), depicted as BFO-P, was added to the mixture of Ethylene glycol and acetic acid in 1:1 ratio and ultra-sonicated for 2.5 hours. rGO aqueous solution (1mg/ml) was prepared as stated early (section 2.3.1.1). After 2.5hours an aqueous solution of rGO (1mg/ml) was added to the mixture and sonicated for additional 15 mins. Then the mixture was heated to 80°C and stirred all along for 2hrs. The

resulting solid was filtered and washed with ethanol and de-ionized water several times. Here also two different weight percentages of rGO was used to make the composite. One of the composite has 1.5wt% and another has 15wt% of rGO and they were designated as Com-P-1.5 and Com-P-15.
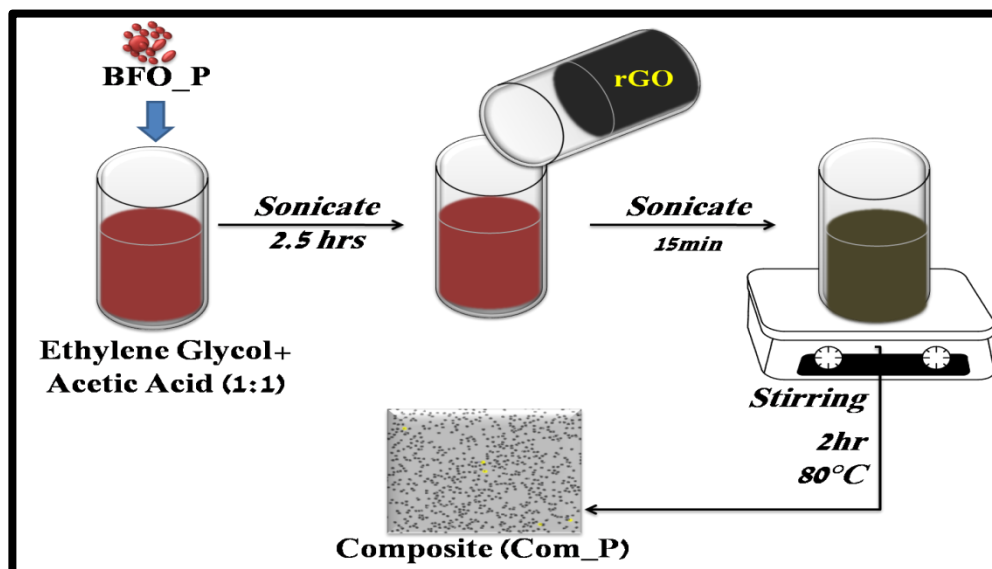
Figure 2.8 Schematic of samples prepared using sono-chemical mixing

2.3.2 Preparation of rGO/ BiFeO₃ heterostructure

The second part of the work involves the synthesis of rGO/BFO heterostructure to find the interaction between different layers. The preparation of rGO solvent is already discussed in section 2.3.1.1. The preparation of BFO stock solution for spin coating process will be discussed in the next section. The details mechanism of building layered heterostructure of BFO/rGO will be discussed in Chapter 5.

2.3.2.1 Synthesis of stock solution for bismuth ferrite film deposition

A mixture of 2-Methoxy ethanol and Glacial acetic acid in 4:1 ratio was taken in a beaker. After mixing the solvents for a while the nitrate precursors- Bismuth Nitrate penta-hydrate [Bi(NO$_3$)$_3$5H$_2$O] and Iron(II) Nitrate nona-hydrate [Fe(NO$_3$)$_3$9H$_2$O] were added to the mixture and stirred vigorously. A homogenous dark brown coloured solution was obtained that was filtered and the collected solution is was the stock solution for BFO film deposition. The details molarity of the solution will be discussed in later chapter 5.
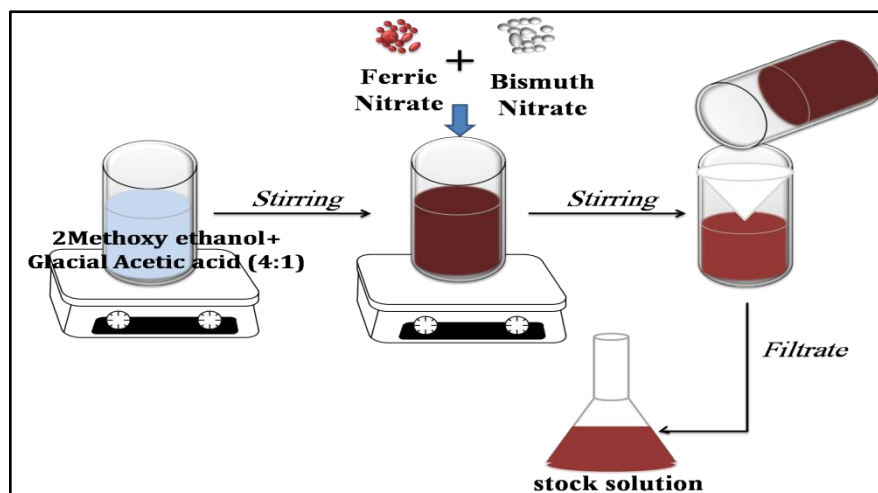
Figure 2.9 Schematic of making Bismuth Ferrite stock solution

2.3.3 Preparation of silver wrapped bismuth ferrite nano chains

The preparation of silver wrapped BFO nano chains is a two step process as discussed here. At first prepared BFO nano powders as discussed in 2.3.1.2 were used for making composite. The as prepared BFO powders were dispersed in 1:4 DI water and Ethanol mixture and sonicated until dissolved. To this was added silver Nitrate [AgNO$_3$] solution of 20wt% wrt BFO. Then the mixture was further reduced using Sodium boro-hydrate [NaBH$_4$] as reducing agent. The solution immediately turned dark brown was further stirred for 30 min. The resulting powder was found to be extremely magnetic in nature as they got to the stir bar. The residual powder was then collected by filtration using PVDF membrane filter of (~0.22μm pore size) followed by deionized water and Ethanol mixture. The sample was depicted as BFO/Ag. Another sample with 2wt% of silver Nitrate [AgNO$_3$] was prepared and was designated as BFO/Ag-2.
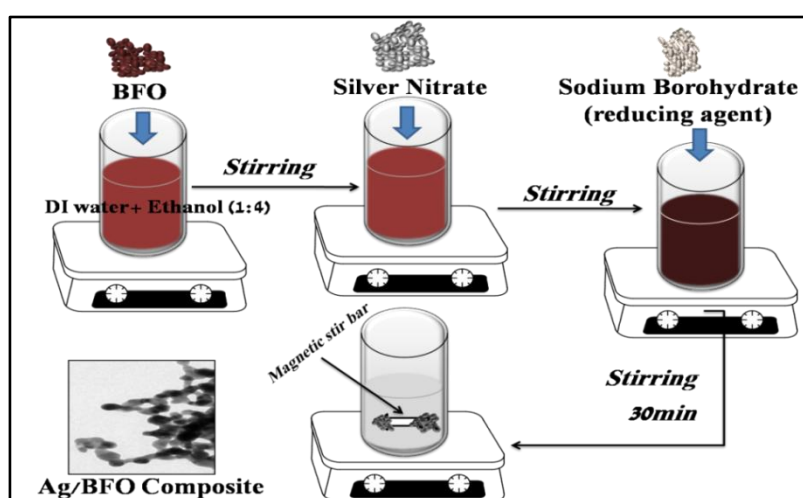
Figure 2.10 Schematic of making silver wrapped bismuth ferrite nano chains

2.3.4 **Preparation of hydrogenated and dehydrogenated Single Layer graphene**

2.3.4.1 **Growth of Single Layer graphene**

Single layer graphene was grown on copper foil (Alfa Aesar with purity 99.8%) via CVD method in MTI Corporation's OTF 1200X series split tube furnace (with Fe Cr-Al heating element) from methane decomposition at 1000°C with prior cleaning with acetone, acetic acid, deionized water and isopropyl alcohol sequentially[55].Single layer graphene grown on Cu foil was then transferred on glass substrate using a 3 Weight % solution of PMMA as previously described[56]. The schematic is shown in Fig. the final product is depicted as SLG.
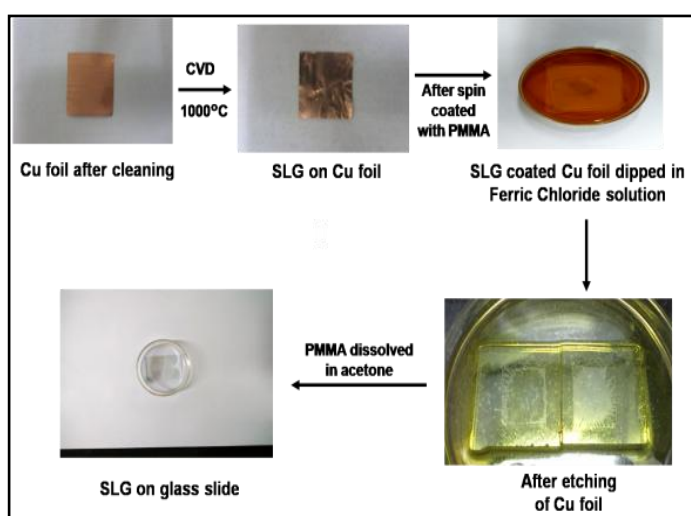
Figure 2.11 Wet Chemical Transfer Process of SLG

2.3.4.2 **Synthesis of hydrogenated SLG by Birch reduction**

The Birch reduction of graphite to yield hydrogenated graphene (graphane) is illustrated in Scheme 1.

Scheme 1: Birch Reduction of SLG

$$SLG + Li + NH_3 \rightarrow [SLG]^-Li^+$$

$$[SLG]^-Li^+ + CH_3OH \rightarrow \text{hydrogenated SLG}$$
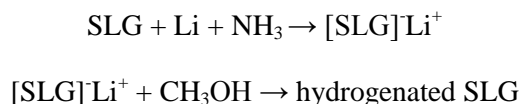
The reaction was carried following reported hydrogenation procedure of graphite. A 250 mL three-neck round-bottom flask equipped was flame-dried under vacuum, flushed with argon, and then maintained under an atmosphere of argon. A dry ice−acetone mixture (−78 °C) was then applied to cool the flask and condenser. Ammonia (160 ml) was condensed into the flask, followed by the addition of one or two beads of lithium metal and single layer graphene transferred on to quartz substrate was added to the mixture with gentle swirling motion given

[75]

for the dissolution of lithium metal in the ammonia. The mixture was kept for 1 h under the protection of argon. The dry ice−acetone bath was then removed, and methanol (~1-2 ml) was added to the reaction mixture. The reaction mixture was refluxed at the boiling temperature of liquid ammonia (−33 °C) and kept for 4 h while refilling the dry ice−acetone condenser as needed. The ammonia in the system was then allowed to evaporate overnight. The reaction was quenched by slow addition of ethanol followed by water. The SLG substrate was taken out of the reaction mixture and washed thoroughly with water, hexane and ethanol. The obtained partially hydrogenated graphene on quartz was dried at 80 °C in a hot air oven in ambient atmosphere for 20-25 minutes. The final product is named as 'hydrogenated SLG'.

2.3.4.3 <u>Synthesis of dehydrogenated SLG</u>

Dehydrogenation of Birch reduced SLG using DDQ as oxidizing agent is shown in Scheme 2.

Scheme 2: Dehydrogenation of SLG

$$\text{hydrogenated SLG } \frac{DDQ, Tolune}{Reflux\ 110°C} \rightarrow \text{Dehydrogeneted SLG}$$
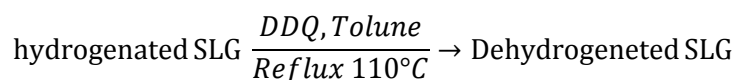
hydrogenated graphene samples were dehydrogenated using excess of DDQ and toluene at 110°C with continuous stirring for 24 hours. The samples were washed thoroughly using excess of toluene to remove unreacted reactants and kept for drying in a hot air oven in ambient atmosphere for 20-25 minutes at 70-80°C. The final product is named as 'Dehydrogenated SLG'.

2.4 <u>Sample characterization</u>

The crystal structure and surface morphology of the as-synthesized materials were determined by Power X-Ray Diffraction (XRD), Field Emission Scanning Electron Microscopy (FESEM), Energy Dispersive X-ray Spectroscopy (EDX), Transmission Electron Microscopy (TEM), Selected Area Electron Diffraction (SAED), High Resolution Transmission Electron Microscopy (HRTEM), and X-ray photoelectron spectroscopy (XPS). The magnetic properties were measured by Magnetic Force Microscopy (MFM), Lake-Shore Vibration Sample magnetometer (VSM) and Quantum Design Super Conducting Quantum Interference Device (SQUID) Magnetometer. Ferromagnetic properties were measured by ferroelectric loop tracer (P-E loop tracer).

2.4.1 <u>Techniques to study of structural characterization</u>

To confirm the phase purity of the as synthesized material, characterizations like XRD, RAMAN, EDX, FTIR, XPS, etc. were carried out.

2.4.1.1 **X-Ray diffraction (XRD)**

X-ray Diffraction is a well-known characterization technique which is basically a diffraction phenomenon following certain conditions, thereby, determining the crystal structure, crystallographic plane orientation, defects, and grain size of materials. It arises because of the interaction of collimated X-ray beam and the periodic arrangements of atoms in a crystal structure. X-ray are generated from Cathode ray tube and after filtered to monochromatic beam and collimated to concentrate are incident on the sample at an angle θ. The X-rays are diffracted from their path while interacting with the atoms in atomic planes and these diffracted rays interfere with each other constructively when certain conditions were met. The conditions were named after English physicists Sir W.H. Bragg and his son Sir W.L. Bragg as Bragg's Law who developed the reason behind XRD techniques in 1913. The schematic is shown in Figure 2.12.

Bragg's Law: $\boldsymbol{2d sin}\theta = \boldsymbol{n\lambda}$

Where,

θ is the angle of incidence of X-ray

d is a variable which is the distance between atomic planes in a crystal

λ is the wavelength of the incident X-ray beam

n is an integer which is the diffraction order.

Each crystallographic plane are identified according to Miller Indices h, k, l and comparing with the existing database one can identify planes, orientations and phases. One of the renowned databases used for this particular purpose is JCPDS (Joint Committee on Powder Diffraction Standard) database. We have used Panalytical (X'Pert Pro) system with a CuKα radiation (λ= 1.54 Å) for characterising all the samples. This is θ- 2θ system in which the X-ray tube is fixed, and the specimen moves at half the rate of the detector to maintain the θ- 2θ geometry as shown in the diagram in Figure 2.12 (a). The data is usually refined using Reitvelt Refinement via fullProf software to find the information of lattice. The plotted data is shown in Figure 2.12 (c).

(a)   **(b)**

(c)
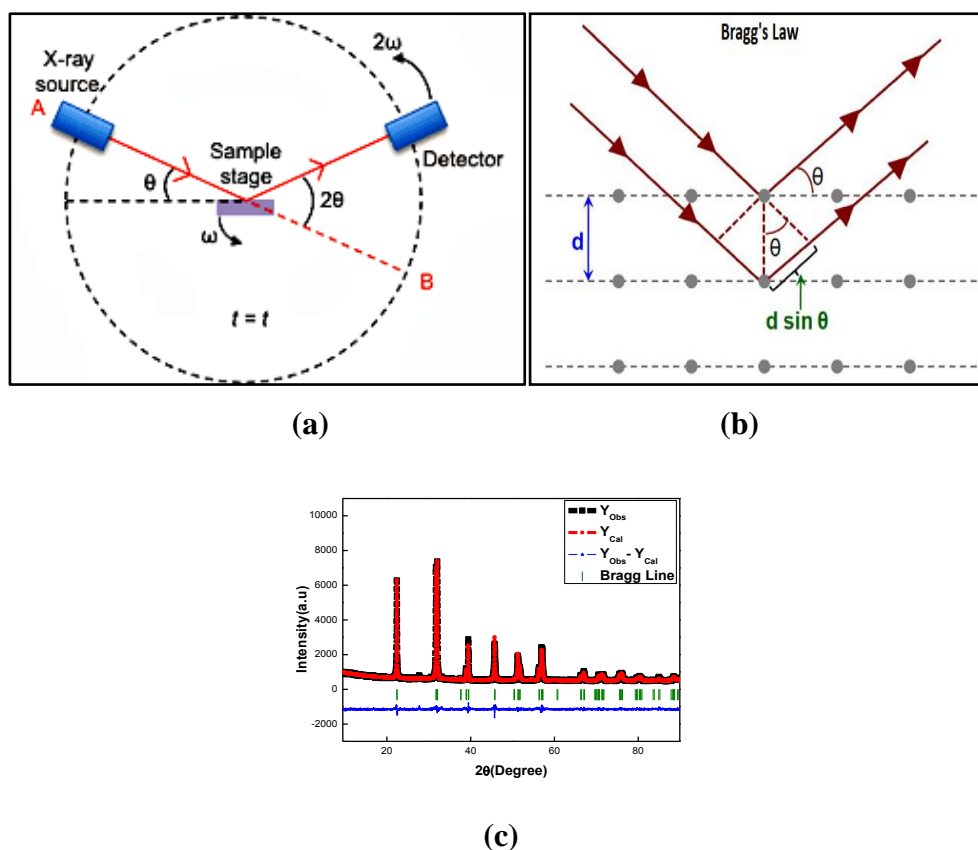
Figure 2.12 Schematic of X-Ray diffractometer (a), Graphical representation of Bragg's Law (b), and XRD of BFO refined using Reitvelt refinement (c)

2.4.1.2 <u>Neutron Diffraction</u>

Neutron diffraction experiments determine the atomic and/or magnetic structure of crystalline solids, gasses, liquids or amorphous materials. Neutron diffraction is a form of elastic scattering. The technique is similar to X-ray diffraction. A sample to be examined is placed in a beam of thermal or cold neutrons and the intensity pattern around the sample gives information of the relative position and motion of atoms in a bulk. X-Rays generally interact with electron cloud. But interaction of Neutron beam with atoms is rather via nuclear forces rather than electrical forces. This is because Neutrons have no charge and zero or very little electric dipole moment hence it can penetrate deep in atoms. X-rays interaction is larger with high atomic no (Z) but can't detect low Z atoms. In Neutron low Z atoms contribute strongly even in the presence of high Z.

Though neutrons have zero charge, but they carry a spin, and therefore interact with magnetic moments, including those arising from the electron cloud around an atom. Neutron diffraction can therefore reveal the microscopic magnetic structure of a material. For our work powder diffraction data were recorded at PD-3 beamline of National Facility for Neutron Beam Research (NFNBR), Dhruva Reactor, Mumbai under magnetic field 0-20kOe at room

[78]

temperature. the monochromatic beam used was of wavelength 2.315 Å. In our case we use Reitvelt Refinement using Full Prof Software to analyze both XRD and Neutron data as shown in Figure 2.13.
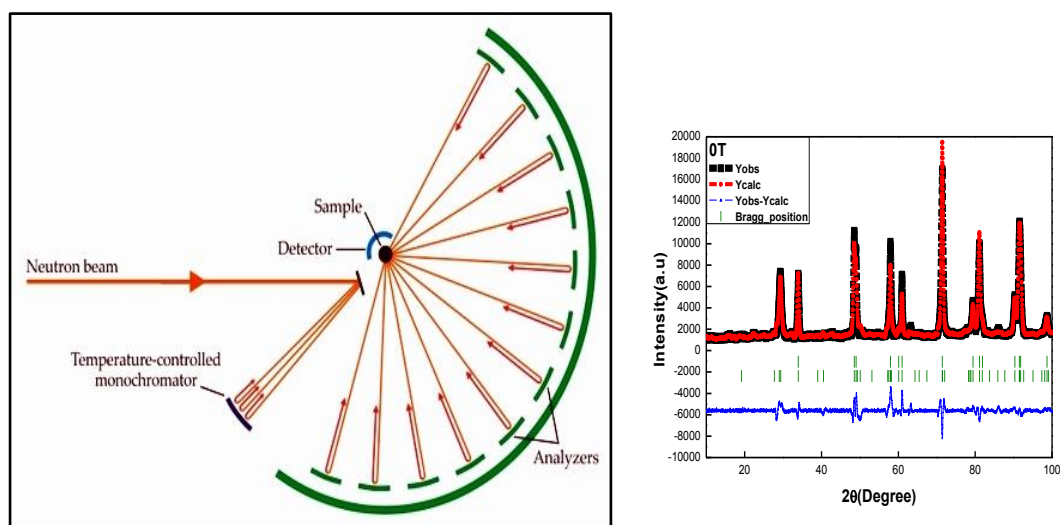
Figure 2.13 The Neutron facility schematic from ILL (Left) , the refined Neutron data (right)

2.4.1.3 **X-Ray Photoelectron Spectroscopy**

X-ray Photoelectron spectroscopy (XPS) is a widely used quantitative tool to obtain the chemical composition, chemical state and electronic state of components in a material. The theory is based on the Photo electric effect proposed by Einstein at 1905. The technique was developed by Kai Siegbahn and his group from Sweden at 1960. The high energy X-Ray beams are used to irradiate the sample surface to eject core electrons and an electron energy analyzer is used to measure the energy of emitted photo-electrons. The relationship between core level photo-electrons and X-ray energy is;

$KE = h\upsilon – BE- e\varphi$

where,

KE is the kinetic energy of the ejected photo-electron

$h\upsilon$ is the characteristic energy of X-ray

BE is the Binding Energy of the atomic orbital from which the electrons are ejected

$E\varphi$ is the spectrometer work function.

At each and every element there are characteristics Binding Energies are associated with the core level of atoms. From the variations in BE or chemical shift of photo- electron lines give information about the chemical state can be derived at. KE of photo-electrons give this information and intensity of photo-electrons is proportional to relative concentration of the elements in the material. Here we have used PHI XPS system and core level spectra of 'MgKα'

are used as excitation source. The raw data are de-convoluted using OriginPro8.5 and the resultant core level spectra of Bi4f state are shown in Figure 2.14.
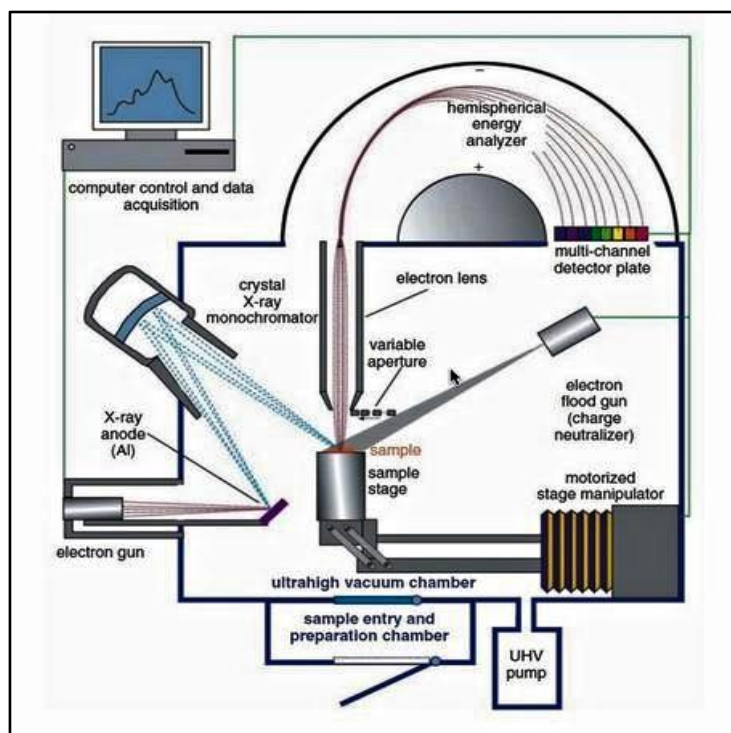
(a)
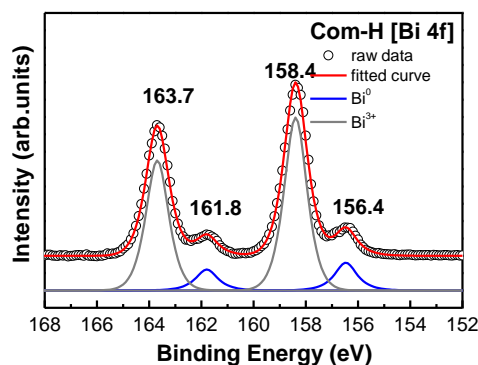
(b)

Figure 2.14 XPS instrument schematic (a), and Bi 4f core level spectra of BFO (b)

2.4.1.4   RAMAN Spectroscopy

Raman spectroscopy is a distinct chemical fingerprint to explore the Chemical structure and identity Phase and polymorphism, intrinsic stress/strain, Contamination and impurity in a material. It was named after Sir Chandrasekhar Venkata Raman for carrying out ground-breaking work in the field of light scattering, which earned him the 1930 Nobel Prize for Physics. This is the inelastic scattering of monochromatic light from Laser when photons are reemitted after interaction with chemical bonds within the material. Most of the Rayleigh

scattered light does not provide any information about material. Whereas typically 0.0000001% is scattered at different wavelengths (or colors) than incident, which depend on the chemical structure of the material which is called Raman Scatter. The frequency changes upon interaction with a specific molecular bond vibration, including individual bonds, groups of bonds, polymer chain vibrations, lattice modes, etc. A sample is normally illuminated with a laser beam in the ultraviolet (UV), visible(Vis) or near infrared (NIR) range. Scattered light is collected with a detector like photo diode array, CCD or PMT and is sent through spectrophotometer to obtain Raman spectrum of a sample (see Figure 2.15) this shift provides information about vibrational, rotational and other low frequency transitions in molecules.
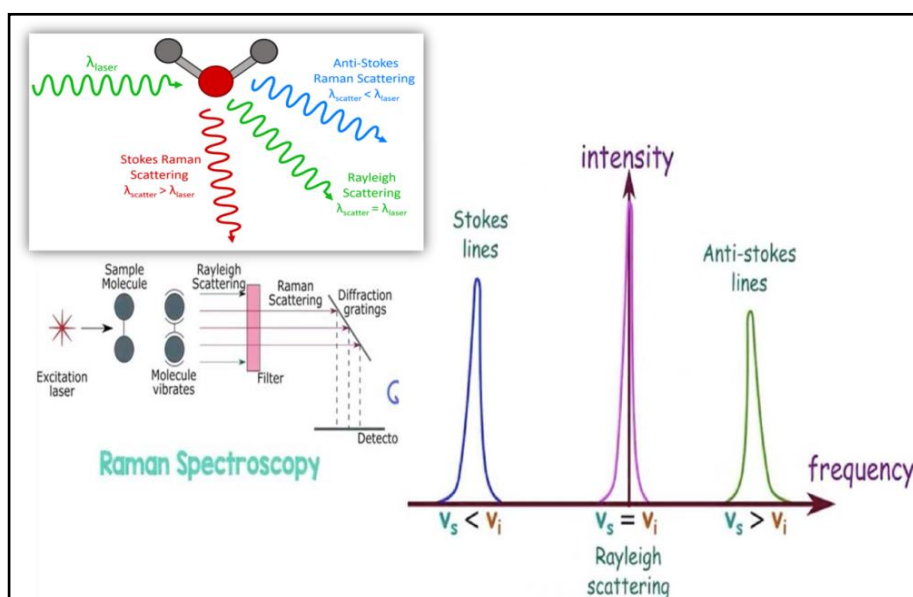
Figure 2.15 RAMAN spectroscopy schematic

When an incident photon interacts with the lattice it creates an electron-hole pair via electron radiation interaction. These electrons after recombining with the hole create a phonon via electron-lattice interaction. Following the conservation rule, the scattered photon frequency and wave vector can be written as,

$$\omega_s = \omega_i \pm \omega$$

$$k_s = k_i \pm k$$

Where, ω_s, ω_i, ω are the frequencies of scattered phonon, incident phonon, and phonons created after recombination.

Where, k_s, k_i, kare the wave vectors of scattered phonon, incident phonon, and phonons created after recombination.

If $\omega_s < \omega_i$, it is called stokes scattering and if $\omega_s > \omega_i$, it is anti-stokes scattering. This change in frequency is called Raman shift which provides the chemical and structural information such as on bond vibration of the material. This bond vibrational energy is useful for

[81]

the analysis of the magneto-electric coupling in the multiferroic material induced by the structural distortion. In our work the RAMAN spectra were obtained using RenishawIn via Reflex Micro RAMAN spectrometer at CGCRI.

2.4.1.5 <u>**Fourier transforms infrared spectroscopy (FTIR)**</u>
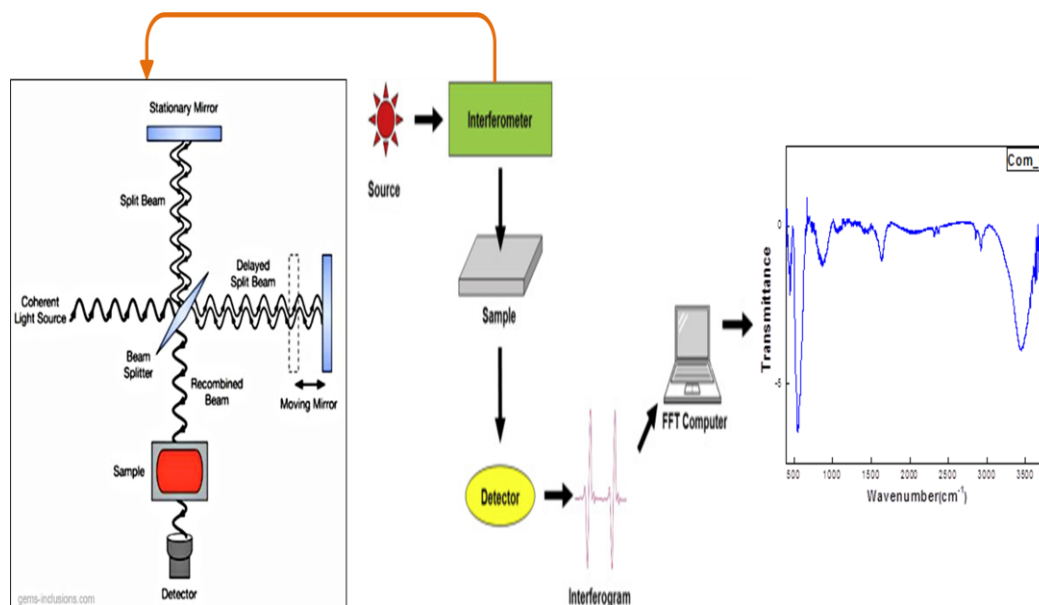
Figure 2.16 Schematic of FTIR

Fourier transform infrared spectroscopy (FTIR) is a spectroscopic technique that work based on the mechanism of Michelson's interferometer (Figure 2.16). It relies on the absorbance, transmittance or reflectance of infrared light from the sample at different frequencies. The resulting signal is fingerprint to identify the sample because the absorption or transmittance of light in a sample depends on their vibrational frequencies of the molecular bonds specific to identify the organic and inorganic compounds present in the sample. Fourier Transform is used to convert the raw data from detector output into an interpretable spectrum. This spectrum provides various structural insight of the sample like heteronuclear functional group vibrations and polar bonds. FTIR differs from RAMAN spectroscopy because FTIR depends on change in dipole moment whereas RAMAN depends on change in polarizibility of a molecule. IR measure the actual frequencies at which sample absorbs or transmit radiation but in RAMAN it measures relative frequencies at which sample scatters radiation. In RAMAN we can have the information about the homo-nuclear bond present in molecule whereas FTIR suggests gives information of the hetero nuclear bonds. FTIR can distinguish between C-C, C=C and C≡C bonds. All the data were collected at Perkin Elmer FTIR spectrometer in reflectance mode at CGCRI. The processed data are shown in Figure 2.16 (right).

[82]

2.4.1.6 **Thermo-gravimetric (TGA) analysis**
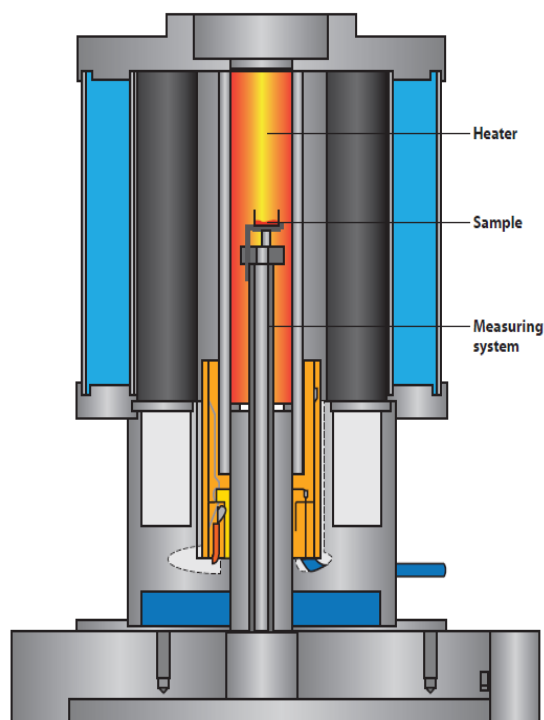
Figure 2.17 Schematic of TGA instrument

Thermo-gravimetric analysis was performed with a thermo-balance as seen in Figure 2.17. The device consists of an electronic balance which is placed inside an oven; the device is coupled to a control microprocessor and a processing station data. Samples in the form of fine powder are slid and placed inside the analysis equipment for testing, they are then calcined to 1000 ° C temperature range that ramp up at the rate of 10 ° C/ minute. The preparation process of the samples can be described as follows,

1) Obtain the geo-polymeric sample by reducing a fine powder in an amount of ~1 g.

2) Add the material in the sample holder very carefully and verify that 5/6 of the total volume are covered.

3) With the sample prepared and by using lab forceps, the sample holder is introduced into the analysis equipment.

4) The software is activated, with the aforementioned parameters.

2.4.2 Techniques to study of morphological characterization

To have the morphological details FE-SEM, TEM, HRTEM are done.

[83]

2.4.2.1   <u>Field emission scanning electron microscope (FESEM)</u>

To have the topological images of the material Scanning Electron Microscopy is most widely used. It gives the information about grain size, distribution of particles, composition and even electrical conductivity. The image is formed by the interaction of atomic surface with the stream of highly energetic electrons. In SEM two different approaches are used to produce electron beam; either it is thermo-ionically or field emitted from an electron gun. In our study the field emission is applied and hence it is named as Field Emission Scanning Electron Microscope (FESEM). A field-emission cathode in the electron gun is called a cold cathode emitter and placed in a huge electrical potential gradient providing narrower probing beams at low as well as high electron energy. The Field emission source is usually a Tungsten wire with sharp tip of a small radius in the range of 100nm. The small tip provides extremely concentrated electric field which lowers the work function of cathode and electrons can leave cathode easily.The electron stream is accelerated towards the specimen (with a positive electrical potential) and is focused and directed in a particular direction using metallic charged plates and magnetic lenses as shown in Figure 2.18. When, the electron beam interacts with the sample, the energy exchange between the electron beam and the sample results in deceleration of incident electrons through the energy dissipation and produces a variety of signals which include secondary electrons (SE), back-scattered electrons (BSE), characteristic X-rays, visible light (cathode-luminescence) (CL), specimen current and transmitted electrons. Secondary and backscattered electrons are conventionally separated according to their energies[57]. The electrons are detected by suitable detectors placed in the microscope in proper positions.

The acceleration voltage between cathode and anode is commonly of the order of magnitude of 0.5 to 30 kV under extreme vacuum of 10^6 Pa. the resolution is of the order of 2 nm at 1keV and 1 nm at 15 keV. Characteristic X-rays are used for elemental analysis. The process is known as energy dispersive analysis of X-ray (EDAX). Due to high energetic and narrower beam, field emission SEM (FESEM) results in both improved spatial resolution and minimized sample charging and damage. Two types of FESEM microscopes are used in this whole thesis work- (i) FESEM, Supra 35Vp, Carl Zeiss Germany (30kV image, resolution 1.5nm); and (ii) FESEM, Zigma, Carl Zeiss Germany (30kV image, resolution 1.3nm).
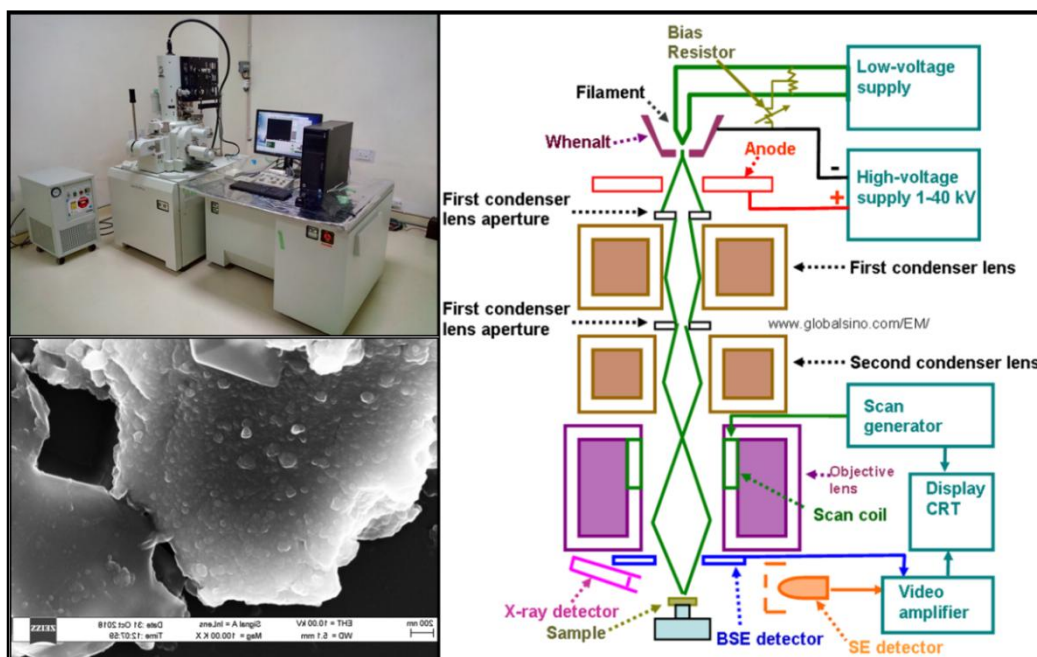
Figure 2.18 The ZEISS SUPRA FESEM facility (LEFT up corner), the FESEM image of Composite at 100 magnification range with EHT 10kV (Left down side), the schematic diagram of FESEM (Right)

2.4.2.2 <u>Transmission electron microscopy</u>

The Transmission Electron Microscope (TEM) developed in 1931 is the characterization technique capable of imaging the material analytically using the diffraction technique of electrons from the specimen. A thin layer of diluted specimen is placed upon conductive grid through which a beam of electrons (with a typical wavelength of less than 1 Å) is passed normally. Without affecting the specimen a fraction of electrons gets scattered either elastically or in elastically. The electrons get diffracted following the Bragg's Law and the scattered electrons from each atomic plane have different scattering angle. These scattered electrons form are collected using magnetic lenses and form a patterned spot each corresponding to specific atomic spacing or crystalline plane. This pattern can then yield information about the atomic orientation, arrangements and phases present in the area of the sample being examined.

The transmitted beam is a collection of not scattered electrons which are responsible of producing 2D image of the sample. The transmittance is inversely proportional to sample thickness like thick areas appear darker and thin areas are appeared lighter. This mode of operation is hence known as Bright Field Imaging technique.

Standard TEM grid has typical diameter of 3.05mm with a thickness of few micrometer and mesh size ranging from a few to 100μm. TEM micrograph of rGO/ BFO using a high resolution TEM or HRTEM (JEOL-2010) system is shown in Figure 2.19. To prepare the sample we have used Lacey carbon grid to have the contrast of graphene other than carbon mesh.

[85]
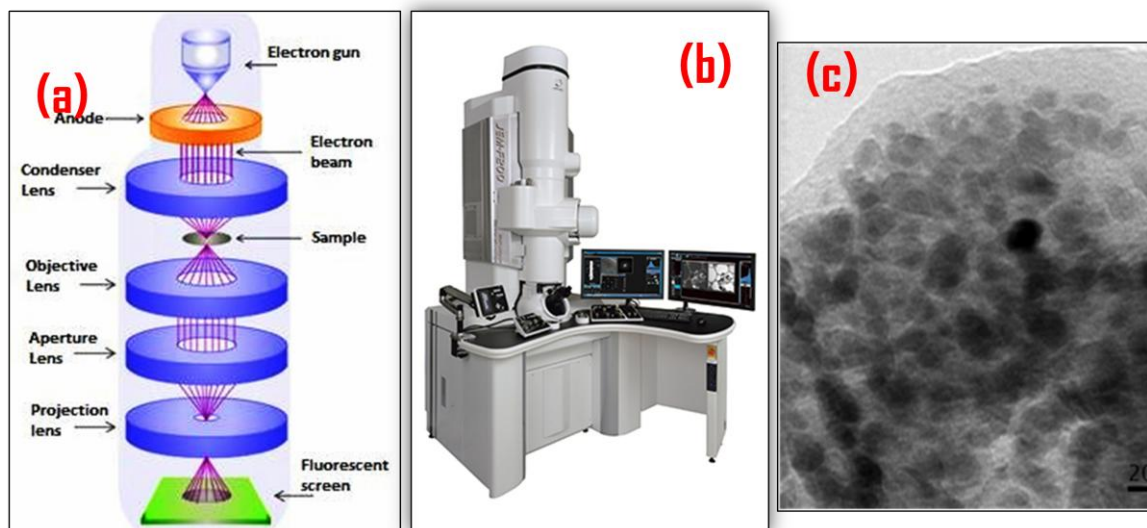
Figure 2.19 (a) Schematic of TEM, (b) JEOL HRTEM instrument, (c) Bright Field image of composite.

2.4.3 <u>Techniques to study of electrical properties</u>

For the measurement of electric properties mainly the ferroelectric property the sample was spin coated the sample onto SiO_2 substrate. The powder sample was firstly taken in the diluted form by dispersing in Ethanol via sonication. The spin coated sample thickness was in the range of 10 nm. The silver paste was pasted on two sides to connect with silver wire as shown in Figure 2.20.
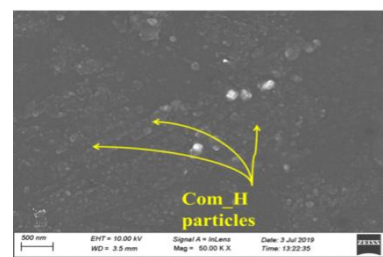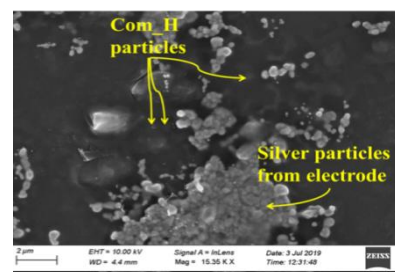
Figure 2.20 Schematic of sample preparation (a); Morphology of samples coated upon Substrate (b), Inter electrode morphology (c)

2.4.3.1   **Ferroelectric hysteresis measurement**
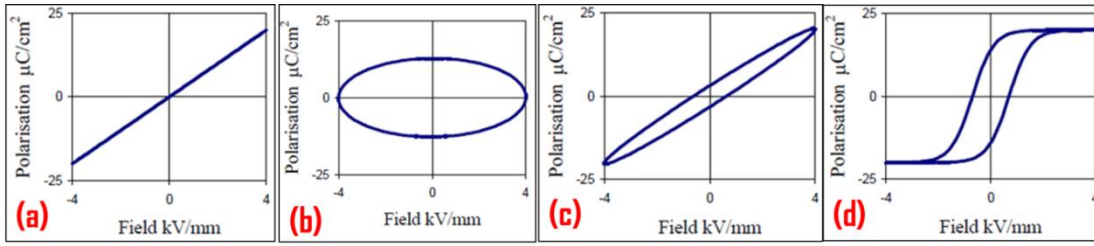
Figure 2.21 P-E loop of Capacitor (a), Conductor (b), Parallel set of Capacitor and resistor (c), and ferro electric material (d)

Ferroelectric property measurement is one of the key features in multiferroic material. A P-E loop of a material is measured as the change in polarization or charge wrt external applied field. There are different plot of P vs E that can be generated for different material as shown in Figure 2.21. In capacitor and ideal resistor P-E plot are straight line and centre respectively because current and voltage are out of phase in capacitor and in phase in capacitor and resistor. Parallel set of Capacitor and resistor gives a leakage nature where slope gives value of capacitance and area gives the value of loss tangent of the material.
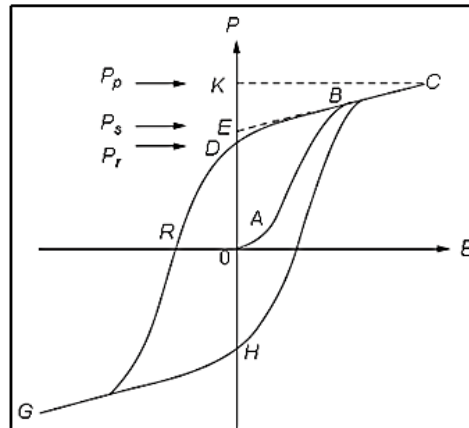
Figure 2.22 Common diagram of a P-E Loop of a ferroelectric material

But for ferroelectric material we get a P-E hysteresis loop from where we have the spontaneous polarization (P_s) and coercive field (E_c). According to the on applying low field the polarization occurs and with gradual increase in field, the polarization increases non linearly (AB portion) because all the domains are start to align in the direction of the applied electric field. After a certain electric field maximum numbers of the domains g*et al.*.igned in the same direction of applied field and polarization attains saturation (BC portion). While decreasing the electric field not all the domains switch to opposite direction instantly. So the decreasing path is different and follows the CBD path. This decreasing path when touches the zero field axis it gives the value of spontaneous polarization P_s and the extrapolation of saturated region cuts at

[87]

K gives the value of remanent polarization P_r. some negative field is needed here to completely align the domains in opposite direction. The external field required to bring Polarization to zero is called coercive field (E_c).
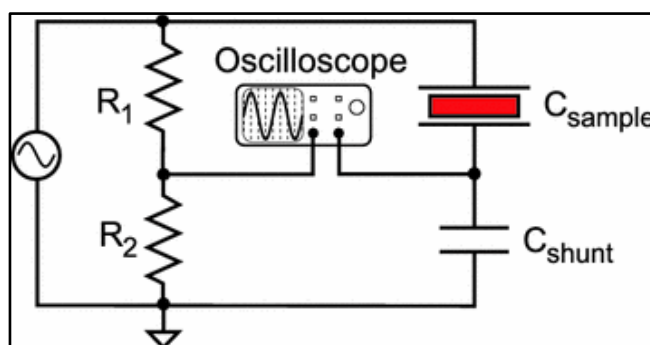
Figure 2.23 Equivalent diagram of Sawyer-Tower Circuit

The P-E loop measurement is dependent on Sawyer Tower circuit. This circuit as shown in Figure 2.23which consists of alternating signal generator (E), a reference capacitor (C_o) and the unknown capacitor (C_x) which is equivalent to the ferroelectric sample attached.

With the application of AC electrical signal both the capacitors are charged to same amount of charge Q as they are connected in series. The voltage appeared across both the capacitor are V_o and V_x respectively. Now Polarization of ferroelectric sample is proportional to charge Q in C_x,

$Q = P \times A$

Now, $Q = V_x C_x = V_0 C_0 = P \times A$

In Sawyer Tower circuit $C_0 \gg C_x$ therefore,

V_x is equivalent to applied electric field and hence P is proportional to V_o.

So, the V_x vs V_0 in the oscilloscope as x channel and y channel results in representation of P vs E.

Leakage conductance, parasitic capacitance, parasitic diode problems can be easily overlooked by using PUND or Remanent protocol we have used in our measurement technique which is discussed below.

There are so many intrusions of external factors in measurement of ferroelectric materials especially in thin film. Large leakage current, linear non-linear components as well as ferroelectricity in local domain are different in different domains and we get an overall average value of the ensemble. The actual intrinsic ferroelectricity is mixed with all these and it is so small that it can be detected from P-E loop measurement. Precision, LC-II, Radiant Technologies P-E loop tracer are used for our data acquisition in both protocols.

[88]

2.4.3.1.1 *Remanent Protocol*

In P-E loop of a sample we get total response to a stimulus including linear & non-linear ferroelectric elements. Linear components include the contribution from linear Capacitor, resistor and diode effects whereasnon-linear contribution is our area of interest corresponding to the inheren ferroelectricity present in the material, this non-linear polarization can be modelled as two or more non-linear components. One of the two major components is remanent and non-remanent Polarization. Remanent polarization does not switch with the switching of external electric field and contains the memory part of the sample. Non remanent polarization does not maintain the switched state but gets randomly affected after achieving a certain quiescent voltage. The hysteresis measurement is a contribution of both linear as well as non-linear part.

Hysterisis response = Linear effect (resistor, capacitor, diode effect) + remanent polarization+ non- remanent polarization.
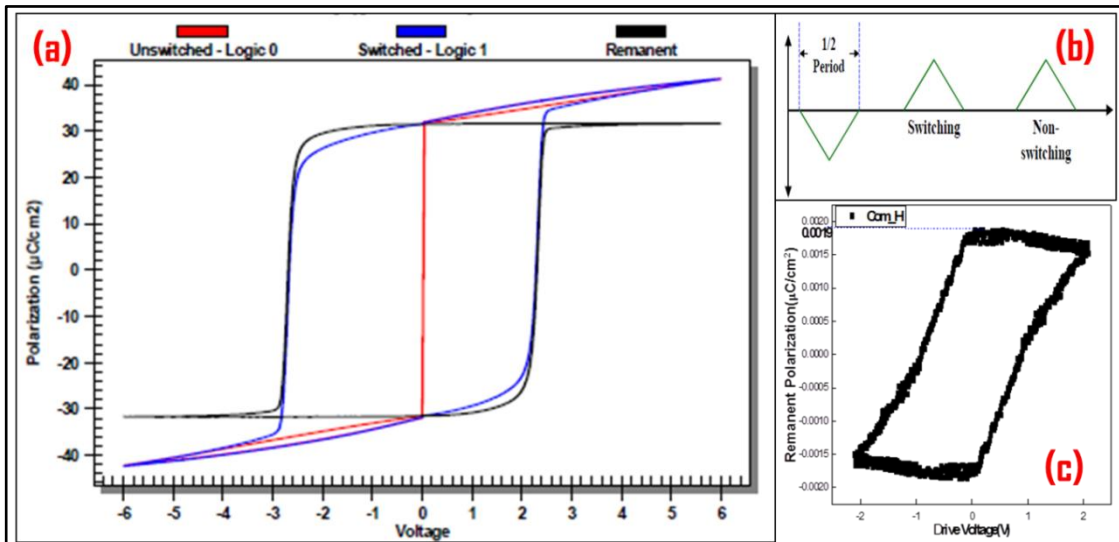
Figure 2.24 (a) Remanent Protocol, (b) schematic of pulses applied in remanent protocol, (c) Remanent Hysteresis plot of composite

Remanent hysteresis measurement is done using two half Hysterisis loop instead of pulses as shown in Figure 2.24 (b). Now the difference of switching and non- switching measurement will give rise to remanent polarization as shown in Figure 2.24 (a)[58].

Hysterisis switching – Non- switching = Remanent Polarization.

We have to achieve the certain saturation voltage where remanent part is equal to original response and the test is executed in both directions to have the full remanent loop vs voltage function loop. The V_c of remanent loop is the true coercive voltage. The loop measured of composite is shown in Figure 2.24 (c).

[89]

2.4.3.1.2 PUND Protocol

To distinguish ferroelectric switching from artefact's a series of voltage pulses is being applied. PUND [positive (P), up (U), negative (N), and down (D)] [59]protocol consists of five pulse sequences consist of preset pulse, Positive switched pulse (P*), positive non-switched pulse (P^) following the same sequence in negative direction (-P*, -P^). The first positive pulse (P*) is to orient the polar domains in a particular direction generating from both hysteretic and non-hysteretic contribution. The second pulse (P^) is to re-orient the non-hysteretic domains in the same direction. Eliminating the P^ contribution from the P* contribution gives the positive remanent polarization. Similarly following the negative part [N: (-P*), D: (-P^)] we have the negative remanent part. The difference between switched and non-switched pulse gives the value of twice the value of remanent polarization[60]. This value equals the remanent polarization as shown in Figure 2.25.

$dP = P* - P^ = 2P_r$
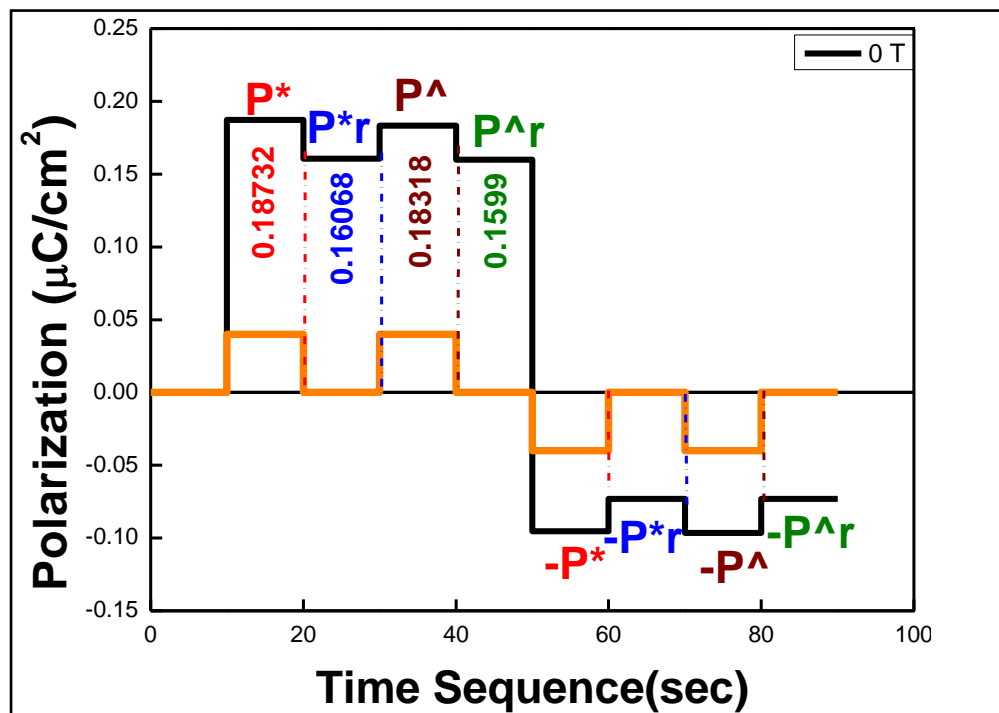
Figure 2.25 The Plot of PUND (Black line) measured on composite are merged with pulses applied (Orange line)

The voltage is held constant for all thee pulses but the relaxation or delay time can be changed. Now two things were observed if the sample had very small leakage then no current being seen and otherwise a constant current is seen. After applying Pulse2 switching will not be seen when the polarization is stable and sometimes the peak was observed after applying Pulse2 which is the net ferroelectric polarization.

2.4.3.2   <u>Study of dielectric properties</u>

A typical schematic diagram of dielectric property measurement setup has been shown in Figure 2.26. We measured the dielectric response of the samples in the frequency range of 42Hz to 5 MHz using HIOKI LCR meter and we covered the higher frequency range of 5MHz-4 GHz with the help of Agilent E 4991A material analyzer. We analyzed the data with the help of Z-View software. The applied field amplitude was varied over 0.1-1 volt. However, no dependence of the dielectric response pattern could be noticed as a result of such variation. The electrodes were made of high quality silver. Data obtained from different electrodes were compared in order to extract the intrinsic features of the samples. Since the samples are basically low resistive, we employed constant current mode for measurement of the dielectric response.
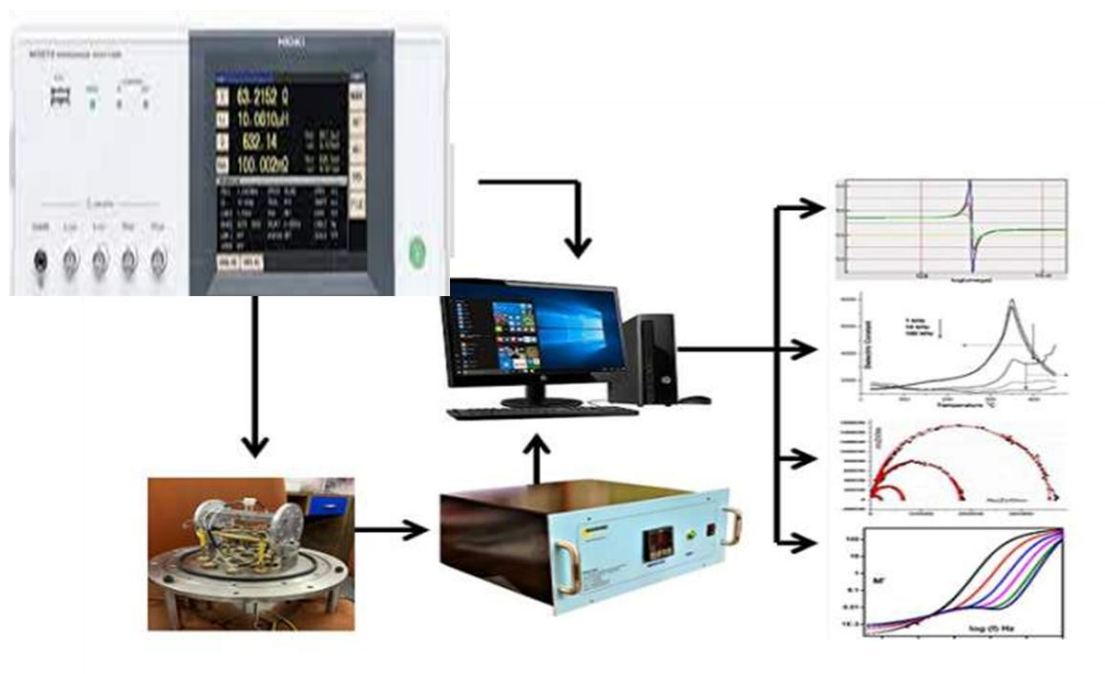
Figure 2.26 Dielectric experiment measurement setup using HIOKI LCR meter

2.4.4 <u>Techniques to study of magnetic properties</u>

In order to have the magneto electric study magnetic property measurement is extremely important to study. Here we have used the sample in the form of either pellet or powder form to measure the magnetic hysteresis loop in room temperature or under various temperature regions. We have performed the magnetic measurement using both VSM and SQUIID techniques.

2.4.4.1   <u>Vibrating sample magnetometer (VSM)</u>

Vibrating sample magnetometer is a versatile technique based on Faraday's Law used to measure room temperature or temperature based on M-H hysteresis loop. Here the sample can

be used in any of the form of powder, pellet or thin film. Faraday's law stated that Electromotive force (EMF) (V) will be generated in the coil if there is change in flux (B) linking the coil.

For a coil with n no of turns and cross- sectional area (A), induced EMF (V) will be,

$$V = -nA\frac{dB}{dt}$$

The direction of EMF can be determined using Lenz's Law.

If we place a magnetic sample having magnetization (M) in a constant magnetization field (H) then Flux around it is,

$$B = \mu_0(H + M)$$

Where, μ_0 = Permeability in vacuum.

The change in flux is, $\Delta B = \mu_0 M$ as H is constant

Comparing with previous equation induced EMF in the pickup coil

$$Vdt = -NA\mu_0 M$$

So, output signal (V) is proportional to magnetization and independent of magnetic field.

Schematic are shown in Figure 2.27 (a). The sample here is attached to a rod which is centred in between two electromagnet pole pieces that can generate a magnetic field uniformly. Now the sample rod is connected to a transducer assembly which is connected to an oscillator or sinusoidal signal generator.

This transducer transforms the signal into sinusoidal vertical vibration so the sample is vibrating under magnetic field. This change in flux originating from vibration induces a voltage which is detected by pickup coils. The stationary pickup coils detect the voltage which is proportional to the magnetization of the sample. This data is also amplified by the lock in amplifiers External magnetic field is only necessary to magnetize the sample. The voltage detected is not only proportional to moment but also the vibration frequency and amplitude which are subject to error if one only count signal amplitude. So nulling technique is introduced by generating a reference signal using a vibrating capacitor. Comparing the induced signal with reference signal we can obtain moments readings that vary only with moment of sample. For our room temperature M-H loop measurements we have used LakeShore Vibrating Sample Magnetometer (VSM; Model 7407).
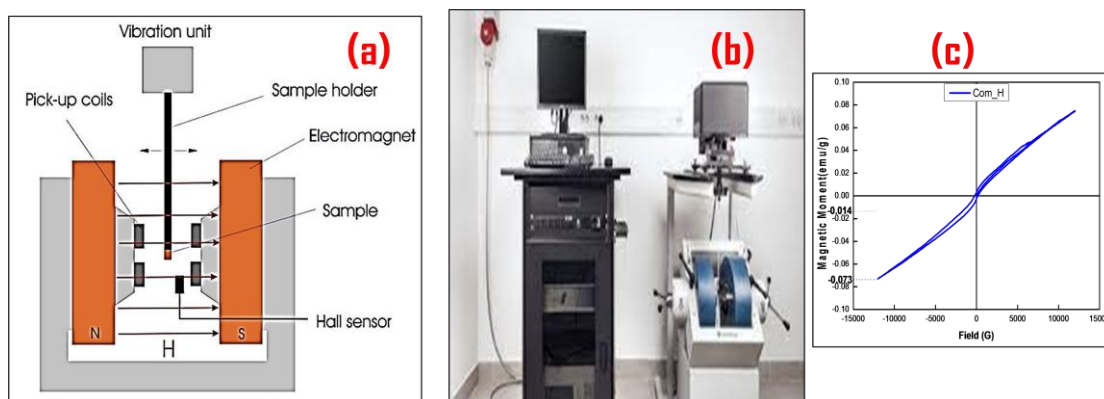
Figure 2.27 (a) Schemetic of VSM, (b) Lakeshore VSM, (c) M-H plot of composite

2.4.4.2 Superconducting quantum interference device (SQUIID)
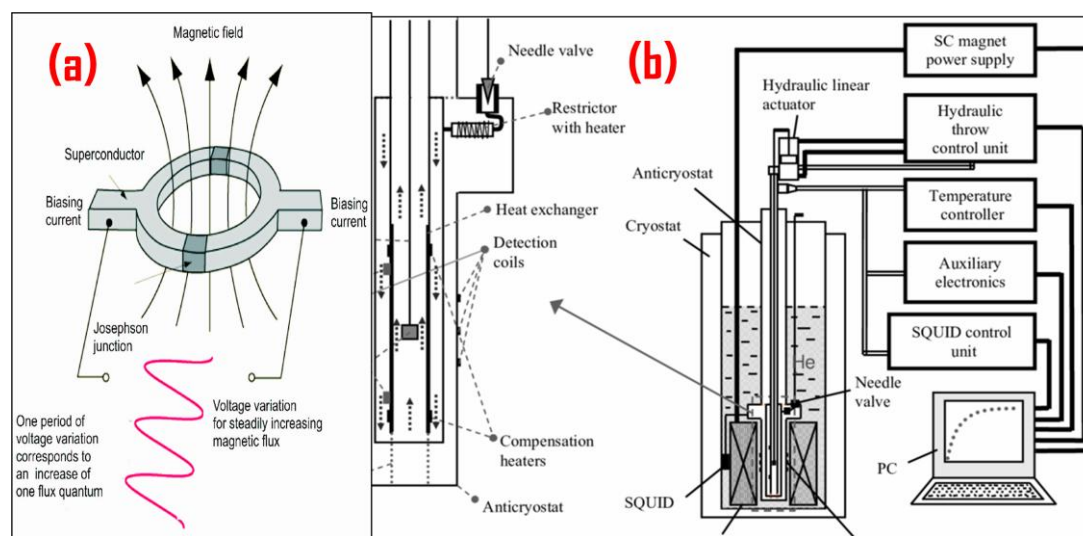
Figure 2.28 (a) Josephson Junction, (b) SQUIID magnetometer system

SQUIID can detect magnetic moment of the order of 10^{-8} emu whereas VSM can detect only upto10^{-5} emu. Also SQUIID is more sensitive.

The working principal is based on tunnelling superconducting electrons or Cooper pairs across a narrow insulating gap called as Josephson junction (Figure 2.28 (a)). Josephson junction consists of two pieces of superconductors separated by a thin barrier.

The total super current is divided into two parts and passed through two identical Josephson Junctions A & B. When magnetic field is applied (let with I_A) and subtract from other junction current (let from I_B).

Due to coupling the changed current will change the magnetic flux in junction and hence change voltage of the device. It is magnetic flux to magnetic voltage converter which directly proportional to magnetic signal.

[93]

2.4.4.3 **Magnetic force microscopy (MFM)**

In case of MFM, the AFM tip is coated with a thin (<50 nm) magnetic film (such as Ni or Co), which have negligible coercivity, so that the tip's magnetic state (or magnetization, M) does not change during the imaging. The magnetic tip is sensitive to the out-of-plane component of the stray field originating from a magnetic sample (e.g. from a domain wall) and each scan line is recorded twice. First, the topographic information of the line is recorded using the AFM Tapping Mode. This information is used during the second scan in order to keep the cantilever always at a certain probe sample distance, called Lift Height. During this scan the magnetic tip is only sensitive to the magnetic stray field from the sample. Therefore the combination of these two modes enables an accurate localization of the magnetic stray fields coming from the magnetic structure. The stray magnetic field from the sample can a affect the magnetic state of the tip, and vice versa. Typical resolution of 30 nm can be achieved, although resolutions as low as 10 to 20 nm are also attainable. Thus, interpretation of the MFM measurement is not straightforward. Figure 2.29 shows schematic diagram of the magnetic tip movement over a magnetic sample. In MFM micrographs, the bright and dark spots correspond to the local magnetic stray field of the sample either in the upward or in the downward direction with respect to sample's horizontal surface. We have used magnetic force microscopy (LT AFM/MFM System of Nano magnetics Instruments Ltd., Ankara, Turkey).
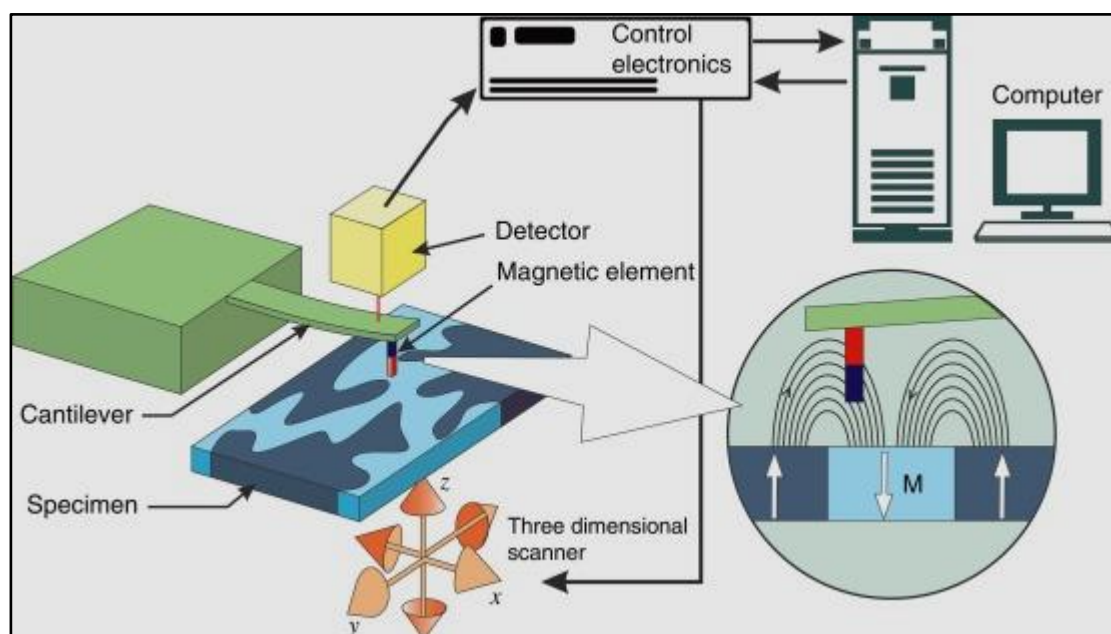
Figure 2.29 Schematic of MFM

[94]

2.5 <u>Chapter summary</u>

In this chapter, the synthesis techniques that were used in this work are briefly outlined. The material synthesis processes are also described in details. Various characterization tools that were used to study different properties of the samples like structural, electrical and magnetic properties are also discussed in details.

1) The graphene and its derivative reduced graphene Oxide were prepared using two different routes. Single Layer graphene was prepared using CVD technique and rGO is prepared from Graphite as a starting materials using Modified Hummer's method. Next, rGO/BFO nano composite in powder form was prepared using two different techniques; namely Hydrothermal and sono-chemical. rGO/BFO heterostructure was fabricated using CSD driven spin coating process. In the next step silver wrapped BFO nano chains was prepared using Hydrothermal and sol-gel process both.

2) To get the structural information all the samples were characterized thoroughly using X-ray diffraction and Reitvelt refinement was used to get the in detail crystallographic information. RAMAN, FTIR, and XPS was further used to support the structure and get further information related to optical modes, bonding and charge states.

3) Neutron diffraction was used to identify cryallographic changes under different magnetic field and Reitvelt refinement was used again here to refine the crystallographic structure.

4) The FESEM and TEM images were taken to study the morphology of the samples.

5) The main properties that we have aimed to study throughout our work are magnetic, ferroelectrical properties. The detailed characterization procedure is discussed in section 2.4.3 and 2.4.4. These measurements were done around room temperature and also in the range of 10K-300K.

2.6 <u>Bibliography</u>

[1]   White, R.J., Luque, R., Budarin, V.L., Clark, J.H. and Macquarrie, D.J., 2009. Supported metal nanoparticles on porous materials. Methods and applications. *Chemical Society Reviews*, *38*(2), pp.481-494.

[2]   Rajput, N., 2015. Methods of preparation of nanoparticles-a review. *International Journal of Advances in Engineering & Technology*, *7*(6), p.1806.

[3]   Ghorbani, H.R., Mehr, F.P., Pazoki, H. and Rahmani, B.M., 2015. Synthesis of ZnO nanoparticles by precipitation method. *Orient. J. Chem*, *31*(2), pp.1219-1221.

[4]   Yang, G. and Park, S.J., 2018. Facile hydrothermal synthesis of NiCo2O4-decorated filter carbon as electrodes for high performance asymmetric supercapacitors. *Electrochimica Acta*, *285*, pp.405-414.

[5]   Yang, G. and Park, S.J., 2018. MnO2 and biomass-derived 3D porous carbon composites electrodes for high performance supercapacitor applications. *Journal of alloys and compounds*, *741*, pp.360-367.

[6]   Kappis, K., Papadopoulos, C., Papavasiliou, J., Vakros, J., Georgiou, Y., Deligiannakis, Y. and Avgouropoulos, G., 2019. Tuning the catalytic properties of copper-promoted nanoceria via a hydrothermal method. *Catalysts*, *9*(2), p.138.

[7]   Murase, N., Jagannathan, R., Kanematsu, Y., Watanabe, M., Kurita, A., Hirata, K., Yazawa, T. and Kushida, T., 1999. Fluorescence and EPR characteristics of Mn2+-doped ZnS nanocrystals prepared by aqueous colloidal method. *The Journal of Physical Chemistry B*, *103*(5), pp.754-760.

[8]   Kim, H. and Popov, B.N., 2002. Characterization of hydrous ruthenium oxide/carbon nanocomposite supercapacitors prepared by a colloidal method. *Journal of Power Sources*, *104*(1), pp.52-61.

[9]   Budnyak, T.M., Pylypchuk, I.V., Tertykh, V.A., Yanovska, E.S. and Kolodynska, D., 2015. Synthesis and adsorption properties of chitosan-silica nanocomposite prepared by sol-gel method. *Nanoscale research letters*, *10*(1), pp.1-10.

[10] Ismail, I., Md Jani, A.M. and Osman, N., 2018. Preparation of nano structured cathode for proton-conducting fuel cell by dispersing agent-assisted sol-gel method. In *Materials Science Forum* (Vol. 917, pp. 78-82). Trans Tech Publications Ltd.

[11] Morey, G.W. and Niggli, P., 1913. The hydrothermal formation of silicates, a review. *Journal of the American Chemical Society*, *35*(9), pp.1086-1130.

[12] Yoshimura, M. and Suda, H., 2017. Hydrothermal processing of hydroxyapatite: past, present, and future. In *Hydroxyapatite and related materials* (pp. 45-72). CRC Press.

[13] Penn, R.L. and Banfield, J.F., 1999. Morphology development and crystal growth in nanocrystalline aggregates under hydrothermal conditions: Insights from titania. *Geochimica et cosmochimica acta*, *63*(10), pp.1549-1557.

[14] Polsongkram, D., Chamninok, P., Pukird, S., Chow, L., Lupan, O., Chai, G., Khallaf, H., Park, S. and Schulte, A., 2008. Effect of synthesis conditions on the growth of ZnO nanorods via hydrothermal method. *Physica B: Condensed Matter*, *403*(19-20), pp.3713-3717.

[15] Sekiguchi, T., Miyashita, S., Obara, K., Shishido, T. and Sakagami, N., 2000. Hydrothermal growth of ZnO single crystals and their optical characterization. *Journal of Crystal Growth*, *214*, pp.72-76.

[16] Dell'Agli, G., Colantuono, A. and Mascolo, G., 1999. The effect of mineralizers on the crystallization of zirconia gel under hydrothermal conditions. *Solid State Ionics*, *123*(1-4), pp.87-94.

[17] Roble, M., Rojas, S.D., Wheatley, R., Wallentowitz, S., Cabrera, A.L. and Diaz-Droguett, D.E., 2019. Hydrothermal improvement for 3R-CuFeO2 delafossite growth by control of mineralizer and reaction atmosphere. *Journal of Solid State Chemistry*, *271*, pp.314-325.

[18] Chandler, C.D., Roger, C. and Hampden-Smith, M.J., 1993. Chemical aspects of solution routes to perovskite-phase mixed-metal oxides from metal-organic precursors. *Chemical reviews*, *93*(3), pp.1205-1241.

[19] Hench, L.L. and West, J.K., 1990. The sol-gel process. *Chemical reviews*, *90*(1), pp.33-72.

[20] Thompson, C.V. and Carel, R., 1996. Grain growth and texture evolution in thin films. In *Materials Science Forum* (Vol. 204, pp. 83-98). Trans Tech Publications Ltd.

[21] Wang, J.B.N.J., Neaton, J.B., Zheng, H., Nagarajan, V., Ogale, S.B., Liu, B., Viehland, D., Vaithyanathan, V., Schlom, D.G., Waghmare, U.V. and Spaldin, N.A., 2003. Epitaxial BFO multiferroic thin film heterostructures. *science*, *299*(5613), pp.1719-1722.

[22] Nechache, R., Harnagea, C., Li, S., Cardenas, L., Huang, W., Chakrabartty, J. and Rosei, F., 2015. Bandgap tuning of multiferroic oxide solar cells. *Nature Photonics*, *9*(1), pp.61-67.

[23] Qin, M., Yao, K. and Liang, Y.C., 2009. Photovoltaic characteristics in polycrystalline and epitaxial (Pb 0.97 La 0.03)(Zr 0.52 Ti 0.48) O 3 ferroelectric thin films sandwiched between different top and bottom electrodes. *Journal of applied physics*, *105*(6), p.061624.

[24] Schwartz, R.W., 1997. Chemical solution deposition of perovskite thin films. *Chemistry of materials*, *9*(11), pp.2325-2340.

[25] Choy, K.L., 2003. Chemical vapour deposition of coatings. *Progress in materials science*, *48*(2), pp.57-170.

[26] Yang, S.Y., Zavaliche, F., Mohaddes-Ardabili, L., Vaithyanathan, V., Schlom, D.G., Lee, Y.J., Chu, Y.H., Cruz, M.P., Zhan, Q., Zhao, T. and Ramesh, A.R., 2005. Metalorganic chemical vapor deposition of lead-free ferroelectric BiFeO 3 films for memory applications. *Applied physics letters*, *87*(10), p.102903.

[27] Ueno, R., Okaura, S., Funakubo, H. and Saito, K., 2005. Crystal structure and electrical properties of epitaxial BFO thin films grown by metal organic chemical vapor deposition. *Japanese journal of applied physics*, *44*(9L), p.L1231.

[28] Stinton, D.P., Besmann, T.M. and Lowden, R.A., 1988. Advanced ceramics by chemical vapor deposition techniques. *American ceramic society bulletin*, *67*(2), pp.350-355.

[29] Yang, S.Y., Liu, B.T., Ouyang, J., Nagarajan, V., Kulkarni, V.N., Ramesh, R., Kidder, J., Droopad, R. and Eisenbeiser, K., 2005. Epitaxial Pb (Zr, Ti) O 3 Capacitors on Si by Liquid Delivery Metalorganic Chemical Vapor Deposition. *Journal of electroceramics*, *14*, pp.37-44.

[30] Castro, Y. and Durán, A., 2019. Control of degradation rate of Mg alloys using silica sol–gel coatings for biodegradable implant materials. *Journal of Sol-Gel Science and Technology*, *90*, pp.198-208.

[31] Schmidt, H., 2006. Considerations about the sol-gel process: From the classical sol-gel route to advanced chemical nanotechnologies. *Journal of sol-gel science and technology*, *40*, pp.115-130.

[32] Wang, X., 2020. Preparation, synthesis, and application of Sol-gel method University Tutor: Pr. *Olivia GIANI Internship Tutor: Mme. WANG Zhen*.

[33] Brinker, C.J. and Scherer, G.W., 1985. Sol→ gel→ glass: I. Gelation and gel structure. *Journal of Non-Crystalline Solids*, *70*(3), pp.301-322.

[34] Kallala, M., Sanchez, C. and Cabane, B., 1992. SAXS study of gelation and precipitation in titanium-based systems. *Journal of non-crystalline solids*, *147*, pp.189-193.

[35] Schwartz, R.W., Reichert, T.L., Clem, P.G., Dimos, D. and Liu, D., 1997. A comparison of diol and methanol-based chemical solution deposition routes for PZT thin film fabrication. *Integrated Ferroelectrics*, *18*(1-4), pp.275-286.

[36] Ramamurthi, S.D. and Payne, D.A., 1990. Structural investigations of prehydrolyzed precursors used in the sol-gel processing of lead titanate. *Journal of the American Ceramic Society*, *73*(8), pp.2547-2551.

[37] Paranthaman, M., Shoup, S.S., Beach, D.B., Williams, R.K. and Specht, E.D., 1997. Epitaxial growth of BaZrO3 films on single crystal oxide substrates using sol-gel alkoxide precursors. *Materials research bulletin*, *32*(12), pp.1697-1704.

[38] Yi, S.W., Kim, S.S., Kim, J.W., Jo, H.K. and Kim, W.J., 2009. Multiferroic properties of BFO/Bi4Ti3O12 double-layered thin films fabricated by chemical solution deposition. *Thin Solid Films*, *517*(24), pp.6737-6741.

[39] Biswas, M. and Su, P.C., 2017. Chemical solution deposition technique of thin-film ceramic electrolytes for solid oxide fuel cells. *Modern technologies for creating the thin-film systems and coatings*.

[40] Scriven, L.E., 1988. Physics and applications of dip coating and spin coating. *MRS Online Proceedings Library (OPL)*, *121*, p.717.

[41] Emslie, A.G., Bonner, F.T. and Peck, L.G., 1958. Flow of a viscous liquid on a rotating disk. *Journal of Applied Physics*, *29*(5), pp.858-862.

[42] Lawrence, C.J. and Zhou, W., 1991. Spin coating of non-Newtonian fluids. *Journal of non-newtonian fluid mechanics*, *39*(2), pp.137-187.

[43] Bornside, D.E., Macosko, C.W. and Scriven, L.E., 1987. MODELING OF SPIN COATING. *Journal of imaging technology*, *13*(4), pp.122-130.

[44] Yonkoski, R.K. and Soane, D.S., 1992. Model for spin coating in microelectronic applications. *Journal of applied physics*, *72*(2), pp.725-740.

[45] Omar, O., Ray, A.K., Hassan, A.K. and Davis, F., 1997. Resorcinol calixarenes (resorcarenes): Langmuir-Blodgett films and optical properties. *Supramolecular Science*, *4*(3-4), pp.417-421.

[46] Demircan, G., Gurses, E.F., Acikgoz, A., Yalcin, S. and Aktas, B., 2020. Effects of spin coating parameters on stress, electrical and optical properties of multilayer ZnO thin film prepared by sol–gel. *Molecular Crystals and Liquid Crystals*, *709*(1), pp.61-69.

[47] Mao, D., Lv, G., Gao, G. and Fan, B., 2019. Fabrication of polyimide films with imaging quality using a spin-coating method for potential optical applications. *Journal of Polymer Engineering*, *39*(10), pp.917-925.

[48] Sbeta, M., Atilgan, A.B.D.U.L.L.A.H., Atli, A.Y.C.A.N. and Yildiz, A., 2018. Influence of the spin acceleration time on the properties of ZnO: Ga thin films deposited by sol–gel method. *Journal of Sol-Gel Science and Technology*, *86*, pp.513-520.

[49] Shivaraj, B.W., Murthy, H.N., Krishna, M. and Sharma, S.C., 2013. Investigation of influence of spin coating parameters on the morphology of ZnO thin films by taguchi method. *Int. J. Thin Film. Sci. Technol*, *2*(2), pp.143-154.

[50] Salje, E., 1990. Phase transitions in ferroelastic and co-elastic crystals. *Ferroelectrics*, *104*(1), pp.111-120.

[51] Kubel, F. and Schmid, H., 1990. Structure of a ferroelectric and ferroelastic monodomain crystal of the perovskite BFO. *Acta Crystallographica Section B: Structural Science*, *46*(6), pp.698-702.

[52] Bhowmik, K., Pramanik, S., Medda, S.K. and De, G., 2012. Covalently functionalized reduced graphene oxide by organically modified silica: a facile synthesis of electrically conducting black coatings on glass. *Journal of Materials Chemistry*, *22*(47), pp.24690-24697.

[53] Hummers Jr, W.S. and Offeman, R.E., 1958. Preparation of graphitic oxide. *Journal of the American chemical society*, *80*(6), pp.1339-1339.

[54] Li, X., Cai, W., An, J., Kim, S., Nah, J., Yang, D., Piner, R., Velamakanni, A., Jung, I., Tutuc, E. and Banerjee, S.K., 2009. Large-area synthesis of high-quality and uniform graphene films on copper foils. *science*, *324*(5932), pp.1312-1314.

[55] Levendorf, M.P., Ruiz-Vargas, C.S., Garg, S. and Park, J., 2009. Transfer-free batch fabrication of single layer graphene transistors. *Nano letters*, *9*(12), pp.4479-4483.

[56] Evans, C., Brundle, R. and Wilson, S., 1992. *Encyclopedia of materials characterization*.

[57] Evans, J.T., 2011. Characterizing ferroelectric materials. *Proc. IEEE ISAF*, pp.1-123.

[58] Chowdhury, U., Goswami, S., Bhattacharya, D., Midya, A. and Mandal, P., 2016. Determination of intrinsic ferroelectric polarization in lossy improper ferroelectric systems. *Applied Physics Letters*, *109*(9), p.092902.

[59] Joseph, A.J. and Kumar, B., 2018. Study of true-remanent polarization using remanent hysteresis task and resistive leakage analysis in ferroelectric 0.64 Pb (Mg1/3Nb2/3) O3-0.36 PbTiO3 ceramics. *Solid State Communications*, *271*, pp.11-15.

3   Chapter

Influence of covalent and van der Waals bonds on crystallographic and physical properties of rGO/BiFeO$_3$ nano composites

3.1 <u>Introduction</u>

In this chapter we will discuss the influence of interfacial Van der Waals bonds and covalent bonds on the crystallographic and physical properties of reduced-graphene-oxide/ BiFeO$_3$ (rGO/BFO) nano composites.

Research on the Van der Waals (vdW) materials [1] [2] [3] - such as multilayered heterostructures - has opened a new era of two-dimensional (2D) multiferroics. The study has extensively been carried out on bilayer perovskites known as Ruddleson-Popper oxide[4] [5] and double perovskites[6]. Graphene, an important vdW material, on the other hand, possesses neither magnetism nor ferroelectricity. However, 3d transition metal ions, adsorbed upon graphene, induce strong hybridization between π and the 3d orbitals and also spin-orbit coupling[7]. In hetero-structures of graphene and YIG[8] [9] [10] [11], or EuS[12] or BiFeO$_3$ (BFO)[13] [14] too, similar observations were made. The vdW bonds at the interfaces of the BFO/graphene hetero-structures play an important role in modulating the contact barriers and depletion width[15] and are quite sensitive to electric field or charge accumulation/depletion on the substrate. These features are also dependent on the surface terminated ions and their electro-negativity. The accumulation of surface charges from 2D materials enhances the possibilities of ferroelectric polarization[15] due to unshared electrons in weak vdW bonds.

The question of the utility of covalent or vdW bonds in influencing the multiferroicity of BFO in graphene/BFO hetero-structure or reduced-graphene-oxide (rGO)/BFO nano composite is, however, still remaining unanswered. The magnetic properties of the rGO/BFO have earlier been studied by others[16] [17] [18]. Of course, the role of covalent bonding at the interface and its influence on multiferroic properties has not been directly addressed so far.

In this work the crystallographic, magnetic, and ferroelectric properties have been measured. It was found that the presence of Van der Waals bonds have rather moderate influence on the structural properties such as distortion, bond lengths and angles, and structural non centrosymmetry compared to covalent bonded composite. The magnetization, coercivity, as well as the remanent polarization (obtained from direct electrical measurements) exhibit significant changes depending on the presence or absence of the Fe-C covalent bonds. However, in sharp contrast to the observation made in the case of the nano composites containing covalent bonds, presence of Van der Waals bonds results in dramatic decrease in the remanent ferroelectric polarization determined from direct electrical measurements. Enhanced functionalities, therefore, could be possible only for covalent bonded oxide-graphene interfaces.

The reduced graphene oxide (rGO) and $BiFeO_3$ (BFO) nano composites were prepared by hydrothermal and sono-chemical mixing of as-prepared BFO and reduced graphene oxide (rGO). We compare the results obtained from hydrothermally and sono-chemically synthesized nano composites - Com-H and Com-P, respectively. They are described in the sections 2.3.1.3 and 2.3.1.4 respectively. We used different wt% of rGO for sono-chemically prepared samples – 1.5 and 15.0 wt% (samples are designated as Com-P-1.5 and Com-P-15) whereas the hydrothermally prepared sample contain 1.5wt% of rGO only (designated as Com-H)

3.2 <u>Result and discussion</u>

All the samples were characterized by powder X-ray diffraction (XRD), Raman spectrometry, scanning electron and tunneling electron microscopy (TEM), and X-ray photoelectron spectroscopy (XPS). The magnetic hysteresis loops were measured by Lake Shore Vibrating Sample Magnetometer (VSM) under ±12 kOe field at room temperature. The thermo-gravimetric analysis (TGA) was done under inert atmosphere (see the supplementary material). The remanent ferroelectric polarization was measured by using the Precision LC-II (Radiant Inc.) ferroelectric loop tracer at room temperature. For ferroelectric polarization measurements, the powder samples were spin coated upon quartz substrate to form uniform films. The thickness of the film was ~10 nm as measured by ellipsometry. Silver dots were used as electrodes.

3.2.1 <u>X-ray diffraction patterns analysis</u>

Figure 3.1 shows the XRD data of Com-H and BFO-H and Figure 3.2 shows the XRD data for the Com-P-1.5 and Com-P-15 and BFO-P. All the data were refined by FullProf. All the samples turn out to be assuming rhombohedral $R3c$ space group symmetry. The details of the crystallographic structure including the fit statistics have been given in Table 3.1. We used the space group, lattice parameters, and ion positions to calculate the bond lengths from VESTA. They are summarized in Table 3.2.

As shown earlier[19], *R3c* space group emerges from the combined influence of polar distortion of the Bi-O bonds along the axis of polarization [111] and anti ferro-distortive rotation of FeO_6 octahedra around [111]. The anti ferro-distortive rotation was shown[19] to be associated with finite magnetic moment. The structural non-centrosymmetry – which is proportional to the ferroelectric polarization – could be determined from the off-centering of Bi and Fe ions with respect to the center of masses of the respective oxygen cages. In the hexagonal setting, where $[111]_R \parallel [001]_H$, the net off-centering of the unit cell is given by |s-t|. where 's' and 't' are the off-centric displacements of 'Bi' and 'Fe' ions along the c-axis $\parallel$ $[001]_H$. Following the Figure 3.1 the results of the calculation of |s-t| are given in the Table 3.4. All the composite samples – with or without covalent bonds – exhibit nearly comparable off-centered displacements. However, the composite Com-P (~1.5 wt% RGO) exhibits slightly smaller extent of non centro-symmetry.

In the hexagonal setting, there are four $Fe - O$ equilateral bonds within (111) plane and two apical bonds normal to the plane of the FeO_6 octahedra (Figure 3.4) Similarly, in BiO_6 octahedra, there are three equilateral $Bi - O$ bond along $a - b$ or {110} plane and three apical bonds normal to the plane or along c-axis. The extent of asymmetry in the equilateral bond lengths both in the FeO_6 and BiO_6 octahedra appears to be smaller in Com-P samples than in the Com-H samples. For instance, the bonds marked as- δFe_A , δFe_B , δBi_A , δBi_B exhibit stretching and contraction. The changes noticed in bonds for both the octahedra are summarized in Table 3.2. The stretching and contraction of the bonds in FeO_6 octahedra is more symmetric both in the Com-P-1.5 and Com-P-15samples. In the case of the BiO_6 octahedra, both the δBi_A and δBi_B bonds exhibit stretching in Com-H and Com-P-1.5 samples. However, in the Com-P-15 sample, while δBi_A increases, δBi_B decreases. Of course, the extent of stretching and contraction is comparable which makes the octahedra still quite symmetric. Structural details of Com-H and Com-P samples containing identical wt% of rGO shows more distortion or asymmetry in the BiO_6 and FeO_6 for Com-H smaple.

Greater distortion occurs in the FeO_6 octahedra of Com-H due to the presence of additional covalent Fe-C bonds. This is reflected in the asymmetric stretching and contraction of the Fe-O bonds. Both the BiO_6 and FeO_6 octahedra are shown in Figure 3.4. Now, when the FeO_6 octahedra distorts, it also distorts the BiO_6 octahedra and accordingly the $Bi - O$ bond lengths change. When 1.5 wt% rGO was introduced in both the non-bonded as well as bonded composites, we find that in both the cases, the Bi-O bond length stretches, but in the bonded one, the stretching is asymmetrical; whereas in the non-bonded one it is symmetrical. In addition, in the case of non-bonded Com-P-15 (with 15 wt% rGO) sample, the BiO_6 octahedra was found to be centro-symmetric. Therefore, it is clear that in the non-bonded cases both the

[103]

$Bi - O$ and $Fe - O$ bond lengths change by the same extent. The short summary in this context are included in Table 3.3.

It is important to point out here that the nanocomposites and nanoscale samples often exhibit a different structural symmetry from what is observed in the bulk form. Lattice strain (including micro-strain in nanoparticles) and chemical pressure generated due to the size induce the structural phase transition in nanoscale[20]. In the case of epitaxial thin films, epitaxial (due to lattice mismatch between the substrate and the film) and chemical strains (due to nonstoichiometry) induce structural transition. For example, rhombohedral ($R3c$) BFO assume monoclinic, orthorhombic or tetragonal structures in thin film form[21]. Of course, such transitions take place beyond a critical strain or pressure. In the present case, such change in structure could not be observed as the size of the BFO nanoparticles is reasonably big (~20-40 nm) and the composite formation did not give rise to sufficiently strong lattice strain generation within the bulk for inducing the structural transition.
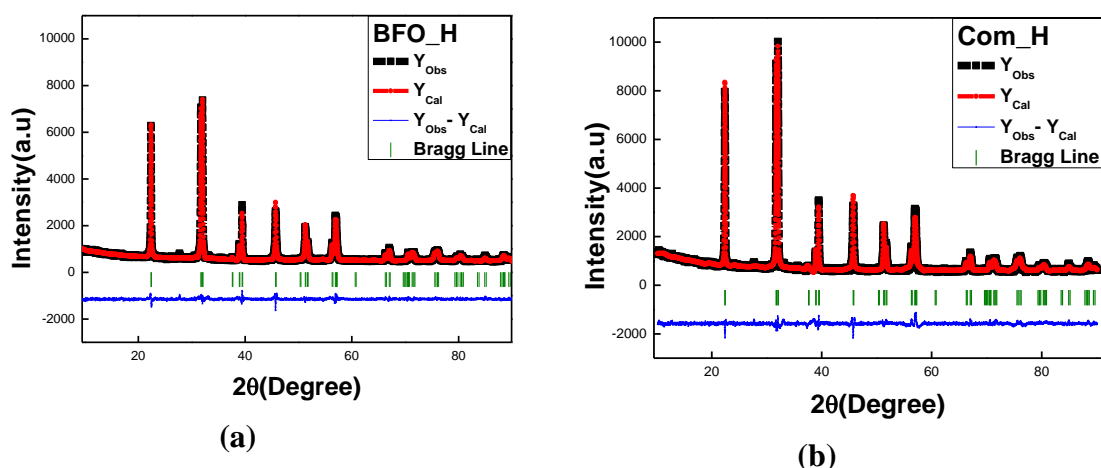
Figure 3.1 Refined room temperature X-ray data of BFO-H (a) and Hydrothermally prepared Composite Com-H (b)

[104]
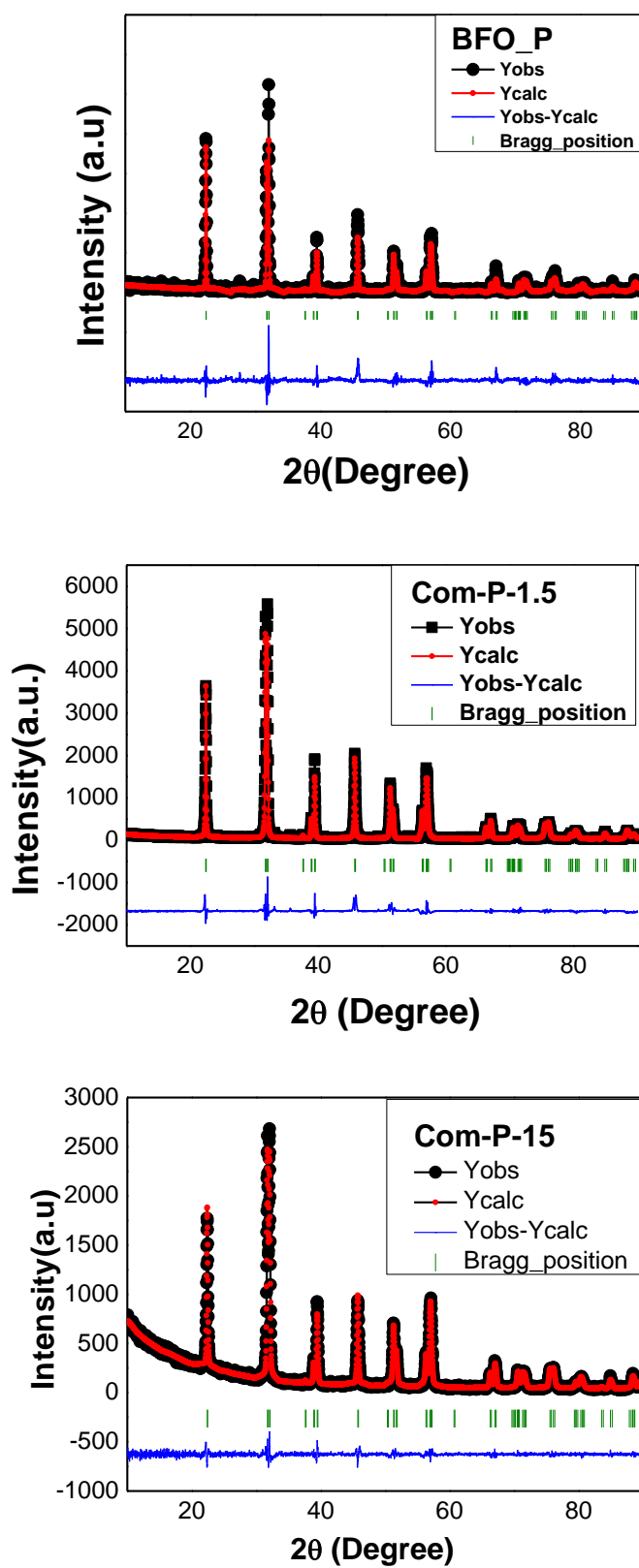
Figure 3.2 Refined room temperature X-ray data of BFO-P and Sono-chemically prepared composites Com-P-1.5 and Com-P-15

[105]
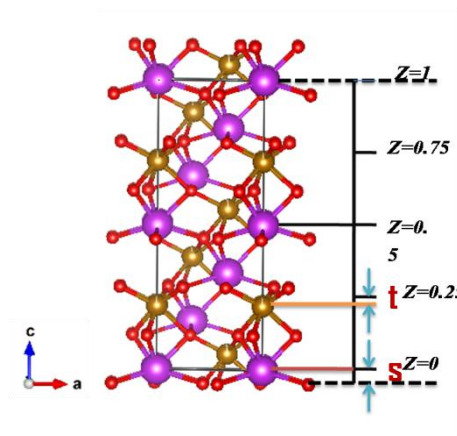
Figure 3.3 Net off-centering of Bi as 's' and Fe as 't' from position of oxygen along axis [001]$_{hex}$
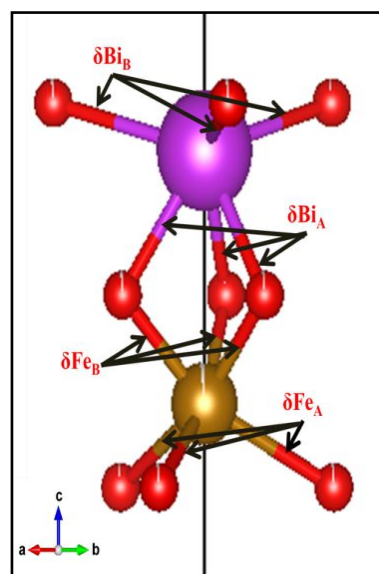
Figure 3.4 Model Picture indicating Bi-O and Fe-O bonds

Ion Pos	x	y	z	Occ	Lattice Parameters			
Table 3.1 Quality of refinement fittings, Ion positions and Lattice Parameters of XRD data								
BFO-H Rp= 25.7, **Rwp**= 17.3, $\chi^2 =$ 2.76								
Bi	0	0	0.33908	0.33793	a	5.5825	α	90
Fe	0	0	0.33901	0.32824	b	5.5825	β	90
O	0.42777	-0.0349	1.15112	1.03101	c	13.8756	γ	120
Com-H Rp= 21.2, **Rwp**= **14.7**, $\chi^2=$ 1.53								
Bi	0	0	0.0001	0.33571	a	5.5804	α	90

Fe	0	0	0.2843	0.33921	**b**	5.5804	β	90
O	0.45233	-0.0153	0.03947	1.07166	**c**	13.8754	γ	120

BFO-P
Rp= 12.5, **Rwp**= 17.6, $\chi^2_=$4.7

Bi	0.00000 0	0	0.00071	0.3294	**a**	5.579809	α	90
Fe	0	0	0.27948	0.33183	**b**	5.579809	β	90
O	0.42062	-0.03361	0.04825	1.01204	**c**	13.87196	γ	120

Com-P-1.5
Rp= 11.3, **Rwp**= 16.1, χ^2= 3.68

Bi	0	0	0.00218	0.34125	**a**	5.580669	α	90
Fe	0	0	0.28299	0.35394	**b**	5.580669	β	90
O	0.44728	0.00435	0.04471	1.15662	**c**	13.87269	γ	120

Com-P-15
Rp= 6.11, **Rwp**= 8.51, χ^2= 1.37

Bi	0	0	0.01842	0.33929	**a**	5.5807	α	90
Fe	0	0	0.29878	0.3333	**b**	5.5807	β	90
O	0.4171	-0.00328	0.06358	1	**c**	13.8733	γ	120

Table 3.2 Shift in Bond lengths calculated for Com-H, Com-P-1.5% and Com-P-15					
Changes in Bond length in composites			**Com-H**	**Com-P-1.5**	**Com- P-15**
Fe-O	**E**	$\Delta(\delta Fe_B)$	0.0023	-0.02235	0.30656
		$\Delta(\delta Fe_A)$	-0.04613	0.01076	-0.3028
	A	$\Delta(\delta Fe_B)$	0.0023	-0.02235	0.30656
		$\Delta(\delta Fe_A)$	-0.04613	0.01076	-0.3028
Bi-O	**E**	$\Delta(\delta Bi_B)$	0.06524	0.02658	-0.1238
	A	$\Delta(\delta Bi_A)$	0.08449	0.03362	0.19694

[107]

Table 3.3 Summary of bond lengths obtained from the XRD data

	Com-H	Com-P-1.5	Com-P-15
Fe-O bond	$\Delta(\delta Fe_B) \ll \Delta(\delta Fe_A)$ ↑ ↓ More non centro-symetric FeO_6	$\Delta(\delta Fe_B) \approx \Delta(\delta Fe_A)$ ↑ ↓ More centro-symetric FeO_6	$\Delta(\delta Fe_B) = \Delta(\delta Fe_A)$ ↑ ↓ More centro-symetric FeO_6
Bi-O bond	$\Delta(\delta Bi_B) < \Delta(\delta Bi_A)$ ↑ ↑ More non centro-symetric BiO_6	$\Delta(\delta Bi_B) \approx \Delta(\delta Bi_A)$ ↑ ↑ Slight non centro-symetric BiO_6	$\Delta(\delta Bi_B) = \Delta(\delta Bi_A)$ ↓ ↑ More non centro-symetric FeO_6
↑ *means increased and* ↓ *means decreased*			

Table 3.4 Summary of all ion positions along [001]c direction and calculation of crystallographic ferro-electric (FE) polarization

sample	Pos of Ion along $[001]_c$ axis				Shift of ion position of		Crystallographic calculation of FE polarization	
	O[f] (i)	Bi (j)	Fe (k)	O[l] (l)	Bi [s= j-i]	Fe [t= (k-i)-0.25]	|s-t|	|sc-tc|
BFO-H	-0.12437	-0.00024	0.28068	0.87563	0.12413	0.15505	0.03092	0.4290
Com-H	-0.1272	0.0001	0.2843	0.8728	0.1273	0.1615	0.0342	0.4745
BFO-P	-0.12166	0.0036	0.28299	0.87804	0.12526	0.15465	0.02939	0.40772
Com-P-1.5	-0.11826	0	0.27948	0.88174	0.11826	0.14774	0.02948	0.40895
Com-P-15	-0.10309	0.01842	0.29878	0.89691	0.12151	0.15187	0.03036	0.42126

3.2.2 <u>Raman spectra analysis</u>

The Raman spectra for all the samples are shown in Figure 3.5, Figure 3.6, Figure 3.7 for hydrothermally and sono chemically prepared composites along with their corresponding BFO samples. The experiments were carried out with both 514 nm and 785 nm He-Ne laser excitations. The characteristic D and G peaks are correspond to, respectively, the dangling bonds from defects containing sp^2 hybridized orbital and planar vibration of C ions bonded via sp^2 hybridized orbital. With respect to the observations made in GO, the D and G peaks appear to have shifted to the higher and lower wave numbers in Com-P (all wt% s). Of course, the corresponding shifts in Com-H were even higher. It is found that the intensity ratio of them $\left[{I_D}/{I_G} \right]$ yields the defect concentration. It turns out that for both the Com-H and Com-P (all wt% s) samples; the defect concentration is quite comparable. Therefore, the extent of decrease in the concentration of dangling bonds with respect to that in GO appears to be nearly same in both the composites. However, the full width at half maximum (FWHM) of D band and the relative shift to the higher mode are larger in Com-H. This could be because of the presence of Fe-C covalent bonds in sp^3 defect sites. The phonon modes are inversely proportional to average mass. Therefore, the covalent bonding of some lighter ions (other than oxygen) reduces the overall average mass which is responsible for the observed D band shifts to higher wave number in Com-H. Absence of such covalent bonds decreases the D band shift in Com-P-1.5 and Com-P-15. Following the relations shown by Cancado *et al.*[22] [23] we calculate inter-defect length and defect concentration and summarize in Table 3.5,

$$L_D^2 = \frac{(1.8 \pm 0.5) \times 10^{-9} \times \lambda_L^4}{\frac{I_D}{I_G}}$$

$$n_D = \frac{10^{14}}{\pi L_D^2}$$

Where, L_D is the effective distance between the defects (in nm)

n_D is the defect concentration (in cm^{-2})

λ is the wavelength of the excitation.

We find that the defect concentration n_D and the spacing between the defects L_D in both composites are 1.98×10^{27} cm^{-2} and 12.67 nm, respectively. The corresponding figures for the Graphite oxide (GO) are 2.77×10^{27} cm^{-2} and 10.70 nm, respectively. The decrease in defect concentration and increase in defect spacing in composites with respect to GO indicates lesser extent of functionalization of the graphene layer in composites. The sp^3 defects are oriented in the same spacings and with same concentration in both composites and are less than in GO.

[109]

The characteristic modes of BFO exhibit substantial red and blue shifts in the Com-H. According to group theory, there are 13 Raman active modes of BFO with the rhombohedral $R3c$ structure which are defined by the following irreducible representations[24][25],

$$\Gamma_{RAMAN,R3c} = 4A_1 \oplus 9E$$

where, $4\ A_1$ modes are polarized along z axis and the rest $9\ E$ doubly degenerate modes are polarized along x-y plane. In BFO-P, BFO-H, Com-P-1.5, Com-P-15 and Com-H, nine active modes could be observed out of the 13 modes. The line shape of the peaks was fitted by Voigt function. Their assignment[24] together with the modes calculated from first-principles[24] are shown in figures and the RAMAN shifts are listed in Table 3.6.

The lower order A_1 and E modes are related to the Bi-O and Fe-O vibration while the higher order peaks arise due to the change in the oxygen motion states. Comparing shifts in composites and in pure BFO, we observe that- the lower order modes (till 167 cm^{-1}), influenced by Bi atoms, do not exhibit any substantial shift while the modes influenced by Fe ions and oxygen motion states are either red or blue shifted. For example, the $A_1(LO) - 2$, $A_1(TO) - 4$ and $E(TO) - 6$ modes at 265 cm^{-1}, 293 cm^{-1}, and 431 cm^{-1} are red shifted by 5-13 cm^{-1} while the $E(TO) - 4$ mode at 371.1 cm^{-1} are blue shifted by 1.4 and $E(LO) - 2$ one at 337.5 cm^{-1} is blue shifted by 13 cm^{-1} in Com-H.

This could be due to the change in the Fe-O bond lengths and the motion states of oxygen. The formation of Fe-C bonds at the BFO/RGO interface (discussed later) could have some influence on the bulk lattice and its distortion. The distortion in the Fe-O bonds has contributions from both polar distortion and anti ferro-distortive tilt. The calculation of the Fe-O bond length shows that indeed the difference in the bond lengths has decreased in Com-H. Similar observation has earlier been made by others in different perovskite oxide systems[26].

In Com-P, for both wt% s, smaller shift is observed in, $A_1(LO) - 2$, $A_1(TO) - 4$, and $E(TO) - 4$ (or $E(LO) - 2$ in Com-P-15) and $A_1(LO) - 5$. The change in $A_1(TO) - 4$ and $A_1(LO) - 5$ are comparable but among them $A_1(TO) - 4$ is red-shifted while mode at $A_1(LO) - 5$ is blue-shifted. This could be related to the change in the Fe-O bond length and oxygen stoichiometry as the graphene layer affects the electronic structure of BFO. Stretching (contraction) of bonds lead to the red (blue) shifts of the Raman modes. Few Raman modes remain nearly invariant in the Com-P (all wt% s) samples. This could be because of compensating changes in the bond lengths of the octahedra.
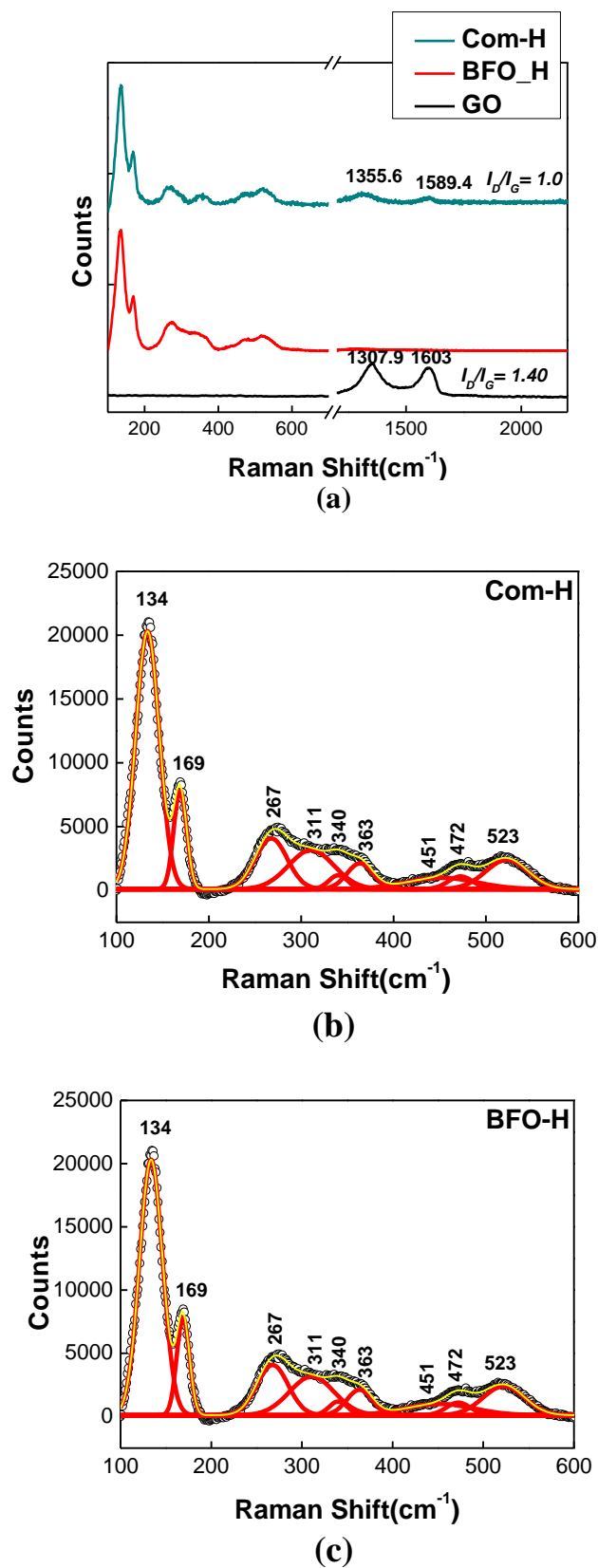
Figure 3.5 RAMAN Spectra of Com-H, BFO-H and GO systems (a); and low-energy portion of the spectra has been blown up for (b) Com-H and (c) BFO-H, respectively.
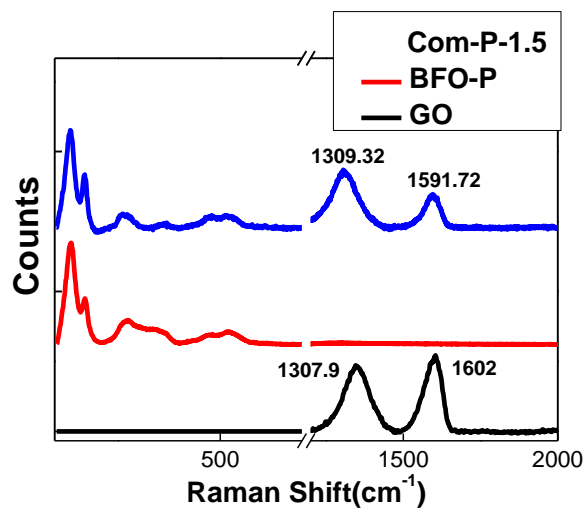
(a)
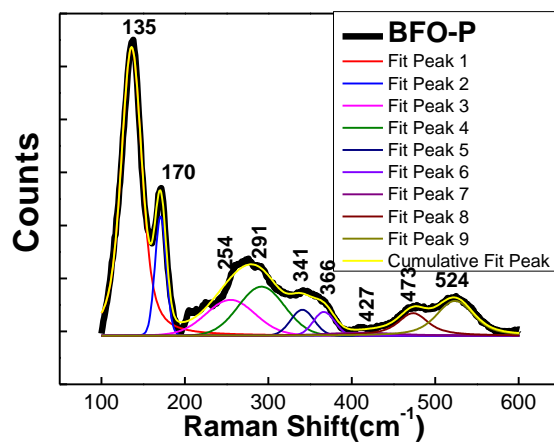
(b)
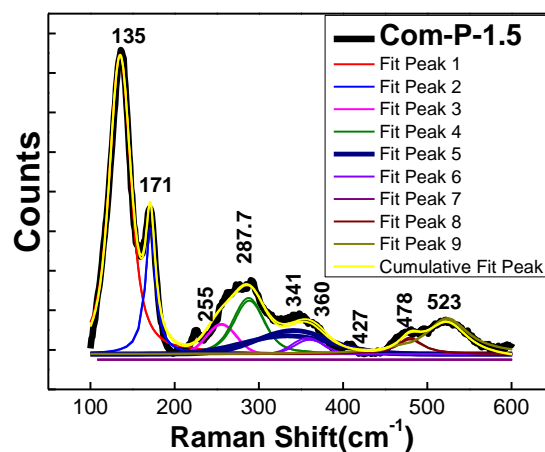
(c)

Figure 3.6 RAMAN Spectra of Com-P-1.5, BFO-P and GO (a) systems; and low-energy portion of the spectra has been blown up for Com-P-1.5 (b) and BFO-P(c)
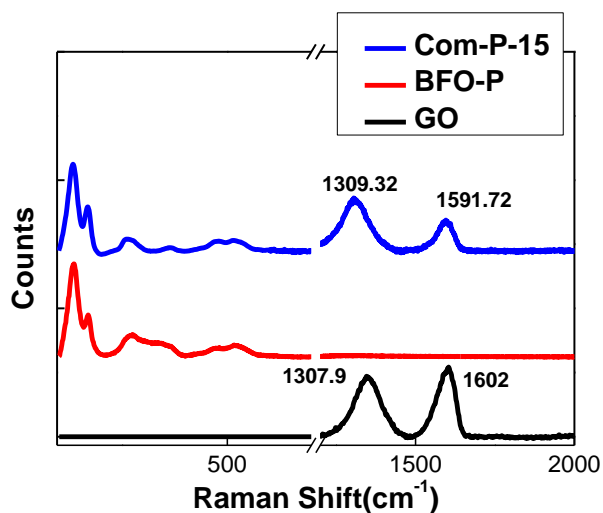
(a)
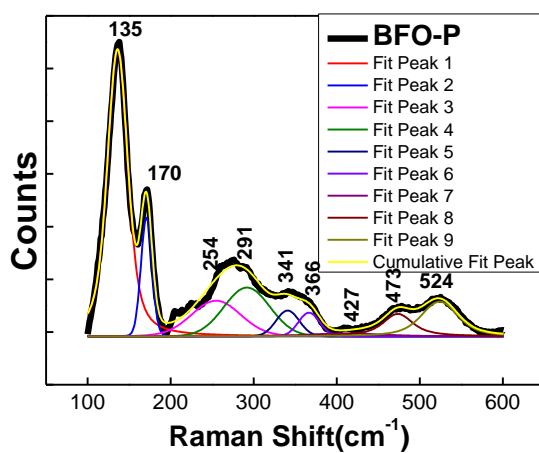
(b)
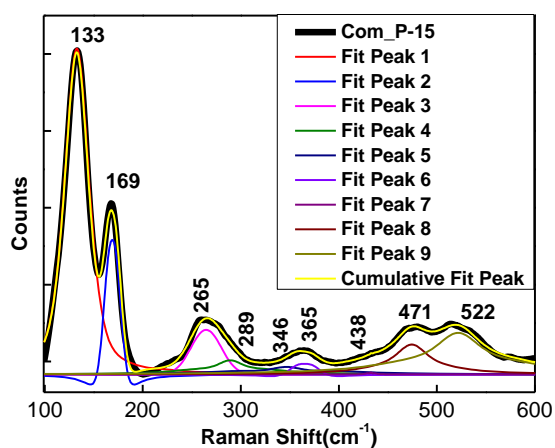
(c)

Figure 3.7 RAMAN Spectra of Com-P-15, BFO-P and GO (a) systems; and low-energy portion of the spectra has been blown up for Com-P-15 (b) and BFO-P(c)

[113]

Table 3.5 Calculation of defect concentration and defect length					
	G	**D**	I_D/I_G	L_D^2 **(nm²)**	L_D**(nm)**	n_D **(cm⁻²)**
GO	1603	1307	1.40	114.67	10.70	2.77×10^{27}
Com_P	1591	1309	1.01	160.53	12.67	1.98×10^{27}
Com_H	1589	1355	1.00	160.53	12.67	1.98×10^{27}

Table 3.6 The RAMAN modes and their shift in Com-H, Com-P-1.5 and Com-P-15							
	Calculated	**Com-H**	**RAMAN SHIFT**	**Com-P-1.5**	**RAMAN Shift**	**Com-P-15**	**RAMAN Shift**
$E(TO)$**-1**	**152**	134.2	**0.7**	135.1	**-0.8**	132.8	**-1.0**
$A_1(TO)$**-1**	**167**	168.7	**-0.6**	171.2	**0.6**	169.0	**-0.3**
$A_1(LO)$**-2**	**277**	265.4	**-4.9**	255.6	**0.8**	264.7	**-1.3**
$A_1(TO)$**-3**	**266**	-	**-**	-	-	-	-
$A_1(TO)$**-4**	**318**	293.1	**-13.1**	287.7	**-4.2**	289.2	**-4.4**
$E(LO)$**-2**	**332**	350.7	**13.2**	341.0	**-0.2**	346.6	**1.8**
$E(TO)$**-3**	**335**	-	**-**	-	-	-	-
$E(TO)$**-4**	**378**	371.1	**1.4**	365.6	**-1.1**	365.0	**-0.5**
$E(LO)$**-5**	**386**	-	**-**	-	-	-	-
$E(TO)$**-6**	**409**	431.2	**-12.2**	426.8	-0.2	438.0	**-0.7**
$E(LO)$**-7**	**436**	-	**-**	-	-	-	-
$A_1(LO)$**-5**	**509**	470.1	**-1.1**	478.9	5.5	474.3	**3.2**
$A_1(TO)$**-6**	**517**	522.4	**0.3**	523.6	-0.6	521.7	**-0.6**

3.2.3 **Fourier transmission infrared (FTIR) spectra analysis**

We have examined FTIR for Com-H and Com-P-1.5. The FTIR spectrum for Com-P-1.5 is shown in Figure 3.8. In Com-H, BFO signature peaks along with peaks of Graphene Oxide are present. But, in Com-P-1.5 the BFO signature peaks are absent. This implies proper composite structure is not present in Com-P-1.5. Moreover, C=C graphitic domain is highly distorted at GO. The corresponding peak of GO at 1537cm⁻¹ is shifted to higher wave number at 1634 cm⁻¹ for Com-H and 1631 cm⁻¹ at Com-P-1.5. This means graphitic domain is retained and the reduction is same in both cases as found in RAMAN also. The other peaks that are present in GO are corresponding to $C-O$ stretching modes (1094 cm⁻¹), C-OH phenolic

[114]

stretching (1224 cm^{-1}), $C = O$ stretching modes of carboxylic group (1736 cm^{-1}), Alkyne group modes (2368 cm^{-1}) and modes due to hydroxyl ($-OH$) group (3444 cm^{-1}).

Now all these peaks are highly diminished in Com-H except modes correspond to hydroxyl group at 3446 cm^{-1}. This means all the functionalities are removed to a great extent. Whereas in Com-P-1.5 there are trace of some functionalities because some modes still appear in the range (1050-1500 cm^{-1}). But they are shifted to lower wave number. There are also small traces of $-CH_2$ vibrational modes at 2600-2900 cm^{-1} range, but they are so small that they can be ignored. Now if we look at the modes related to BFO at Com-H we have found that peak at 449 cm^{-1} is due to $Fe - O$ stretching vibrational modes of FeO_6 octahedra and peak at 544 cm^{-1} correspond to $O - Fe - O$ bending vibration of FeO_4 octahedra. Peak at 862.03 cm^{-1} and 1070 cm^{-1} can be addressed from literature as $Bi - O$ vibrational modes. Peak at 544 cm^{-1} and 862 cm^{-1} are shifted to higher wave number compared to literature. Now, there is an ambiguity regarding peak at 1070 because it can be due to $Bi - O$ vibrational modes or due to shift in $C - O$ stretching modes. But here we have taken it as $Bi - O$ signature peaks. The high shifts in BFO signature peaks are indicative towards new structural deformation in the BFO structure.
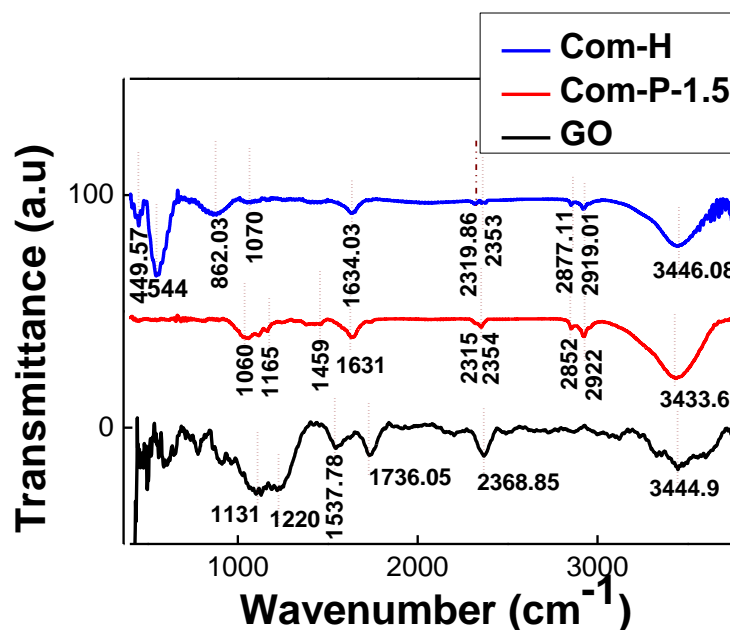
Figure 3.8 FTIR of GO Com-P-1.5 and Com-H

3.2.4 Thermo gravimetric analysis (TGA)

The TGA result in Figure 3.9 shows that in Argon atmosphere mass loss takes place in GO because of heating the disruption of dangling bonds (through which functionalities were attached) upon heating[27]. Now, Com-P shows a noticeable mass loss near 500-600° but Com-H does not show any mass loss. This is because there is no composite structure exists in Com-P-

1.5 so existences of some dangling bonds are still there. Figure 3.9 (RHS) shows the TGA of Com-H in air which shows a mass loss of ~2% totally due to the complete oxidation of aromatic C network in air. TGA thermogram shows that 98.49% BFO and 1.5wt% GO exist in sample which justifies the wt% taken in synthesis. This justifies that Com-H is stable structure but Com-P-1.5 is not, as bonded composite is not formed here.
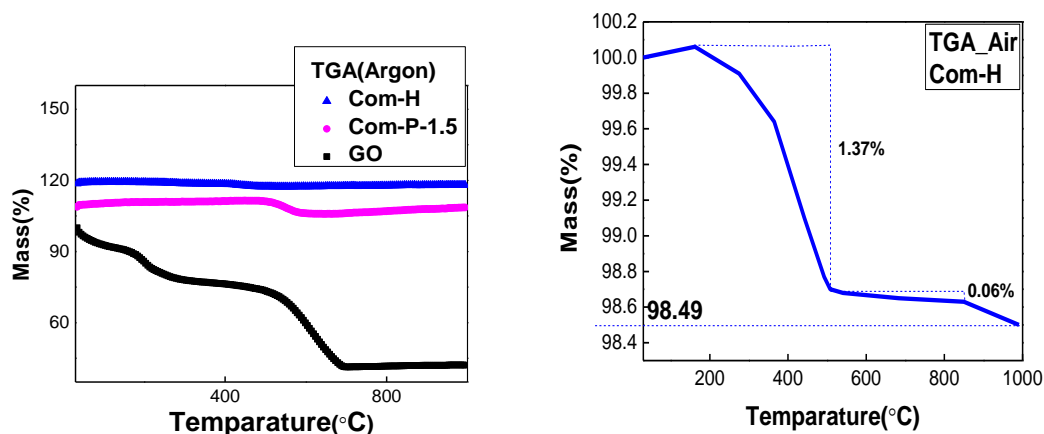
Figure 3.9 TGA of GO Com-P-1.5 and Com-H in Argon atmosphere (left); TGA of Com-H in Air (Right)

3.2.5 <u>Transmission electron microscopy (TEM) analysis</u>

Figure 3.11(a), (b) show the bright field TEM and high resolution TEM (HRTEM) images for BFO-H and Com-H. The image analysis yields the average size of BFO particles to be ~18-20 nm which is comparable to the particle size of BFO-H. A certain fraction of the BFO particles are anchored onto the RGO layers. The bright field images of BFO-P, Com-P-1.5 are shown in Figure 3.10 (a) & (b). We have seen clearly that though the same wt% percentage is used in preparing both the composites, Com-P-1.5 has a little trace of BFO on graphene sheets. Whereas in Com-H we have found array of BFO particles attached to the graphene sheets. High resolution TEM (HRTEM) images showed the lattice fringes of both BFO and rGO Figure 3.11 (c) & (d). The HRTEM image shows the interface between (012) plane of BFO (d = 0.39 nm) particle and the RGO layer with interlayer spacing 0.51 nm. It indicates deposition of graphene layer onto the $(100)_c$ plane of BFO. The interlayer spacing of RGO is much larger than that in graphite (d = 0.37 nm) due to exfoliation. As shown in Figure 3.10 (c) here, these evidences are missing in Com-P-1.5. The lattice planes of BFO could only be seen in HRTEM and selected area electron diffraction (SAED) images. The global structure – studied by powder XRD – and the local structure – studied by SAED and HRTEM – provide evidence of rhombohedral R3c structure of nanoscale BFO.

[116]
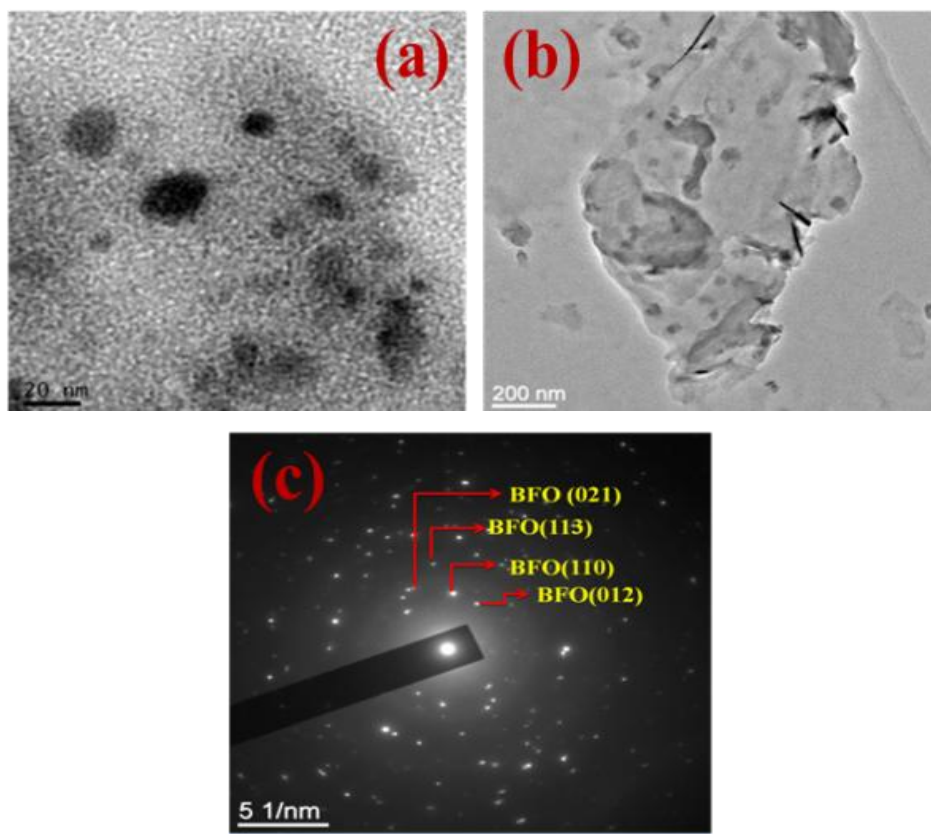
Figure 3.10 TEM Bright field image of BFO-P (a) and Com-P-1.5(b), SAED image of Com-P-1.5(c)

[117]
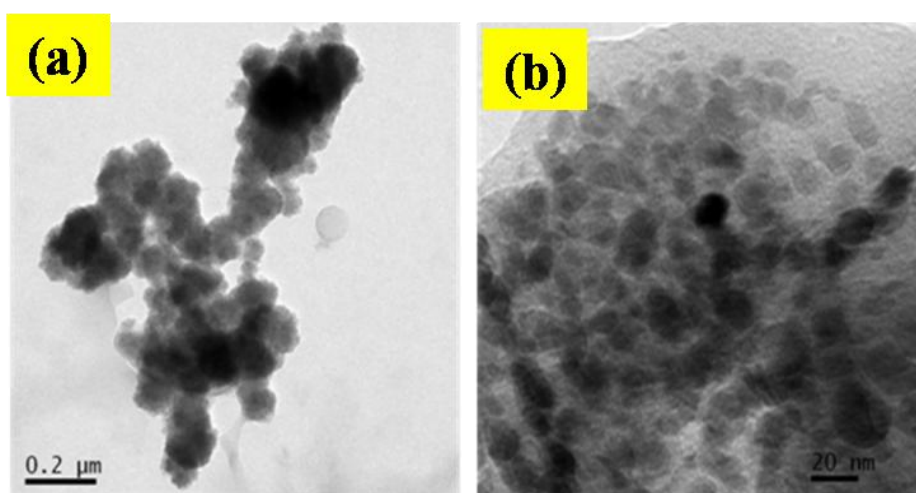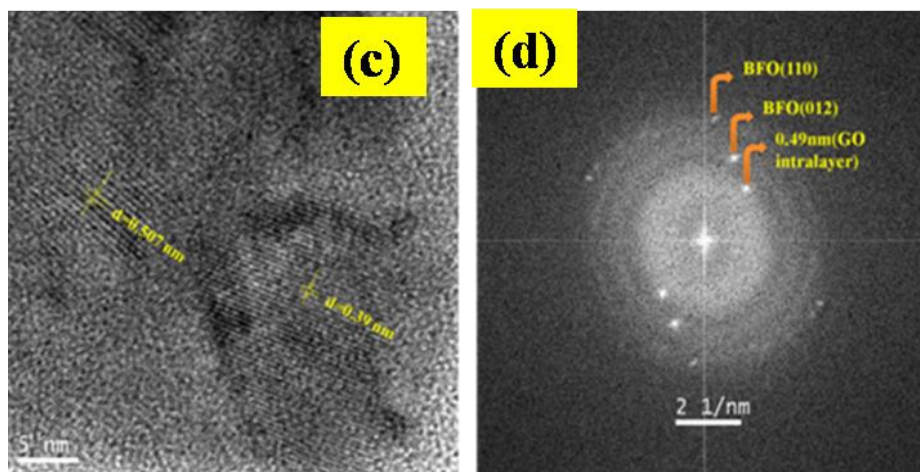
Figure 3.11 TEM Bright field image of BFO-H (e) and Com-H (b), HRTEM and SAED image of Com-H (c) & (d)

3.2.6 X-ray photoelectron spectroscopy (XPS) analysis

We investigated the x-ray photoelectron spectra (XPS) for Com-P-1.5 and Com-H along with GO to determine the surface/interface chemical states of the Bi, Fe, O, and C ions.

The high resolution spectra of Com-P-1.5 for Bi $4f$, Fe $2p$, C $1s$ and O $1s$ are shown in Figure 3.13. The Bi $4f_{7/2}$ and $4f_{5/2}$ spin-orbit doublet peaks corresponding to Bi^{3+} appear at 158.3 and 163.7 eV, respectively. No additional peak corresponding to a different charge state could be observed and no indication exists of doping or substitution at the Bi^{3+} site. The fitted Fe 2p spectra show the characteristic doublet peaks of Fe(II)-O and Fe(III)-O species for Fe $2p_{3/2}$ and $2p_{1/2}$ at ~709.7 eV and ~722.9 eV, and at ~711.84 eV and ~725.3 eV respectively. Figure 3.13 (c) shows the O $1s$ peaks attributed to the lattice oxygen (Olatt) present in the samples, loss of oxygen (O_{loss}) and absorbed oxygen (O_{absor}) on the surface, respectively. The relative percentage of the oxygen vacancy (O_{loss}) is found to be 38.7% for the Com-P-1.5. Figure 3.13 (d) shows the XPS spectra of C $1s$. The peaks at 284.6 and 284.8 eV are attributed to the sp^2 C=C and sp^3 C–C containing groups, respectively. In addition, two carbon–oxygen environments were identified at 286.3 eV [for ether/phenolic components (C–O–C)] and 288.6 eV [for carboxylic groups (O=C–O)]. The amount of sp^2 or sp^3 bonded carbon was estimated using the area under the peaks corresponding to the sp^2 or sp^3 hybridized carbon and their total area. The relative extent of sp^2 (C=C) and sp^3 (C–C) hybridizations were estimated to be 52.5%, and 47.5%, respectively, in Com-P-1.5.

Similarly, the high resolution spectra of Com-H for Bi $4f$, Fe $2p$, C $1s$ and O $1s$ are shown in Figure 3.14. The Bi $4f_{7/2}$ and $4f_{5/2}$ spin-orbit doublet peaks corresponding to Bi^{3+} appear at 158.3 and 163.7 eV respectively and an additional weak pair of doublet peaks was

[118]

observed in Com-H in the lower-binding energy side, which indicates the presence of Bi^0 states. There is also no indication exists of doping or substitution at the Bi^{3+} site. The fitted Fe 2p spectra highlight the characteristic doublet peaks of Fe^{2+}–O species at 709.6 and 722.9 eV for Fe $2p_{3/2}$ and Fe $2p_{1/2}$, respectively, and the doublet peaks of Fe^{3+}–O species at 711.4 and 725.2 eV for Fe $2p_{3/2}$ and Fe $2p_{1/2}$, respectively. The relative percentage of the oxygen vacancy (O_{loss}) is turned out to be 26.5% for the Com-H. Figure 3.14 (c) shows the O 1*s* peaks attributed to Olatt, O_{loss} and O_{absor} are at 529.2eV, 530.8 eV and 532.3 eV respectively similar to Com-P-1.5.

The peak at 283.9 eV corresponds to the Fe─C bonds. Existence of this peak proves the presence of Fe─C bonds in the Com-H sample. The relative extent of sp^2 and sp^3 hybridizations were estimated to be 9.67% and 29.04%, respectively, in Com-H with an additional bonding feature Fe-C with 22.69%. They were estimated to be 57.8%, and 42.2%, respectively in GO.The rise in the sp^3 bonds in the Com-P-1.5 at the expense of sp^2 bonds reflects the transformation due to the reduction process. The quantitative estimate of the fraction of bonds for both Com-H,Com-P-1.5 and GO are shown in Table 3.7. Very interestingly, the Fe-C covalent bonds, observed in the sample prepared by hydrothermal technique (Com-H), turns out to be absent in the case of Com-P-1.5. Small change in oxygen stoichiometry too could be noticed in the case of Com-P-1.5 with respect to the Com-H. Absence of the signature of Fe-C covalent bonds in the XPS data of Com-P-1.5 is one of the central results of this paper. Therefore, the BFO particles are attached with rGO layers via van der Waals (vdW) bonds[15].
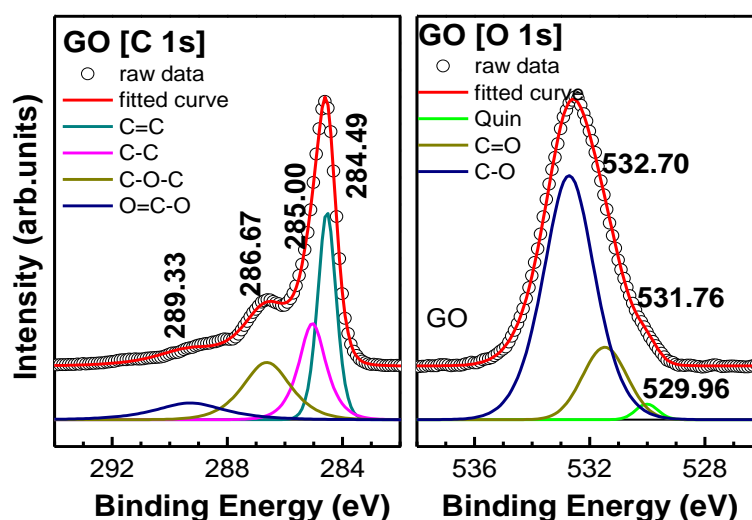
Figure 3.12 High-resolution C 1s and O 1s X-Ray photoelectron spectra of GO highlighting the presence of different species on its surface.
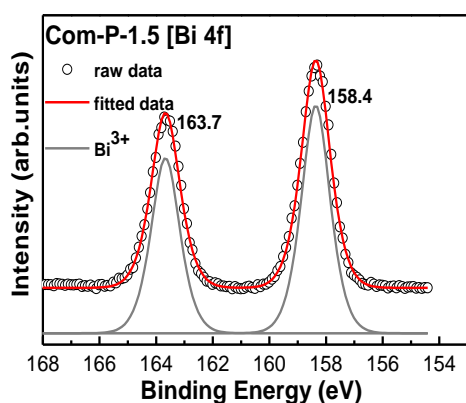
(a)
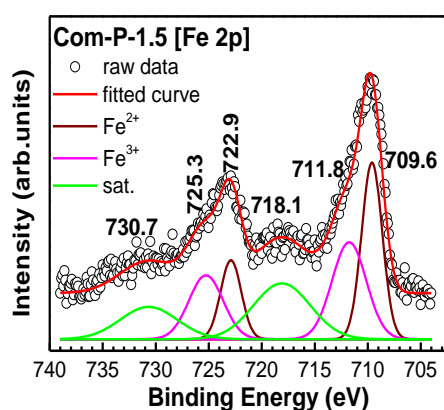
(b)
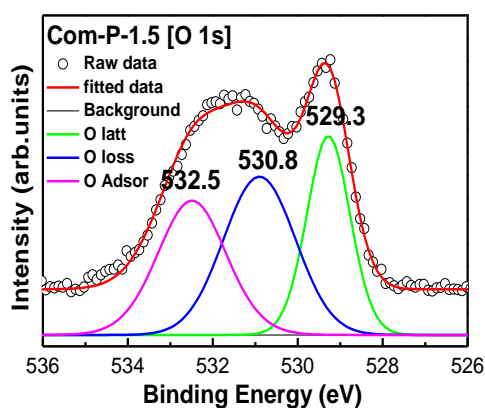
(c)
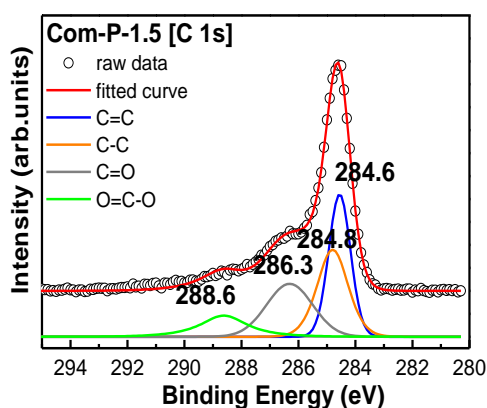
(d)

Figure 3.13 X-Ray photoelectron spectra and their fitting for (a) Bi 4f and (b) Fe 2p (c) O1s and (d) C1s in composite (Com-P-1.5) system
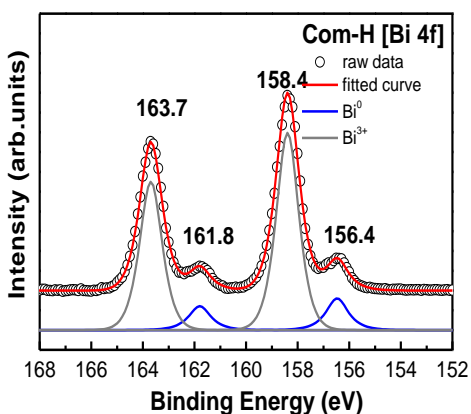
(a)
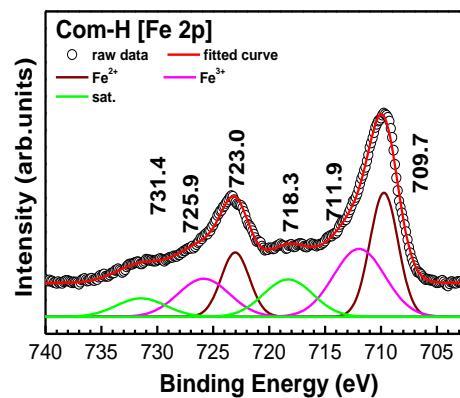
(b)
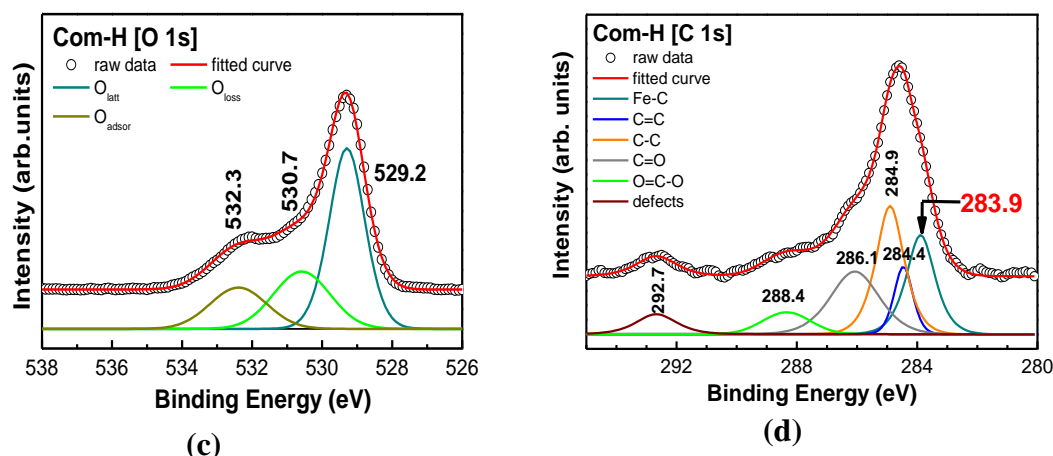
Figure 3.14 X-Ray photoelectron spectra and their fitting for (a) Bi 4f and (b) Fe 2p (c) O1s and (d) C1s in composite (Com-H) system.

	GO		Com_P-1.5		Com-H	
Bonds	**Center**	**% of bonds**	**Center**	**% of bonds**	**Center**	**% of bonds**
Fe-C	-	-	-	-	283.9	22.7
C=C	284.5	36.0	284.6	21.0	284.5	9.7
C-C	285.0	26.2	284.8	19.1	284.9	29.0
O-C-O	286.6	26.4	286.3	18.3	286.1	23.7
O=C-O	289.3	11.5	288.6	9.4	288.3	8.2
Defects	-	-	-	-	292.7	6.7

Table 3.7 Summary of percentage of bonds

3.2.7 **Magnetic property analysis**

Figure 3.15 shows the room temperature magnetization versus field hysteresis loops for composites Com-H and Com-P-1.5 as well as for the remnant BFO particles BFO-H and BFO-P. Figure 3.16 shows room temperature magnetization vs field hysteresis loop for the Com-P-1.5 and Com-P-15 of both wt% s. The data in Table 3.8 lists the coercivity, exchange bias, and magnetization (at 12 kOe field) for the samples.

It is found that the ferromagnetic component in the Com-P-1.5 samples has weakened although the extent of weakening was far stronger in the Com-H sample where Fe-C covalent bonds formed. It is also important to point out, in this context, that among all the nano

[121]

composite samples – either covalent or van der Waals bonded – the extent of ferromagnetism is stronger in the Com-P-15 sample. In general, it appears then that the van der Waals bonded nano composites exhibit magnetic properties quite comparable to those of the isolated BFO nano particles. In the present case, the variation in the ferromagnetic component could partially result from variation in the particle size. Size dependence of magnetization has earlier been studied by many others. Finer particles exhibit higher ferromagnetic component till the size reaches the super paramagnetic limit. However, it is also true that in the cases of Com-H and BFO-H, the particle size is comparable. Yet, the ferromagnetic component appears to have weakened significantly in Com-H. This could result from formation of new set of covalent bonds and change in the charge states of the ions in Com-H. The new bonds could influence the Fe-O-Fe exchange coupling interaction significantly in order to reduce the spin canting angle which, in turn, weakens the ferromagnetic component of the magnetization.

We now turn our attention to another interesting feature of the magnetic property of the samples - enhancement of coercivity (H_C) in Com-H. The change in coercivity was large in Com-H (1.5 wt %) but smaller in Com-P-1.5 and even smaller in Com-P-15. In spite of weakening of the ferromagnetic component, the domain size and pinning of domains by defects appear to be stronger in Com-H. It has been shown earlier that in nano scale particles, ferromagnetism appears at the surface while the core assumes anti-ferromagnetic structure. In fact, magnetic force microscopy on assembled nano particles of BFO provides evidence of surface ferromagnetism with domain size greater than the size of individual particles. In the case of the Com-H, similar spin picture could give rise to enhanced coercivity.

More interesting, however, is the observation of finite exchange bias and its switch from negative to positive in different samples. The exchange bias field develops because of exchange coupling between ferromagnetic and anti-ferromagnetic components across an interface. It has been shown earlier that H_E could be negative or positive depending on the nature of exchange coupling (ferromagnetic or anti-ferromagnetic) and competition between the exchange coupling across the interface and that between anti-ferromagnetic core and applied field H. While ferromagnetic interaction in all the cases yields negative exchange bias, competition between ferromagnetic core spin-applied field interaction and anti-ferromagnetic core spin-surface spin interaction may yield positive exchange bias. We also noticed finite exchange bias in all these nano composites because of exchange coupling interactions across the BFO-graphene interface. If this exchange coupling is ferromagnetic, negative exchange bias develops. In the case of anti ferromagnetic exchange coupling across the interface, the exchange bias becomes positive. It is found that the exchange bias is negative in Com-H (1.5 wt %) and positive in Com-P-1.5. This could be due to the difference in the surface/interface states. In the Com-P-15, the surface states possibly resemble the ones in pure BFO nano particles. Therefore, both the coercivity and the exchange bias in Com-P-15 appear to be comparable to those in pure BFO nano particles.

In Com-H (1.5 wt %) and Com-P-1.5 we have used same content of rGO which provides huge surface area as substrate for BFO particles. In the non-bonded composite Com-P (all wt% s), the extent of surface functionalization also depends on rGO wt%. This is reflected in the exchange bias and coercivity data more prominently since lower rGO content provides higher surface area and higher functionalization. Comparing the bonded and non-bonded samples we notice that the interfacial Fe-C covalent bonds in Com-H play more important role in changing the magnetization of the nano composites.

(a)

(b)

(c)
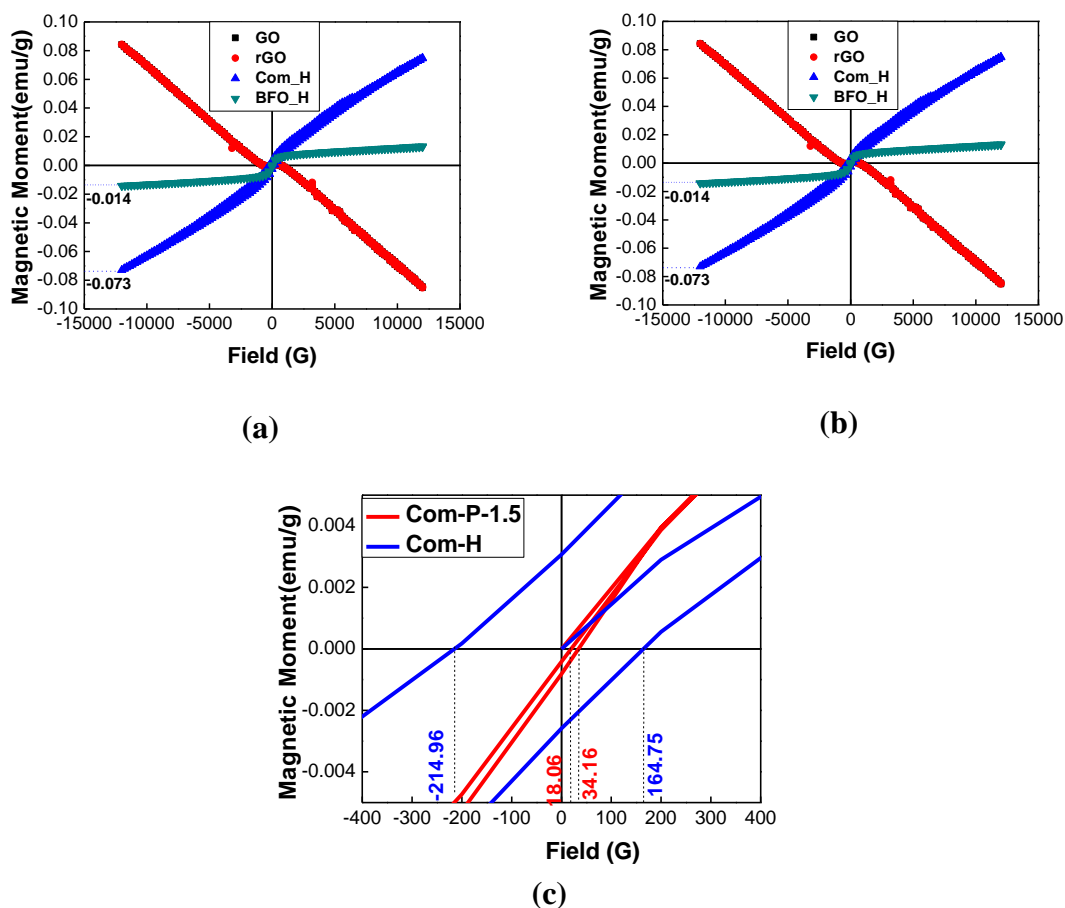
Figure 3.15 Room temperature magnetic hysterisis data of Com-H (a) and Com-P-1.5 (b); and enlarged portion near the origin of both composites (c)

[123]
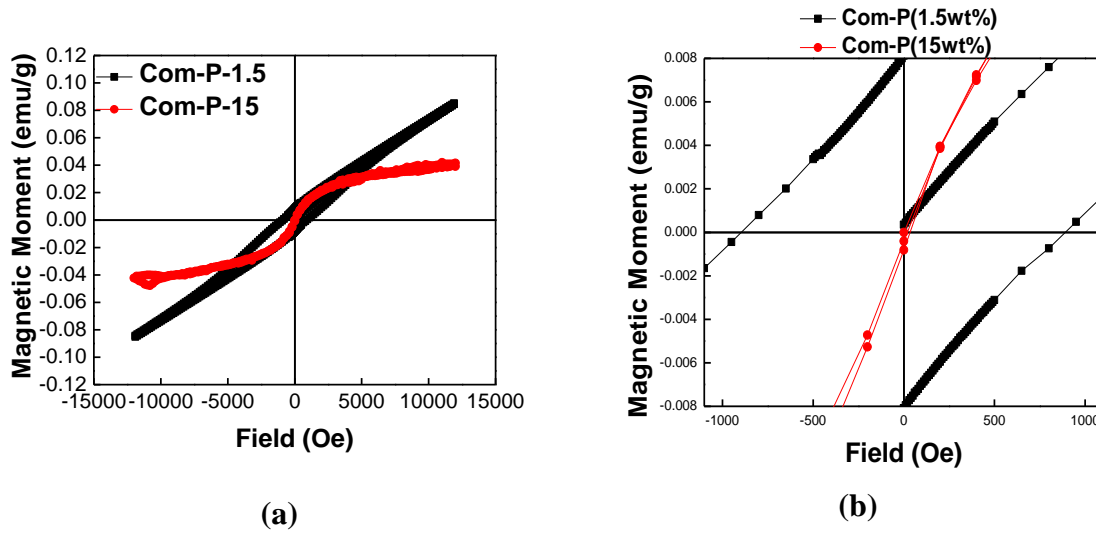
Figure 3.16 Room temperature magnetic hysterisis data of Com-P-1.5 and Com-P-15 (a); and enlarged portion near the origin of both composites (b)

Table 3.8 Summary of magnetic data of the samples Com-H, Com-P-1.5 and Com-P-15			
Sample	**Coercivity (Oe)**	**Exchange Bias $H_e=(H_{c1}+H_{c2})/2$ (Oe)**	**Magnetic Moment M_S (at ~12 kOe) (emu/g)**
Com-H	189.0	-25.0	0.072
Com-P-1.5	895.0	33.0	0.11
Com-P-15	8.0	27.0	0.042

3.2.8 <u>Ferroelectric property analysis</u>

We finally discuss the results of measurement of remanent ferroelectric polarization (P_R) under zero magnetic fields at room temperature. The remanent hysteresis P_R-bias voltage (V) loops have been measured using a specialized protocol[28] which eliminates spurious effects and extracts the intrinsic hysteretic ferroelectric component of polarization. Figure 3.17 shows the results for both the Com-P-1.5 and Com-P-15 nano composites along with those for the covalent bonded composite (Com-H). The relevant data are summarized in the Table 3.9. the normalized data are shown in. For the covalent bonded composite Com-H, we observe that the remanent polarization P_R is more than twice larger than that in the pure nanoscale BFO. However, the P_R decreases drastically in Com-P of all wt% s. This is another important result of this work. We have already observed (discussed before) that the structural parameters including the structural non centrosymmetry are more or less comparable in all the nanoscale samples – pure BFO, Com-H, Com-P-1.5 and Com-P-15. Therefore, observation of dramatic drop in P_R –

when measured directly – in Com-P-1.5 sample is quite remarkable. From the report of Li *et al* group we have seen that Graphene as electrode does not affect the Ferroelectric behavior of BFO. We can say that in sono-chemical composite just because BFO nano particles are attached to the Graphene surface via Van der waals attraction without any bond formation, the ferroelectric polarization is not enhanced in BFO via introduction of Graphene. In fact, the polarization decreases. As Graphene is a very good conductor hence it promotes a path for electrons to traverse. Due to change in oxygen stoitiometry some electrons of BFO broke the dipole dipole interaction and becomes mobile in the viscinity of surface which lowers the ferroelectricity. Its again proved that in this bonded composite of Com-H the Fe-C bond promotes ferroelectricity in BFO.

It has been pointed out earlier that in the case of Van der Waals bond formation at the interface of BFO nano particles and RGO layers, the electron mobility at the surface could be high. Also the interface could give rise to the formation of stronger dead layer with large depolarizing field. In the case of weak Van der Waals bonds (where coupling originates from fluctuating dipoles), the role of actual charge transfer across the interface is limited. Therefore, reconstruction of the interface was not as strong as it is in the case of interfacial Fe-C covalent bonds. Weaker reconstruction could be instrumental in forming stronger dead layers. Combined effect of higher electron mobility at the interface and large dead layers gives rise to the observed drastic decrease in the ferroelectric polarization. Of course, more detailed investigation of the interface electron and lattice states is required to completely unearth the origin of decrease in ferroelectric polarization in the nano composite containing Van der Waals bonds.

(a)

(b)

[125]
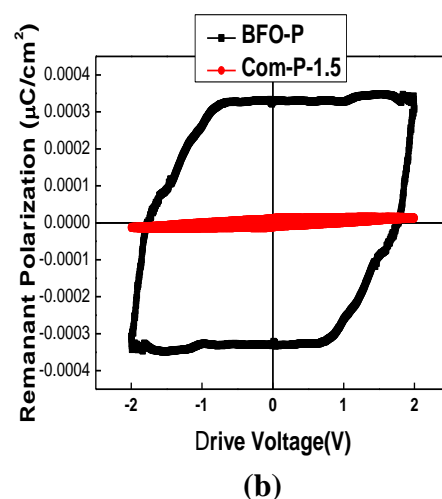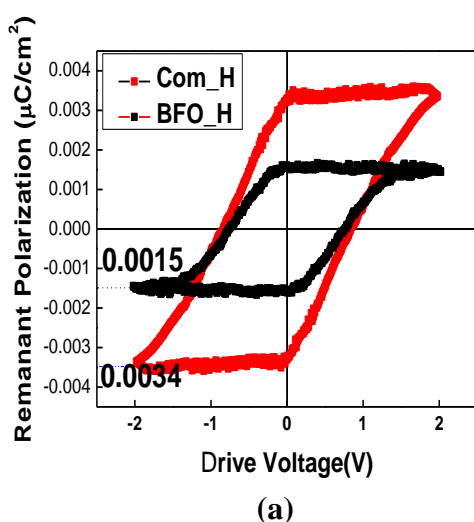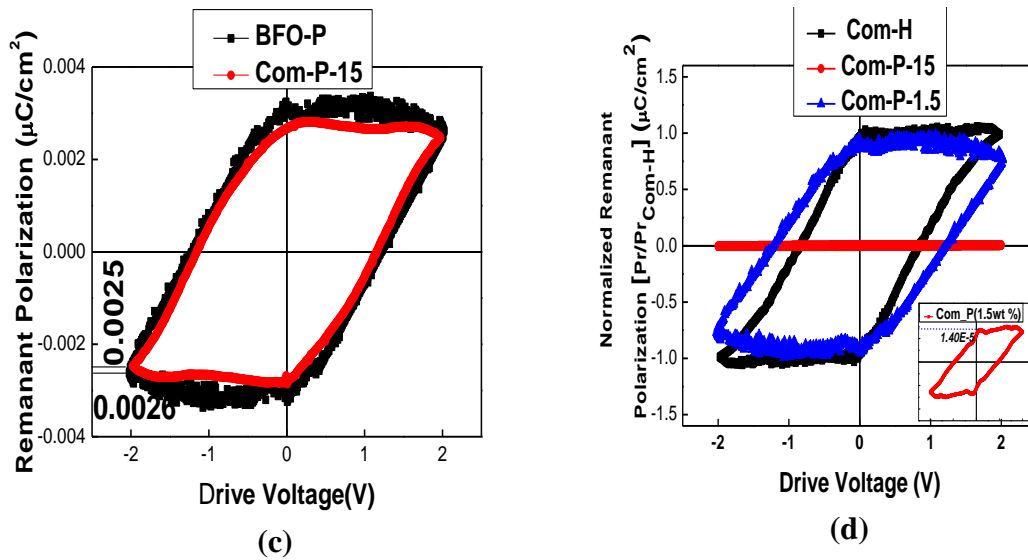
Figure 3.17 Room temperature remanent ferroelectric hysteresis loops for (a) Com-H & BFO-H; (b) Com-P-1.5 & BFO-H and (c) Com-P-15 & BFO-H samples; and Normalized remanent ferroelectric hysteresis loops for Com-H, Com-P-1.5 and Com-P-15 samples; inset: loop for the Com-P-1.5 sample is blown up. (d)

Table 3.9 Summary of crystallographic polarization and remanent ferroelectric polarization of the samples Com-H, Com-P-1.5 and Com-P-15			
Sample	**Net off-centred displacement in an unit cell**		**Remanent Polarization ($\mu C/cm^2$)**
	|s-t|	**(|s-t|)×c (Å) (c = lattice parameter)**	
Com-H	0.0342	0.4745	0.0034
Com-P-1.5	0.02948	0.40895	1.4×10^{-5}
Com-P-15	0.03036	0.42126	0.0025

3.2.9 Discussion

In order to trace the origin of formation of Fe-C covalent bonds in the samples prepared by hydrothermal technique, we point out that the precursors were put in an autoclave to reach high-pressure as well as high temperature (~170°C). Presence of high pressure and temperature was instrumental in forming the Fe-C bonds at the interface of BFO nanoparticles and reduced-graphene-oxide (RGO) nanosheets. On the other hand, in sonochemical synthesis, acoustic cavitation effect develops[29] as a result of acoustic wave driven bubble formation, growth, and their collapse. This, in turn, generates pressure and temperature too (in the present case, the temperature was found to be ~85 °C at the frequency of 20 kHz), for the chemical reactions to take place. However, our observation shows that the pressure and temperature used in an autoclave during hydrothermal synthesis were more appropriate to form the Fe-C covalent

[126]

bonds across the interface of the BFO nanoparticles and the RGO nano sheets. The cavitation effect in sonochemical synthesis might be suitable for exfoliation of the RGO nanosheets but not for giving rise to the formation of Fe-C bonds. Ion mobility and charge transfer across the interfaces are associated with specific activation energies and, therefore, they require higher pressure and temperature, i.e., higher energy[30]. It could be all the more important in the context of the precursor solution we used for these synthesis processes. Since we used salts of the raw chemicals within the KOH solution, the ion mobility decreases[31]. Therefore, higher energy was necessary for forming the Fe-C bonds. In addition, it has been demonstrated earlier[32] that during hydrothermal process, the chemical environment of the reduced graphene oxide changes with enhanced population of OH$^-$ ions and dangling bonds of C. This, in turn, influences the formation of Fe-C covalent bonds too. It appears, therefore, that the conditions of hydrothermal synthesis could fulfil the requirement of forming the Fe-C bonds across the interfaces while the sonochemical process did not; at least, in the present case.

Study on the graphene/ferroelectric hetero-structure shows that the ferroelectric materials change the carrier mobility, contact barrier, Fermi energy level, and intrinsic resistance in graphene[33][34]. In graphene, each carbon atoms (sp^2 hybridized) are covalently bonded to 3 near-neighbor carbon atoms forming a hexagonal planar structure. The single electron in sp^3 hybridized orbital, on the other hand, forms π electron cloud normal to the hexagonal plane and promotes higher mobility. When GO is reduced to rGO the oxygen functionalities are removed and provides some active π sites in the surface. In covalent bonded nano composite, these sp^3 hybridized C atoms are attached with BFO via Fe-C bonds but, in contrast, in non-bonded nanocomposite there are only vdW bonds. The covalent bonding is responsible for the decrease in kinetic energy of electrons. These bonds are stronger. However, the van der Waals bonds originate from the time-dependent fluctuations of the electron charge density of the neutral atoms and molecules and consequent fluctuating dipoles. The dipole-dipole interaction is weak and does not involve actual charge transfer. Van der Waals bonds, therefore, were shown to be useful for producing clean and defect-free interfaces suitable for electronic device applications[35]. However, we observe here that because of large electron mobility of the graphene layers, the absence of covalent bond and consequent charge transfer and localization (due to decrease in electron kinetic energy), van der Waals bonds between nano particle of BFO and graphene layers impart metallicity in the overall nano composite. It is also possible that the van der Waals bonds between the graphene layer (with large electron mobility) and BFO nanoparticles generates large dead layer at the interface which, in turn, reduces the overall ferroelectric polarization (when measured electrically) because of strong depolarization. The observation of significant drop in the remanent ferroelectric polarization in the RGO/BFO nano composite – when measured directly electrically – highlights that the van der Waals bonds

between a ferroelectric and graphene could be detrimental for enhancing the functionality of a ferroelectric device. A semiconducting system, e.g., Si, on the contrary, could be more useful[35]. Of course, we also observe here that a nano composite with 15 wt% of rGO exhibits larger remanent ferroelectric polarization than the nano composite with ~1.5 wt% rGO. This could be because of lower surface to volume ratio in the former case. As discussed earlier, presence of Van der Waals bonds (and absence of covalent bonds) has a moderate influence on the structural parameters – distortion, bond length and angles – including structural non centrosymmetry. However, how such parameters change under a magnetic field in the RGO/BFO nano composites containing van der Waals bonds needs to be investigated separately.

High surface area of rGO appears to have played an important role in the formation of Fe-C covalent bonds. In order to examine this issue in the context of Van der Waals bonded composite, we have used two different wt% of rGO. In this case too, the extent of Van der Waals Fe-C bonds at the interface depends on the surface area to volume ratio. Because of smaller surface area to volume ratio in the composite containing 15 wt% rGO, the particles behave as isolated ones. In Table 3.8 and Table 3.9 we have seen that, in comparison to the properties of the isolated BFO nanoparticles, the magnetic coercivity, exchange bias and magnetic moment are higher in Com-P-1.5 but the remanent polarization is drastically smaller. Such a change highlights the influence of the Van der Waals Fe-C bonds at the interface. However, the Com-P-15 sample exhibits reasonably comparable remanent ferroelectric polarization even though the saturation magnetization and coercivity are smaller. This is because the nanoparticles in Com-P-15 samples are nearly isolated. Therefore, distinct role of Van der Waals bonds and its dependence on the wt% of the rGO could be clearly noticed in the results reported here for Com-P-1.5 and Com-P-15 samples.

In conclusion, we addressed the issue of influence of covalent vis-à-vis van der Waals bonds (between the graphene layer and BFO nano particles) on the crystallographic and physical properties of reduced-graphene-oxide-BFO nano composites. While, covalent bond appears to have resulted in novel multiferroicity, van der Waals bonds yield a significant drop in the remanent polarization even though the crystallographic structure including the structural non-centrosymmetry does not appear to have changed substantially. It could be because of very large electron mobility of the graphene layers. Either in presence of van der Waals bonds, graphene layers impart enhanced metallicity or resulted in large depolarizing field. Van der Waals bonds, therefore, do not appear to be suitable for graphene/ferroelectric nanocomposite or hetero-structure devices. The synthesis process should be suitably optimized for enhancing the formation of covalent bonds at the graphene/ferroelectric interfaces.

3.3 <u>Chapter summary</u>

The focus of this chapter is on variation in the physical properties observed in BFO/RGO nano composites containing Fe-C covalent and Van der Waals bonds. We examined the bond formation by Raman spectrometry and also the electronic structure of the surface ions by using X-ray photoelectron spectroscopy (XPS). We used X-ray diffraction (XRD) for investigating the crystallographic structures. The particle morphology was studied by transmission electron microscopy (TEM) while high resolution TEM (HRTEM) and selected area electron diffraction (SAED) were used for examining the local crystallographic structures. Following the thorough characterization of the samples, we finally examined their magnetic and ferroelectric properties to reveal how change in the nature of Fe-C bonds – covalent to Van der Waals – across the BFO/RGO interfaces affect the physical properties of the nano composites. We observed that while the change in the magnetic properties is relatively smaller, the ferroelectric polarization decreases drastically in the samples containing Van der Waals bonds. This could be due to enhanced electron mobility and/or development of strong dead layer at the interface between BFO nanoparticles and the RGO nanosheets.

3.4 <u>Bibliography</u>

[1]   Huang, C., Du, Y., Wu, H., Xiang, H., Deng, K. and Kan, E., 2018. Prediction of intrinsic ferromagnetic ferroelectricity in a transition-metal halide monolayer. *Physical review letters*, *120*(14), p.147601.

[2]   Qi, J., Wang, H., Chen, X. and Qian, X., 2018. Two-dimensional multiferroic semiconductors with coexisting ferroelectricity and ferromagnetism. *Applied Physics Letters*, *113*(4), p.043102.

[3]   Hu, T. and Kan, E., 2019. Progress and prospects in low-dimensional multiferroic materials. *Wiley Interdisciplinary Reviews: Computational Molecular Science*, *9*(5), p.e1409.

[4]   Oh, Y.S., Luo, X., Huang, F.T., Wang, Y. and Cheong, S.W., 2015. Experimental demonstration of hybrid improper ferroelectricity and the presence of abundant charged walls in (Ca, Sr) 3 Ti 2 O 7 crystals. *Nature materials*, *14*(4), pp.407-413.

[5]   Yoshida, S., Fujita, K., Akamatsu, H., Hernandez, O., Sen Gupta, A., Brown, F.G., Padmanabhan, H., Gibbs, A.S., Kuge, T., Tsuji, R. and Murai, S., 2018. Ferroelectric Sr3Zr2O7: competition between hybrid improper ferroelectric and antiferroelectric mechanisms. *Advanced Functional Materials*, *28*(30), p.1801856.

[6]   Zhang, J., Shen, X., Wang, Y., Ji, C., Zhou, Y., Wang, J., Huang, F. and Lu, X., 2020. Design of two-dimensional multiferroics with direct polarization-magnetization coupling. *Physical Review Letters*, *125*(1), p.017601.

[7]   Qiao, Z., Yang, S.A., Feng, W., Tse, W.K., Ding, J., Yao, Y., Wang, J. and Niu, Q., 2010. Quantum anomalous Hall effect in graphene from Rashba and exchange effects. *Physical Review B*, *82*(16), p.161414.

[8]   Wang, Z., Tang, C., Sachs, R., Barlas, Y. and Shi, J., 2015. Proximity-induced ferromagnetism in graphene revealed by the anomalous Hall effect. *Physical review letters*, *114*(1), p.016603.

[9]   Leutenantsmeyer, J.C., Kaverzin, A.A., Wojtaszek, M. and Van Wees, B.J., 2016. Proximity induced room temperature ferromagnetism in graphene probed with spin currents. *2D Materials*, *4*(1), p.014001.

[10]   Mendes, J.B.S., Santos, O.A., Meireles, L.M., Lacerda, R.G., Vilela-Leão, L.H., Machado, F.L.A., Rodríguez-Suárez, R.L., Azevedo, A. and Rezende, S.M., 2015. Spin-current to charge-current conversion and magnetoresistance in a hybrid structure of graphene and yttrium iron garnet. *Physical review letters*, *115*(22), p.226601.

[11]   Evelt, M., Ochoa, H., Dzyapko, O., Demidov, V.E., Yurgens, A., Sun, J., Tserkovnyak, Y., Bessonov, V., Rinkevich, A.B. and Demokritov, S.O., 2017. Chiral charge pumping in graphene deposited on a magnetic insulator. *Physical Review B*, *95*(2), p.024408.

[12]   Wei, P., Lee, S., Lemaitre, F., Pinel, L., Cutaia, D., Cha, W., Katmis, F., Zhu, Y., Heiman, D., Hone, J. and Moodera, J.S., 2016. Strong interfacial exchange field in the graphene/EuS heterostructure. *Nature materials*, *15*(7), pp.711-716.

[13]   Wu, Y.F., Song, H.D., Zhang, L., Yang, X., Ren, Z., Liu, D., Wu, H.C., Wu, J., Li, J.G., Jia, Z. and Yan, B., 2017. Magnetic proximity effect in graphene coupled to a BiFe O 3 nanoplate. *Physical Review B*, *95*(19), p.195426.

[14]   Song, H.D., Wu, Y.F., Yang, X., Ren, Z., Ke, X., Kurttepeli, M., Tendeloo, G.V., Liu, D., Wu, H.C., Yan, B. and Wu, X., 2018. Asymmetric modulation on exchange field in a graphene/BiFeO3 heterostructure by external magnetic field. *Nano letters*, *18*(4), pp.2435-2441.

[15]   Li, Y., Sun, X.Y., Xu, C.Y., Cao, J., Sun, Z.Y. and Zhen, L., 2018. Ferroelectric resistive switching behavior in two-dimensional materials/BiFeO 3 hetero-junctions. *Nanoscale*, *10*(48), pp.23080-23086.

[16]   Li, T., Shen, J., Li, N. and Ye, M., 2013. Hydrothermal preparation, characterization and enhanced properties of reduced graphene-BiFeO3 nanocomposite. *Materials Letters*, *91*, pp.42-44.

[17] Moitra, D., Dhole, S., Ghosh, B.K., Chandel, M., Jani, R.K., Patra, M.K., Vadera, S.R. and Ghosh, N.N., 2017. Synthesis and microwave absorption properties of BiFeO3 nanowire-RGO nanocomposite and first-principles calculations for insight of electromagnetic properties and electronic structures. *The Journal of Physical Chemistry C*, *121*(39), pp.21290-21304.

[18] Jalil, M.A., Chowdhury, S.S., Alam Sakib, M., Enamul Hoque Yousuf, S.M., Khan Ashik, E., Firoz, S.H. and Basith, M.A., 2017. Temperature-dependent phase transition and comparative investigation on enhanced magnetic and optical properties between sillenite and perovskite bismuth ferrite-rGO nanocomposites. *Journal of Applied Physics*, *122*(8), p.084902.

[19] Ederer, C. and Spaldin, N.A., 2005. Weak ferromagnetism and magnetoelectric coupling in bismuth ferrite. *Physical Review B*, *71*(6), p.060401.

[20] Liu, J., Chen, L., Yang, H., Zhang, Z. and Wang, Y., 2019. Size-dependent solid-solid phase transition process of Ag2S nanoparticles. *Progress in Natural Science: Materials International*, *29*(4), pp.397-401.

[21] Xu, G., Li, J. and Viehland, D., 2006. Ground state monoclinic (M b) phase in (110) c Bi Fe O 3 epitaxial thin films. *Applied physics letters*, *89*(22), p.222901.

[22] Yang, J.C., He, Q., Suresha, S.J., Kuo, C.Y., Peng, C.Y., Haislmaier, R.C., Motyka, M.A., Sheng, G., Adamo, C., Lin, H.J. and Hu, Z., 2012. Orthorhombic BiFeO 3. *Physical review letters*, *109*(24), p.247606.

[23] Zeches, R.J., Rossell, M.D., Zhang, J.X., Hatt, A.J., He, Q., Yang, C.H., Kumar, A., Wang, C.H., Melville, A., Adamo, C. and Sheng, G., 2009. A strain-driven morphotropic phase boundary in BiFeO3. *science*, *326*(5955), pp.977-980.

[24] Cançado, L.G., Jorio, A., Ferreira, E.M., Stavale, F., Achete, C.A., Capaz, R.B., Moutinho, M.V.D.O., Lombardo, A., Kulmala, T.S. and Ferrari, A.C., 2011. Quantifying defects in graphene via Raman spectroscopy at different excitation energies. *Nano letters*, *11*(8), pp.3190-3196.

[25] Ferreira, E.M., Moutinho, M.V., Stavale, F., Lucchese, M.M., Capaz, R.B., Achete, C.A. and Jorio, A., 2010. Evolution of the Raman spectra from single-, few-, and many-layer graphene with increasing disorder. *Physical Review B*, *82*(12), p.125429.

[26] Palai, R., Schmid, H., Scott, J.F. and Katiyar, R.S., 2010. Raman spectroscopy of single-domain multiferroic BiFeO 3. *Physical Review B*, *81*(6), p.064110.

[27] Hermet, P., Goffinet, M., Kreisel, J. and Ghosez, P., 2007. Raman and infrared spectra of multiferroic bismuth ferrite from first principles. *Physical Review B*, *75*(22), p.220102.

[131]

[28] Martín-Carrón, L., De Andres, A., Martínez-Lope, M.J., Casais, M.T. and Alonso, J.A., 2002. Raman phonons as a probe of disorder, fluctuations, and local structure in doped and undoped orthorhombic and rhombohedral manganites. *Physical Review B*, *66*(17), p.174303.

[29] Chhetri, S., Adak, N.C., Samanta, P., Murmu, N.C. and Kuila, T., 2017. Functionalized reduced graphene oxide/epoxy composites with enhanced mechanical properties and thermal stability. *Polymer Testing*, *63*, pp.1-11.

[30] Chowdhury, U., Goswami, S., Bhattacharya, D., Midya, A. and Mandal, P., 2016. Determination of intrinsic ferroelectric polarization in lossy improper ferroelectric systems. *Applied Physics Letters*, *109*(9), p.092902.

[31] Savun-Hekimoğlu, B., 2020, October. A review on sonochemistry and its environmental applications. In *Acoustics* (Vol. 2, No. 4, pp. 766-775). MDPI.

[32] Gao, T., Chen, Z., Huang, Q., Niu, F., Huang, X., Qin, L. and Huang, Y., 2015. A review: preparation of bismuth ferrite nanoparticles and its applications in visible-light induced photocatalyses. *Rev. adv. mater. sci*, *40*(2), pp.97-109.

[33] Han, J.T., Huang, Y.H., Wu, X.J., Wu, C.L., Wei, W., Peng, B., Huang, W. and Goodenough, J.B., 2006. Tunable synthesis of bismuth ferrites with various morphologies. *Advanced Materials*, *18*(16), pp.2145-2148.

[34] Li, Z., Shen, Y., Guan, Y., Hu, Y., Lin, Y. and Nan, C.W., 2014. Bandgap engineering and enhanced interface coupling of graphene–BiFeO 3 nanocomposites as efficient photocatalysts under visible light. *Journal of Materials Chemistry A*, *2*(6), pp.1967-1973.

[35] Lu, H., Lipatov, A., Ryu, S., Kim, D.J., Lee, H., Zhuravlev, M.Y., Eom, C.B., Tsymbal, E.Y., Sinitskii, A. and Gruverman, A., 2014. Ferroelectric tunnel junctions with graphene electrodes. *Nature communications*, *5*(1), p.5518.

[36] Dai, J.Q., Cao, T.F. and Wang, X.W., 2018. Effect of surface termination on charge doping in graphene/BiFeO3 (0001) hybrid structure. *The Journal of Physical Chemistry C*, *122*(30), pp.17250-17260.

[37] Wu, M., 2021. Two-dimensional van der Waals ferroelectrics: Scientific and technological opportunities. *Acs Nano*, *15*(6), pp.9229-9237.

4 Chapter

Study of bonding and physical properties of covalently bonded rGO/BiFeO₃ nano composites

4.1 <u>Introduction</u>

In our previous chapter we have noticed that the covalently bonded hydrothermally prepared composite has shown esoteric magnetic and ferroelectric properties due to structural distortion caused by the emergence of Fe-C bonds. In this chapter we summarize the detail study of magnetoelectric coupling in this new type of covalently bonded nano composite.

The reconstruction of crystallographic, magnetic, and electronic structures at the interface turns out to be quite an effective way of preserving the multiferroic orders and augmenting the coupling among the order parameters in multiferroic-based hetero-structures/composites[1].Large exchange field B_{ex} (of the order from ten to hundred tesla) in graphene/BiFeO₃ hetero-structure induces proximity effect-driven magnetism [2] [3] while, in graphene/BaMnO₃ systems [4],the magnetic structure of BaMnO₃exhibits change from anti-ferromagnetic to ferromagnetic orientation at the interface[5]. It has also been shown[6] that graphene–methylammonium-lead-iodide (CH₃NH₃PbI₃) composite exhibits ferroelectricity because of the reconstruction of the crystallographic structure in the interface regions. Given all these results, it is important to examine how reconstruction of magnetic and electronic structures by exchange-coupled surface atoms of graphene and nano scale BiFeO₃ (BFO) influences the multiferroicity in BFO. In this chapter, we will show that the reduced-graphene-oxide–Bismuth Ferrite (rGO/BFO) nano composite exhibits significantly different multiferroic properties than what has been observed in bulk and nano scale BFO. The remanent ferroelectric polarization is found to follow non-monotonic magnetic field dependence at room temperature as the applied magnetic field is swept across 0–20 kOe on a pristine sample. The remanent ferroelectric polarization, in the present case is determined, both from powder neutron diffraction patterns recorded under 0–20 kOe field.

In different systems, ferroelectric polarization is found to exhibit both increase and decrease under an applied magnetic field. For example, ortho-ferrite $DyFeO_3$[7] or Z-type hexaferrite$Sr_3Co_2Fe_{24}O_{41}$[8] exhibits a rise in polarization under a magnetic field. Bulk BFO, on the other hand, exhibits[9] suppression of off-centering of Fe ions (and consequently, suppression of ferroelectric polarization (P)) below the magnetic transition temperature T_N (off centering of Bi ions remains unaffected) as it is driven by negative bulk magneto-striction within the $Fe-O-Fe$ spin structure. Therefore, one observes monotonic suppressionof P under H. Suppression of P under H is found to continue[10] across a magnetic field range as wide as0–500 kOe and across a magnetic phase transition from spin cycloid to canted anti-ferromagnetic structure. In contrast, in the case of the RGO/BFO nano composite, the H dependence of P turns out to be non-monotonic possibly because of field dependent competition between positive and negative magneto-striction arising, respectively, in the interface and bulk regions of the nano composite. Obviously, this is quite different from the P-H patterns observed in bulk or nano scale BFO.

The RGO/BFO nano composite was prepared by the hydrothermal technique. The preparations of rGO and rGO/BFO nano composite have been described in sections 2.3.1.1 and 2.3.1.3 respectively. Here we have prepared Com-H using threes different wt% s of rGO in order to examine the influence of rGO wt% on the Fe-C bonding and room temperature magnetic properties. The composite prepared with weight 0.5%, 1.5% and 2.5% of rGO are designated as Com-H-0.5, Com-H and Com-H-2.5. The multiferroic study was done on 1.5wt% sample i.e. on Com-H only. We have also carried out the hydrothermal treatment over different time scales- 2, 4, 5, 6hr to find out the optimum one necessary for the preparation of phase pure sample. The sample treated hydrothermally for 6 h turned out to be phase pure and was designated as Com-H.

4.2   Result and Discussion

All the samples were characterized by powder X-Ray diffraction (XRD), and X-Ray photoelectron spectroscopy (XPS). The XPS measurements were performed by PHI 5000 VERSAPROBE II, Physical Electronics System, equipped with a monochromatic Al Kα (1486.7 eV)-focused X-Ray source and a multi-channeltron hemispherical electron energy analyzer. The magnetic hysteresis loops were measured by Lake Shore vibrating sample magnetometer (VSM; Model 7407) under 20 kOe field at room temperature, while the ferroelectric polarization was measured by the Precision LC-II(Radiant Technologies Inc.) ferroelectric loop tester. For preparing the samples for electrical measurements, nano particles were dispersed within ethanol and spin coated onto the Si/SiO_2 substrate to form films (section 2.4.3). Thickness of the film was ~10 nm, as measured by ellipsometry. Silver dots were used as electrodes. The powder Neutron diffraction patterns were recorded at room temperature at

the PD-3 beamline of National Facility for Neutron Beam Research (NFNBR),Dhruva Reactor, Mumbai, using a monochromatic beam of wavelength2.315 Å. The magnetic field was varied across 0–20 kOe.

4.2.1 <u>X-ray diffraction (XRD) pattern analysis:</u>

Figure 4.1 shows the comparative XRD plot of GO, rGO, BFO-H and nano composite Com-H prepared at different working temperatures. From Figure 4.1 it is seen that GO shows characteristics peaks at 11.7° corresponding to the (001) plane and at 42.5° corresponding to the (101) plane. Upon reduction it is supposed to retain 2D graphitic structure. Though, rGO is multilayer stack of graphene planes but the plane is not fully restored so we got a broad peak at 24.86º which is nearly close to 26.6º of graphite plane (002). It can be concluded that rGO have weak crystallinity. BFO-H shows pure phase of BFO according to JCPDS card no 86-1254. Now we see that at 2hr BFO phases are not created but after 4hr it shows BFO phases along with many impurity phases. The leached product shows pure phase BFO. After, 6hr, desired phase is achieved with no impurity peaks. As we know that through leaching we can eliminate the other phases but it can be easily stated that other phase particles were also grown at 5hr which is not desired. But at 6hr we got single phase of BFO in the composite. So we took Com-H for further characterizations. In the composite, rGO peak is not noticed because rGOwt% is less than 5 whereas BFO peaks matched those observed in BFO-H.
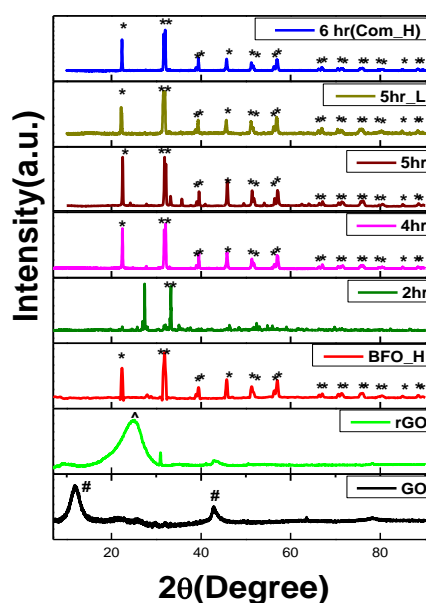
Figure 4.1 Time variation opted during hydrothermal synthesis of Com-H

[135]

4.2.2 X-Ray photo-electrcon spectroscopy (XPS) analysis

The XPS measurements were performed by PHI 5000 VERSAPROBE II, Physical Electronics System, equipped with a monochromatic Al Kα (1486.7 eV)-focused X-Ray source and a multi-channeltron hemispherical electron energy analyzer. All the spectra were collected at an emission angle of 45° with the base vacuum of 5.0×10^{10} mbar. The binding energies were referenced by measuring C 1s and keeping it at 284.6 eV. The total energy resolution was estimated to be 400 meV for monochromatic Al Kα line with pass energy of 11.750 eV. A charge neutralizer was used to compensate the surface charging of the samples. A background was subtracted from the measured raw data.

The high-resolution XPS data for Bi 4f and Fe 2p are shown in Figure 4.2 (a) & (b), respectively. The Bi $4f_{7/2}$ and $4f_{5/2}$ spin–orbit doublet peaks are located at 158.4 and 163.7 eV, respectively, which are found to correspond to Bi^{3+} states from Bi─O bonds. Interestingly, the binding energy of Bi^{3+} states remains same in both the BFO-H and Com-H samples. It indicates that no substitution has taken place at the Bi^{3+} sites in the Com-H sample. Of course, an additional weak pair of doublet peaks was observed in Com-H in the lower-binding energy side, which indicates the presence of Bi^0 states. To estimate the percentage of Bi^0 states in the Com-H sample, we adopted the χ2 iterative fit of the Bi $4f$ core-level region using two pairs of doublet components corresponding to the Bi^{3+} (grey) and Bi^0 (blue) states, as shown Figure 4.2 (a). Except for the peak area, the energy positions, line shapes, widths, and all other parameters were kept same during the fitting of the two pairs of doublet peaks. The Bi^0 states $4f_{7/2}$ and $4f_{5/2}$ (spin–orbit doublet peaks) are centered at 156.5 and 161.8 eV respectively. The relative percentage of Bi^0 states is found to be 14.3%.

The Fe $2p_{3/2}$ and $2p_{1/2}$ spin–orbit doublet peaks are located at around 709.6 and 722.9 eV, respectively, with a pair of shakeup satellite peaks[11] located at 8.0 eV above their spin–orbit doublet peaks. We have carefully fitted the spectra using the following fitting parameters for Fe2p: spin–orbit splitting 13.3 eV, branching ratio 2.0, full width at half maximum (FWHM) 2.3 eV; and an integral background was subtracted before fitting. Similarly, the spectra for Fe3p were fitted by considering spin–orbit splitting 13.8 eV, branching ratio 2.0, and FWHM 3.8 eV. The fitted Fe 2p spectra highlight the characteristic doublet peaks of $Fe2+-O$ species at 709.6 and 722.9 eV for Fe $2p_{3/2}$ and Fe $2p_{1/2}$, respectively, and the doublet peaks of $Fe3+-O$ species at 711.4 and 725.2 eV for Fe $2p_{3/2}$ and Fe $2p_{1/2}$, respectively. It is to be noted that the composite sample shows no change in the peak positions, except for the Fe^{3+} oxidation state which shows a shift of 0.6 eV toward higher binding energy. This chemical shift of $Fe3p$ arises due to the variation in the electro-negativity of Fe and O in the composite

sample. The Fe^{2+}:Fe^{3+} ratio turn out to be 45.4: 54.6 and 49.4: 50.6 in BFO-H and Com-H, respectively.

Figure 4.2 (d) shows the C 1s core-level spectra for both BFO-H and Com-H. The spectra corresponding to Com-H were fit using the contribution of the following six components: 1) defects; 2) $O=C-O$; 3) $C=O$; 4) $C-C$; 5) $C=C$; and 6) $Fe-C$ bonds. The peak at 283.9 eV corresponds to the $Fe-C$ bonds. Existence of this peak proves the presence of $Fe-C$ bonds in the Com-H sample. Figure 4.2 (c) shows the O 1s peak fit with the contribution from lattice oxygen, oxygen loss, and surface oxygen. Their characteristic peaks appear at lower, intermediate, and higher binding energies. For both the samples, the O 1s peaks were fitted by keeping the peak position, line shape, and the width same. The oxygen loss turns out to be 18.1 and 26.5%, respectively, for BFO-H and Com-H.

We analyzed the C 1s spectra for Com-H quantitatively for determining the concentration of different bonds such as $Fe-C$, $C-C$, $C=C$, $O=C-O$, $O-C-O$ and compared the results with those obtained from the analysis of the spectra with pure GO. The comparison is given in Table 4.1. The concentration of $C=C$ bonds is found to have decreased in Com-H in comparison with that in GO because of the rise in the $Fe-C$ bonds in Com-H. The differences between the concentrations of $C=C$ bonds alone in GO and that of $C=C$ and $Fe-C$ bonds (3%) in Com-H is accounted for in the rise in $C-C$ bonds in Com-H. Expectedly, the concentration of $O=C-O$ and $O-C-O$ bonds decreased in Com-H because of reduction of GO in the composite. The presence of $C-C$ bonds also indicates that not all the surface carbon ions of graphene are bonded to the Fe ions of BFO particles. Therefore, both bonded and non-bonded BFO particles coexist in the Com-H sample. As discussed later, relative concentration of the bonded BFO particles plays an important role in governing the magnetoelectric properties of the nano composite.

To examine the interface region and its variation with the wt% of the RGO in BFO/RGO nano composites, we, as well, carried out XPS on the samples containing 0.5 and 2.5 wt% RGO as seen in Figure 4.3 and Figure 4.4 respectively. The XPS data and their fitting together with the results obtained from such analysis have been given in the Table 4.1. Remarkably, the concentration of the $Fe-C$ bonds is found to vary directly with the wt% of RGO in the nano composite. From nearly 24.3% in the sample with 0.5 wt% RGO, the $Fe-C$ bond concentration decreased to nearly 22.7% in Com-H to even 6.3% in the sample with 2.5 wt% RGO. Because of higher surface area, the $Fe-C$ bond concentration is higher in the sample containing smaller wt% RGO. As discussed later, this variation influences the magnetic properties significantly.

[137]
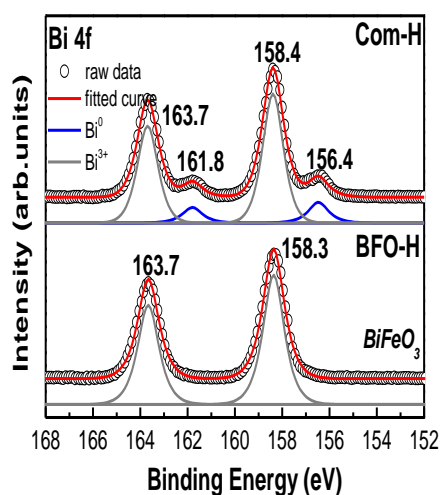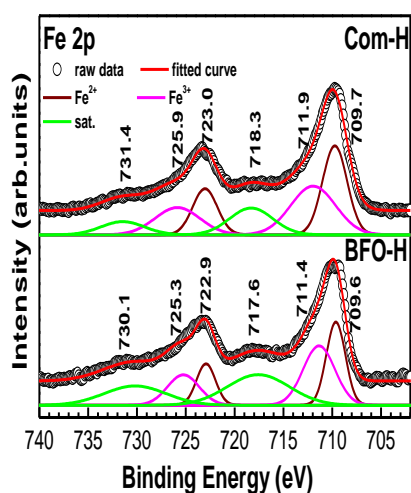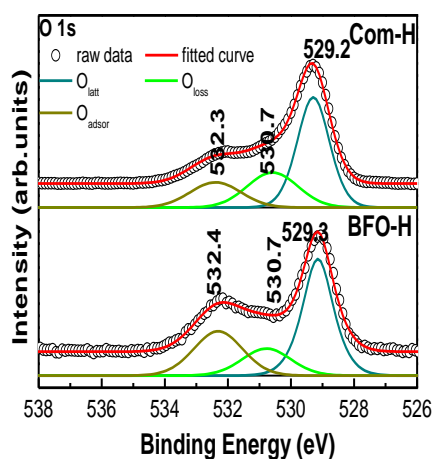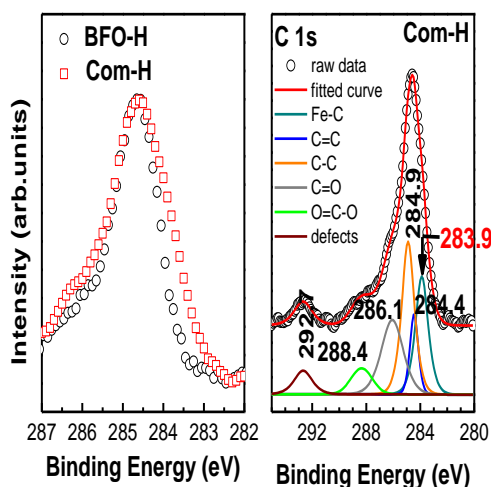
Figure 4.2 X-Ray photoelectron spectra and their fitting for (a) Bi 4f, (b) Fe 2p, (c) O 1s and (d) C 1s in pure BFO (BFO-H) and composite (Com-H) systems
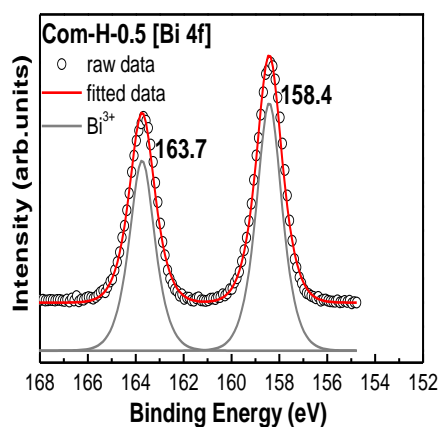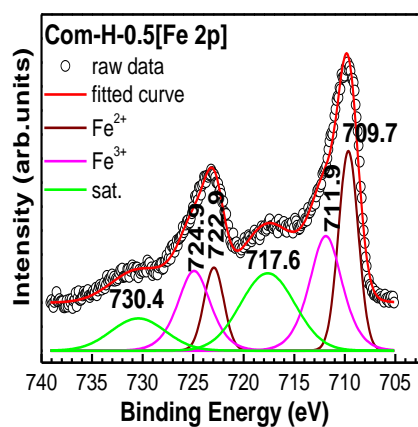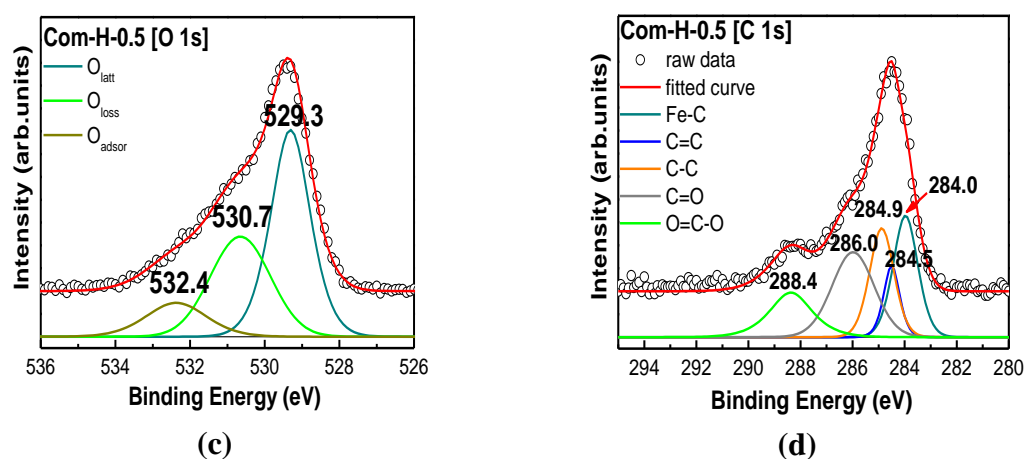
Figure 4.3 X-Ray photoelectron spectra and their fitting for (a) Bi 4f, (b) Fe 2p, (c) O 1s and (d) C 1s in composite Com-H-0.5 systems
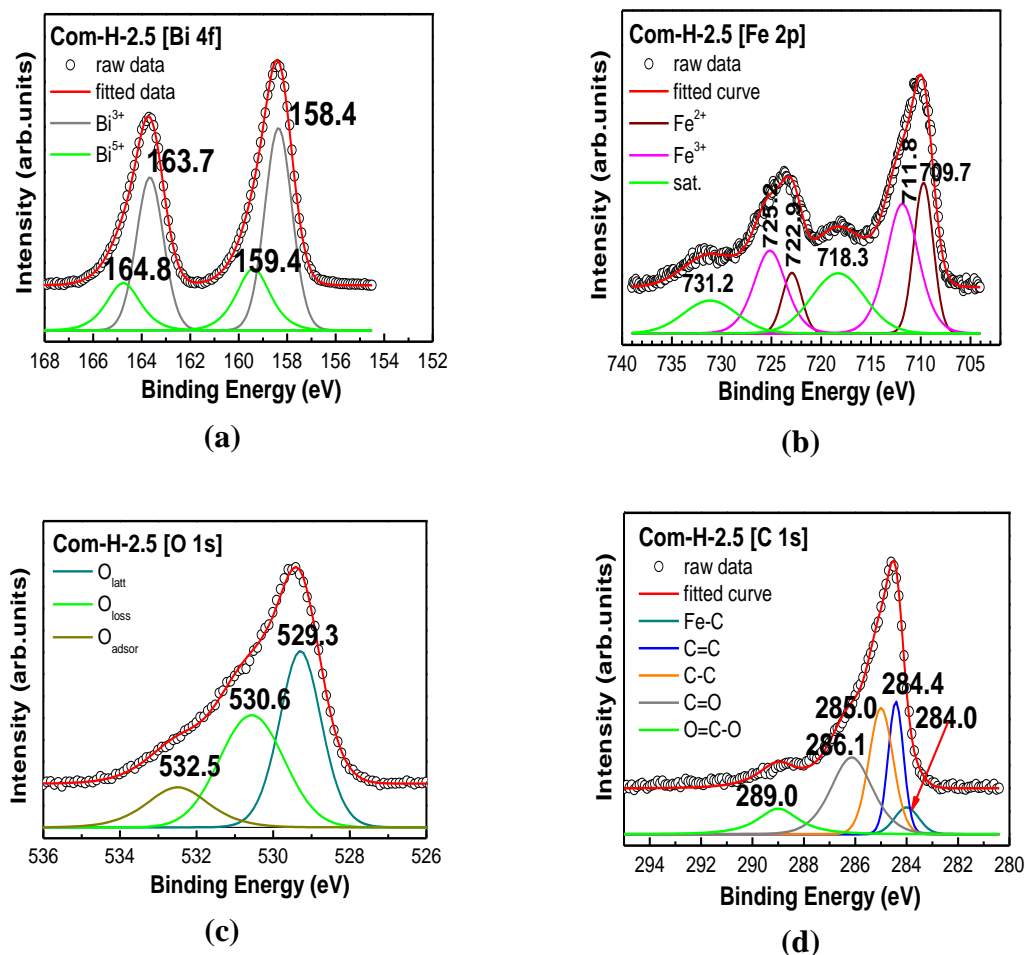
Figure 4.4 X-Ray photoelectron spectra and their fitting for (a) Bi 4f, (b) Fe 2p, (c) O 1s and (d) C 1s in composite Com-H-2.5 systems

[139]

Table 4.1 Percentage of Bond calculations from C1s data XPS from Com-H and GO			
Bonds	**Center**	**Area**	**% of bonds**
Com-0.5 wt%			
Fe-C	284.0	0.644	24.3
C=C	284.5	0.251	9.5
C-C	284.9	0.569	21.5
O-C-O	286.0	0.758	28.6
O=C-O	288.4	0.427	16.1
Defects	-	-	-
Com-2.5 wt%			
Fe-C	284.0	0.138	6.3
C=C	284.4	0.435	19.8
C-C	284.9	0.652	29.7
O-C-O	286.1	0.71	32.4
O=C-O	289.0	0.259	11.8
Defects	-	-	-
Com-1.5 wt% (Com-H)			
Fe-C	283.9	441.240	22.7
C=C	284.5	188.074	9.7
C-C	284.9	564.678	29.0
O-C-O	286.1	459.962	23.7
O=C-O	288.3	159.504	8.2
Defects	292.7	131.099	6.7
GO			
C=C	284.5	0.640	35.9
C-C	285.0	0.467	26.2
O-C-O	286.6	0.470	26.4

O=C-O	289.3	0.206	11.5

4.2.3 **Magnetic property analysis:**

4.2.3.1 **M-H Study at room temperature:**

The room-temperature magnetization (M) versus field (H) hysteresis loops for Com-H and BFO-H are discussed in previous chapter which is contrary to the prediction made in the case of graphene/$BaMnO_3$, the ferromagnetic component is found to have weakened in Com-H. The magnetization (M) does not tend to saturate within the applied field limit (20 kOe). The coercivity (H_C), of course, turns out to be much larger in Com-H. It is well known now that, for BFO, the nano particles exhibit enhancement in the ferromagnetic component because of larger spin canting and incomplete spin spiral (this is effective in particles smaller than 62 nm, the wavelength of the spin spiral in BFO). It has been shown[12] from the powder neutron diffraction experiment that the canting angle could enhance to6° (from 1° in bulk sample [12]) in particles of size 25 nm. In the present case, variation of the ferromagnetic component could result from the change in the charge states of ions and the formation of $Fe-C$ bonds at the RGO/BFO interface inCom-H. The Fe–C exchange coupling interaction (which leads to exchange splitting of the Dirac bands in graphene layer as well as renormalization of the Fe moments in the interface; exchange field was shown[2, 3] to be of the order of 10–100 T at the BFO/graphene interface) possibly gives rise to the renormalization of the exchange coupling parameters at the bulk as well which, in turn, could give rise to drop in the spin-canting angle. The ferromagnetic component, therefore, weakens. Interestingly, inspite of weakening of the ferromagnetic component, the coercivity (H_C) turns out to be larger in Com-H. The pinning of domains by defects appears to be stronger in Com-H. Because of the surface ferromagnetism and core anti-ferromagnetism, a small amount of exchange bias field (H_E) could also be observed ($H_E = 31$Oe and25 Oe, respectively, for BFO-H and Com-H).

We have also examined the magnetic properties of the nano composites containing 0.5 and 2.5 wt% RGO as seen in Figure 4.5. Interestingly, the parameters such as magnetization at 20 kOe field M_{20kOe}, coercivity H_C, remanent magnetization M_R, and the shape of the room-temperature magnetic hysteresis loop vary significantly. In Table 4.2, we show the parameters. The change in the loop shape results from change in magnetic anisotropy. Using Akulov function we could calculate the overall magnetic anisotropy K as follows:

$$M(H) = M_s \left[1 - \frac{1}{15}\left(\frac{H_a}{H}\right) \right]$$

$$H_a = \frac{2K}{M_s}$$

[141]

Where, M_s is the saturation magnetization.

The results are seen in Figure 4.6. Clearly, large variation in K reflects influence of the variation in the interface region in the nano composites containing different wt% RGO. Combining the results obtained from the XPS and the magnetic hysteresis loop measurements, it is possible to observe that from pure BFO to nano composites of BFO/RGO containing different wt% RGO, the magnetic properties, such as hysteresis loop shape, anisotropy, H_C, M_R, M_{20kOe}, exhibit direct correlation with the concentration of the Fe─C bonds.

(a)   **(b)**
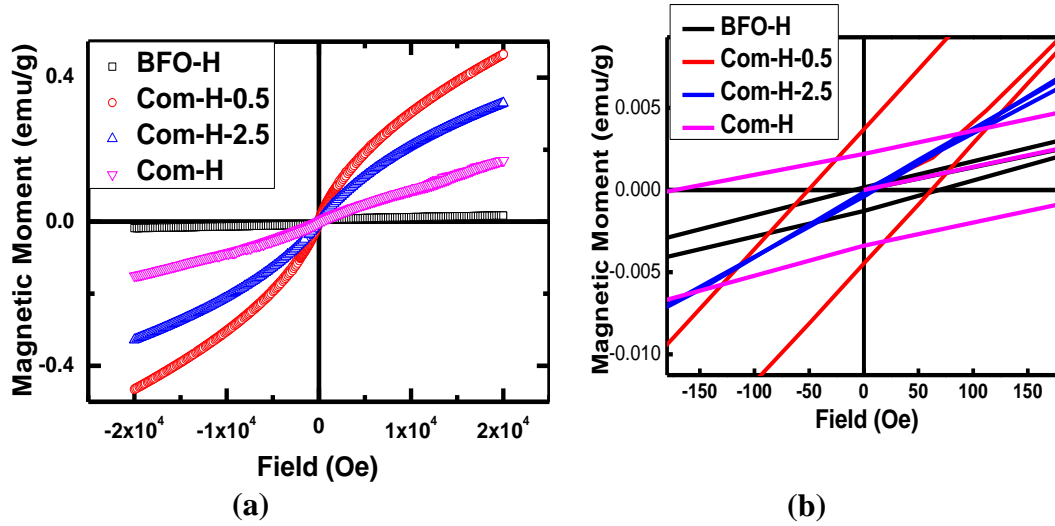
Figure 4.5 The room temperature magnetic hysteresis loops for BFO-H and all the composites of 0.5wt%, 2.5wt% and 1.5 wt% (Com-H)

(a)   **(b)**

[142]
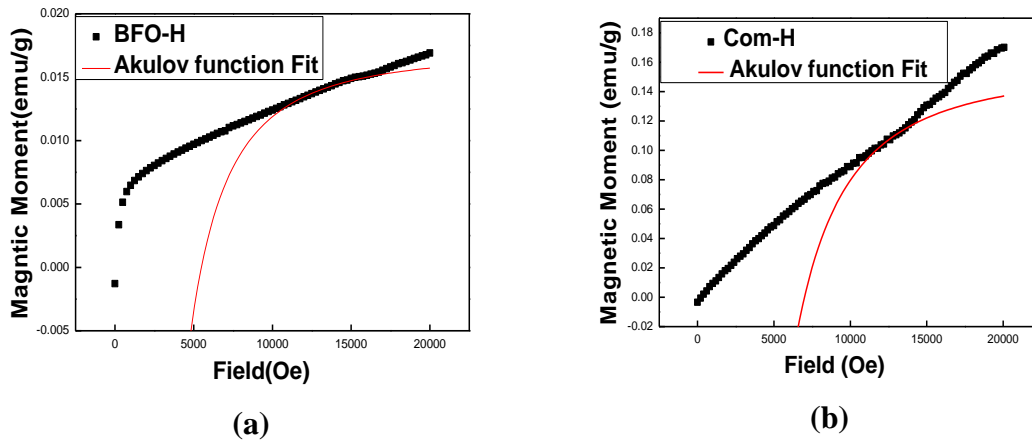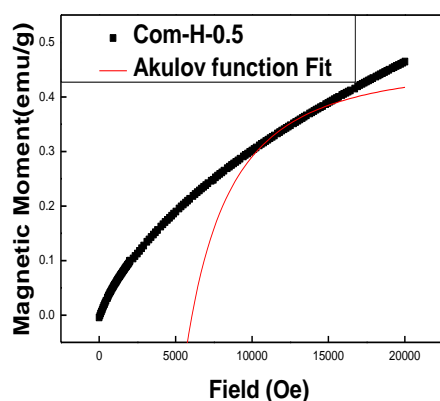
(c)
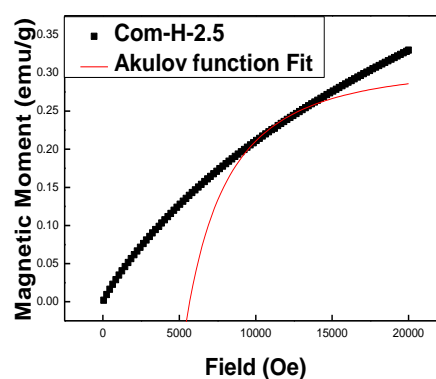
(d)

Figure 4.6 The fitted Akulov function to the room temperature magnetic hysteresis loops in the region 0-2T for BFO-H and all the composites of 0.5wt%, 2.5wt% and 1.5 wt% (Com-H)

Table 4.2 Summary of parameters calculated from M-H loop of all the samples							
Sample	**Coercivity (H_c) in Oe**	**Exchange Bias (H_e)in Oe**	**Moment M_{s2T} inemu/g**	**Remanent moment (emu/g)**		**Critical field (H_a) in Oe**	**An-isotropy K_I**
				M_r	**$-M_r$**		
BFO_H	38.33	30.76	0.017	1.58E-4	-0.0013	21250	180.625
Com-H-0.5	57.51	-0.26	0.467	0.00041	-0.0041	23535	5413.05
Com-H	-204.89	37.43	0.171	0.0022	-0.0034	27100	2303.5
Com-H-2.5	-3.18	6.67	0.33	0	0	22000	3421

4.2.3.2 Magnetic properties at low temperature

DC magnetic measurements have been carried out with external magnetic field 500 Oe in the wide temperature range of 5K to 300K. M (T) measurements are recorded at two different modes zero field cooled (ZFC) and field cooled (FC). The Figure 4.7(a) shows the Magnetization vs Temperature plot from 5K to 300K and the susceptibility vs temperature plot is shown in Figure 4.7 (b). The nature of the curve signifies antiferromagnetism with transition like feature near 50K. The ZFC and FC curves do not coincide till room temperature.

This indicates that the blocking temperature (T_B) is at above room temperature. The M-H loops at various temperatures such as 50K, 150K and 300K are shown in Figure 4.7(c). The changes in coercivity with various temperatures are shown in Figure 4.7(d) and are summarized in Table 4.3. Here we have seen an interesting feature that both the coercivity and exchange bias change with temperature anomalously. They first decreases and then rise again with rise in temperature. This is useful for spintronics application.
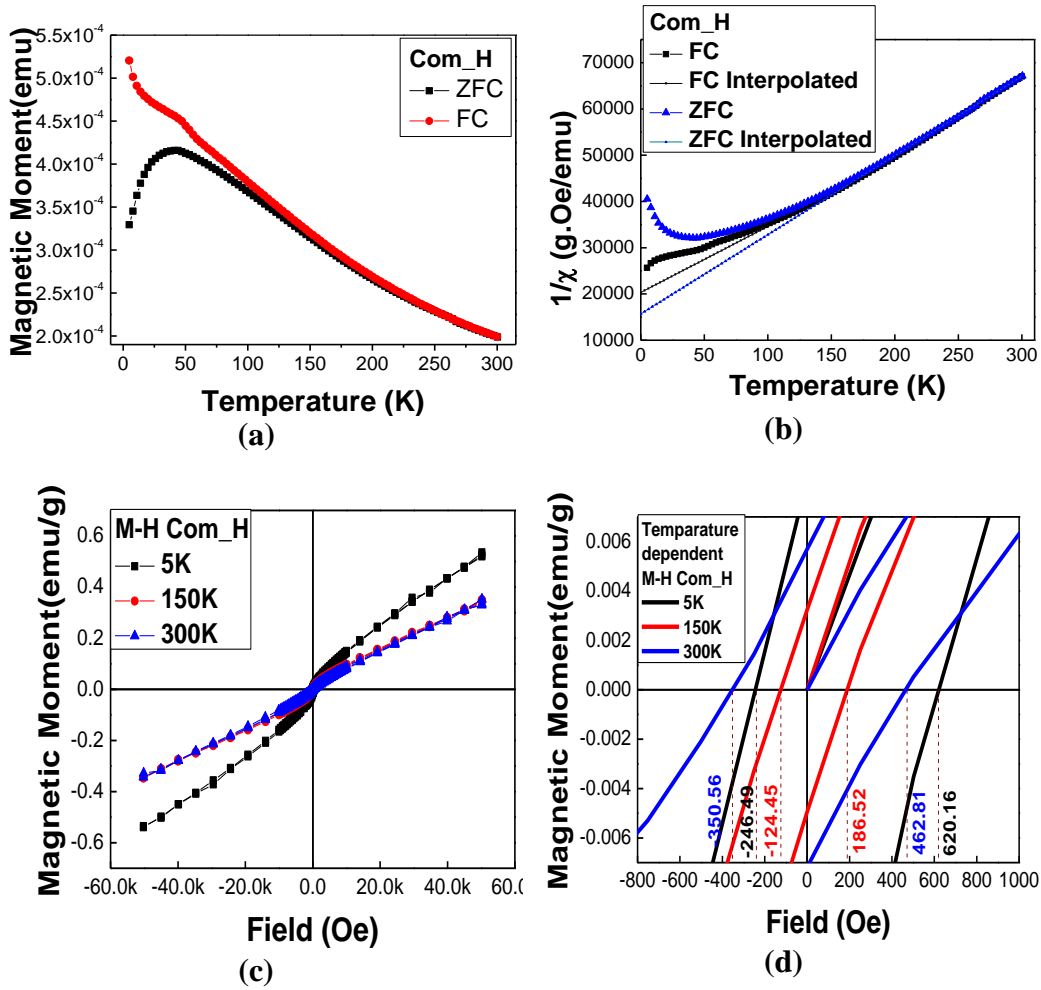
Figure 4.7 (a) Temperature (T) vs Magnetic Moment plot from 5K to 300K; (b)Reciprocal of Susceptibility (1/χ) vs T plot; (c)M-H loop at temaparure 5K, 150K & 300K; (d) Temperature dependent coercivity and exchange bias changes are shown of Composite

Table 4.3 Summary of coercivity and Exchange bias Calculated of Com_H at various temperature					
Sample	H_{c1}	H_{c2}	Coercivity (H_c) in Oe[$|H_c|= (H_{c1}-H_{c2})/2$]	Exchange Bias (H_e)in Oe [$|H_e|= (H_{c1}+H_{c2})/2$]	Moment Ms_{5T} inemu/g
5K	-	620.16	433.32	186.83	0.52

[144]

	246.49				
150K	-124.45	186.52	155.48	31.04	0.34
300K	-350.46	462.81	406.68	56.13	0.33

4.2.4 <u>Temperature dependent ferroelectric polarization study under different magnetic fields:</u>

We have performed the Ferro electric polarization measurement under different magnetic field at the temperature range over a temperature range 190K-300K. At any given tememperature within the 190-300K range the Ferroelectric polarization changes non monotonically with varying magnetic field. The remanent polarization (under different magnetic field) is plotted as a function of temperature in Figure 4.8. The remanent value was calculated from PUND protocol. The graph shows there is gradual decrease in remnant value with increasing temperature from low to high.
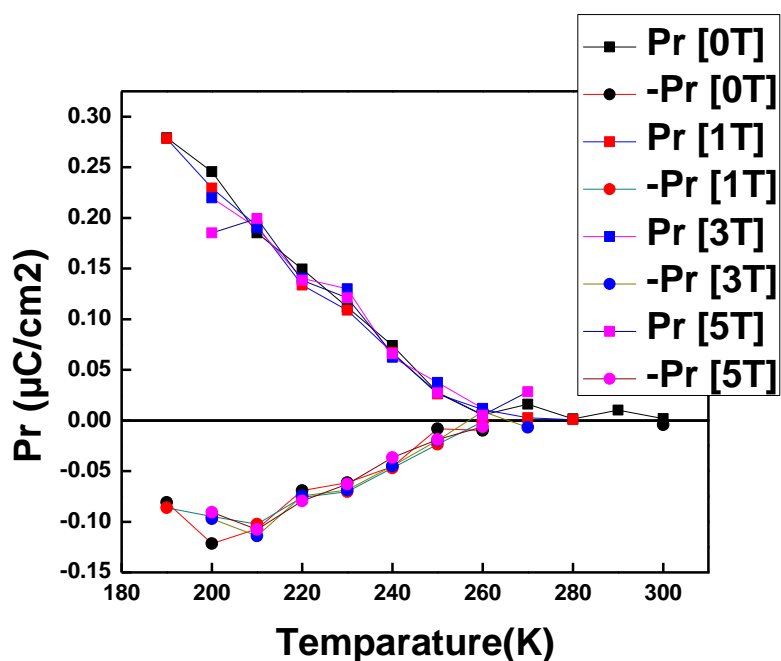
Figure 4.8 Temperature dependence of remanent Ferroelectric polarization plotted at different magnetic field

4.2.5 <u>Magneto-dielectric study of rGO/BiFeO₃ nano composite</u>

Here we have also performed the Dielectric measurements under different magnetic field to analysis the magneto-dielectric properties of this composite. Hence we have measured some

parameters such as dielectric constant (D), specific heat capacity at constant pressure (C_p), impedance (Z) and phase angle (φ). Those parameters were measured using HIOKI LCR meter under different magnetic field from 0T to 2T under the frequency range of 10Hz to 1MHz. measured parameters are dielectric constant, specific heat capacity at constant pressure, impedance and phase angle respectively. From where we have calculated the real and imaginary part of impedance Z' and Z" as follows,

$$Z' = |Z|cos\varphi \text{ And } Z'' = |Z|sin\varphi$$

Moreover from the impedance parts we have calculated the real and imaginary part of dielectric permittivity as follows,

$$\epsilon' = \frac{|Z''|}{2\pi f(Z'^2 + Z''^2)} \text{ and } \epsilon'' = \frac{|Z'|}{2\pi f(Z'^2 + Z''^2)}$$

Both the real and imaginary part of permittivity (ϵ' and ϵ'' respectively) values decreases with increasing frequency. At low frequency, the permittivity values consist of contributions from the interfacial polarization, which can be explained by Maxwell-Wagner theory. The heavier dipoles are able to follow the external field at low frequency, so that values are higher. As the frequency starts to increase, the dipoles lag behind the field and ϵ value decreases. Here, tan δ values of the order $5E10^{-2}$ are achieved at frequency greater than 10 kHz. For clear view the magnetic dependence of dielectric constant (D) and loss tangent (tanδ) is plotted in Figure 4.9(c) and Figure 4.9(d) at various frequencies. To understand the nature of dielectric relaxation in these composite, complex Argand plane plot, also known as Cole-Cole plot, was examined and plotted as (ϵ' vs ϵ'') under different magnetic fields. The Bode plot under different magnetic field is also plotted at Figure 4.9(a). There is distinct difference between 0T and magnetic field driven Cole-Cole plot. The loss tangent (tanδ) and percentage change of Dielectric constant (D) shows a non monotonic change with increasing of magnetic field. But at higher frequency there is a certain jump seen after 1.5T at 100 kHz and 1 MHz. the similar jump is seen after 1.5T for all frequencies 100Hz to 1MHz for C_p plot (Figure 4.9(e)). There are certain interesting features have been observed in magneto-dielectric study which need further study for justification.

(a)

(b)
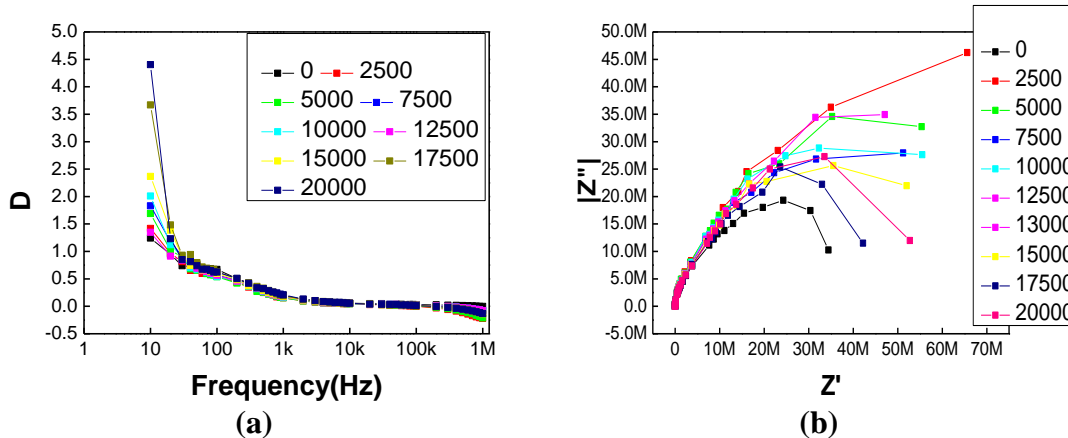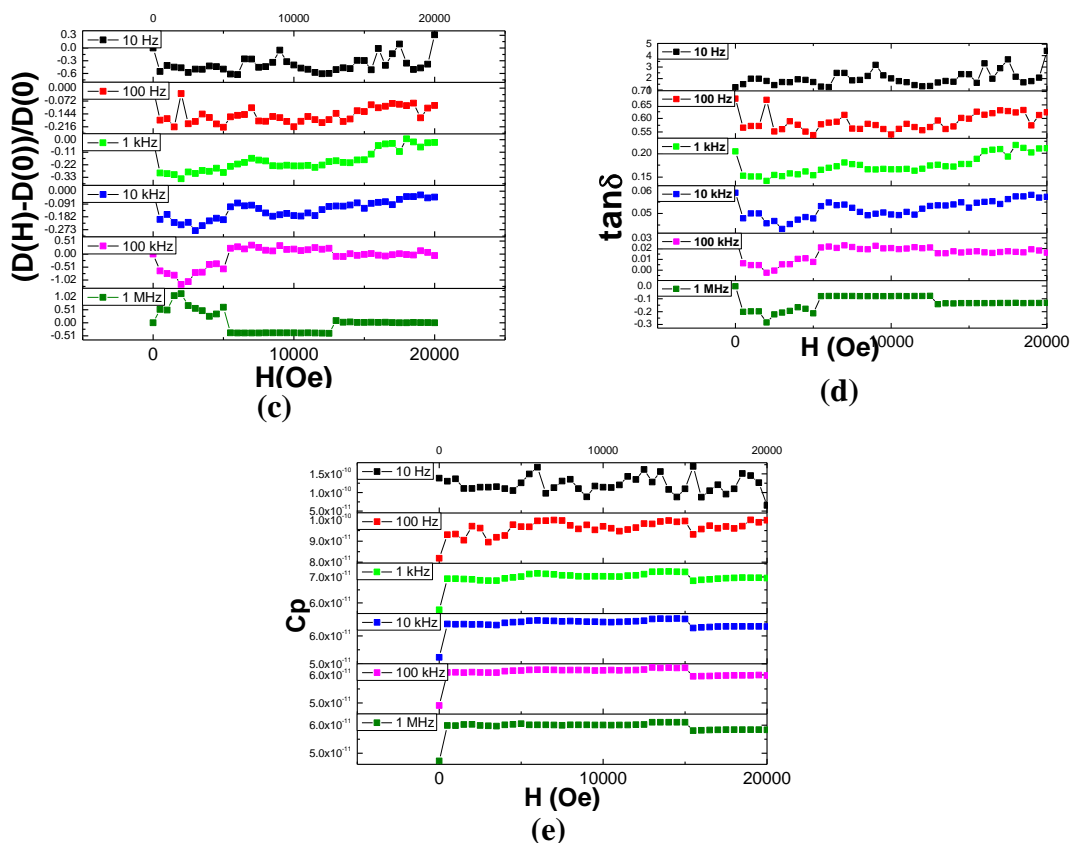
Figure 4.9 (a) Bode Plot, (b) Cole-Cole plot, variation of loss tangent (c), specific heat(d), percentage change of dielectric constant (e) vs magnetic field data under different frequencies

4.2.6 **Magnetoelectric Study**

We also used the positive-up-negative-down (PUND) [13] and remanent ferroelectric hysteresis loop protocols[14]for the direct electrical measurement of remanent polarization (P_R) on an assembly of nano particles.

4.2.6.1 **Magnetoelectric Study using Remanent Protocol:**

To investigate magnetoelectric coupling ferroelectric polarization of the sample was measured under Magnetic field ranging from 0T to 2T and have seen a strange coupling. Upon increasing Magnetic field the remanent ferroelectric polarization (P_R) oscillates as seen from Figure 4.10.

[147]
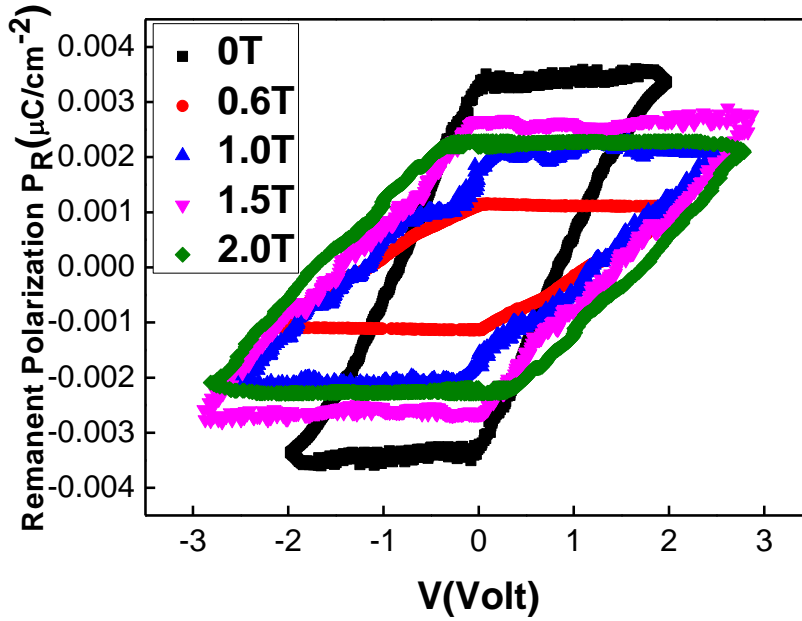
Figure 4.10 Polarization obtained from remanent polarization measurement protocol for Com-H under different magnetic field

4.2.6.2 Magnetoelectric Study using PUND Protocol:

To investigate magnetoelectric coupling the ferroelectric polarization of the sample was measured under Magnetic field ranging from -2T to 2T. The magnetoelectric coupling measured using PUND protocol is shown in Figure 4.11

PUND [positive (P), up (U), negative (N), and down (D)] protocol consists of five pulse sequences such as preset pulse, positive switched pulse (P*), positive non-switched pulse (P^), neative switched pulse (-P*) and negative non-switched pulse (-P^). Eliminating the P^ contribution from the P* contribution gives the positive remanent polarization. Similarly from the negative part [N: (-P*), D: (-P^)] we have the negative remanent part. The difference between switched and non- switched pulse gives the value of twice the value of remanentpolarization . This value equals the remanent polarization.

$$dP = P* - P^\wedge = 2P_r$$

The PUND protocol enable us to measure the parameters dP, dPr, -dP, -dPr. The Remanent Polarization is calculated as, $Pr = (|dP| +/2)$.

The changes in remanent value wrt magnetic field under repetitive cylcles are shown in Figure 4.12.This is may be due to the presence of magnetic anisotropy in this nano composite.

[148]
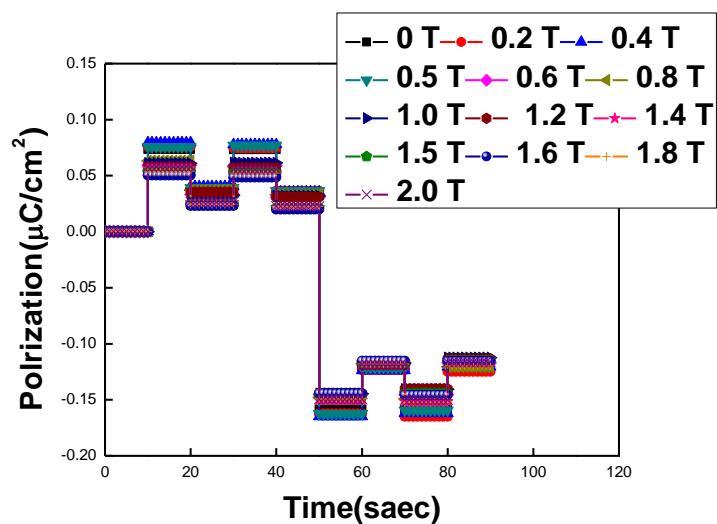
Figure 4.11 Polarization profile obtained from PUND protocol for Com-H under different
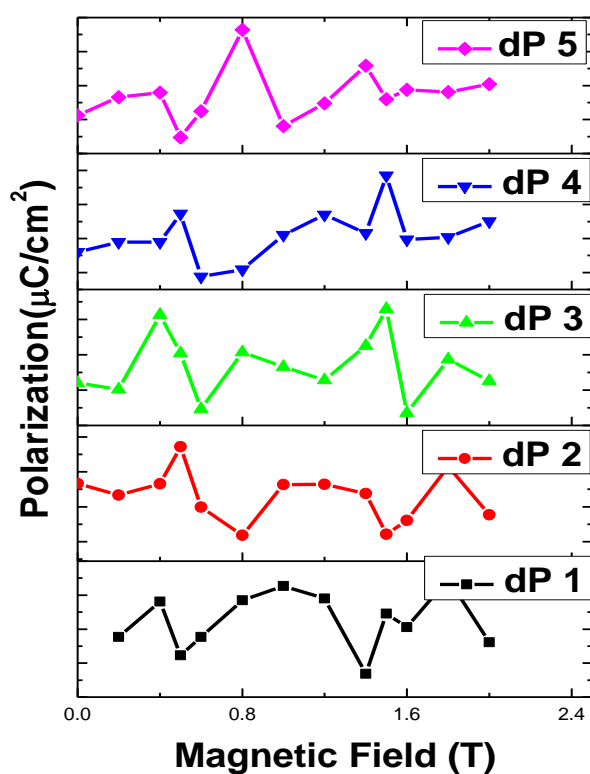
Figure 4.12 Remanent Polarization value wrt magnetic field under repetitive cycles

[149]

4.2.7 <u>Neutron diffraction study</u>

Multiferroicity in the BFO/RGO nano composite was further examined by powder neutron diffraction experiments. The neutron diffraction data were recorded on the Com-H sample at room temperature under different magnetic fields across 0–20 kOe. We considered collinear spin structure. Long spiral length (62nm) in BFO allows such consideration. The data were refined by FullProf by considering the R3c space group and Γ_1 irreducible representation (propagation vector $\vec{k} = 0$). Group theory analysis of the spin structure for $R3c$ and propagation vector $\vec{k} = 0$ yields three irreducible representations: Γ_1, Γ_2 and Γ_3 (reducible representation **$\Gamma(\mathbf{Fe, 6a}) = \Gamma_1 + \Gamma_2 + 2\Gamma_3$**. Refinement shows that Γ_1 (G-type antiferromagnetic structure) offers the best fitting. The refinement is shown in Figure 4.13. The lattice parameters, magnetic moment, ion positions, and the fit statistics are included in the Table 4.4.

The variation of lattice parameters and spin parameters are shown in Figure 4.14 (a) and (b). The plots of positions of bismuth, iron, and oxygen ions as a function of magnetic field as obtained from refinement of neutron diffraction data are shown in Figure 4.14(c) & (d). The variation of the magnetic moment along c-axis (c_3) with the applied magnetic field together withthe collinear spin structure corresponding to Γ_1 is shown inFigure 4.15. The non-monotonic field dependence of $c_3$possibly reflects field-dependent competition between interface and bulk magnetization and consequent renormalization of the average bulk magnetic moment calculated from powder neutron diffraction by considering collinear G-type spin structure Γ_1.

Interestingly, the lattice volume (V_L) is found to decrease andthen increase (Figure 4.15), indicating switch from negative to positive magneto-striction as the applied magnetic field is enhanced across 0–20 kOe. This could be (as discussed later) due to field dependent competition between bulk and surface/interface magnetic anisotropy. The anti-correlation between c_3 and V_L is notable. While $c_3(V_L)$ increases (decreases) with increase in applied field (H) initially, they exhibit a converse trend there after (Figure 4.15). Such anti-correlation has not been reported in pure BFO.

The average bonds lengths of Bi-O and Fe-O are calculated from refinement are also plotted against magnetic field in Figure 4.16(a). It shows the perfect mirror image to each other that means when $BiO6$ octhedra squeezes then $FeO6$ octahedra enhances and vice-versa.

We have also plotted the magnetic field dependence of the lattice constants and the rotation angle (φ) of the oxygen octahedron along the c axis. The oxygen octahedral distortion parameter d is related to the distortion of the $FeO6$ octahedra parallel to the $[001]_{hex}$ axis, whereas the parameter e is linked to the antiferrodistortive rotation of the octahedra by the angle Φ about the $[001]_{hex}$ axis by,

$$2e\sqrt{3} = \tan\Phi.$$

The parameters d and e are calculated as follows,

$$d = \frac{4z - y}{4}$$

$$e = \frac{2x - 2d - x}{2}$$

The octahedral strain parameter is calculated as,

$$\eta = c_{hex} \cos\varphi / a_{hex} \sqrt{6}$$

Where, η= 1, < 1, and > 1 are represented as regular, compressed, and elongated oxygen octahedra along the [001]hex axis, respectively .

The Figure 4.17 (a) shows the plot of distortion parameter and Figure 4.17 (b) shows the plot of φ and η vs magnetic field. In all magnetic field the d and η are both positive and $\eta<1$. Hence the composite system is compressed in nature. The d value follows the trend of ΔBi.

We finally discuss the results of the measurement of intrinsic structural off-centering by high-resolution powder neutron diffraction under different magnetic fields. The net off-centering within a unit cell was estimated from the off-centering of Bi and Fe ions (s and t, respectively) along the polarization axis[001]$_{hex}$ in the hexagonal setting as well as from off-centering of the Bi and Fe ions with respect to their oxygen cages. Both the results are summarized in Table 4.5 and **Error! Reference source not found.** which are plotted in Figure 4.16 (b). It is important to point out here that high-resolution neutron diffraction is more effective than XRD in determining the crystallographic structure (including ion positions) which contains lighter ions such as oxygen. The magnetic field (H) dependence of net off-centered displacement(δ) in the unit cell, estimated from the powder neutron diffraction data, is plotted in Figure 4.18 along with remanent polarization values obtained from remanent and PUND protocol both. Interestingly, δ exhibits non-monotonic pattern of variation with the magnetic field (H) across 0–20 kOe. The result corroborates the one obtained from direct electrical measurement (described earlier in this chapter).

(a)

(b)

[151]

(c)

(d)

(e)
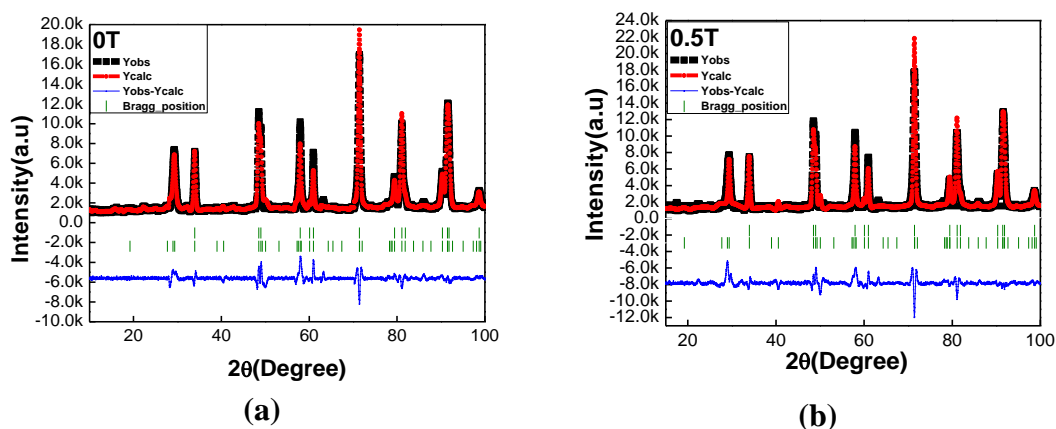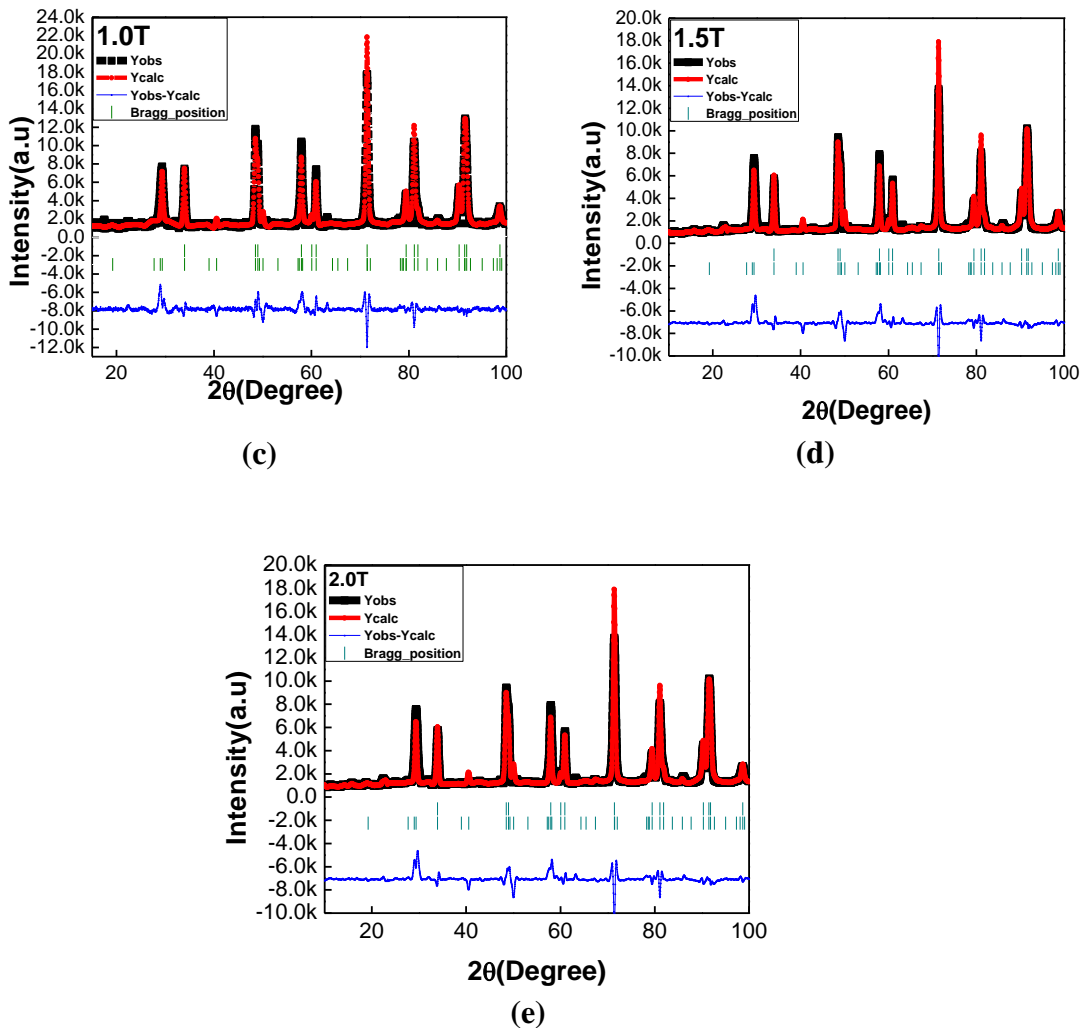
Figure 4.13 Powder neutron diffraction data and their refinement by FullProf; R3c and Γ1 phases have been considered; the data were recorded at room

(a)

(b)
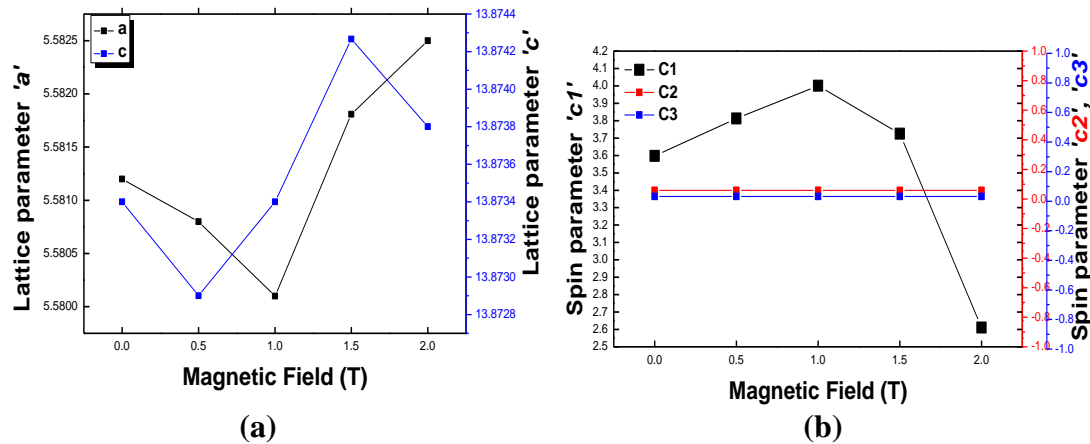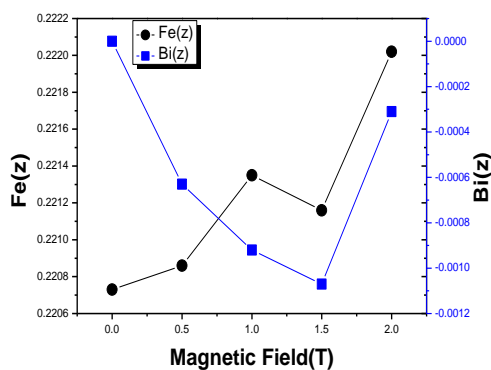
(c)
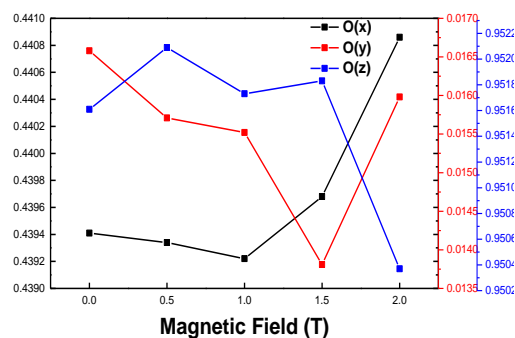
(d)

Figure 4.14 (a) Variation of lattice parameters (a and c); (b)Variation of Spin parameters c1, c2, c; (c) Variation of z coordinates of ion positions of Bi and Fe; (d)Variation of x, y and z coordinate of ion positions of O; with magnetic field
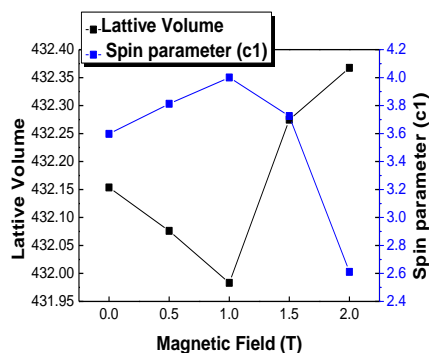
(a)
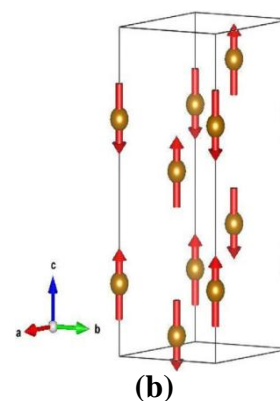
(b)

Figure 4.15 (a) Variation of lattice volume and spin along Γ_1 axis wrt magnetic field; (b)Variation of Spin parameters (b)The spin structure corresponding to Γ_1 irreducible representation
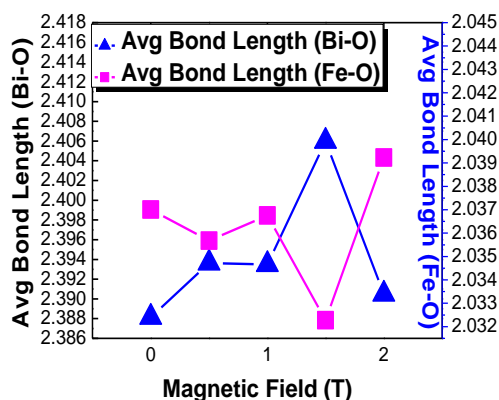
(a)
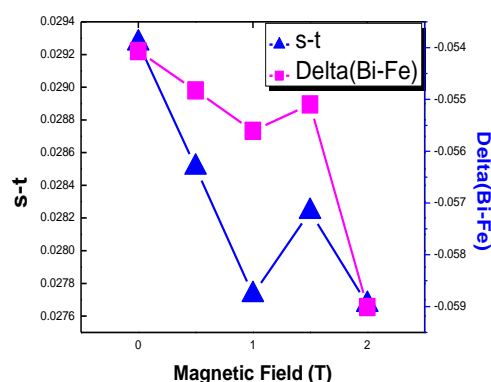
(b)

Figure 4.16 (a) Average bond length variation of both Bi-O and Fe-O; (b) The variation of unit cell off-centered displacement, 's-t' (left axis), and net off-centering with respect to the oxygen cages (right axis) obtained from refinement of powder neutron diffraction data

[153]
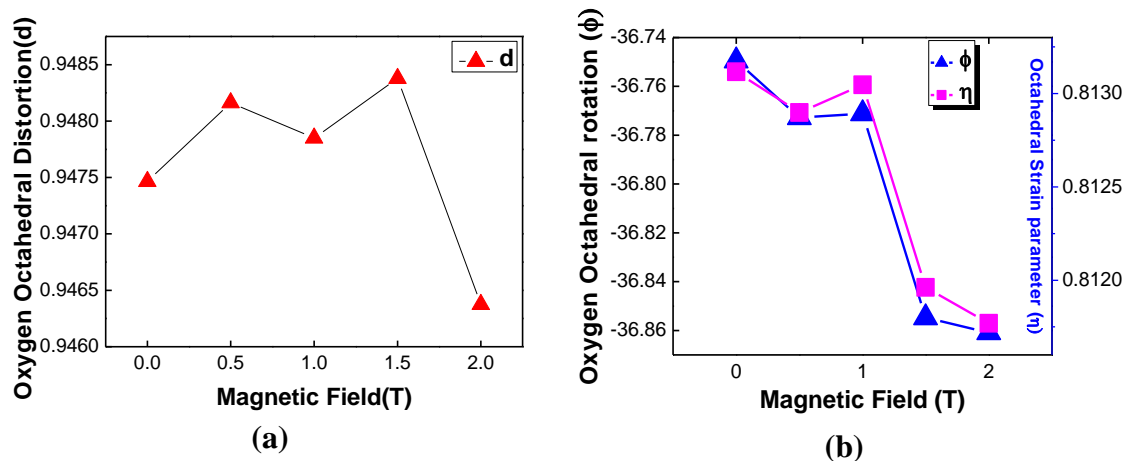
Figure 4.17 Variation of (a) Oxygen octahedral distortion and (b) Oxygen octahedral tilt and rotation wrt magnetic field
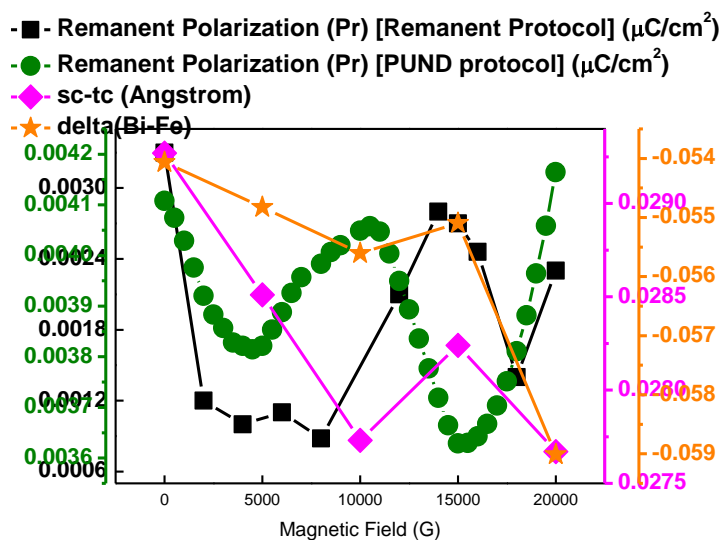
Figure 4.18 Variation of normalized remanent polarization obtained from remanent protocol (left inner axis) and PUND protocol (left outer axis) with applied magnetic field; variation of off-centre displacement (sc-tc) (right inner axis) and d (right outer axis) – obtained from refinement of powder neutron diffraction data – with magnetic field.

Ion Pos	x	y	z	Occ	Lattice Parameters		Spin Parameters	
Table 4.4 Refinement fitted Neutron data of Com_H under various magnetic fields								
Field: 0T **Rp**= 23.1, **Rwp**= 20.8, χ^2=19.05								
Bi	0	0	0	0.33793	**a**	5.5812	**c1**	3.598

Fe	0	0	0.22073	0.32824	**b**	5.5812	**c2**	0.058
O	0.43941	0.01658	0.95161	1.03101	**c**	13.8734	**c3**	0.032
Field: 0.5T **Rp**= 24.4, **Rwp**= 22.0, χ^2= 23.44								
Bi	0	0	-0.0006	0.35078	**a**	5.5808	**c1**	3.813
Fe	0	0	0.22086	0.33876	**b**	5.5808	**c2**	0.058
O	0.43934	0.01571	0.95209	1.05478	**c**	13.8729	**c3**	0.032
Field: 1.0T **Rp**= 24.1, **Rwp**= 22.8, χ^2=25.23								
Bi	0	0	-0.0009	0.34899	**A**	5.5801	**c1**	4.001
Fe	0	0	0.22135	0.33631	**b**	5.5801	**c2**	0.058
O	0.43922	0.01552	0.95173	1.04899	**c**	13.8734	**c3**	0.032
Field: 1.5T **Rp**= 21.0, **Rwp**= 22.6, χ^2=21.85								
Bi	0	0	-0.0011	0.30978	**a**	5.581808	**c1**	3.725
Fe	0	0	0.22066	0.31841	**b**	5.581808	**c2**	0.058
O	0.43968	0.01381	0.95183	0.98148	**c**	13.874267	**c3**	0.032
Field: 2.0T **Rp**= 33.8, **Rwp**= 25.7, χ^2=9.26								
Bi	0	0	-0.0003	0.3383	**a**	5.5825	**c1**	2.611
Fe	0	0	0.22202	0.33008	**b**	5.5825	**c2**	0.058
O	0.44086	0.01598	0.95037	1.00958	**c**	13.8738	**c3**	0.032

Table 4.5 Crystallographic Ferroelectric polarization calculations from ion Position along [001]c axis

Field (T)	Pos of Bi and O in BiO$_6$Octahedra		Non centro symmetry position of Bi (δBi)	Pos of Fe ad O in FeO$_6$Octahedra		Non centro symmetry position of Fe (δFe)	|δBi-δFe|
	Pos(Bi)	COP (O)		Pos(Fe)	COP (O)		
0	0.5	0.534945	-0.03495	0.72073	0.70161	0.01912	0.054065
0.5	0.49937	0.535425	-0.03606	0.72086	0.70209	0.01877	0.054825
1	0.49908	0.535065	-0.03599	0.72135	0.70173	0.01962	0.055605
1.5	0.4989	0.535165	-0.03627	0.72066	0.70183	0.01883	0.055095
2	0.49969	0.53705	-0.03736	0.72202	0.70037	0.02165	0.05901

Table 4.6 Crystallographic Ferroelectric polarization calculations from ion Position along [001]c axis

Magnetic Field (T)	Pos of Ion along [001]$_c$ axis				Shift of ion position of		Crystallographic calculation of FE polarization
	O[f] (i)	Bi (j)	Fe (k)	O[l] (l)	Bi[s= j-i]	Fe[t= (k-i)-0.25]	s-t
0	-0.04839	0	0.22073	0.95161	0.04839	0.01912	0.02927
0.5	-0.04791	-0.00063	0.22086	0.95209	0.04728	0.01877	0.02851
1	-0.04827	-0.00092	0.22135	0.95173	0.04735	0.01962	0.02773
1.5	-0.04817	-0.0011	0.22066	0.95183	0.04707	0.01883	0.02734
2	-0.04963	-0.00031	0.22202	0.95037	0.04932	0.02165	0.02767

4.2.8 <u>Discussion</u>

Interestingly, in spite of the influence of several factors such as the presence of surface defects, poor particle–particle electrical connectivity, poor electrode–nano particle connectivity,

etc., the net magnetic field dependence of P_R turns out to conform to the non-monotonic pattern obtained from the analysis of powder neutron diffraction data. The non-monotonic nature of P_R-H in RGO/BFO nano composite, therefore, is intrinsic. Pristine BFO, on the contrary, exhibits monotonic suppression of P_R with the increase in magnetic field because of negative magnetoelectric coupling[9]. Stabilization of the $R3c$ structure in BFO yields coupling of polarization and magnetization via coupling between polar distortion and antiferrodistortion of $FeO6$ octahedra. It has been demonstrated[15] that indeed the deterministic 180° switching of magnetic domains takes place (as a result of that of the ferroelectric domains) under electric field in two steps, first, in-plane rotation by 71° and then out-of-plane rotation by 109°. Piezo- and magneto-striction associated with this complex pathway of domain rotation influences the magnitude of the polarization and magnetization of the domains.

As the magnetic field is swept from zero to a maximum, negative magnetoelectric coupling (arising from influence of negative magneto-striction on piezo-striction) in pure BFO yields decrease in polarization with increase in magnetization9.Suppression of polarization under magnetic field was observed not just in bulk form of the sample but in nano scale samples as well[1617].The bulk and surface magneto crystalline anisotropy (K_B and K_S) results in negative bulk and surface magnetostriction (λ_B and λ_S) in nano scale BFO, assuming $R3c$ structure. Negative magneto-striction leads to negative magnetoelectric coupling, that is, suppression of polarization under magnetic field. In an assembly of single-crystalline nano particles, averaging over the domain configurations and the properties, therefore, yields similar decrease (increase) in polarization (magnetization) at any given state. This magneto-strictive suppression of piezo-striction, observed in pure BFO, can be altered and consequent enhancement of magneto-striction driven polarization is possible. In BFO/reduced graphene oxide nano composite, emergence of Fe—C bonds (from strong hybridization of $3d_{x^2-y^2} = 3d_{z^2}$ orbitals of Fe and p_z orbitals of C) and consequent magnetization at the graphene−BFO interface regions open up this possibility. It has already been shown[318]that the $Fe—C$ bonding leads to the generation of a large exchange field(of the order of 10−100 T) which gives rise to the split of the Dirac bands in the graphene layer as well as proximity-induced magnetization. This exchange field alters the magnetization at the interface reflected in the enhancement of the anti-ferromagnetic component in RGO/BFO nano composite. Change in the magnetic moment at the interface was earlier predicted by theoretical calculations [19].The anisotropy (K_I) associated with this interfacemagnetization could yield positive surface magnetostriction.This, in turn, could give rise to the rise in P_R with H, that is, positive magnetoelectric coupling. It has been shown[20]earlier that indeed the ratio of surface/interface anisotropy and bulk anisotropy$\left(K_I / K_B \right)$ governs the spin structure significantly. A different structure emerges as K_I or K_S increases with respect to K_B . Therefore, different spin structures at the interface change the magnitude of K_I

with respect to that of K_B, which, in turn, yields positive interface magneto-striction. Field-dependent switch from negative to positive magneto-striction has indeed been observed in the present case (Figure 4.15). The mapping of lattice volume (V_L) with the applied magnetic field (Figure 4.15) shows decrease and then increase in V_L as the field is swept across 0–20 kOe. This observation underlines the important role of interface magnetization arising from the $Fe-C$ bonds. Of course, how K_I, in the present case, yields positive interface magnetostriction and how the ratio $\left({K_I}/{K_B}\right)$ governs the field dependent switch in magnetostriction, from negative to positive, have to be studied in detail separately. Based on earlier discussion, in Figure 4.19, we present the schematic of the model which describes the physics behind the observed non-monotonic P_R-H pattern. The Com-H sample contains both bonded (via $Fe-C$ bonds) and nonbonded (attached via van der Waals bonds) BFO particles. While magneto-striction due to symmetric exchange interaction across $Fe-O-Fe$ bonds, in the absence (relevant for BFO-H) and presence of proximity coupling via formation of $Fe-C$ bonds (relevant for Com-H because of the presence of these bonds at the interface regions), yields, respectively, negative and positive magnetoelectric coupling, the field-dependent competition (shown in Figure 4.19) between the positive and negative magnetoelectric coupling in bonded and non-bonded BFO particles yields the observed non-monotonic pattern of variation of P_R with H. P_R decreases initially and then rises and finally decreases again as the applied magnetic field is swept from 0 to 20 kOe. Relative volume fraction of the bonded and non-bonded BFO nano particles, therefore, governs the relative strength of increase and decrease in the PR as a function of H. The coexistence of positive and negative magneto-strictive regions and engineering of their respective volume fractions have earlier been demonstrated[21] within the bulk of the Fe–Ga alloys. This was projected to yield field-dependent switch in ferroelectric polarization in ferroelectric/Fe–Ga alloy multilayer composites. In the present case, reconstruction of the interface in reduced-graphene-oxide/BFO nano composite is shown to actually yield the result projected in the study by Gou et al. engineering of the bulk and interface anisotropies and hence of the bulk and interface magneto-strictions further could yield eventually an interesting custom-designed periodic non-monotonic pattern of variation of P_R with H. This will assume immense significance in the context of the emerging field of straintronics [22] and thus expand the horizon of applications of single-phase-multiferroic/graphene nano composite or hetero-structure by a great extent.
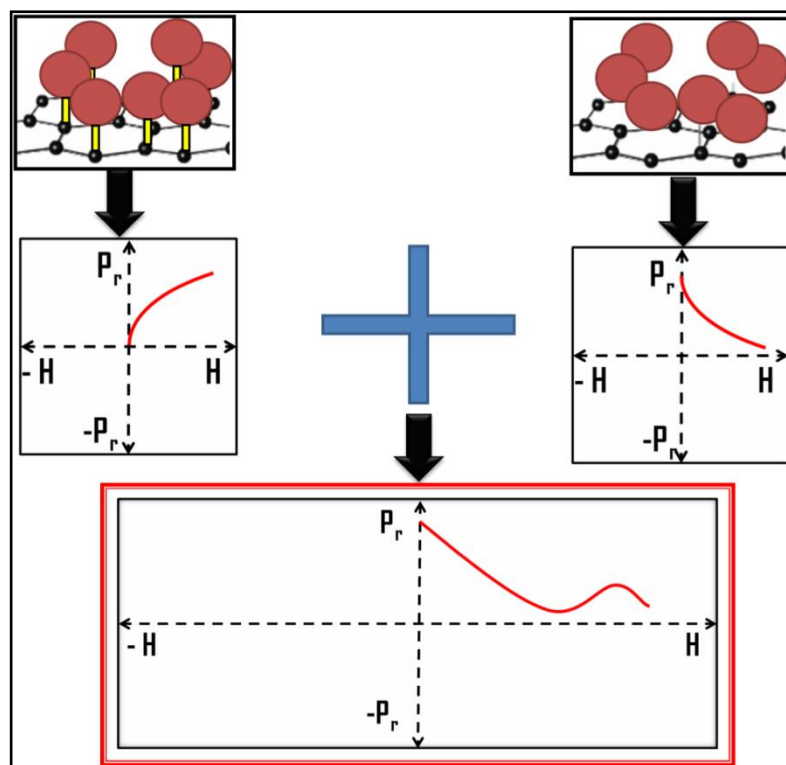
Figure 4.19 The schematic of the bonded and nonbonded BiFeO3 particles with RGO layers; the bonded particles because of the presence of Fe─C bonds and exchange coupling interactions across them could offer positive magnetostrictivemagnetoelectric coupling; the nonbonded ones, on the other hand, would exhibit negative magnetoelectric coupling; fielddependent competition between these two fractions eventually yields the nonmonotonic variation of PR with H. Tuning of the volume fractions of the bonded and nonbonded BiFeO3 particles, therefore, offers a pathway to tune the switching of magnetoelectric coupling, from purely negative to mixed positive and negative to purely positive.

4.3 <u>Chapter summary</u>

The RGO/BFO nano composite exhibits a range of interesting properties. The ferromagnetic component of the spin structure weakens while the coercivity exhibits significant enhancement, from 38 Oe in pure BFO to 190 Oe in the composite. Finite negative exchange bias has also been observed in the composite. Most importantly, the ferroelectric remanent polarization as well as the net off-centered displacement of the ions within the unit cell is found to exhibit a non-monotonic dependence on the applied magnetic field. We show that this remarkable non-monotonic field dependence of polarization results from field-dependent competition between the negative and positive magneto-striction at the bulk and interface of the composite. This competition yields the field-dependent switch in the variation of the unit cell volume with the magnetic field, from decrease to increase as the field is enhanced across 0–20 kOe. While pure bulk BFO is known to exhibit negative magneto-striction and hence negative magnetoelectric coupling which results in decrease in ferroelectric polarization under a magnetic field, observation of competition between negative and positive magneto-striction and

hence between negative and positive magnetoelectric coupling in the reduced graphene oxide–BFO nano composite reveals the significant role played by the $Fe{-}C$ bonds. A significant role of Fe—C bonds in the nano composite could be further observed in the samples containing different wt% RGO (e.g., 0.5 and 2.5) and hence different concentrations of $Fe{-}C$ bonds. The magnetic properties were found to change significantly with the change in the $Fe{-}C$ bond concentration. This reconstruction of the BFO/graphene interface via formation of $Fe{-}C$ bonds could find many applications in the area of straintronics because of field-driven tuning of compressive and tensile lattice strain. It could also trigger fresh research on atomic scale engineering of the interfaces in the composites or hetero-structures for far enhanced functionalities.

4.4 <u>Bibliography</u>

[1]   Huang, W., Yin, Y. and Li, X., 2018. Atomic-scale mapping of interface reconstructions in multiferroic heterostructures. *Applied Physics Reviews*, *5*(4), p.041110.

[2]   Song, H.D., Wu, Y.F., Yang, X., Ren, Z., Ke, X., Kurttepeli, M., Tendeloo, G.V., Liu, D., Wu, H.C., Yan, B. and Wu, X., 2018. Asymmetric modulation on exchange field in a graphene/BiFeO3 heterostructure by external magnetic field. *Nano letters*, *18*(4), pp.2435-2441.

[3]   Wu, Y.F., Song, H.D., Zhang, L., Yang, X., Ren, Z., Liu, D., Wu, H.C., Wu, J., Li, J.G., Jia, Z. and Yan, B., 2017. Magnetic proximity effect in graphene coupled to a BiFe O 3 nano plate. *Physical Review B*, *95*(19), p.195426.

[4]   Zanolli, Z., 2016. Graphene-multiferroic interfaces for spintronics applications. *Scientific reports*, *6*(1), pp.1-6.

[5]   Zanolli, Z., Niu, C., Bihlmayer, G., Mokrousov, Y., Mavropoulos, P., Verstraete, M.J. and Blügel, S., 2018. Hybrid quantum anomalous Hall effect at graphene-oxide interfaces. *Physical Review B*, *98*(15), p.155404.

[6]   Volonakis, G. and Giustino, F., 2015. Ferroelectric graphene–perovskite interfaces. *The journal of physical chemistry letters*, *6*(13), pp.2496-2502.

[7]   Tokunaga, Y., Iguchi, S., Arima, T.H. and Tokura, Y., 2008. Magnetic-field-induced ferroelectric state in DyFeO 3. *Physical review letters*, *101*(9), p.097205.

[8]   Soda, M., Ishikura, T., Nakamura, H., Wakabayashi, Y. and Kimura, T., 2011. Magnetic ordering in relation to the room-temperature magnetoelectric effect of Sr 3 Co 2 Fe 24 O 41. *Physical review letters*, *106*(8), p.087201.

[9]   Lee, S., Fernandez-Diaz, M.T., Kimura, H., Noda, Y., Adroja, D.T., Lee, S., Park, J., Kiryukhin, V., Cheong, S.W., Mostovoy, M. and Park, J.G., 2013. Negative

magnetostrictive magnetoelectric coupling of BiFeO 3. *Physical Review B*, *88*(6), p.060103.

[10] Huang, S., Hong, F., Xia, Z., Yang, F., Zhang, X., Xiao, G., Song, Y., Jiang, D., Deng, H., Ouyang, Z. and Wang, J., 2020. Multiferroic behavior from synergetic response of multiple ordering parameters in BiFeO3 single crystal under high magnetic field up to 50 Tesla. *Journal of Applied Physics*, *127*(4), p.044101.

[11] Chauhan, S., Kumar, M. and Pal, P., 2016. Substitution driven structural and magnetic properties and evidence of spin phonon coupling in Sr-doped BiFeO 3 nano particles. *RSC advances*, *6*(72), pp.68028-68040.

[12] Goswami, S. and Bhattacharya, D., 2018. Magnetic transition at~ 150 K in nano scale BiFeO3. *Journal of Alloys and Compounds*, *738*, pp.277-282.

[13] Feng, S.M., Chai, Y.S., Zhu, J.L., Manivannan, N., Oh, Y.S., Wang, L.J., Yang, Y.S., Jin, C.Q. and Kim, K.H., 2010. Determination of the intrinsic ferroelectric polarization in orthorhombic HoMnO3. *New Journal of Physics*, *12*(7), p.073006.

[14] Chowdhury, U., Goswami, S., Bhattacharya, D., Midya, A. and Mandal, P., 2016. Determination of intrinsic ferroelectric polarization in lossy improper ferroelectric systems. *Applied Physics Letters*, *109*(9), p.092902.

[15] Heron, J.T., Bosse, J.L., He, Q., Gao, Y., Trassin, M., Ye, L., Clarkson, J.D., Wang, C., Liu, J., Salahuddin, S. and Ralph, D.C., 2014. Deterministic switching of ferromagnetism at room temperature using an electric field. *Nature*, *516*(7531), pp.370-373.

[16] Goswami, S., Bhattacharya, D., Choudhury, P., Ouladdiaf, B. and Chatterji, T., 2011. Multiferroic coupling in nano scale BiFeO3. *Applied Physics Letters*, *99*(7), p.073106.

[17] Goswami, S., Bhattacharya, D., Keeney, L., Maity, T., Kaushik, S.D., Siruguri, V., Das, G.C., Yang, H., Li, W., Gu, C.Z. and Pemble, M.E., 2014. Large magnetoelectric coupling in nano scale BiFeO 3 from direct electrical measurements. *Physical Review B*, *90*(10), p.104402.

[18] Qiao, Z., Yang, S.A., Feng, W., Tse, W.K., Ding, J., Yao, Y., Wang, J. and Niu, Q., 2010. Quantum anomalous Hall effect in graphene from Rashba and exchange effects. *Physical Review B*, *82*(16), p.161414.

[19] Liu, X., Wang, C.Z., Yao, Y.X., Lu, W.C., Hupalo, M., Tringides, M.C. and Ho, K.M., 2011. Bonding and charge transfer by metal adatom adsorption on graphene. *Physical Review B*, *83*(23), p.235411.

[20] Labaye, Y., Crisan, O., Berger, L., Greneche, J.M. and Coey, J.M.D., 2002. Surface anisotropy in ferromagnetic nano particles. *Journal of applied physics*, *91*(10), pp.8715-8717.

[21] Gou, J., Liu, X., Wu, K., Wang, Y., Hu, S., Zhao, H., Xiao, A., Ma, T. and Yan, M., 2016. Tailoring magnetostriction sign of ferromagnetic composite by increasing magnetic field strength. *Applied Physics Letters*, *109*(8), p.082404.

[22] Bukharaev, A.A., Zvezdin, A.K., Pyatakov, A.P. and Fetisov, Y.K., 2018. Straintronics: a new trend in micro-and nano electronics and materials science. *Physics-Uspekhi*, *61*(12), p.1175.

5   Chapter

Study of morphological and physical properties of rGO/BiFeO$_3$ heterostructure

5.1 Introduction

We have developed rGO/BiFeO$_3$ nanocomposite with covalent and non-covalent bonding and have thoroughly studied their structura, magnetic and electrical properties to identify the differences among them. The unique magnetoelectric property has also been observed in covalently bonded composite when it was investigated using neutron and direct electrical measurements. There were numerous reports that mentioned graphene to experience strong exchange field in hybrid heterostructures with magnetic materials. Graphene's electronic structure can be significantly modulated by proximity effect which induces the spin-orbit coupling.Exchange proximity interaction with magnetic insulator with substantial exchange field was theroretically predicted for ferromagneti[1,2], antiferromagnetic[3], topological[4], magnetoelectric[5], multiferroi[6] materials. The experimental demostration was done by some groups by synthesizing heterostructure of Graphene/YIG[7,8,9,10], Graphene/EuS[11] and Graphene/ BiFeO$_3$[12,13]. Quio *et. al.*[3] first observed strong hybridization between C and Fe 3d shell which led to macroscopic exchange field when Iron (Fe) was adsorbed on Graphene. The same group also theoretically showed that π band of Graphene undergoes a spin split hen deposited on a BiFeO$_3$ thin film substrate and calculated the exchage splitting to be 70meV. Both Wu[12] and Song[13] had used such magnetic materials/graphene heterostructure to directly correlate the Zeeman splitting and quantum anomalous hall effect (QAHE). Song[13] *et. al.* showed that the exchange field could be as high as 19.8-287.9T and also showed that it is large under positive magnetic field than negative. It appears, therefore, that the electronic hybridization with proximity material can modulate the band structure of graphene. Single atomic layer provides stronger hybridization with the substrate than few layers but multi-layer Graphene generate strong spin charge coupling that has been confirmed by Elton J. G. Santos[14] who studied the Neodymium di phosphate (NPD) functinalized graphene and addressed that the magnetoelectric

coupling coefficient is dependent on number of layers of Graphene; higher the number of layers the coefficient would be comparable to perovskite. There are possibilities of lattice mismatch and or atomic diffusion in covalent bonded heterostructure and in contrast to it surface interacting with VdW bonds are quite sensitive to external stimulus like electric field or charge accumulation/ depletion of underlying layer and accumulation ofsurface charges from 2D materials enhances possibilities of Ferroelectric polarization. These features was first studied by Li *et. al.*[15] in Graphene/BiFeO$_3$ heterojunction experimentally. They observed ferroelectric polarization of BiFeO$_3$ can modulate the contact barriers and depletion width at the heterointerface. The modulation of multiferroic properties with the introduction of graphene or rGO has not been reported yet in heterostructures. We already observed the effect of rGO upon the properties of BFO in bonded and non-bonded nanocomposites. We now aim to investigate the effects in rGO/BFO heterostructures.

5.2 <u>Preparation of BiFeO$_3$ Film</u>

The first BFO thin film was prepared by RF sputtering in 1986[16]. Since then upto '90s there were only a few articles published on BFO thin film preparation using Pulse Laser Deposition or sputtering techniques[17181920]. After 2000 the preparation of BFO film started to grow exponentially since it was found in ref [20] that the low remanent polarization exhibited by BiFeO$_3$ bulk ceramics can be increased by several orders of magnitude when it is processed as a thin film. But, according to Pavlovicet. Al.[21] there is a critical thickness below which secondary phases develop.

Relatively cheaper techniques such as sol-gel or spin coating have also been used for the preparation of multiferroic/graphene heterostructure of varyig thickness[22,23,24,25,26,27,28,29,30,31,32,33,34]. Some of researchers pointed out how the magnetic and electrical properties were varying with thickness[22] or grain size[26] and also discussed the contribution of concentration of precursor solutions towards the thickness, micro-structure and physical properties[35]. However, the sol–gel + (spin/dip)-coating technology suffers from several drawbacks as it yields samples with secondary phases, porous microstructures, large defect concentration (which results in higher leakage current) etc. Therefore, preparing highly textured or single crystalline films- as obtained from expensive molecular Beam epitaxy (MBE), pulse laser deposition (PLD), chemical vapour deposition (CVD) or RF sputtering techniques – is quite challenging. Moreover, fabrication of highly textured films on non-single crystal or even glass substrates and increase in grain size is also a challenge till date in chemical solution deposition (CSD) driven spin coating process. However, Nakamura *et. al.*[36] [37] reported best properties of CSD driven BFO film with good P-E loop and low leakage current.

In recent studies it has been found that the homogeneity is dependent on the competition between solvent evaporation and precursor gelation. Controlling this balance among them yield

epitaxial and phase pure films. Zhang *et. al.*.[38] investigated the bonding chemistry of BFO precursors before and after heating process.

It is also important to avoid precipitate formation because it can cause Bi and Fe phase segregation which can lead to inhomogeneous films with impurities or secondary phases.

The Bi:Fe stoichiometry also plays an important role here. Excess metal nitrate concentration can cause precipitation during gelation and in contrast low metal nitrate concentration may lead to an inhomogeneous and porous surface in film. Therefore the ideal concentration is needed to be tuned properly.

Drying schedule can also affect the gelation. We can opt for heating the sample for gelation at a temperature higher than 70° C (at 90° C), followed by completely removing the remnant solvent at 270°C.

Since the solid-vapour area to volume ratio in gel thin film is large, the driving force for sintering the gel is strong even at low temperature, making the final sintering temperature comparatively lower compared to bulk BFO processing.

In addition to the heating rate and the absolute temperatures, even the role of ambient has been investigated in the CSD synthesis of BFO thin films. Yun *et. al.*.[39] reported that using stoichiometric BFO precursor, secondary phases, such as $Bi_2Fe_4O_9$, form when annealing at oxygen atmosphere, while polycrystalline BFO of single phase is obtained when heating at the nitrogen atmosphere. High performance polycrystalline BFO films with pure phase and high polarization have also been achieved by using a precursor with excess Bi and annealing at nitrogen atmosphere.

So we have to tune some of the parameters to check the best quality of the film as follows-

- Molarity of stock solution
- Choice of substrate
- Spin coating schedule
- Heating schedule

5.2.1 BiFeO₃ film Deposition schedule

5.2.1.1 Precursor solution preparation:

The precursor solution was prepared following the procedure described in the experimental section 2.3.2.1 and we have stored the stock solution for a long time. The stock solution was prepared in different molarity like 0.01M, 0.05M, 0.1M and 0.3M.

5.2.1.2 Substrate cleaning:

Two types of substrates were used- p type Silicon (Si) substrate from Tedpella with resistance 1-30 Ohms and fluorine doped Tin Oxide (FTO) coated Glass substrate from Techinstro with resistance $10\Omega/sq$ which were cut into 5mm×5mm square size using Diamond cutter. In both substrates a proper cleaning schedule has been opted which is essential in producing adherent and uniform thin films and remove external particles from the surface.

➢ Fluorine-doped Tin Oxide (FTO) coated glass substrates were ultrasonically cleaned in three steps:

   a) First, the substrates were ultra-sonicated in a 10% NaOH solution at 55° C for 10 mins.
   b) Then the substrates rinsed in running DI water
   c) Next, ultra-sonication was done in DI water for 10 mins at room temperature.
   d) Then blow dry the substrates.
   e) Finally, ultra-sonication was done in an ethanol solution for 10 mins at room temperature.
   f) Then again blows dry the substrates or dry in ambient air.

➢ Silicon substrates were ultrasonically cleaned in three steps:

   a) First dip the Si substrates in Hydro fluoric acid (40% from Emplura) for approx 20-30 sec.
   b) Then drop a DI water upon a substrate if the water droplet become hydrophobic then we can say that the upper SiO_2 layer has been etched out otherwise dip for another 10 sec.
   c) Then put the samples in Ethanol/DI water (50:50 ratio) mixture for another 5 min or sonicate and dry in ambient air.

5.2.1.3 Substrate preheating:

Before spin coating the cleaned substrates are pre heated at 70°C for approx 5-10 min in oven.

5.2.1.4   Solution dispensation

A fixed amount of stock solution (depending on substrate size) was dispensed using a micropipette on preheated substrates. The technique of dispensing the solution was found to be very important in controlling film coverage on the substrate. Two methods were evaluated for solution dispensing:

a) The solution was dispensed on the central region of a static substrate and then spinning was started. This is the easiest and simplest method.

b) Dispensation was done while the substrate began rotating. This is called a dynamic dispense and can potentially give better coverage than static dispense.

Since our substrates had to be preheated as well, this meant that the procedure had to be done quickly in order to avoid a substantial loss of substrate temperature.

5.2.1.5   Spinning schedule

A spin coater, SPIN NXG-P, from Apex Instruments (Figure 5.1) was used to deposit the films using the following schedule. The acceleration time was 10 sec that means in 10 sec the substrate was reaching the desired speed. The rpm of the coater was varied (i) 3000 rpm (ii) 5000 rpm (iii) 7000 rpm and was fixed at one desired rpm for 40 sec. We have to spin before starting or after reaching the fixed rotational speed. This time is very crucial also just because it helps to quickly evaporate the remaining solvent.

We have dispensed the solution once, twice or thrice to achieve single, 2-layer and 3-layer films to check the continuity.

In single layer films we have drop casted (i) 10 µL (ii)50 µL and (iv) 1000 µL; solution in one time to check the proper amount to be dispensed for uniform film.

Figure 5.1 Spin coating System

5.2.1.6   Gelation Schedule:

After spin coating, the films were heated at 90° C for 1 min for gelation and dried at 270° C for 3 min for drying. It was done on top of a hot plate. Another drying schedule has been

[167]

opted where we dried the samples at 180°C for 5 min in oven directly. The entire procedure was repeated as many times as required to obtain the desired thickness of the films.

5.2.1.7 <u>Pyrolysis and annealing schedule:</u>

At this point an amorphous film is present. To remove the organic components the films were first pyrolized at 380° C for 10 mins and then annealed/sintered for another 60 mins for crystallization and phase formation to take place, in a muffle furnace under Argon atmosphere. Annealing temperatures of 550°C and 600°C were tested. Heating rate was 5° C/min and samples were cooled slowly in the furnace.
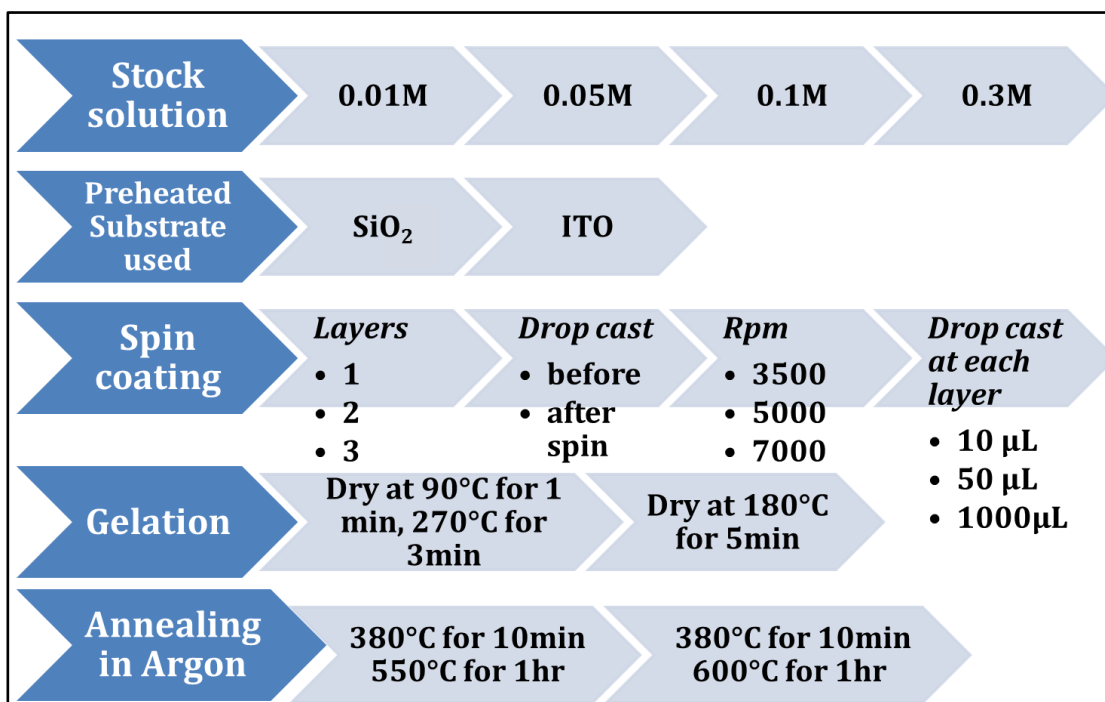
Figure 5.2 Schematic of preparation of BFO film

5.3 <u>Preparation of rGO film</u>

Monolayer graphene reportedly exhibits the strongest templating effect, allowing the face-on orientation of π-conjugated organic molecules based on π–π interactions between the molecules and π-conjugated planes of graphene[40 41 42]. However, graphene grown by chemical vapor deposition must be transferred to objective substrates by using a supporting polymer layer[43 44]; and the polymer residue on the graphene hampers the orientation control[45]. Such a complicated transfer process hinders the practical use of the graphene template in the field of organic electronics that aims for the fabrication of low-cost and large-area devices.

While graphene has dominated the electronic applications, Graphene Oxide (GO) is one of the most attractive 2D carbon materials for bulk applications, such as composites, films,

fibres, and membranes. GO is derived easily by exfoliation from graphite oxide, which was first synthesized by Brodie in 1859. GO can be produced in large scale by chemical oxidation of graphite, and is water dispersible; thus, it can be processed in environmentally friendly methods without using organic solvents. GO aqueous dispersions inevitably contain un-exfoliated graphite oxide bundles, resulting in rough surfaces. The templating effect is very sensitive to the surface state. GO can be reduced by numerous methods, resulting in an electrically conducting material, reduced Graphene Oxide (RGO). RGO resembles many of the graphene properties, such as being atomically thick, electrically conductive, 2D, and exhibiting a very similar chemical composition. Low cost and easy production method of reduced graphene oxide (rGO) makes them useful as a substitute of graphene. GO and RGO can be prepared in large quantities by the modified Hummer's method using potassium permanganate as an oxidizer, instead of Brodie's method.

One of the most interesting challenges in the research field of graphene related materials is to develop macroscopic scale films due to their potential applications in many areas. Many reports[46][47] are there on researched methods to obtain stable RGO or to control the oxygen content of GO in a solution without agglomeration of the RGO sheets. Various research groups have made rGO film by using different techniques like Spray deposition technique, dip coating technique[48][49][50], vacuum filtration technique[51][52][53], drop casting technique[54], spin coating technique[49][55] and electrophoresis deposition[56][57], blade coating[58], spin coating and Langmuir–Blodgett assembly[59]. Some of the disadvantages are noted in Table 5.1.

Apart from oxygen functionalities, other structural defects, such as vacancies, adatoms, and grain boundaries, are inevitably generated either in synthetic procedure of rGO or film assembly process. Thermal annealing in vacuum, or an inert or reducing atmosphere shows much higher efficiency on the removal of oxygen, rearranging carbon atoms in the basal plane, repairing of the inherent structural damages, such as vacancies and cracks.

Table 5.1 Different methods and their disadvantages of producing rGO film	
Methods	**Disadvantages[60]**
Electro spray deposition	Limited she*et. al.*ignment
Vacuum filtration	High time consumption and limited film size
Dip coating	High time consumption and limited she*et. al.*ignment
Drop casting	Alignment
Electrophoresis deposition	Restrict to conductive substrate

Among them we have opted spin coating technique to obtain rGO film with low thickness yet superior surface without cracks and agglomerations.

➢ We have opted two types to make rGO/BFO heterostructure-

    a) We drop cast rGO solution on annealed BFO film surface. This sample is depicted as 'AH'. This schedule is taken to check whether the high temperature during annealing schedule could be able to form any type of new bonding or create new phase in the sample.

    b) We drop cast rGO solution on dried BFO film surface and then pyrolisized and annealed following the same schedule opted for BFO film. This sample is depicted as 'HA'.

5.3.1 <u>rGO film deposition schedule:</u>

5.3.1.1   <u>Precursor solution preparation:</u>

The precursor solution was prepared following the experimental section 2.3.1.1. The aqueous stock solution was prepared in different wt% as follows -0.0005g/ml and 0.001g/ml.

5.3.1.2   <u>Substrate preheating:</u>

We have drop casted upon BFO film either annealed or dried; so we didn't pre-heat it.

5.3.1.3   <u>Solution dispensation</u>

A fixed amount of stock solution (depending on substrate size) was dispensed using a micropipette on substrates containing BFO film. Only one method was opted for solution dispensing- The solution was dispensed on the central region of a static substrate before spinning was started.

5.3.1.4   <u>Spinning schedule</u>

Only one spinning schedule is followed in the same spin coater. The acceleration time was 10 sec. The rpm of the coater was varied (i) 3000 rmp was fixed at one desired rpm for 40 sec. we have to spun before starting reaching the fixed rotational speed. We have dispensed the solution only once of different wt% s.

5.3.1.5   Gelation Schedule:

After spin coating, the films were heated at 90° C for 5 min for drying in oven directly. The entire procedure was repeated only once to obtain the desired thickness of the films. More drying can result in oxidation of rGO layers. This time is very crucial.

5.3.1.6   Pyrolysis and annealing schedule:

The AH sample was not further annealed but the sample HA was further taken for a heating schedule to remove the organic components. The films were first pyrolized at 380° C for 10 mins and then annealed/sintered for another 60 mins at 550°C under Argon atmosphere.
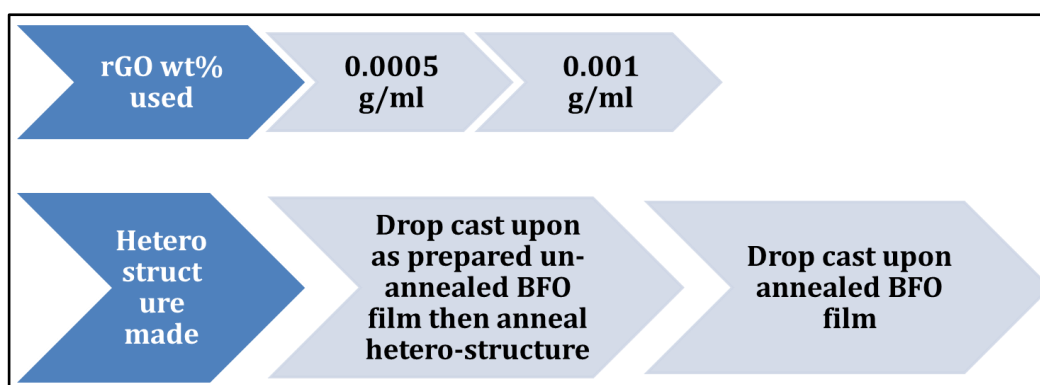
Figure 5.3 Schematic of preparation of BFO/rGO heterostructure

5.4 Result and discussion

Initial morphology and topography of the films were observed using a field emission scanning electron microscope (FESEM) to ascertain the grain size/distribution/shape as well as absence/presence of voids or micropores. Cross-sectional SEM images were also obtained to get an idea about film thickness. Diffraction patterns of as deposited and annealed films were obtained for phase and structural analysis in the usual Grazing Incidence X-ray diffractometer (GIXRD) at Saha Institute of Nuclear Physics. The magnetic hysteresis loops were measured by LakeShore vibrating sample magnetometer (VSM; Model 7407) under 20 kOe fields at room temperature, while the ferroelectric polarization was measured by the Precision LC-II (Radiant Technologies Inc.) ferroelectric loop tester.

5.4.1 Effect of molarities of stock solution

The films were prepared using 0.01M, 0.05M, 0.1M and 0.3M stock solutions. The FESEM micrographs of annealed films prepared by using stock solutions of different molarities are shown in Figure 5.4. The film of 0.01M contains isolated particles and some portions of substrates are also seen. In 0.05M film there are more cracking regions compared to others.

There are discrete yet more particles seen on the surface of 0.1M film. 0.3M film is found to be more homogeneous compared to others with less defect regions. We have aimed for uniformity on the surface rather than traces of nano particles in the surface.
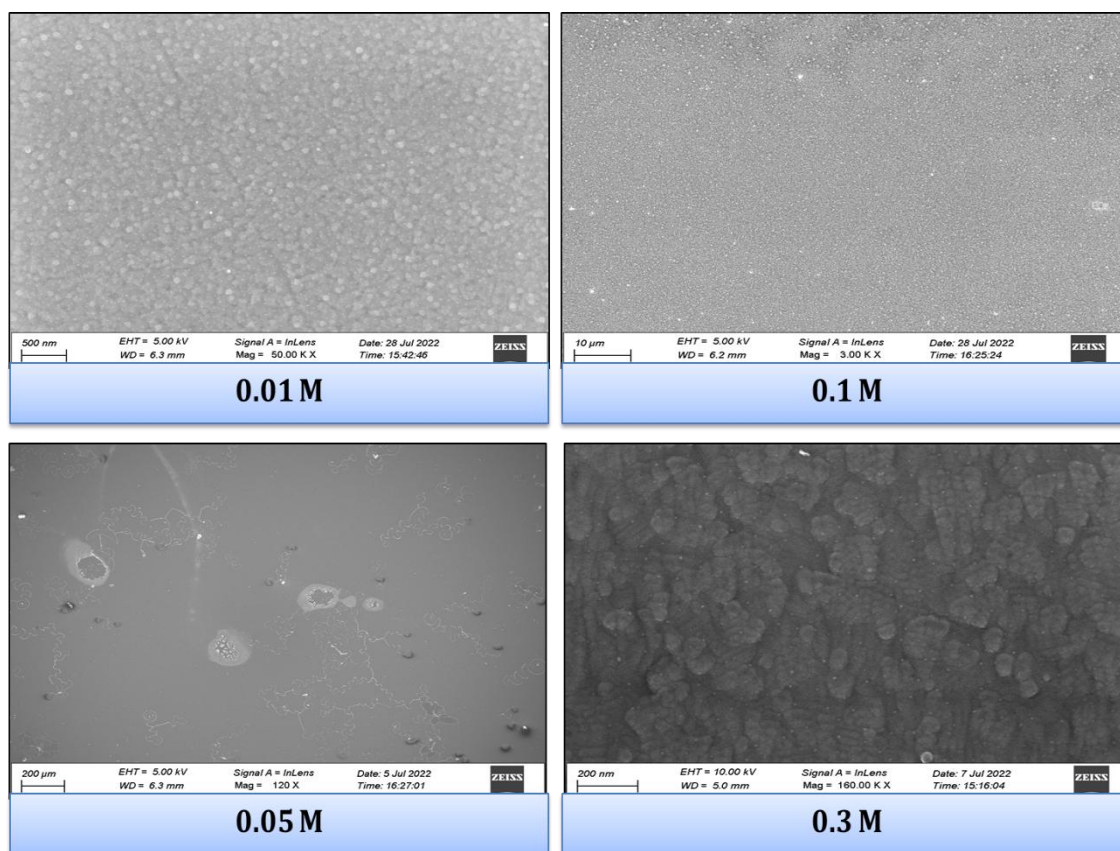
Figure 5.4 FESEM micrographs with variation of molarities of stock solution

5.4.2 Effect of pre-heated substrates

As mentioned earlier, some films were made on FTO-coated glass substrates to facilitate electrical characterization of the films. During deposition and spinning, the wet-ability of FTO was found to be somewhat better than Si substrate. However, this had little or no influence on the final film quality as SEM image and XRD pattern both resembled films deposited.

5.4.3 Effect of dispensing method

To ensure coverage of the entire substrate with the precursor solution before the excess liquid is spun off, a very good wetting between the solution and substrate is required. The appearance of the film made using this method is shown in Figure 5.5. There are very little differences seen morphologically in static and dynamic dispensing methods. The excess liquid seems to have flung off from the substrate before coating the entirety of the surface. Dynamic dispense sometimes gave complete coverage but at other times it produced films like that

shown in Figure 5.5. It contains more cracks. So we have opted for static dispensing for further that means we drop cast before spin starts.
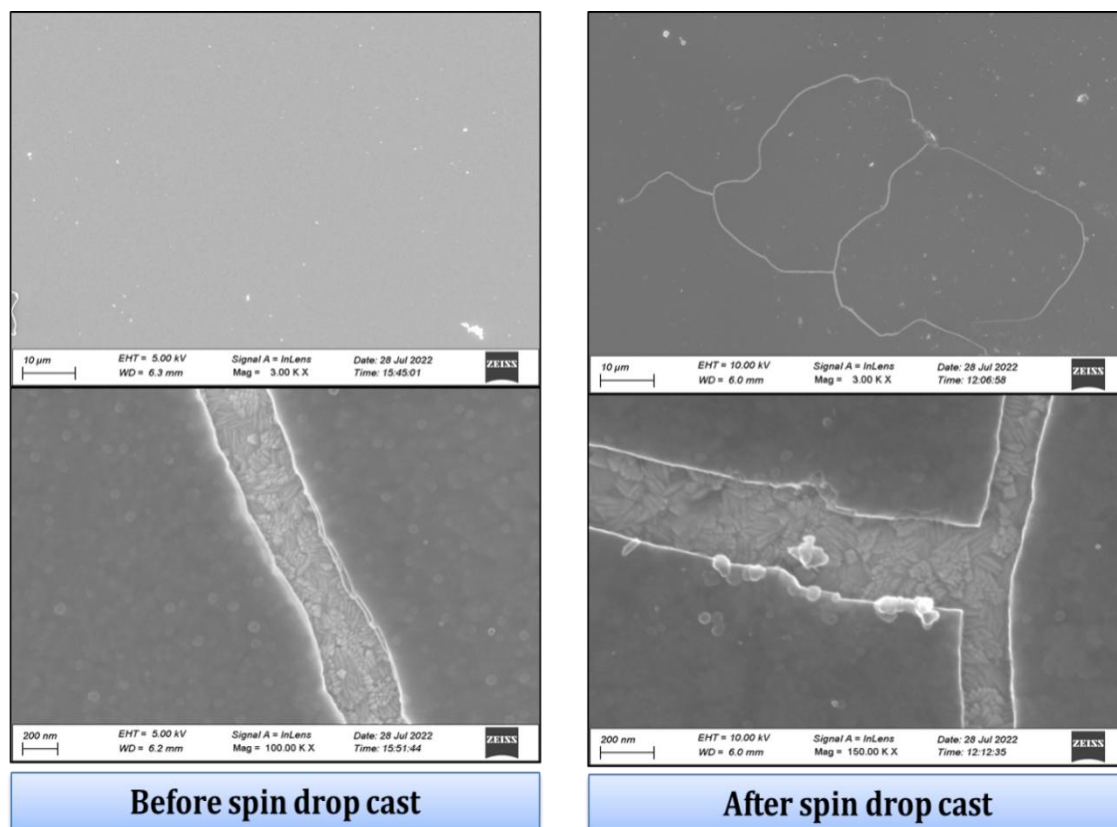
Figure 5.5 FESEM micrographs with variation of drop-casting method before or after spin starts

5.4.4 <u>Effect of variation in drop casting amount in each layer</u>

10 μL, 50 μL and 1000 μL was drop casted in each layer and then FESEM micrographs were taken on the annealed films as seen in Figure 5.6. We have seen the entire substrate was not covered when small amount 10 μL was drop casted. When the drop-casting was done in 1ml then the film thickness is very high and the surface roughness is very high. So we have chosen the 50μL drop casting in each layer to be perfect as seen in figure also.
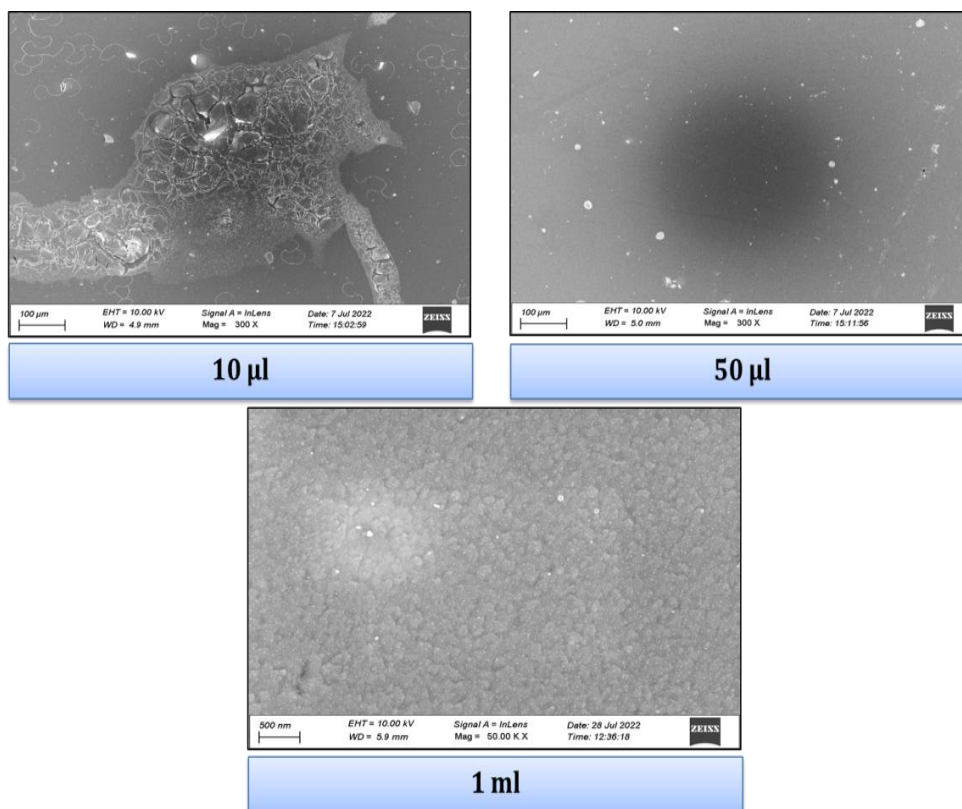
Figure 5.6 FESEM micrographs with variation in drop casting amount in each layer

5.4.5 Effect of varying number of layers
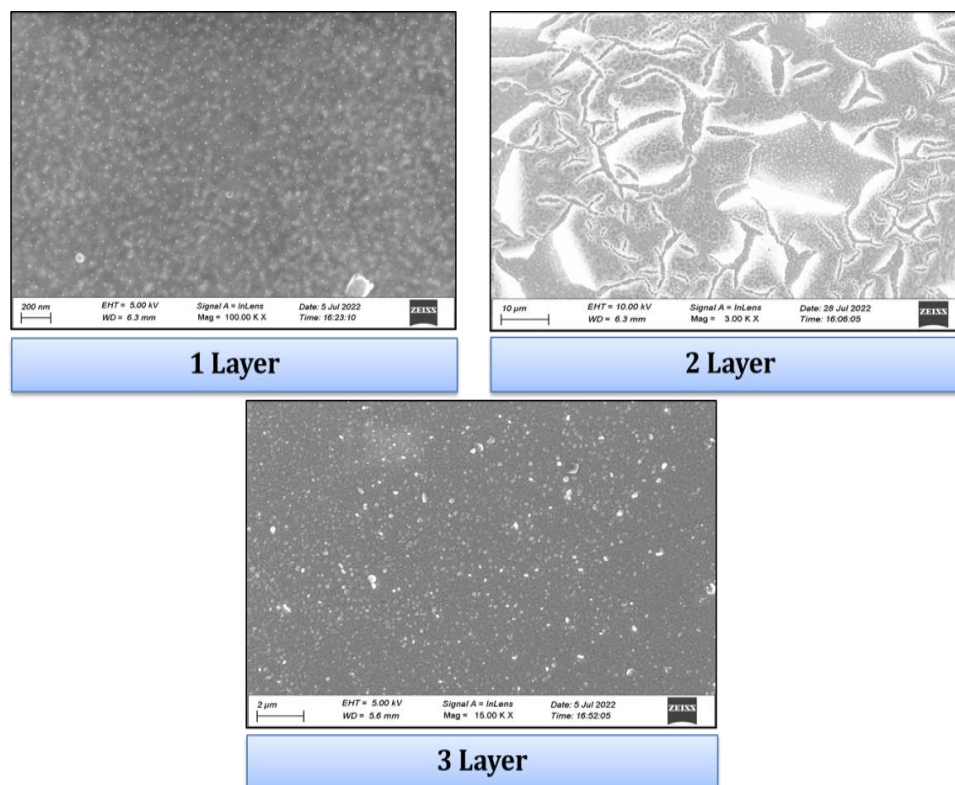
Figure 5.7 FESEM micrographs with variation in layers

In varying layers we ensure to follow same gelation and drying methods and after achieving desired thickness we have annealed the overall films. In each layer we have drop casted 50μL of 0.3M solution. The FESEM micrographs under same resolution are shown in Figure 5.7. When the drop casting was done in only one layer then it is found that uniformity is achieved. In 2-layered film the outer layers are cracked during heating. The similar observation is seen in 3-layered film also. In 3-layered film there were traces of more nano particles formed on the surface. So the single layer method is opted further.

5.4.6 <u>Effect of variation in rotation speed</u>
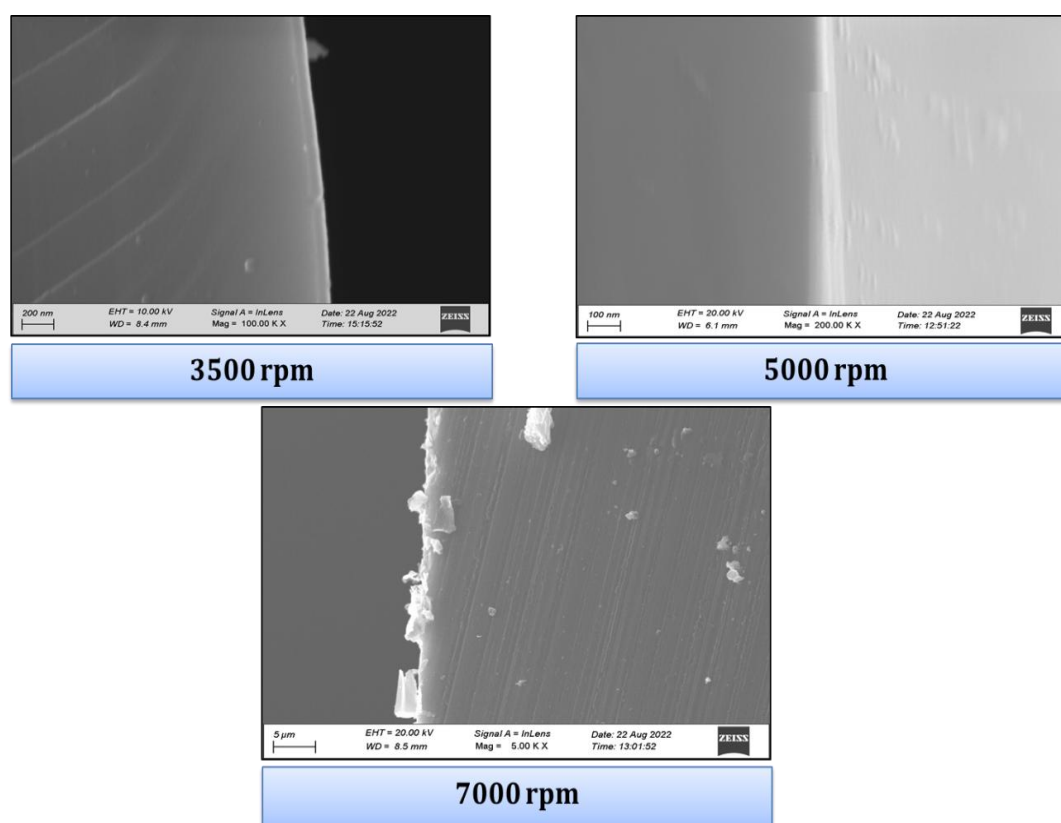
Figure 5.8 FESEM micrographs with variation in rotational speed

The FESEM images in Figure 5.8 are taken by varying the rotational speed and making the acceleration time and rotational time fixed in each case. The crucial differences are seen while taking the cross-sectional image by checking whether rotational speed have any effect on the thickness or uniformity. There are no as such differences present there so we have opted for lower speed i.e. 3000rpm in every case.

5.4.7 <u>Effect of variation in rGO wt%</u>

We aim to find differences in thickness while varying the wt% of rGO stock solution. The thicknesses are found to be ≈20nm and ≈50nm for the films prepared by using0.0005g/ml and 0.001g/ml stock solutions respectively as seen in Figure 5.9. In order to achieve highest

hybridization among rGO and BFO we want thickness of rGO to be equivalent with single layer graphene. Though the thickness of graphene is in the range of ~1nm range but we can achieve near to that. But here thickness is not the only crucial parameter; we also want to ensure the full coverage of the BFO film by rGO.
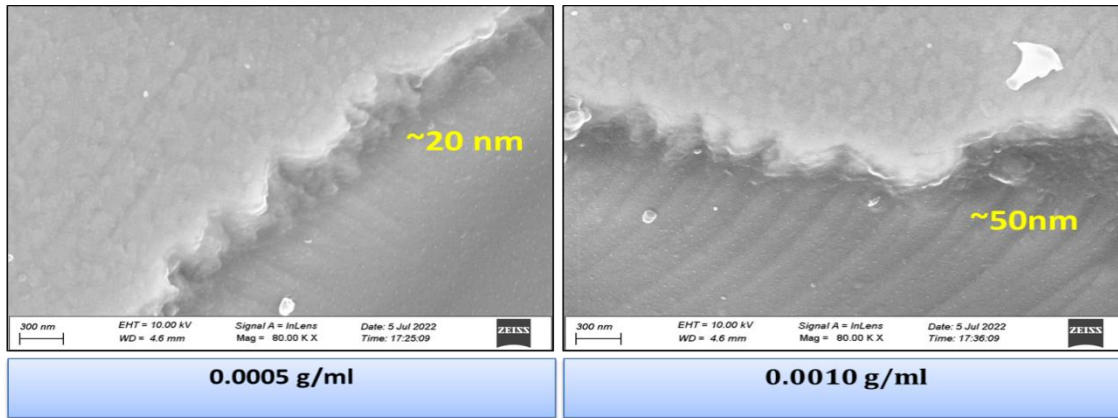
Figure 5.9 FESEM micrographs with variation in rGOwt%s

5.4.8 Effect of gelation and drying schedule

The central region of the dried films at 180°C had white appearance which is not desirable. These might be artefacts resulting from rapid gas evolution during drying. So we opted for two step method- gelation at 90°C for 1 min followed by drying at 270°C for 5min on hot plate directly.

5.4.9 Effect of annealing temperature

After the drying step the film that is present is in an amorphous state. Annealing at high temperatures is required to form BFO. The films were annealed at two different temperatures to find the most suitable one for desired phase formation and suppression of secondary/parasitic phases. Unless otherwise noted, all films discussed from this point on, were made from a precursor solution of 1:1 solvent ratio and on a 70° C preheated substrate. XRD patterns of the films annealed at 500° C and 550° C are shown in Figure 5.10. It can be clearly seen that the rhombohedral phase of BFO is the dominant one when the film was annealed at 550° C, and also when annealing temperature was 500° C. In the as prepared film, the formation of the rhombohedral BFO phase is not complete as apparent from the observed peaks in the diffractogram. The peaks corresponding to FTO substrate could be observed at approximately 21°, 30°, 35°, 45°, 50° and 60°. The unit cell of BFO was also observed to shrink with increasing annealing temperature as evidenced by the shifting of peaks to the higher angle (i.e. higher 2θ values) for both the samples, prepared at 500°C and 550°C, there are additional peaks present along with the characterized peak of FTO which are depicted as "#". These additional

peaks at 2θ~ 22°, 32°, 37°, 38° and 57° correspond to (012), (110), (113), (006) and (300) planes, respectively. The formations of phases suggest that $BiFeO_3$ belongs to space group R3c as per JCPDS card number 86-1518. There is no trace of any secondary or impurity phases.

We did not use a temperature higher than 550°C because then it will reach the low softening point of the ordinary glass and there will be the possibility that the film probably gets incorporated into the glass itself. Now as there is no such variation seen with annealing temperature so we choose 500°C as the annealing temperature because it is lower.
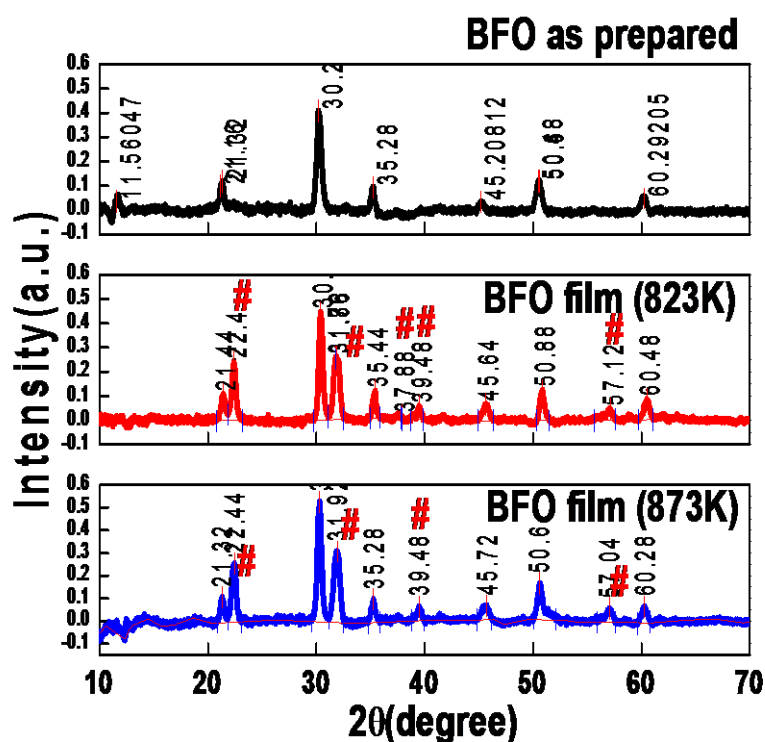
Figure 5.10 Room temperature GIXRD data of BFO as prepared, annealed at 823K and 873K

5.4.10   Effect of methods in making heterostructure

We have opted two methods in forming heterostructure of rGO. In AH sample rGO solution was spun on annealed BFO surface and in HA sample rGO was spun upon as prepared dried surface of BFO and then annealed. The diffractogram image is shown in Figure 5.11. The rGO is amorphous and so that there are no traces of any hump near 25°C. Moreover, in both cases there are small peaks found corresponding to BFO planes along with FTO peaks. There are no other differences present between the AH and HA samples. In AH there are peaks present at approximately 32°, 64° correspond to (110) and (208) plane. Whereas, in HA there are peaks at approximately 32°, 37° and 64° correspond to (110), (113) and (208) planes. Here,

[177]

additional peaks are corresponding to FTO phases. Here also no additional peak formed corresponds to a secondary or impurity phases. The summary of all peaks found in all the samples are shown in Table 5.2.
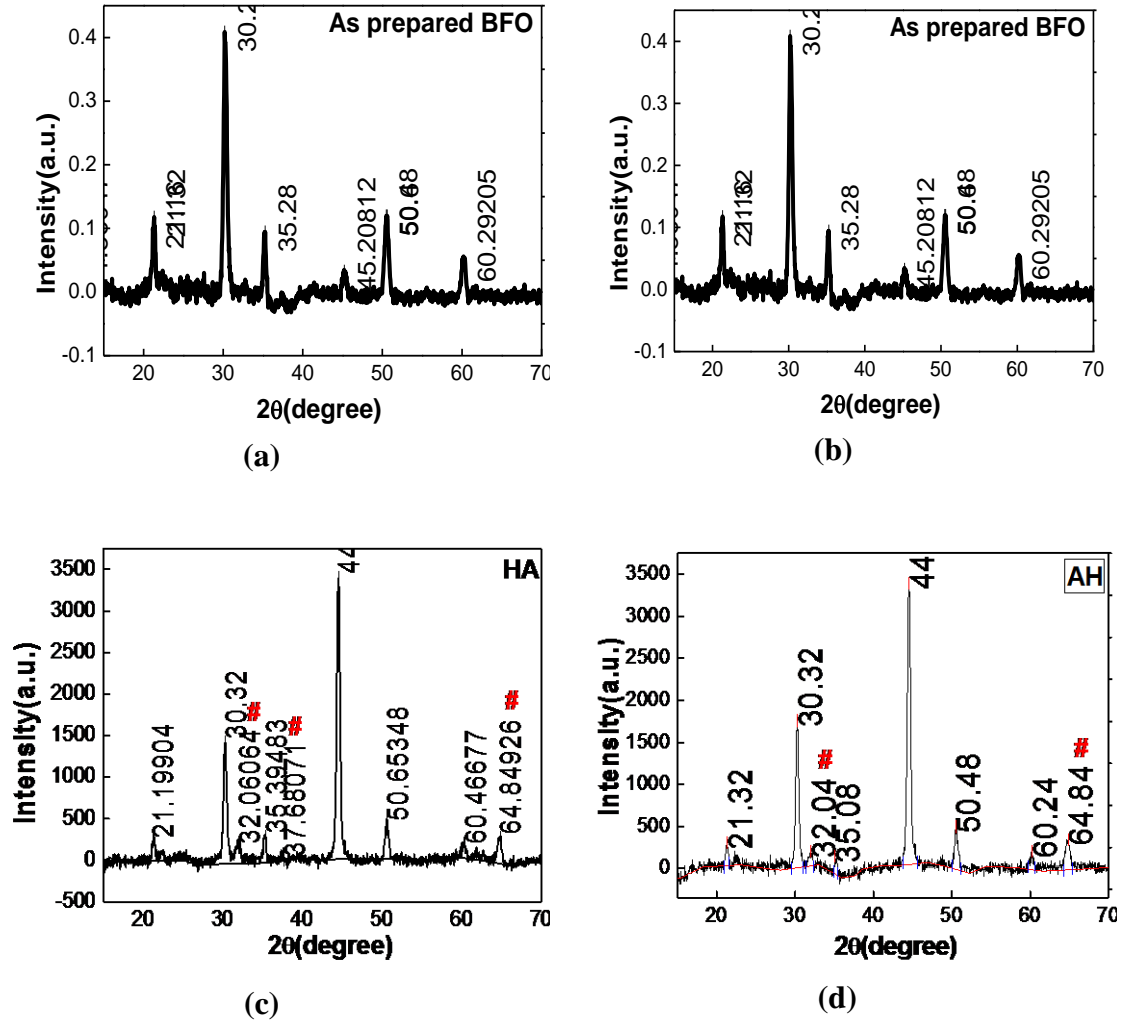
Figure 5.11 Room temperature GIXRD data of BFO (a)as prepared;(b) annealed at 823K; (c) heterostructure (HA); and (d) heterostructure (AH)

Table 5.2 Summary of peaks present in GIXRD data of all samples			
Un-annealed BFO	*BFO annealed*	*AH*	*HA*
21	21	21	21
-	22 (012)	-	-
30	30	30	30
-	32 (110)	32 (110)	32 (110)
35	35	35	35
-	37 (113)	-	37 (113)
-	38 (006)	-	-

[178]

45	45	45	45
50	50	50	50
-	57 (300)	-	-
60	60	60	60
-	-	64 (208)	64 (208)

In both the cases we are able to achieve uniform rGO/BFO heterostructure with clean and uniform surface and phase purity. No preferential orientation of any particular crystallographic plane could be seen in GIXRD and FESEM of the films.
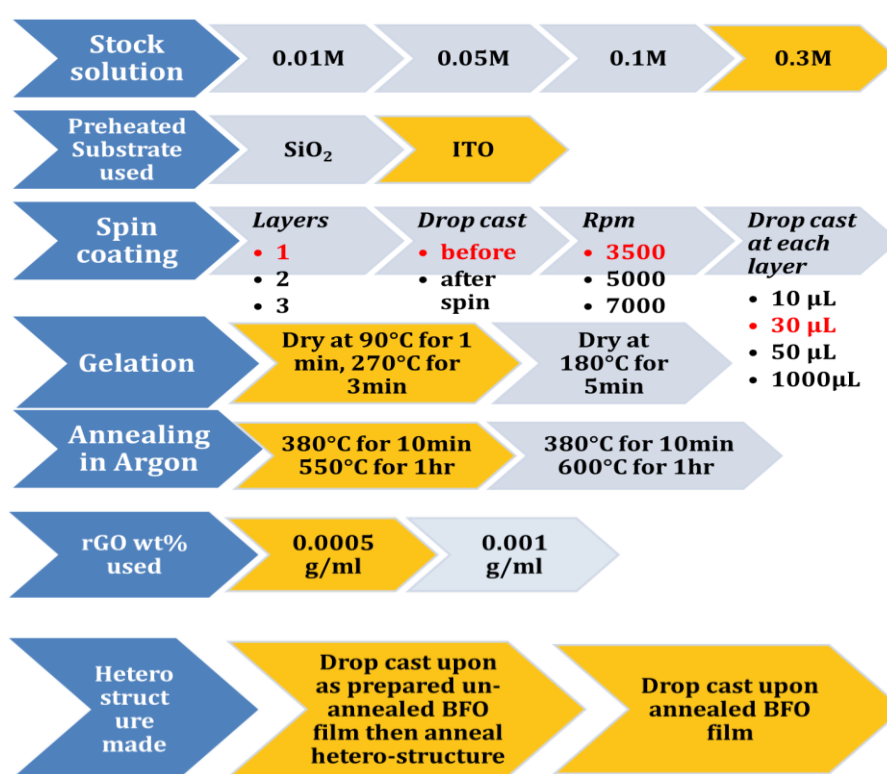
Figure 5.12 The Final schedule of making heterostructure

The FESEM micrograph we have taken of the rGO/BFO heterostructure is shown in Figure 5.13. The well-developed grains are seen in the film with no traces of porosity. The micro-structural image thus correlates agreeably with the diffraction patterns. Analysing the image in ImageJ software we have calculated the thickness and can identify the heterostructure interface as seen in Figure 5.13. The BFO film and rGO film thickness were calculated to be ≈70nm and ≈15nm approximately and the overall thickness is nearly ≈85nm. One of the photographs of heterostructure (BiFeO$_3$/rGO deposited upon FTO substrate) is shown in Figure 5.14.

[179]
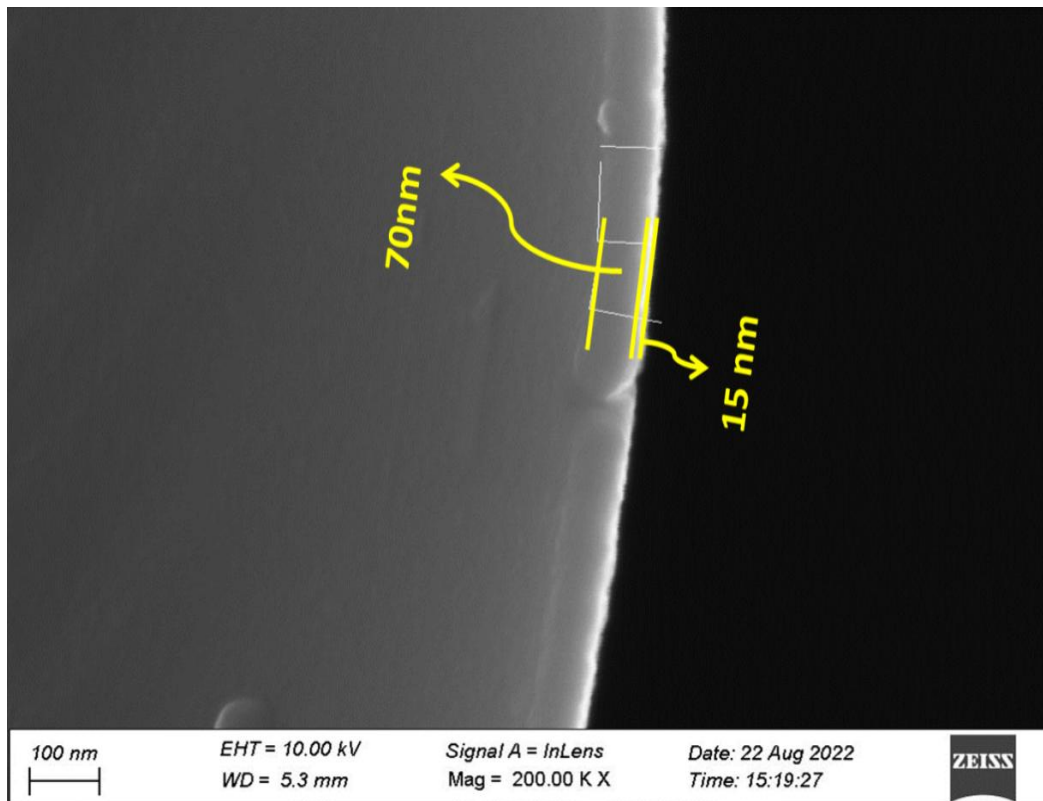
Figure 5.13 Thickness calculated from FESEM micrograph of BFO/rGO heterostructure

Figure 5.14 Picture of Hetero-structure upon FTO coated substrate

5.4.11 <u>Magnetic study</u>
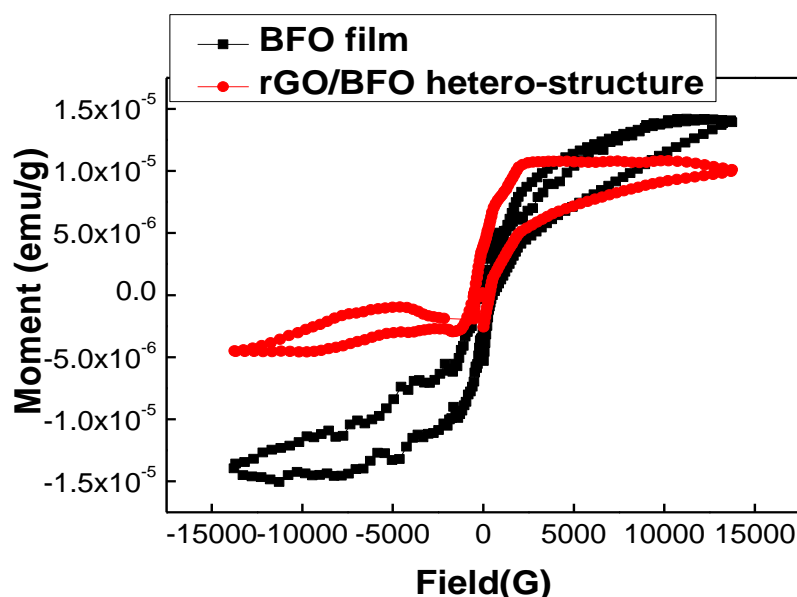
Figure 5.15 Room temperature M-H loop of BFO film and AH heterostructure

We have studied the M-H loop at room temperature from 0-20 kOe with a step size of 150Oe. After eliminating the bare substrate contribution from the data of BFO and AH both we plotted the M-H loop data in Figure 5.15. The BFO shows anti-ferromagnetic nature because the thickness of BFO is 70nm. The AH sample shows nearly ferromagnetic nature. The 70nm thickness is higher than the period of spin cycloid >62nm. As a result the anti-ferromagnetic nature persists in phase pure BFO thin film. With only addition of 15nm rGO layer upon BFO it is possible to change the nature of M-H loop from anti-ferro to ferro. The hybridization that we have seen in rGO/BFO covalent bonded structure show similar result. So we can crudely say that there is some sort of hybridization happening in the heterostructure also that we have found in literature on Graphene/BFO heterostructure.

5.4.12 <u>Ferroelectric polarization study</u>

For ferroelectric polarization we have made an array of circular electrodes- each of size 0.2 mm with a gap of 0.7 mm (see Figure 5.16 (c))- upon films using Precision Etching Coating system from Gatan (Model 682), as shown in Figure 5.16. The electroding material used was Gold. Then we have taken ferroelectric Hysteresis measurement using 2 probes upon BFO film and AH film in top-bottom electroding configuration. Figure 5.18 shows the hysteresis measurement upon BFO at 3 different positions as seen in Figure 5.17. The measurements were done at 20V and have shown no variation in polarization values. This confirms the uniformity of the film. The hysteresis P-E loop measurement also shows that as the thickness of the film is so low so that it reaches saturation value near to low voltage ~20V with a saturation value of

[181]

approximately $0.4\mu C/cm^2$. The remanent polarization was also measured under remanent protocol under 20V and 25V and shows a perfect variation of loop P_r-E with increasing voltage. The remanent values as seen in Figure 5.19 are measured to be $0.26\mu C/cm^2$ and $0.14\mu C/cm^2$ at 25V and 20V approximately.

While measuring P-E loop upon rGO/BFO heterostructure (AH) we have seen that it does not attain saturation even up to 100V. From Figure 5.20 we have seen that there is a perfect rise in P-E loop when voltage is varied from 60V to 99.9V. This also validates the fact that the saturation value of heterostructure is much higher than BFO film. Due to limitation of our voltage amplifier we cannot give substantial proof of that. We have also checked the uniformity of AH film while taking P-E loop measurements at 2 positions under 3 voltages 80V, 90V and 99.9V as seen in Figure 5.21. The Figure 5.21 authenticates the consistency of AH film also. The different positions are shown in

Figure **5.22**. As the AH film doesn't saturate even at 100V so we cannot opt for remanent protocol measurements.

The data are validating the facts that there is concomitant rise in polarization in heterostructure compared to BFO bare film.

(a)

(b)

(c)
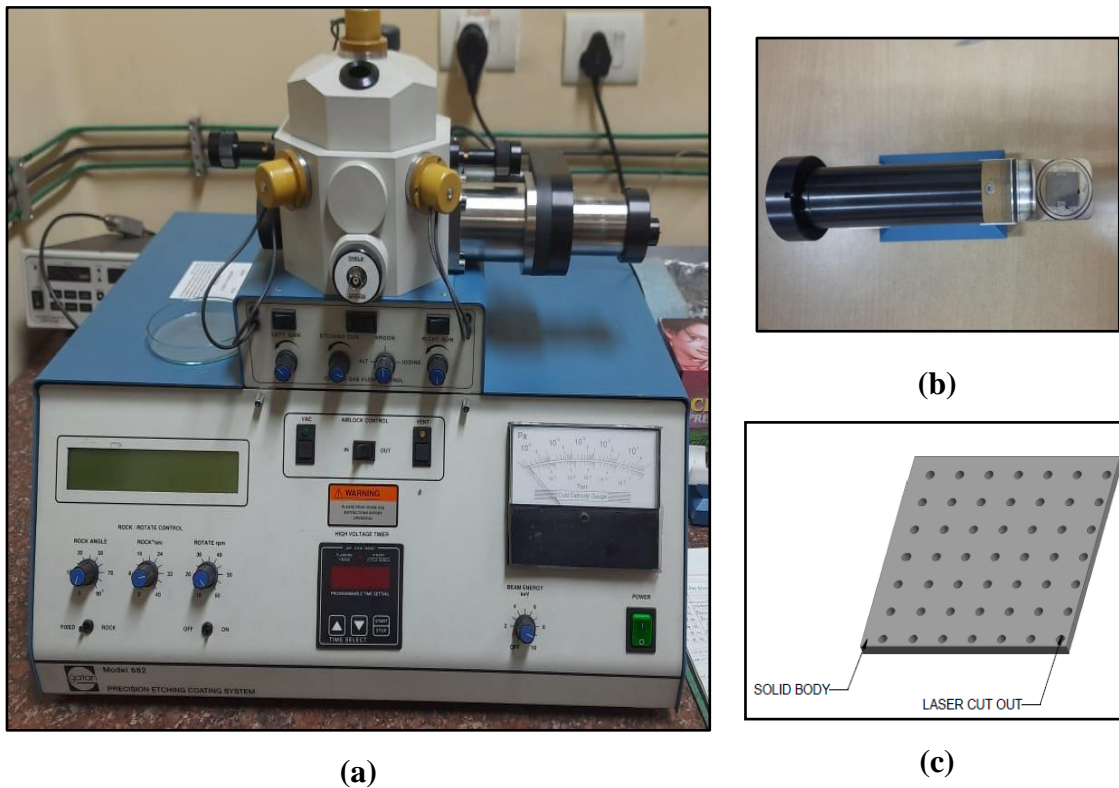
Figure 5.16 The Precision Coating System (a); The substrate holder for deposition (b); the electroding mask layout (c).
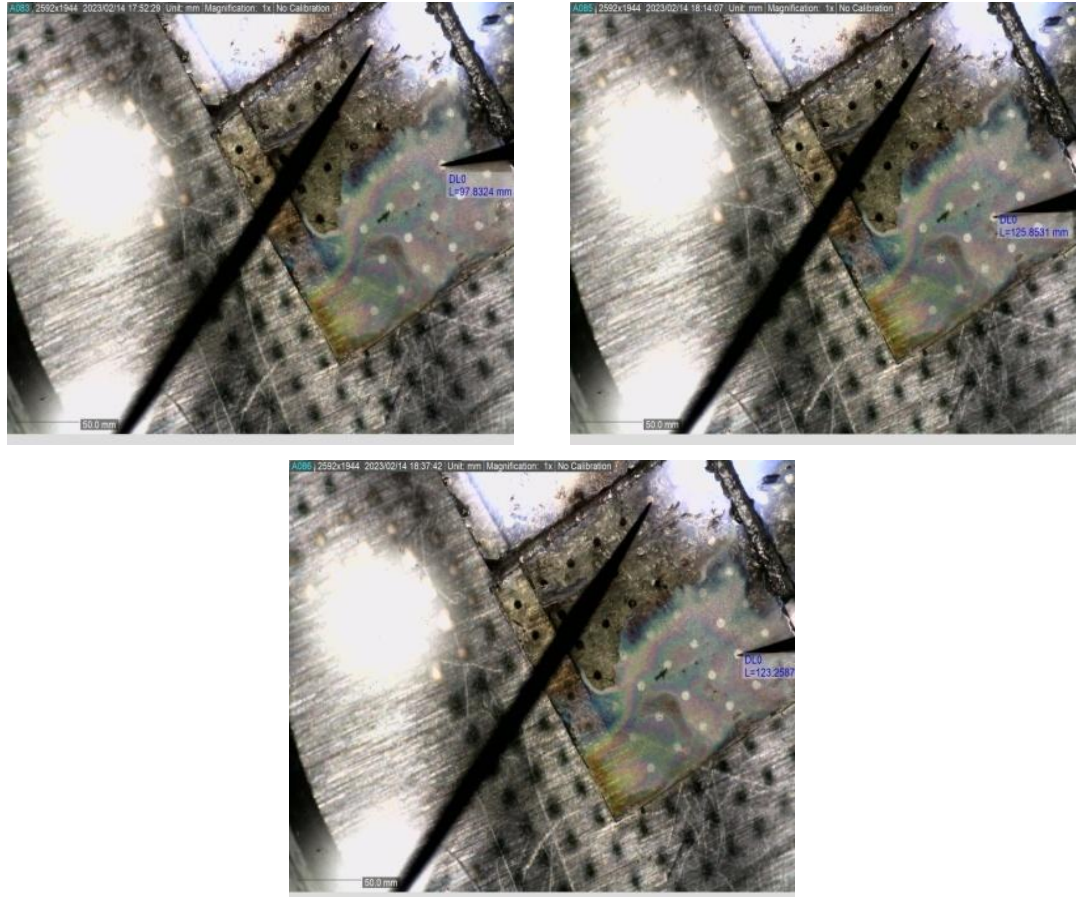
Figure 5.17 position of 2 probes corresponds to Pos1, Pos2 and Pos3 for BFO
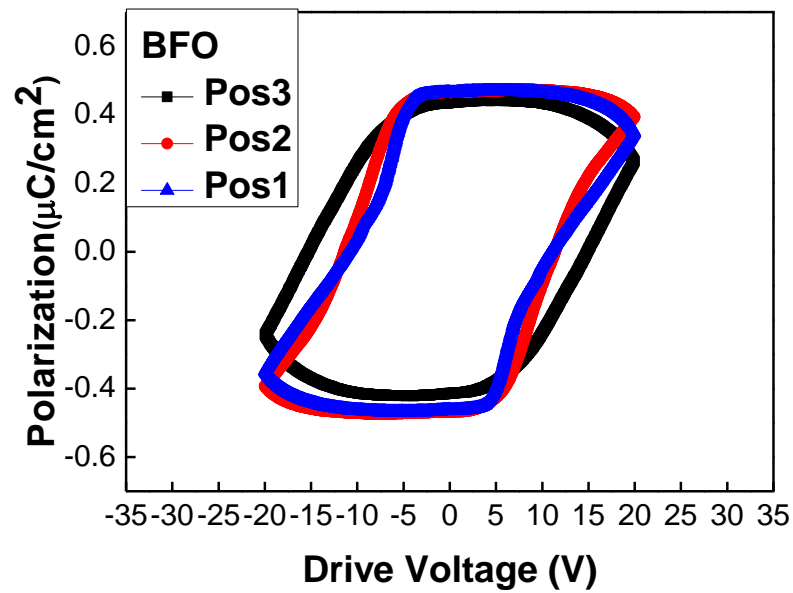
Figure 5.18 Room temperature P-E Hysteresis loop of BFO measured at 20V at various positions
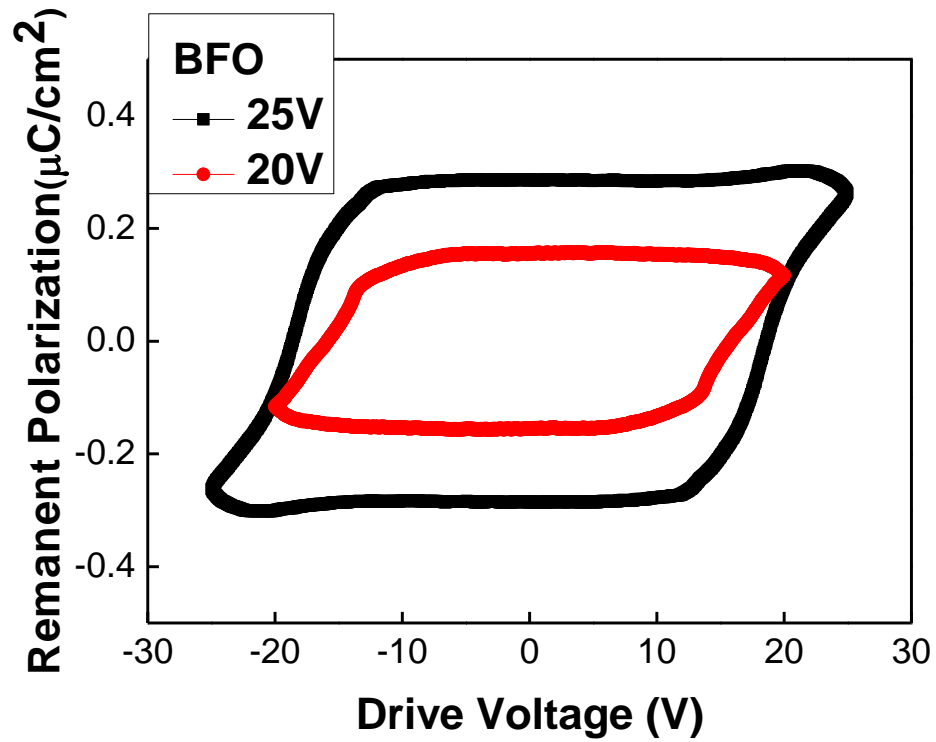
Figure 5.19 Room temperature Remanent loop of BFO measured at 20V and 25V
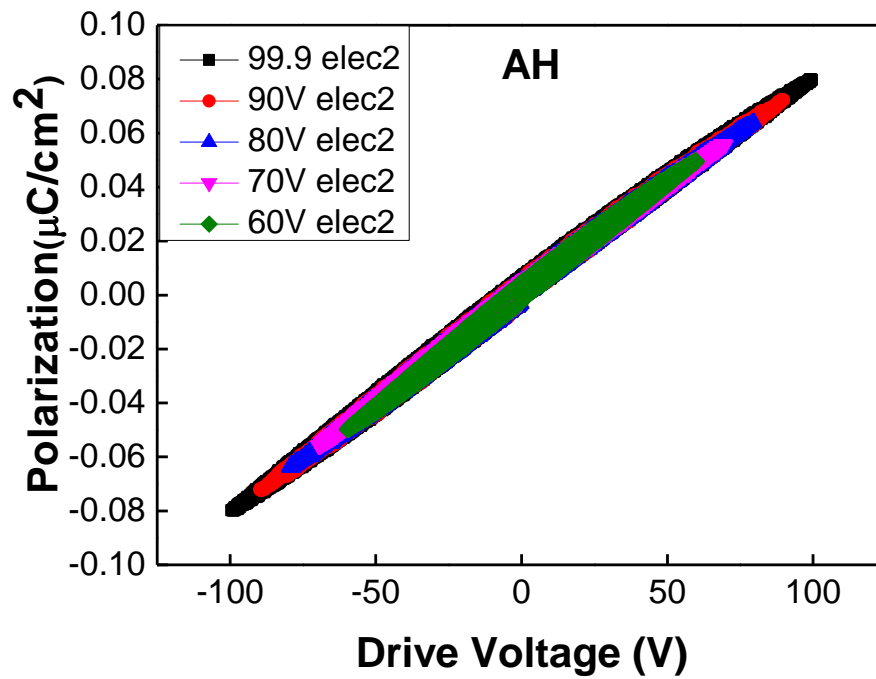
Figure 5.20 Room temperature P-E Hysteresis loop of heterostructure (AH) measured under different voltages

(a)

(b)

(c)
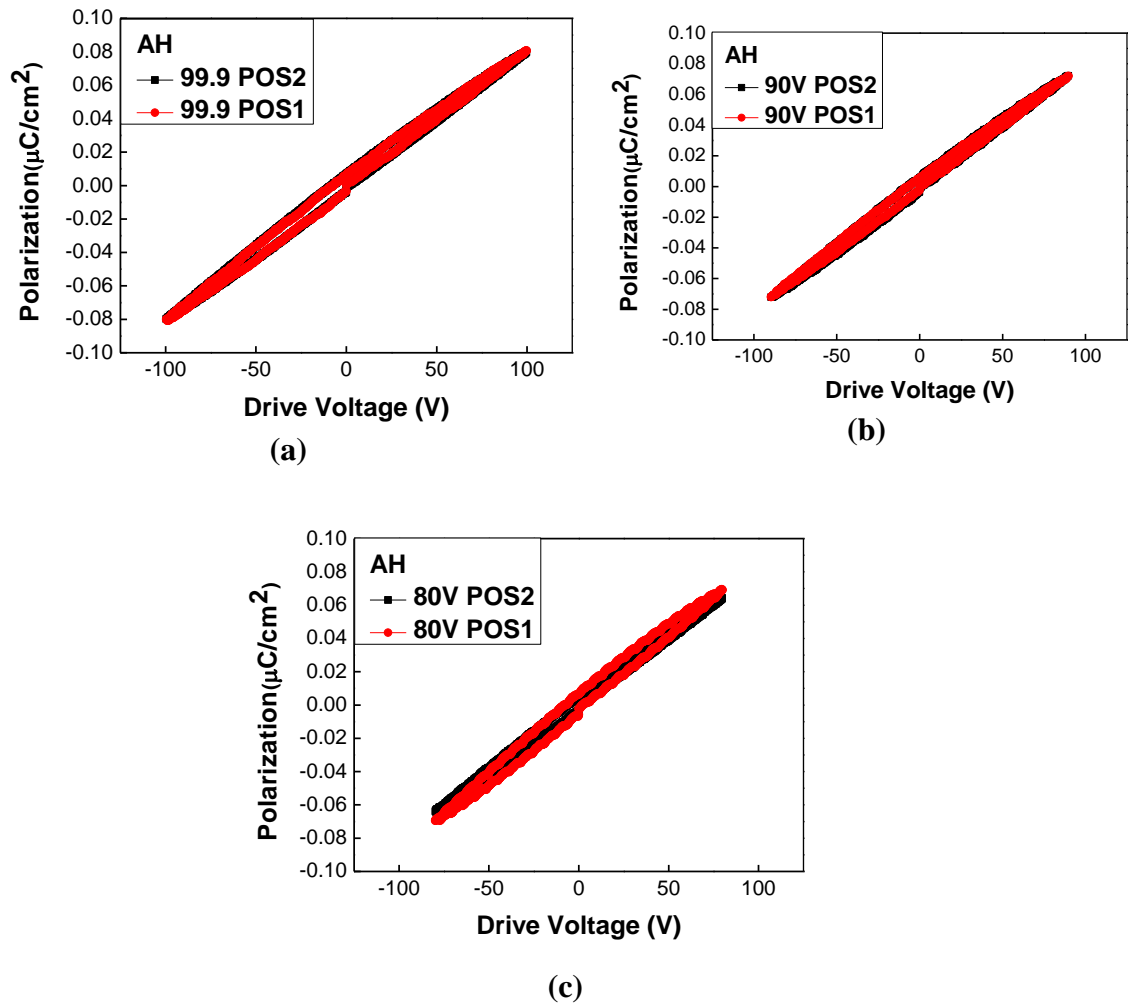
Figure 5.21 Room temperature P-E Hysteresis loop of heterostructure (AH) measured under different voltages at various positions
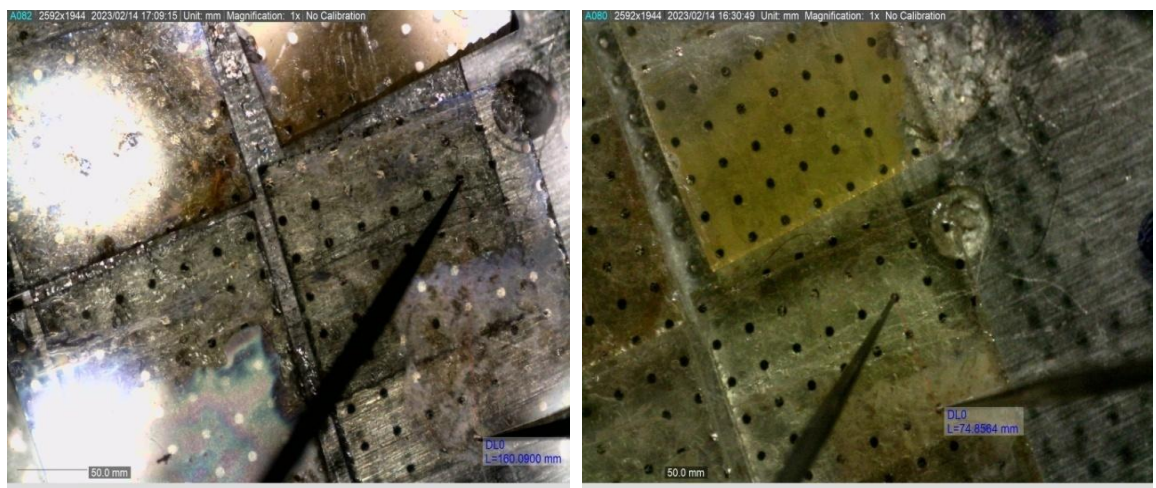
Figure 5.22 position of 2 probes corresponds to Pos1, Pos2 for heterostructure (AH)

[185]

5.5 <u>Chapter summary</u>

The primary focus of this work was to produce good quality BFO thin films using cost effective raw materials and simple sol-gel/spin coating processing route. To minimize the costs, we have used metal nitrates instead of the more expensive metal alkoxides and have employed acetic acid instead of acetic anhydride as chelating agent. Although some limitations were faced, we believe our goal has been largely achieved in that as we have managed to tune the processing parameters and fabricate dense, well crystallized films with very good phase purity. Our findings can be summarized as follows:

a) The method of solution dispensation is very important in producing films with maximal coverage of the substrate. We have found that dispensing the liquid solution in static mode that is before spin starts yielded the best results. We have opted for 50μL dispersion in each layer at 3000 rpm spinning and single layer capitulates the ideal homogeneity.

b) Preheating of substrates is an essential step in producing smooth, continuous films. A preheat temperature of 70° C was enough for smooth film formation than rougher and more discontinuous films. On the other hand, preheat temperature did not have any effect on phase formation.

c) The choice of substrate was found to be of lesser significance. Both the substrates were used for different study. FTO substrate was used for morphological study and electrical measurements. The magnetic study was performed on Si substrate.

d) To remove unwanted white cast we have chosen gelation along with drying schedule. For satisfactory formation of the perovskite phase and suppression of parasitic phases, 500° C was deemed the most suitable annealing temperature. Lower temperatures produced phase mixtures and/or underdeveloped microstructure whereas the glass substrate could not tolerate higher temperatures.

e) Surprisingly, our chosen processing route and starting chemistry was proven to be quite effective in producing phase pure BFO, even in case of stoichiometric Bi:Fe ratio was taken instead of excess Bi. The molarity of the solution 0.3M yielded perfect film. Similarly, 0.005g/ml wt% of rGO stock solution provides thin layer.

f) Magnetization measurements confirmed the change in magnetic nature of the heterostructure compared to BFO pure films.

g) The ferroelectric measurement also reconfirms the huge change in Polarizartion in heterostructure compared to BFO bare film.

So, we noticed that not only composite structure but also heterostructure of rGO/BFO can spontaneously alter the natures of BFO's magnetic as well as ferroelectricity. The aim that we have taken to make uniform films under cheapest and easiest techniques is totally accomplished

and has been authenticated by not only morphologically but also from the measurement of ferroelectricity.

This genre of field is still untouched and we also need more rigorous measurements to completely understand the state of art of physics of these changes.

5.6 <u>Bibliography</u>

[1] Yang, H.X., Hallal, A., Terrade, D., Waintal, X., Roche, S. and Chshiev, M., 2013. Proximity effects induced in graphene by magnetic insulators: first-principles calculations on spin filtering and exchange-splitting gaps. *Physical review letters*, *110*(4), p.046603.

[2] Sakai, S., Majumdar, S., Popov, Z.I., Avramov, P.V., Entani, S., Hasegawa, Y., Yamada, Y., Huhtinen, H., Naramoto, H., Sorokin, P.B. and Yamauchi, Y., 2016. Proximity-induced spin polarization of graphene in contact with half-metallic manganite. *ACS nano*, *10*(8), pp.7532-7541.

[3] Qiao, Z., Ren, W., Chen, H., Bellaiche, L., Zhang, Z., MacDonald, A.H. and Niu, Q., 2014. Quantum anomalous Hall effect in graphene proximity coupled to an antiferromagnetic insulator. *Physical review letters*, *112*(11), p.116404.

[4] Vobornik, I., Manju, U., Fujii, J., Borgatti, F., Torelli, P., Krizmancic, D., Hor, Y.S., Cava, R.J. and Panaccione, G., 2011. Magnetic proximity effect as a pathway to spintronic applications of topological insulators. *Nano letters*, *11*(10), pp.4079-4082.

[5] Takenaka, H., Sandhoefner, S., Kovalev, A.A. and Tsymbal, E.Y., 2019. Magnetoelectric control of topological phases in graphene. *Physical Review B*, *100*(12), p.125156.

[6] Zanolli, Z., 2016. Graphene-multiferroic interfaces for spintronics applications. *Scientific reports*, *6*(1), pp.1-6.

[7] Wang, Z., Tang, C., Sachs, R., Barlas, Y. and Shi, J., 2015. Proximity-induced ferromagnetism in graphene revealed by the anomalous Hall effect. *Physical review letters*, *114*(1), p.016603.

[8] Leutenantsmeyer, J.C., Kaverzin, A.A., Wojtaszek, M. and Van Wees, B.J., 2016. Proximity induced room temperature ferromagnetism in graphene probed with spin currents. *2D Materials*, *4*(1), p.014001.

[9] Mendes, J.B.S., Santos, O.A., Meireles, L.M., Lacerda, R.G., Vilela-Leão, L.H., Machado, F.L.A., Rodríguez-Suárez, R.L., Azevedo, A. and Rezende, S.M., 2015. Spin-current to charge-current conversion and magnetoresistance in a hybrid structure of graphene and yttrium iron garnet. *Physical review letters*, *115*(22), p.226601.

[187]

[10] Evelt, M., Ochoa, H., Dzyapko, O., Demidov, V.E., Yurgens, A., Sun, J., Tserkovnyak, Y., Bessonov, V., Rinkevich, A.B. and Demokritov, S.O., 2017. Chiral charge pumping in graphene deposited on a magnetic insulator. *Physical Review B*, *95*(2), p.024408.

[11] Wei, P., Lee, S., Lemaitre, F., Pinel, L., Cutaia, D., Cha, W., Katmis, F., Zhu, Y., Heiman, D., Hone, J. and Moodera, J.S., 2016. Strong interfacial exchange field in the graphene/EuS heterostructure. *Nature materials*, *15*(7), pp.711-716.

[12] Wu, Y.F., Song, H.D., Zhang, L., Yang, X., Ren, Z., Liu, D., Wu, H.C., Wu, J., Li, J.G., Jia, Z. and Yan, B., 2017. Magnetic proximity effect in graphene coupled to a BiFe O 3 nanoplate. *Physical Review B*, *95*(19), p.195426.

[13] Song, H.D., Wu, Y.F., Yang, X., Ren, Z., Ke, X., Kurttepeli, M., Tendeloo, G.V., Liu, D., Wu, H.C., Yan, B. and Wu, X., 2018. Asymmetric modulation on exchange field in a graphene/BiFeO3 heterostructure by external magnetic field. *Nano letters*, *18*(4), pp.2435-2441.

[14] Santos, E.J., 2013. Carrier-mediated magnetoelectric coupling in functionalized graphene. *ACS nano*, *7*(11), pp.9927-9932.

[15] Li, Y., Sun, X.Y., Xu, C.Y., Cao, J., Sun, Z.Y. and Zhen, L., 2018. Ferroelectric resistive switching behavior in two-dimensional materials/BiFeO 3 heterojunctions. *Nanoscale*, *10*(48), pp.23080-23086.

[16] Fujii, T., Shimizu, S., Kajima, A. and Miyama, T., 1986. Film fabrication of solid solution of the BiFeO3-BaTiO3 system by rf-reactive sputtering. *Journal of Magnetism and Magnetic Materials*, *54*, pp.1303-1304.

[17] Rao, B.U.M., Srinivasan, G., Babu, V.S. and Seehra, M.S., 1991. Magnetic properties of amorphous BiFeO3-PbZrO3 sputtered films. *Journal of applied physics*, *69*(8), pp.5463-5465.

[18] Huang, C.W., Chu, Y.H., Chen, Z.H., Wang, J., Sritharan, T., He, Q., Ramesh, R. and Chen, L., 2010. Strain-driven phase transitions and associated dielectric/piezoelectric anomalies in BiFeO 3 thin films. *Applied Physics Letters*, *97*(15), p.152901.

[19] Emery, S.B., Cheng, C.J., Kan, D., Rueckert, F.J., Alpay, S.P., Nagarajan, V., Takeuchi, I. and Wells, B.O., 2010. Phase coexistence near a morphotropic phase boundary in Sm-doped BiFeO 3 films. *Applied physics letters*, *97*(15), p.152902.

[20] Ueda, K., Tabata, H. and Kawai, T., 1999. Coexistence of ferroelectricity and ferromagnetism in BiFeO 3–BaTiO 3 thin films at room temperature. *Applied physics letters*, *75*(4), pp.555-557.

[21] Pavlovic, N., D'Haen, J., Modarresi, H., Riskin, A., De Dobbelaere, C., Van Bael, M.J., Temst, K., Hardy, A. and Van Bael, M.K., 2015. BiFeO 3 thin films via

aqueous solution deposition: a study of phase formation and stabilization. *Journal of Materials Science*, *50*, pp.4463-4476.

[22] Tang, X., Dai, J., Zhu, X., Lin, J., Chang, Q., Wu, D., Song, W. and Sun, Y., 2012. Thickness-dependent dielectric, ferroelectric, and magnetodielectric properties of BiFeO3 thin films derived by chemical solution deposition. *Journal of the American Ceramic Society*, *95*(2), pp.538-544.

[23] Singh, S.K., Ishiwara, H. and Maruyama, K., 2006. Enhanced polarization and reduced leakage current in Bi Fe O 3 thin films fabricated by chemical solution deposition. *Journal of applied physics*, *100*(6), p.064102.

[24] Gumiel, C., Vranken, T., Bernardo, M.S., Jardiel, T., Hardy, A., Van Bael, M.K. and Peiteado, M., 2018. Thin film composites in the BiFeO3–Bi4Ti3O12 system obtained by an aqueous solution-gel deposition methodology. *boletín de la sociedad española de cerámica y vidrio*, *57*(1), pp.19-28.

[25] Shah, S.M.H., Akbar, A., Riaz, S., Atiq, S. and Naseem, S., 2014. Magnetic, structural, and dielectric properties of Bi 1-x K x FeO 3 thin films using sol-gel. *IEEE Transactions on Magnetics*, *50*(8), pp.1-4.

[26] Tang, X., Zhu, X., Dai, J. and Sun, Y., 2013. Self-limited grain growth, dielectric, leakage and ferroelectric properties of nanocrystalline BiFeO3 thin films by chemical solution deposition. *Acta materialia*, *61*(5), pp.1739-1747.

[27] Zeng, J., Tang, Z.H., Tang, M.H., Xu, D.L., Xiao, Y.G., Zeng, B.W., Li, L.Q. and Zhou, Y.C., 2014. Enhanced ferroelectric, dielectric and leakage properties in Ce and Ti co-doping BiFeO 3 thin films. *Journal of sol-gel science and technology*, *72*, pp.587-592.

[28] Li, Z., Zhao, Y., Li, W., Song, R., Zhang, Y., Zhao, W., Wang, Z., Peng, Y. and Fei, W., 2021. Enhanced energy storage properties of amorphous BiFeO3/Al2O3 multilayers. *Journal of Materials Research and Technology*, *11*, pp.1852-1858.

[29] Liu, L., Xu, K., Li, Q., Daniels, J., Zhou, H., Li, J., Zhu, J., Seidel, J. and Li, J.F., 2021. Giant domain wall conductivity in self-assembled BiFeO3 nanocrystals. *Advanced Functional Materials*, *31*(1), p.2005876.

[30] Tan, G., Ren, X., Liu, Y., Guo, M., Lv, L., Li, J., Xue, M., Ren, H., Xia, A. and Liu, W., 2021. Diode-like rectification characteristics of BiFeO3-based/Zn1-xNixFe2O4 bilayered films for application of ferroelectric field effect transistors. *Journal of Alloys and Compounds*, *851*, p.156818.

[31] Wang, Y., Jiang, Q.H., He, H.C. and Nan, C.W., 2006. Multiferroic Bi Fe O 3 thin films prepared via a simple sol-gel method. *Applied Physics Letters*, *88*(14), p.142503.

[189]

[32] Wang, Y. and Nan, C.W., 2006. Enhanced ferroelectricity in Ti-doped multiferroic Bi Fe O 3 thin films. *Applied Physics Letters*, *89*(5), p.052903.

[33] Kharel, P., Talebi, S., Ramachandran, B., Dixit, A., Naik, V.M., Sahana, M.B., Sudakar, C., Naik, R., Rao, M.S.R. and Lawes, G., 2008. Structural, magnetic, and electrical studies on polycrystalline transition-metal-doped BiFeO3 thin films. *Journal of Physics: Condensed Matter*, *21*(3), p.036001.

[34] Singh, S.K., Ueno, R., Funakubo, H., Uchida, H., Koda, S. and Ishiwara, H., 2005. Dependence of ferroelectric properties on thickness of BiFeO3 thin films fabricated by chemical solution deposition. *Japanese journal of applied physics*, *44*(12R), p.8525.

[35] Tang, X., Dai, J., Zhu, X., Yin, L., Ang, R., Song, W., Yang, Z., Sun, Y. and Zhang, R., 2010. Individual-Layer Thickness Effects on the Preferred c-Axis-Oriented BiFeO3 Films by Chemical Solution Deposition. *Journal of the American Ceramic Society*, *93*(6), pp.1682-1687.

[36] Nakamura, Y., Nakashima, S. and Okuyama, M., 2009. Improvement of ferroelectric properties of BiFeO 3 thin films by postmetallization annealing and electric field application. *Journal of Applied Physics*, *105*(6), p.061616.

[37] Nakamura, Y., Yun, K.Y., Nakashima, S. and Okuyama, M., 2007. Sol-gel preparation and characterization of multiferroic BiFeO3 thin films with various Bi/Fe ratio. *Integrated Ferroelectrics*, *95*(1), pp.226-233.

[38] Valasek, J., 1921. Piezo-electric and allied phenomena in Rochelle salt. *Physical review*, *17*(4), p.475.

[39] Yun, K.Y., Noda, M. and Okuyama, M., 2003. Effects of annealing atmosphere on crystallization and electrical properties in BiFeO {sub 3} thin films by chemical solution deposition (CSD). *Journal of the Korean Physical Society*, *42*.

[40] Xiao, K., Deng, W., Keum, J.K., Yoon, M., Vlassiouk, I.V., Clark, K.W., Li, A.P., Kravchenko, I.I., Gu, G., Payzant, E.A. and Sumpter, B.G., 2013. Surface-induced orientation control of CuPc molecules for the epitaxial growth of highly ordered organic crystals on graphene. *Journal of the American Chemical Society*, *135*(9), pp.3680-3687.

[41] Mrkyvkova, N., Hodas, M., Hagara, J., Nadazdy, P., Halahovets, Y., Bodik, M., Tokar, K., Chai, J.W., Wang, S.J., Chi, D.Z. and Chumakov, A., 2019. Diindenoperylene thin-film structure on MoS2 monolayer. *Applied Physics Letters*, *114*(25), p.251906.

[42] Skrypnychuk, V., Boulanger, N., Yu, V., Hilke, M., Mannsfeld, S.C., Toney, M.F. and Barbero, D.R., 2015. Enhanced vertical charge transport in a semiconducting

P3HT thin film on single layer graphene. *Advanced Functional Materials*, *25*(5), pp.664-670.

[43] Jo, S.B., Kim, H.H., Lee, H., Kang, B., Lee, S., Sim, M., Kim, M., Lee, W.H. and Cho, K., 2015. Boosting photon harvesting in organic solar cells with highly oriented molecular crystals via graphene–organic heterointerface. *ACS nano*, *9*(8), pp.8206-8219.

[44] Nguyen, N.N., Jo, S.B., Lee, S.K., Sin, D.H., Kang, B., Kim, H.H., Lee, H. and Cho, K., 2015. Atomically thin epitaxial template for organic crystal growth using graphene with controlled surface wettability. *Nano Letters*, *15*(4), pp.2474-2484.

[45] Lee, W.H., Park, J., Sim, S.H., Lim, S., Kim, K.S., Hong, B.H. and Cho, K., 2011. Surface-directed molecular assembly of pentacene on monolayer graphene for high-performance organic transistors. *Journal of the American Chemical Society*, *133*(12), pp.4447-4454.

[46] Wang, D.W., Li, F., Zhao, J., Ren, W., Chen, Z.G., Tan, J., Wu, Z.S., Gentle, I., Lu, G.Q. and Cheng, H.M., 2009. Fabrication of graphene/polyaniline composite paper via in situ anodic electropolymerization for high-performance flexible electrode. *ACS nano*, *3*(7), pp.1745-1752.

[47] Cao, X., Qi, D., Yin, S., Bu, J., Li, F., Goh, C.F., Zhang, S. and Chen, X., 2013. Ambient fabrication of large-area graphene films via a synchronous reduction and assembly strategy. *Advanced Materials*, *25*(21), pp.2957-2962.

[48] Karthick, R., Brindha, M., Selvaraj, M. and Ramu, S., 2013. Stable colloidal dispersion of functionalized reduced graphene oxide in aqueous medium for transparent conductive film. *Journal of colloid and interface science*, *406*, pp.69-74.

[49] Sun, H.B., Yang, J., Zhou, Y.Z., Zhao, N. and Li, D., 2014. Preparation of reduced graphene oxide films by dip coating technique and their electrical conductivity. *Materials Technology*, *29*(1), pp.14-20.

[50] Rosas-Laverde, N.M., Pruna, A. and Busquets-Mataix, D., 2020. Improving electrochemical properties of polypyrrole coatings by graphene oxide and carbon nanotubes. *Nanomaterials*, *10*(3), p.507.

[51] Sundramoorthy, A.K., Wang, Y., Wang, J., Che, J., Thong, Y.X., Lu, A.C.W. and Chan-Park, M.B., 2015. Lateral assembly of oxidized graphene flakes into large-scale transparent conductive thin films with a three-dimensional surfactant 4-sulfocalix [4] arene. *Scientific Reports*, *5*(1), pp.1-13.

[52] Kumar, P., Shahzad, F., Yu, S., Hong, S.M., Kim, Y.H. and Koo, C.M., 2015. Large-area reduced graphene oxide thin film with excellent thermal conductivity and electromagnetic interference shielding effectiveness. *Carbon*, *94*, pp.494-500.

[191]

[53] Shi, L., Yang, J., Huang, Z., Li, J., Tang, Z., Li, Y. and Zheng, Q., 2013. Fabrication of transparent, flexible conducing graphene thin films via soft transfer printing method. *Applied Surface Science*, *276*, pp.437-446.

[54] Shen, B., Zhai, W. and Zheng, W., 2014. Ultrathin flexible graphene film: an excellent thermal conducting material with efficient EMI shielding. *Advanced Functional Materials*, *24*(28), pp.4542-4548.

[55] Bi, H., Wan, S., Cao, X., Wu, X., Zhou, Y., Yin, K., Su, S., Ma, Q., Sindoro, M., Zhu, J. and Zhang, Z., 2019. A general and facile method for preparation of large-scale reduced graphene oxide films with controlled structures. *Carbon*, *143*, pp.162-171.

[56] An, S.J., Zhu, Y., Lee, S.H., Stoller, M.D., Emilsson, T., Park, S., Velamakanni, A., An, J. and Ruoff, R.S., 2010. Thin film fabrication and simultaneous anodic reduction of deposited graphene oxide platelets by electrophoretic deposition. *The Journal of Physical Chemistry Letters*, *1*(8), pp.1259-1263.

[57] Chen, Y., Zhang, X., Yu, P. and Ma, Y., 2010. Electrophoretic deposition of graphene nanosheets on nickel foams for electrochemical capacitors. *Journal of Power Sources*, *195*(9), pp.3031-3035.

[58] Liu, Y., Li, P., Wang, F., Fang, W., Xu, Z., Gao, W. and Gao, C., 2019. Rapid roll-to-roll production of graphene films using intensive Joule heating. *Carbon*, *155*, pp.462-468.

[59] Zheng, Q., Ip, W.H., Lin, X., Yousefi, N., Yeung, K.K., Li, Z. and Kim, J.K., 2011. Transparent conductive films consisting of ultralarge graphene sheets produced by Langmuir–Blodgett assembly. *ACS nano*, *5*(7), pp.6039-6051.

[60] Huang, P., Li, Y., Yang, G., Li, Z.X., Li, Y.Q., Hu, N., Fu, S.Y. and Novoselov, K.S., 2021. Graphene film for thermal management: A review. *Nano Materials Science*, *3*(1), pp.1-16.

6 Chapter

Study of soft ferromagnetism in BiFeO$_3$/Ag nano composites at room temperature

6.1 <u>Introduction</u>

We have already seen in Chapter 3 and Chapter 4 that rGO when covalently bonded can tune the magnetic property of multiferroic BiFeO$_3$ (BFO) but in hybrid structure without bonding even rGO nano film can change the magnetic property by a noticeable extent. We would now like to examine the properties of the nano composite or heterostructure of graphene and ferromagnetic BFO where the ferromagnetism in BFO is substantially stronger than what has so far been observed because of size effect alone. In this chapter we discuss or observation of enhanced ferromagnetism with more than an order of magnitude rise in saturation magnetization in a nano composite of BFO and silver (Ag) (BFO/Ag). Such enormous enhancement of room temperature ferromagnetism in nano scale BFO in presence of Ag has not yet been reported by others.

BFO is extensively used room temperature multiferroic material in different forms. The magnetic saturation can be tuned in BFO nano structures by tuning particle size[1], shapes[2], adding various individual dopants [3] [4] [5] [6] [7] [8], co-dopants [9] [10] [11] [12], surfactant[13] and making composite [14]. In the previous work of our groups[15] we have seen the importance of self-assembled BFO nano particle structures vis-a-vis isolated nano particles. Self-assembled nano composites of BFO–CoFe$_2$O$_4$, BFO–MgO, or BFO–MgAl$_2$O$_4$ were synthesized earlier[16] [17] [18] [19]by complicated techniques such as pulsed laser deposition combined with electron beam lithography. Nevertheless, an efficient process rendering self-assembled large area of perfectly ordered magnetoelectric nano composites has not been yet achieved[20].

Moreover, the finding of ferromagnetic magnetic nano particles (MNPs) or their clusters with relatively small size and high magnetic moment is still a subject of intense research. High magnetic moment metallic nano particles like Fe, Co and Ni and their oxide materials are

strongly reactive to oxygen and itself they are toxic which hinders their bio-application. Granados-Miralles *et al.*[21]showed that cobalt ferrite binary alloy family could be a great choice to match or surpass the high magnetic moment of permenant magnets of rare earth elements[22] [23]. As an approach towards rare earth free magnets $Fe_{65}Co_{35}$ alloy[24] among $Fe_{100-x}Co_x$ inter-metallic alloy family shows a high curie temperature low magnetocrystalline anisotropy, and high saturation magnetization of 240 emu/g that is more than three times higher than that of iron oxide MNPs (~ 70–80 emu/g)[25] [26].The main concern of these high moment particles are that they are unstable in air and difficult to synthesize compared to magnetic oxide materials[27]. To make the materials potent for in vivo bio-application we need core- shell sample where MNPs act as the core and biocompatible materials such as Gold (Au), silver (Ag), Silica (SiO_2) etc. and serve as the shells[28] [29].Among various types of nano particles, Ag nano particles are well-recognized as promising antimicrobial agents[30] and have the highest scattering cross section of existing plasmonic materials. There lies the difficulty in covering the FeCo MNPs with Ag partly because of the galvanic replacement reaction between FeCo and Ag ions[31].

In various cases diamagnetic Ag is used as shell to protect the large magnetic moment of the core even though it often results in decrease in the magnetic moment of the core. But in our work we report a novel approach of introducing Ag in BFO nano particle matrix. It enhances the magnetic moment of the particles so that we get a new material with high bio compatibility and magnetic moment much higher than bare nano particles. The charge transfer across the BFO/Ag interface and the specific pattern of self-assembly of the nanoparticles appear to be responsible for such an enormous enhancement in magnetization like an order of magnitude rise in saturation magnetization at room temperature than what is observed in bare BFO nano particles. The methods described in section 2.3.1.2 and 2.3.3 is followed for preparing BFO nanoparticles and BFO/Ag nano composites respectively. 2wt% nano composite (BFO/Ag-2) is only used to compare the magnetic properties.

6.2 <u>**Result and discussion**</u>

The nano composite, thus prepared, was characterized by powder x-ray diffraction. The particle morphology, pattern of self-assembly, and the concentration distribution of the elements (Bi, Fe, O, Ag) across different regions of the nano composite were investigated by using transmission electron microscopy (TEM) and energy dispersive x-ray spectra (EDX). The surface/interface electronic structure of Bi, Fe, O, and Ag was determined by x-ray photoelectron spectroscopy (XPS). The magnetization was measured by a Vibrating Sample Magnetometer (Lake Shore Model 7407). The magnetic domain structure was imaged at room temperature by magnetic force microscopy (LT AFM/MFM System of Nanomagnetics Instruments Ltd., Ankara, Turkey).

6.2.1 X-ray diffraction (XRD) pattern analysis

Figure 6.1 shows the room-temperature powder x-ray diffraction data of the BFO/Ag nano composite and also of bare nano particles (depicted as BFO) and their refinement by FullProf using both structural fitting and profile fitting. The crystallographic structure turns out to be rhombohedral ($R3c$ space group). Peaks corresponding to Ag could also be observed. The Ag assumes cubic structure of $Fm3m$ space group symmetry with lattice parameter $a = 4.087$Å. Multiphase refinement consisting of 3 phases of BFO turn out to be good fit compared to 2 as seen in Table 6.1 for both cases BFO and BFO/Ag.

Multiphase refinement yields the volume fraction of the respective phases - ~64.54% $R3c$, ~14.30% of $I23$ phases, ~5.05% of $Pbam$ phases of BFO and ~16.11% of Ag cubic phase. The refined data of bare BFO nano particles also consists of multiphases of the respective phases - ~96.08% of $R3c$, ~3.01% of $I23$ phases, and ~0.91% of $Pbam$ phases of BFO. A small amount of impurity $Bi_{25}FeO_{39}$ (I23) and $Bi_2Fe_4O_9$ (Pbam) phases were also found to be present in both BFO and BFO/Ag so that the impurity phases contribute same in both BFO and BFO/Ag. Comparing with the data of bare BFO nano particles does not indicate formation of BFO/Ag solid solution. Therefore, interface interaction appears to be more important in the present case. The structural details such as the ion positions, lattice parameters, as well as the fit statistics are included in Table 6.2.

(a)
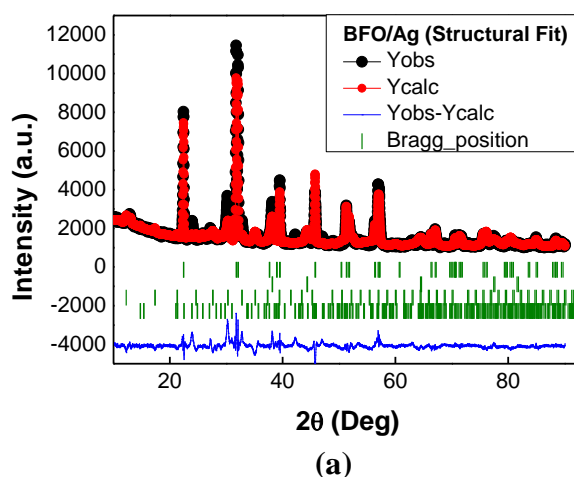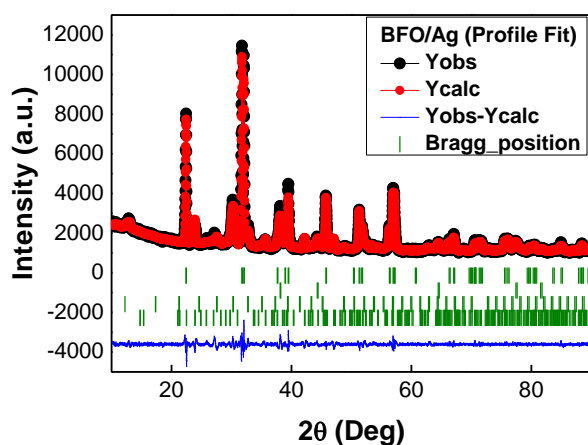
(b)
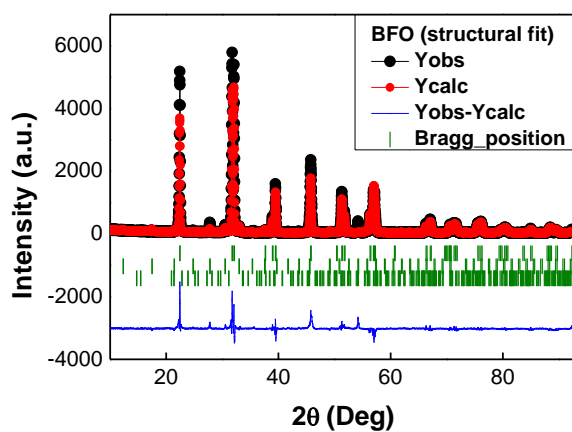
(c)
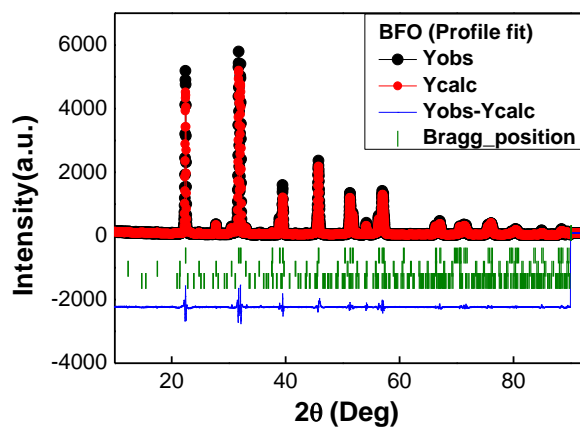
(d)

Figure 6.1The room temperature powder x-ray diffraction (XRD) pattern and its refinement by FullProf of BFO/Ag nano composite of Structural fit (a) and profile fitting (b); and of BFO of Structural fit (c) and profile fitting (d)

[196]

Table 6.1 Summary of Goodness of fit of samples considering multiphase analysis

Sample	No of phases	Volume percentage of phases				Goodness of Fit
		R3c	*Ag*	*I23*	*Pbam*	
BFO/AG	4 phase	64.54	16.11	14.3	5.05	R-Factors: 6.08 8.58 Chi²: 11.4
	3 phase	67.97	16.97	15.06	-	R-Factors: 6.06 8.68 Chi²: 11.7
	2 phase	80.02	19.98	-	-	R-Factors: 6.09 10.1 Chi²: 15.8
BFO	3 phase	96.08	-	3.01	0.91	R-Factors: 16.5 22.0 Chi²: 6.80
	2 phase	98.35	-	1.65		R-Factors: 17.0 22.6 Chi²: 7.14
	1 phase	100	-	-	-	R-Factors: 17.8 24.0 Chi²: 8.11

Table 6.2 Summary of ion positions and lattice parameters along with goodness of fit from the refinement of XRD data for BFO and BFO/Ag

BFO/Ag composite
$R_p=6.08, R_{wp}=8.58, \chi^2=11.4$

Sample	Space group	Ion Pos	x	y	z	Occ	Lattice Parameters			
BFO 64.54 vol%	Hexagonal R3c	**Bi**	0	0	0.00619	0.33656	a	5.580052	α	90
		Fe	0	0	0.28289	0.3333	b	5.580052	β	90
		O	0.44523	0.01036	0.03435	1	c	13.87313	γ	120
Bi₂₅FeO₃₉ 14.3 vol%	Cubic I23	**Bi1**	0.23314	0.28626	0.00297	1.18752	a	10.22322	α	90
		Bi2	0	0	0	0.07184	b	10.22322	β	90
		Fe	0	0	0	0.04398	c	10.22322	γ	90
		O1	0.43993	0.43993	0.43993	0.66636				
		O2	0.76098	0.46415	1.43628	1				

[197]

		O3	2.77206	2.77206	2.77206	0.33				
Bi₂Fe₄O₉ 5.05 vol%	Cubic Pbam	Bi	0.20678	0.17093	0	0.59967		7.910437		90
		Fe1	0.5	0	0.29473	0.5		8.439855		90
		Fe2	0.69462	0.52178	0.5	0.5		6.00317		90
		O1	0	0	0.5	0.25				
		O2	0.93213	4.11763	0.51397	1				
		O3	-0.31779	5.32817	0.5	0.5				
Ag 16.11 vol%	Cubic Fm-3m	Ag	0	0	0	1	a	4.085553	α	90
							b	4.085553	β	90
							c	4.085553	γ	90

<div align="center">

BFO
$R_p=16.05, R_{wp}=22.0, \chi^2=6.80$

</div>

BFO 96.08 vol%	Hexagonal R3c	Bi	0	0	0.00157	0.33015	a	5.580049	α	90
		Fe	0	0	0.27948	0.33585	b	5.580049	β	90
		O	0.42046	-0.03243	0.04841	1	c	13.87601	γ	120
Bi₂₅FeO₃₉ 3.01 vol%	Cubic I23	Bi1	0.19814	0.29264	0.05401	1	a	10.15813	α	90
		Bi2	0	0	0	0.04333	b	10.15813	β	90
		Fe	0	0	0	0.035	c	10.15813	γ	90
		O1	0.37431	0.37431	0.37431	0.33333				

		O2	0.2316	1.21713	1.34701	1					
		O3	3.90874	3.90874	3.90874	0.33333					
Bi₂Fe₄O₉ 0.91 vol%	Cubic Pbam	**Bi**	0.31896	0.14354	0	0.59967	**a**	7.803404	**α**	90	
		Fe1	0.5	0	0.29473	0.5	**b**	8.492556	**β**	90	
		Fe2	0.69462	0.52178	0.5	0.5	**c**	6.024457	**γ**	90	
		O1	0	0	0.5	0.25					
		O2	0.93213	4.11763	0.51397	1					
		Bi	-0.31779	5.32817	0.5	0.5					

6.2.2 <u>Morphological analysis</u>

The particle morphology, self-assembly pattern, and the charge transfer across the BFO and Ag nanoparticle interface were investigated in detail by TEM, EDX. Figure 6.2 shows the representative bright field TEM images of the nano composite under different length scales (~100nm and ~2μm). The pattern of self-assembly and the particle size could be observed and determined from these images. The average size of the BFO particles is ~32 nm as seen in histogram image. It appears that a chain-like self-assembled structure has formed with finer Ag nano particles (average size ~5 nm) surrounding the BFO ones. From, Figure 6.2 we can be easily seen that BFO nano particles are a chain like structure which is wrapped up in silver matrix. The representative TEM images of the nano scale BFO reference sample is shown in Figure 6.3 and where the average particle size is found to be ~36nm from the histogram plot.

We recorded the high resolution TEM (HRTEM) images across the BFO and Ag nano particle interfaces. The images were fast Fourier transformed (FFT) and then inverted (inverse FFT) to generate clearer views of the lattice fringes. HRTEM image is analysed region wise using ImageJ software and found both the presence of BFO and Ag planes as shown in Figure 6.4. The planes in the RHS of Figure correspond to enlarged view of the region marked in rectangle in the LHS. The corresponding `d' values were determined. It appears that images

showing the orientation of the- (a) (012) and (200); (b) (104) and (111); (c) (012) and (111) planes of, respectively, BFO and Ag. These are the evidences of composite formation of BFO/Ag with the existence of distinct phases and also the dominance of R3c space group in BFO.

The scanning tunneling electron microscopy (STEM) and the high-angle annular dark field (HAADF) images were also recorded at different regions of the nano composite (Figure 6.5). The EDX mapping of the elements Bi, Fe, O, and Ag across those regions confirms the distribution pattern of the BFO and Ag nano particles. In order to obtain a clearer view, the line scans of the element concentration were recorded across the interfaces between the BFO and Ag nano particles at different regions of the nano composite (Figure 6.6).

Combining the TEM, HRTEM, STEM images and the mapping of the concentration of the elements across the interfaces between BFO and Ag nano particles by line scans it is possible to clearly notice how the nano particles are distributed or, in other words, the specific self-assembly patterns of the BFO and Ag nano particles. Such a pattern of self-assembly appears to have maximized the interface area which, in turn, yields such enormous rise in saturation magnetization.

(a)

[200]
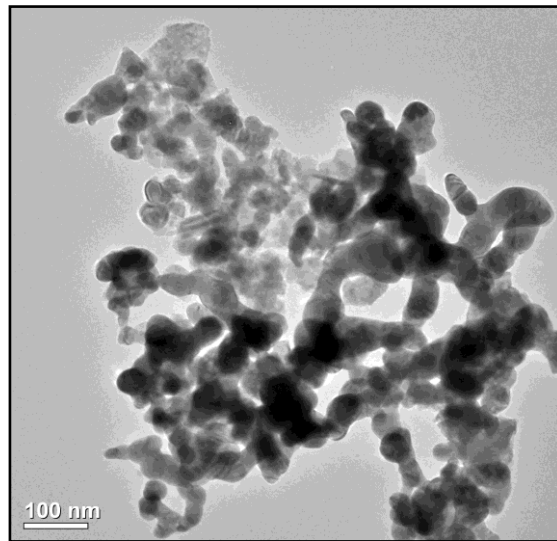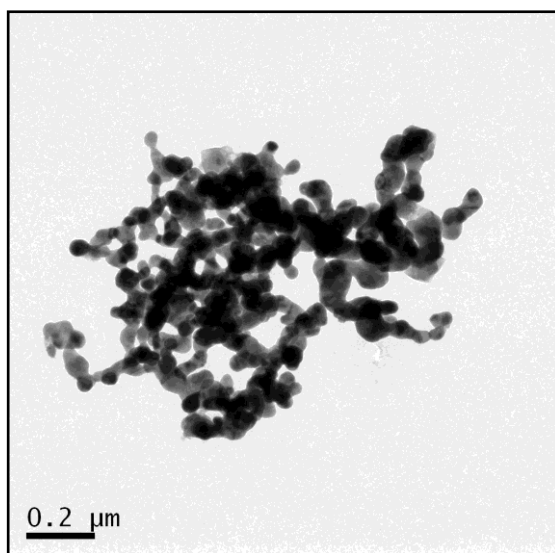
(b)
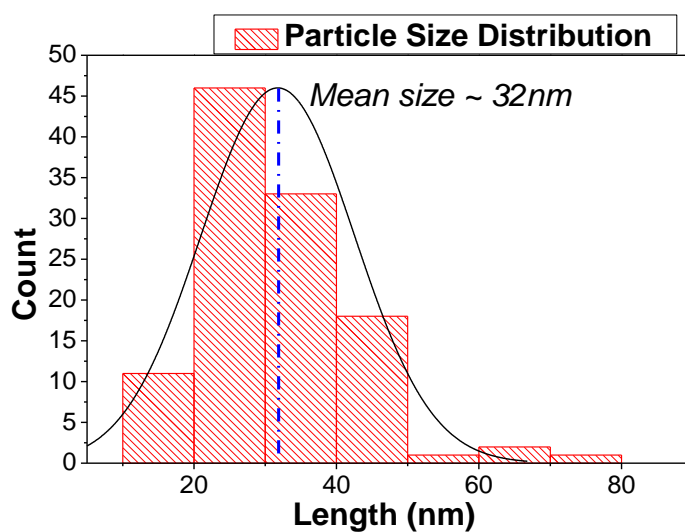
(c)

Figure 6.2 Bright Field transmission electron microscopy (TEM) image of the BFO/Ag nanocomposite under 100nm (a) and 0.2µm (b) length scale; and (c) Histogram plot of particle size of BFO nano particles in BFO/AG nano composite.
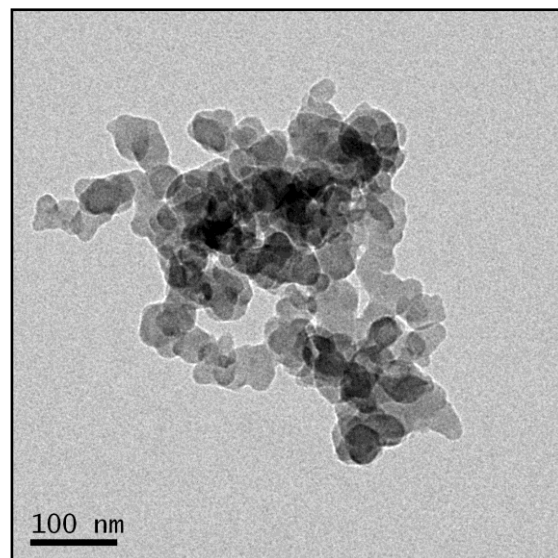
(a)
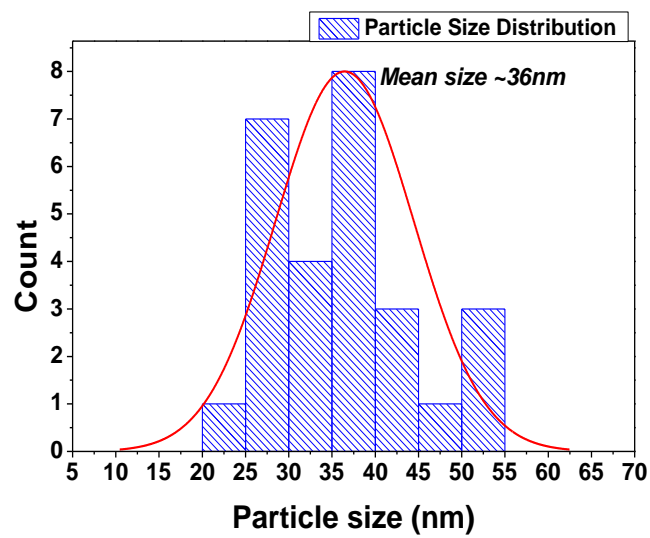
(b)

Figure 6.3 Representative transmission electron microscopy (TEM) image of the reference BFO nano particles; (b) Histogram plot of particle size of BFO nano particles.
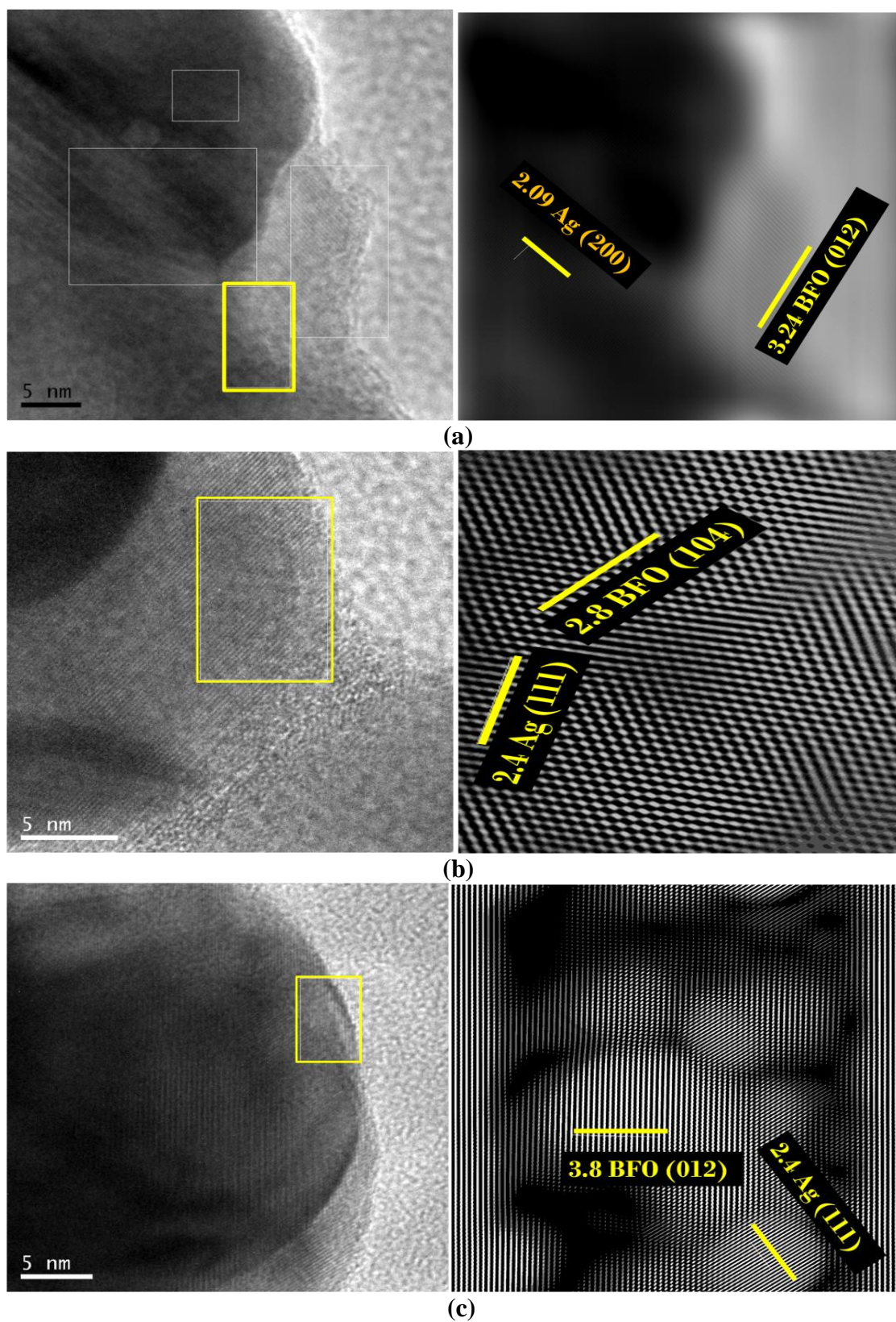
Figure 6.4 high resolution TEM (HRTEM) image and their inverse FFT corresponding to the rectangular part seen for various regions (a), (b) and (c).
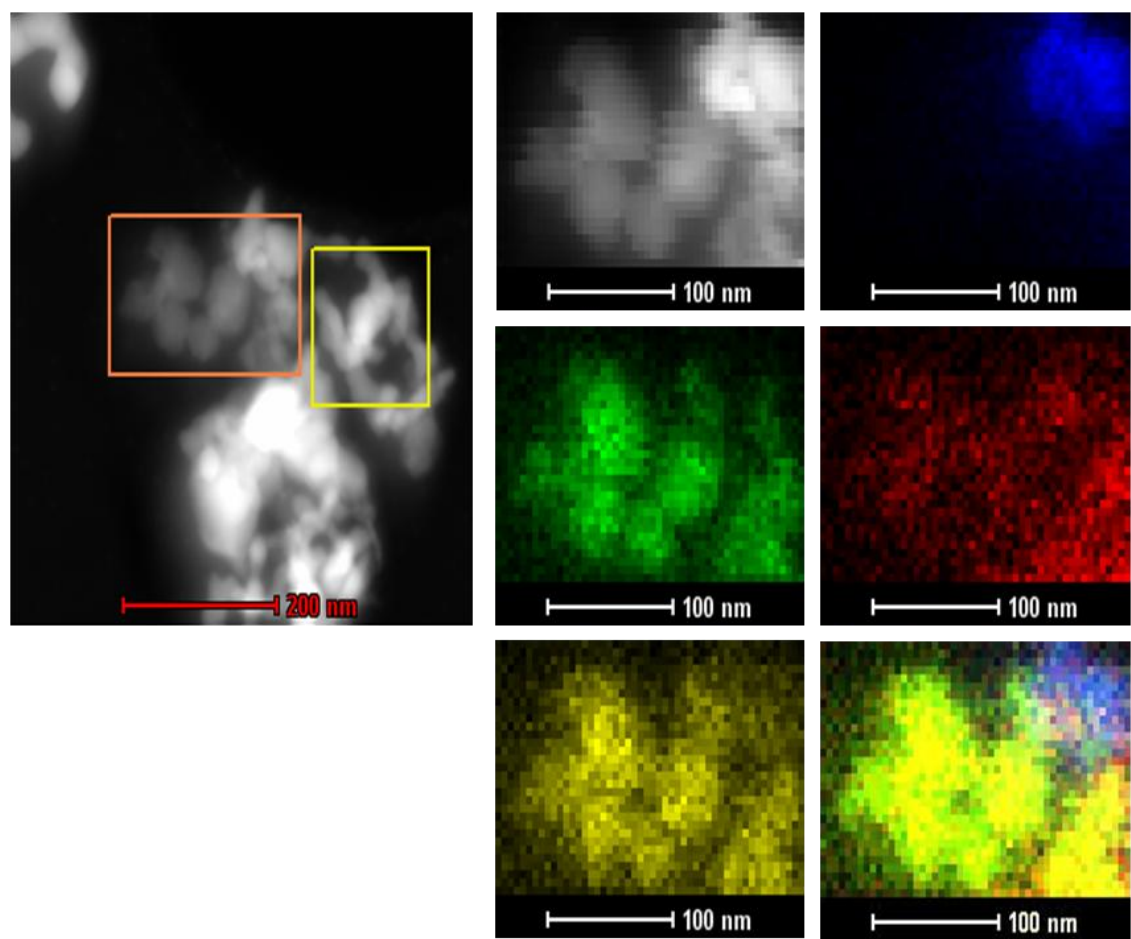
Figure 6.5 scanning tunneling electron microscopy (STEM) and the high-angle annular dark field (HAADF) images of the BFO/Ag along with mapping of the distribution of the concentration of elements Bi, Fe, O, and Ag.

(a)

(b)
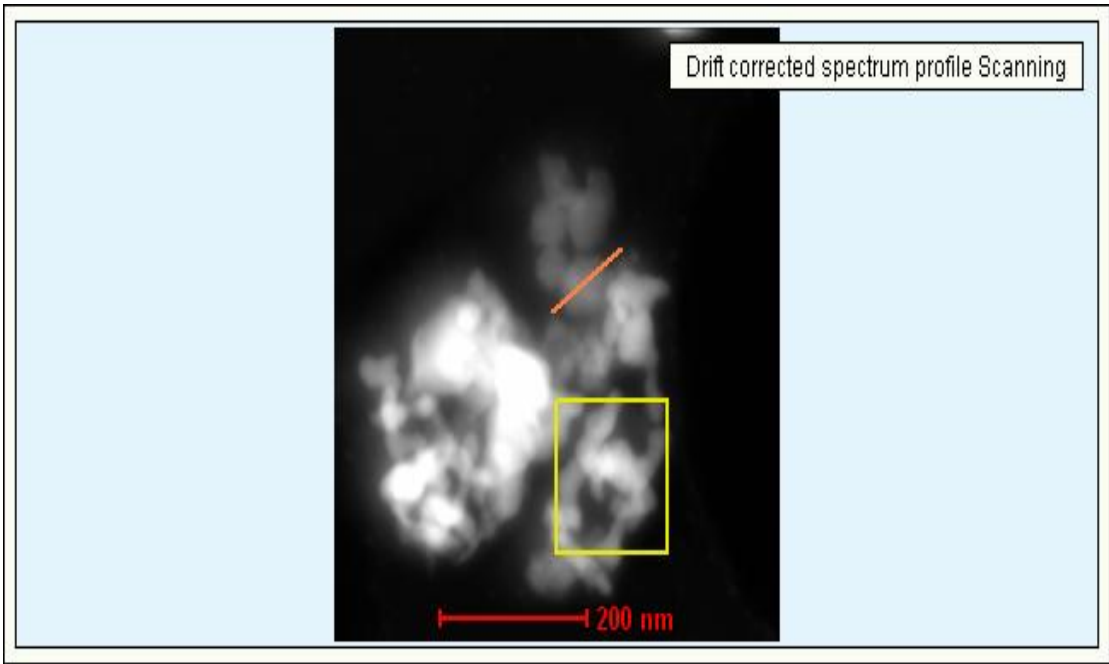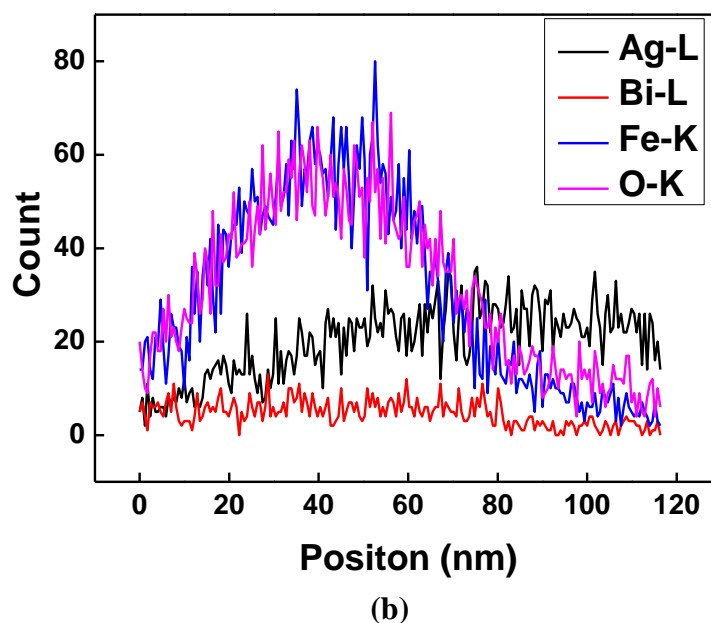
Figure 6.6 (a) the line scan of the element concentration across the BFO and Ag nanoparticle interface; (b) the mapping of the quantitative data on element concentration across the line shown in the image (a)

6.2.3 X-Ray photo-electrcon spectroscopy (XPS) analysis

The charge states of the ions have been examined by x-ray photoelectron spectroscopy (XPS). In Figure 6.7, we show the spectra corresponding to the Bi, Fe, O, and Ag ions of BFO/Ag composite sample. The peaks have been fitted by using appropriate model following the background subtraction and tabulated in Table 6.3.

The main spin-orbit doublet peaks seen in Bi 4f spectra correspond to Bi^{3+} charge states are located at 158.3 and 163.7 eV, respectively. In-addition to that, a pair of shoulder peaks on the lower binding energy side correspond to metallic Bi^{0} charge states are located at 156.3 and 161.6 eV. The relative percentage of Bi^{3+} and Bi^{0} charge states is estimated to be ~90.5% and ~9.5%, respectively.

The Fe 2p spectra of the composite samples are deconvoluted into two spin-orbit doublet peaks of Fe(II)-O species located at ~709.5 and ~723.0 eV of Fe $2p_{3/2}$ and Fe $2p_{1/2}$, respectively. The higher binding energy side spin-orbit doublet peaks located at ~711.6 and ~725.5 eV have attributed to Fe(III)-O species.

The O 1s spectra are deconvoluted into two peaks of lattice oxygen (O_{latt}) present in the samples and loss of oxygen (O_{loss}) on the surface located at 529.5 and 530.9 eV, respectively.

The Ag 3d spectra deconvoluted into two peaks of Ag $3d_{5/2}$ ~367.5 eV and Ag $3d_{3/2}$ ~373.6 eV of the composite sample are shown in Figure 6.7 (d) which are characteristic of the

[205]

Ag^0 charge state emanating from the surface of the sample. There is no trace of other charge states of Ag observed in the spectra.

One consequence of the doing of Ag into BFO lattice is a shift of the Fermi-level, which results in decreased binding energies of the core-level electrons compared with that of bare BFO sample. These observations exclude the possibility of doping of Ag atoms in BFO nano particles have highlighted the electronic structure of BFO with average particle size ~38 nm. Now compare our results from BFO/Ag composite to those from the BFO[32] and Ag[33] samples (Table 6.3), we observed a negative shift (~0.7eV) in Ag^0 core-level between composite and bare Ag nanoparticles, while a positive shift (~0.7eV) observed in lattice oxygen core-level between composite and BFO nanoparticles. The shifts in binding energy in core-level spectra are generally caused by several acting mechanisms that are associated with initial and final state effects. A qualitative interpretation based on the possibility on the local mechanism like a chemical interactions is a source of the observed shifts. The difference among bare BFO, Ag nanoparticles and composite is the presence of orbital overlapping at the interface. This means that a charge transfer occurs from Ag 3d to O 1s orbital at the interface.

Contrary to the observations made in other cases, in the present case, electron transfer appears to have taken place from O to Ag creating holes in the O p states.

(a)

(b)

(c)

(d)
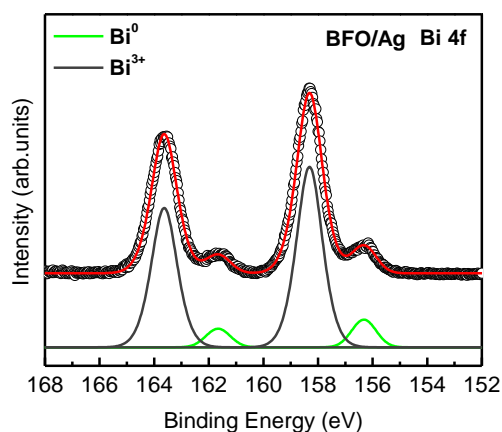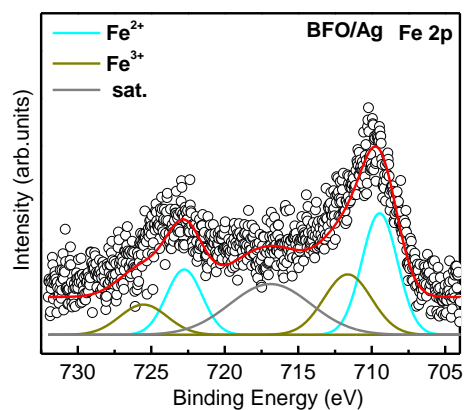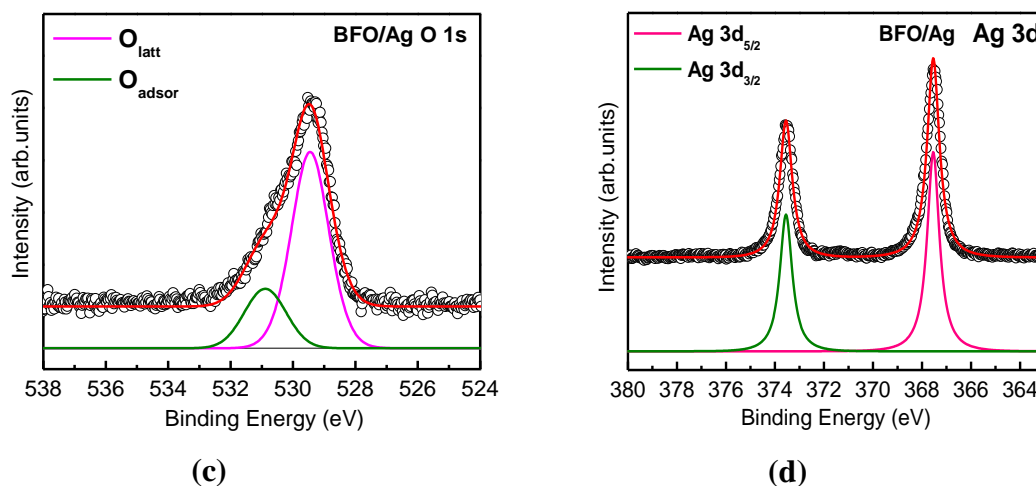
Figure 6.7 The deconvoluted x-ray photoelectron core level spectra for (a) Bi 4f, (b) Fe 2p, (c) O 1s, and (d) Ag 3d

Table 6.3 The XPS peaks for bare BFO, Ag nano particles, and BFO/Ag nano composite				
Core level	**Ions**	**BFO/Ag**	**Bare Nano BFO** [32]	**Shift**
Bi 4f	**Bi⁰**	156.3	156.8	**-0.5**
	Bi⁰	161.6	162.1	**-0.5**
	Bi⁺³	158.3	158.8	**-0.5**
	Bi⁺³	163.7	164.1	**-0.5**
Fe 2p	**Fe⁺²**	709.5	710.7	**-1.2**
	Fe⁺²	723.0	724.2	**-1.2**
	Fe⁺³	711.6	711.4	**0.2**
	Fe⁺³	725.5	725.3	**0.2**
	Sat	716.9	717.6	
			730.1	
O 1s	**Lat Oxygen**	529.5	528.8	**0.7**
	Desorption (oxygen vacancies²⁾	530.9	529.7	**1.2**
	Surface absorbtion		531.0	
		BFO/Ag	**Bare Nano Ag** [33]	**Shift**
Ag 3d	**3d 5/2**	367.5	368.2	**-0.7**
	3d 3/2	373.6	374.2	**-0.7**

[207]

6.2.4 **Magnetic property analysis**

6.2.4.1 **M-H Study at room temperature**

Figure 6.8 shows the room temperature magnetization (M) versus applied magnetic field (H) magnetic hysteresis loops for the bare BFO nano particles and BFO/Ag nano composites (BFO/Ag and BFO/Ag-2) containing different wt% of Ag. Clearly, more than an order of magnitude jump in saturation magnetization (M_S) could be observed (from ~0.56 emu/g to ~11.12 emu/g i.e. from 0.03 μ_B/formula unit to 0.06μ_B/formula unit) in the nano composite. The coercivity H_C, of course, turns out to be quite small (~60 Oe). Its turn out to be that the anti-ferromagnetic BFO becomes super paramagnetic with magnetic saturation 20 times larger than the as prepared BFO. The summary of the data are shown in Table 6.4. The net exchange bias is zero in both cases.
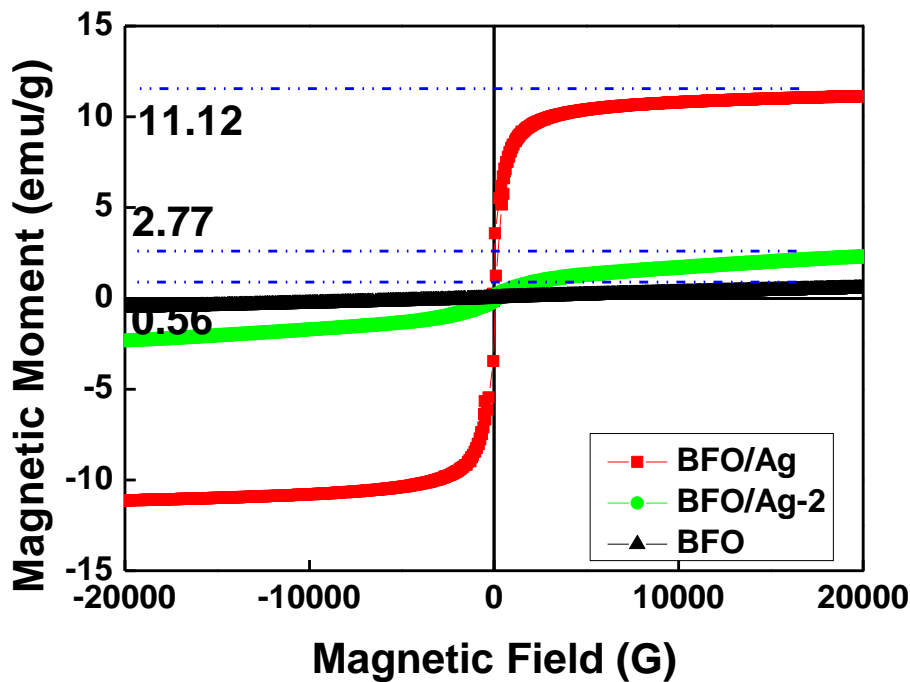
Figure 6.8 The room temperature M-H hysteresis loops for the BFO and BFO/Ag of two wt% (BFO/Ag and BFO/Ag-2)

Sample	H_{c1} (Oe)	H_{c2} (Oe)	Coercivity $|H_c|=(H_{c1}-H_{c2})/2$ (Oe)	Exchange Bias $H_e=(H_{c1}+H_{c2})/2$ (Oe)	Magnetic Moment $Ms_{2.0T}$ (emu/g)
BFO	-248	248	124.00	0	0.56
BFO/Ag-2	-151	151	75.50	0	2.77
BFO/Ag	-65.7	65.7	32.85	0	11.12

Table 6.4 Summary of various magnetic parameters

6.2.4.2 <u>Study of magnetic force microscopy</u>

We further employed magnetic force microscopy (MFM) to observe the influence of large saturation magnetization on the phase contrast as well as on the magnetic domain structure.

The nano composite (BFO/Ag) particles were dispersed in ethanol and deposited onto a glass substrate. The dried substrate was used for recording the MFM scan. Figure 6.9 shows the MFM topography image, the phase contrast image and their 3D plot. The line scans recorded across different regions of the phase-contrast image (Figure 6.9 (d)) reveals the size of the magnetic domains in different regions of the nano composite cluster. The lines are shown in the phase contrast image. It turns out to be 1.0-1.5 μm. Therefore, across the particle clusters, the magnetic domains form by encompassing large number of individual particles. This has been observed by others as well[34]. We compare the phase-contrast data observed in this case with those obtained for the reference BFO nano particle cluster and the standard magnetic thin film (surface of magnetic hard disk) (Figure 6.10 (c)) - black, red, and blue lines (Figure 6.10 (c)), respectively, represent the phase-contrast line profiles for the reference BFO cluster, magnetic hard disk, and the BFO/Ag nano composite cluster. The corresponding phase-contrast MFM images are shown in Figure 6.10 (a) and Figure 6.10 (b), respectively. Clearly, the phase contrast is enormous in the case of the BFO/Ag nano composite. Since, $\Delta_\phi \propto K_p \frac{\partial F_z}{\partial z}$ [35] [36], large force gradient $\left(\frac{\partial F_z}{\partial z}\right)$ resulting from large stray field gradient leads to large Δ_ϕ. It is important to mention here that the same cantilever (Co-alloy coated Si cantilever-tip, coercivity ~300 Oe) has been used to map the MFM images for all the samples - hard disk surface, BFO nanoparticles, and BFO/Ag nano composite. Therefore, the constant factor K_p remains invariant in all these cases. The plot in Figure 6.10 (c), shows that the Δ_ϕ in the nanocomposite is even higher than that in the hard disk. Therefore, the signature of large magnetization could be observed in MFM images as well. The crosstalk between topography and phase-contrast images

in MFM, of course, often poses difficulty in imaging the magnetic domains clearly. However, since the magnetization is large in the present case (resulting in large stray field gradient and hence large phase contrastΔ_ϕ) and dual pass technique with large cantilever lift height (~120-150 nm) has been used, the influence of topography on the phase-contrast images is minimal. The utility of dual pass technique and large cantilever lift height in eliminating the influence of topography on phase-contrast MFM images has been highlighted by others as well[37][38]. The line scans, taken on the topography image (Figure 6.9 (a)), reveals the difference between the nanoparticle cluster size and the size of the magnetic domains (Figure 6.9 (c)). This difference highlights the negligible influence of topography on the phase-contrast MFM image. In fact, complete reversal of the magnetic domains could also be observed[39] even in bare BFO nanoparticles upon reversal of applied magnetic field (+20 and -20 kOe).

(a)   **(b)**

(c)   **(d)**
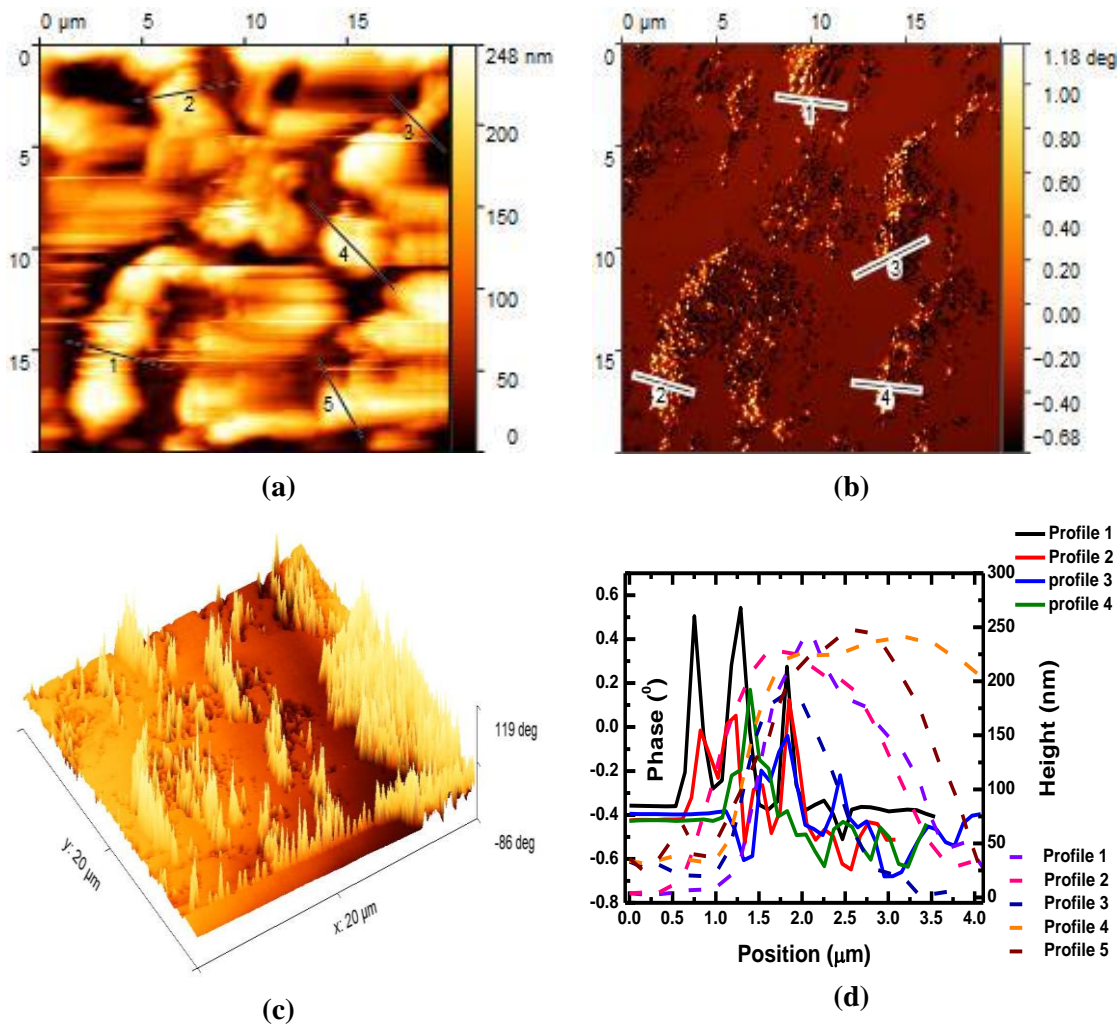
Figure 6.9 Representative magnetic force microscopy (MFM) (a) topography and (b) phase-contrast images of BFO/Ag at room temperature; (c) 3D plot of phase contrast image [as shown in (b)]; (d) line scan mapping of the topography and phase-contrast MFM images [corresponding lines are shown, respectively, in (a) and(b)] which indicates the size of the nanoparticle clusters and the magnetic domain size; the solid lines represent the magnetic domain size (left axis) while the dashed lines represent the size of the nanoparticle clusters (right axis).

[210]

(a)

(b)

(c)
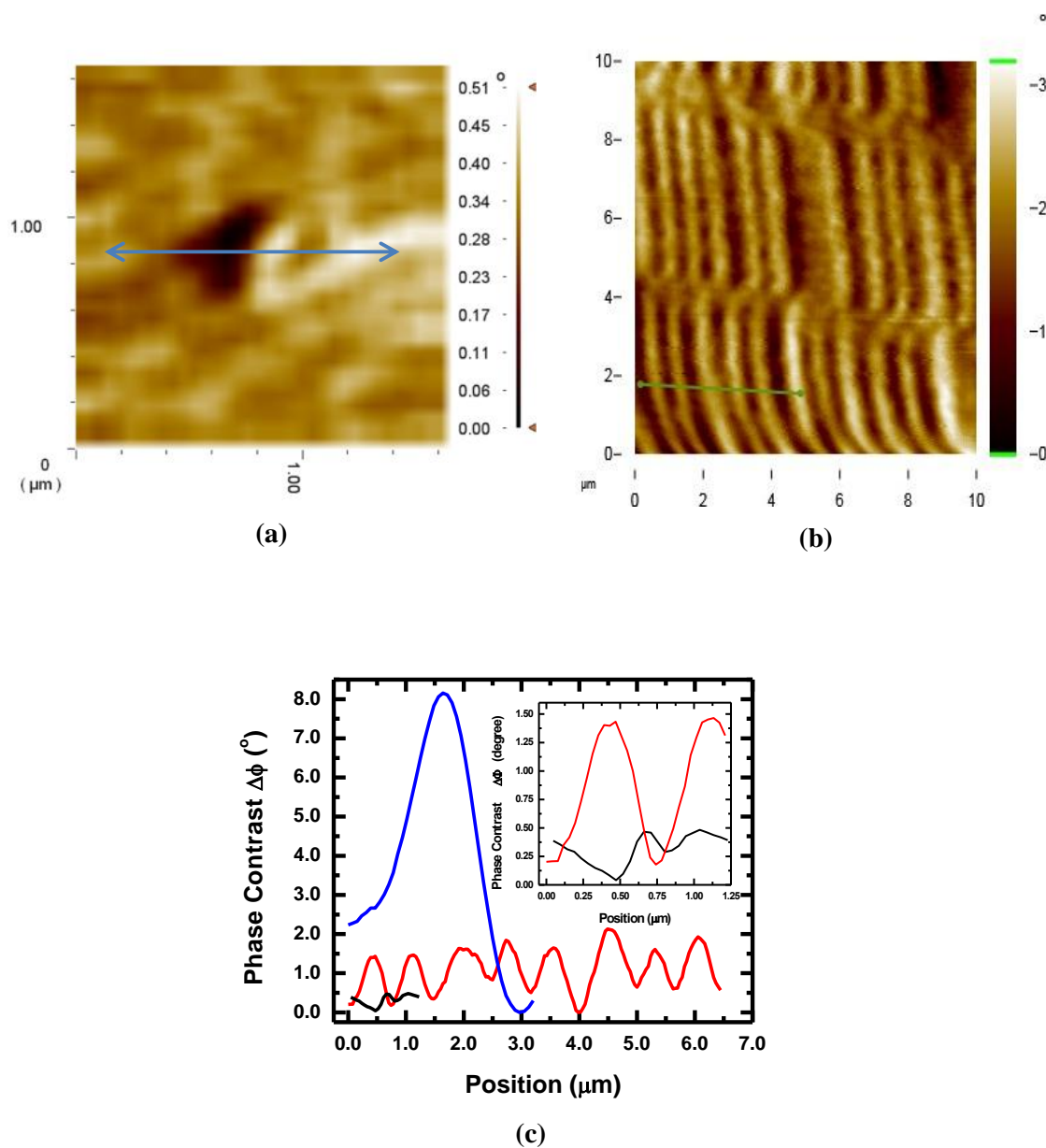
Figure 6.10 (a) and (b) are the representative phase-contrast MFM images of the BFO nanoparticle cluster and hard-disk surface commonly used in MFM as a standard sample; (c) line scan data with normalized phase contrast ($\Delta\phi$) for diferent samples - BFO/Ag nanocomposite (blue line), pure BFO (black line), and the hard disk (red line); inset zooms in on the data for BFO nanoparticles (black line) and hard disk (red line).

6.2.5 <u>Discussion</u>

Neither bare BFO nano particles of average size ~30 nm nor bare Ag^0 nano particles exhibit such a large magnetization. It is important to point out here that even though the $Bi_{25}FeO_{40}$ and $Bi_2Fe_4O_9$ phases are present in the nano composite, they do not contribute much to the room temperature ferromagnetism since the magnetic transition temperature (T_N) of these

[211]

compounds are around 272 K[40] and 250 K. respectively. Moreover, these impurity phases are found to be present in the reference BFO sample (which is used here for comparing the magnetization) as well.

The bulk Ag is diamagnetic with $[Kr]4d^{10}5s^1$ electronic configuration. There were efforts to make isolate nano particles of coinage metals (Cu, Au, Ag) so that unbound atoms, consisting of unpaired 's' electron, will give rise to ferromagnetism. S Mahapatra *et al.*[41] reported ferromagnetism in uncapped gold nano particles but there is only one report made on paramagnetic behaviour of Ag nano particles below 80K by Hoa Le Trong group [42]. Ferromagnetism in cluster of bare noble metals was reported using theoretically[43 44]. There are few theoretical studies that reported ferromagnetism in Ag nano clusters resulted from the charge transfer among the central atom and the other neighbouring atoms because 4d orbital of central atom overlaps with those if its outer shell atoms[4543].This charge transfer played an important role also in the origin of ferromagnetism in thiol capped Ag nano particles where charge transfer occurred between metal and metal ligands[46]. Similar results of ferromagnetic ordering associated with localized magnetic moments at the surface of the Ag nanoparticle were also reported due to the spins of 4d localized holes generated through Ag-S bonds[47]. The details were reported by Y. Kunsida *et al.*[48] where they have shown if Ag(111) film exposed to Oxygen then direct super exchange interaction between 4d orbitals of Ag and O 2p orbitals results in ferromagnetic behaviour while interaction between 5s orbital of Ag and O 2p orbitals results in anti- ferromagnetic behaviour. This fact were further justified by a group that higher magnetization in Ag nano particles (3.3- 7.8 nm) were found when the surface were oxidized[49].

The highest saturation magnetisation was reported ~ 2.3 emu/g in Ag-BFO composite (in both form of powder[50] as well as film[51]), where M_s was readily higher than any Ag doped BFO reported [52]. In both cases composite and doping, Ag content doesn't even affect the magnetisation if compared with bare BFO nano particles. Similarly in all cases found in Ag composite of various form of Fe_3O_4 like Fe_3O_4-polyindole-Ag[53], Fe_3O_4/SiO2/Ag microsphere[54], Fe_3O_4/PCTP/Ag, Fe_3O_4/MPCTP/Ag [55], silver ring-coated super paramagneticiron oxide nanoparticles (SPIONs) with ligand gaps[56] showed that there was decrement in magnetic saturation compared to bare particle.

Ferromagnetism in low temperature was found in Ag decorated MoS_2 sheets where charge transfer from silver to MoS_2 which introduced additional impurity levels at the Fermi energy and enhanced magnetic coupling among the spins of localized holes in Ag nano particles[33]. In MoS_2/Ag nano composite, it was observed that the holes in Ag and formation of Ag-S bonds could induce ferromagnetism and metal-insulator transition.

In the present case, it appears that the charge transfer has taken place from O to Ag and thus creating holes in O 2p states. Therefore, p-state ferromagnetism seems to be relevant in this case. It is important to mention here that, in nanoscale magnetic oxides, the magnetization

is generally expected to be influenced by uncompensated spins arising out of surface defects. The surface defects of Ag-free nanosized BFO particles were earlier studied by XPS[57]. Though the ferromagnetism indeed depends on particle size in nanoscale BFO[58], we compared here magnetic properties of two samples of comparable average particle size (~30 nm) to rule out the influence of particle size. So, the magnetization data for the reference (i.e., Ag-free) BFO sample clearly show that the BFO/Ag nanocomposite comprising of comparable BFO nanosized particles exhibits more than an order of magnitude jump in magnetization. Therefore, the distinct influence of Ag and consequent charge transfer is discernible in the case of the nano composite. The p-state ferromagnetism has earlier been observed in SiC as well.

6.3 <u>Chapter summary</u>

In this chapter we report observation of more than an order of magnitude jump in room-temperature saturation magnetization in BFO/Ag nano composite. This could be p-state ferromagnetism resulting from charge transfer between Ag and O. Both the saturation magnetization and the magnetic phase contrast (observed in MFM imaging) turn out to be quite enormous. The morphological analysis is also evident of self assembly of BFO nano chains. This type of highly ferromagnetic particle would be quiet useful for our next genre of research work.

Soft ferromagnetism with such a large saturation magnetization at room temperature could be extremely useful for various applications including biomedical, especially, decoration of the malignant tumors necessary for efficacious radiotherapy. Because of magnetoelectric multiferroicity, the nanocomposite could be useful for ion channel gating action as well where remote application of magnetic field can locally trigger onset of finite electric potential if BFO/Ag based multiferroic ion channel gates replace the faulty ones. MNPs with high magnetic moment can provide enough signals while used in relatively low dose and promote high signal-to-noise ratio[59].

6.4 <u>Bibliography</u>

[1] Goswami, S., Bhattacharya, D., Ghosh, C.K., Ghosh, B., Kaushik, S.D., Siruguri, V. and Krishna, P.S.R., 2018. Nonmonotonic particle-size-dependence of magnetoelectric coupling in strained nanosized particles of BiFeO3. *Scientific Reports*, *8*(1), p.3728.

[2] Sahoo, A. and Bhattacharya, D., 2019. Shape-dependent magnetoelectric coupling in nanoscale BiFeO3. *Journal of Alloys and Compounds*, *772*, pp.193-198.

[3] Mohammadi, S., Shokrollahi, H. and Basiri, M.H., 2015. Effects of Gd on the magnetic, electric and structural properties of BiFeO3 nanstructures synthesized by co-precipitation followed by microwave sintering. *Journal of Magnetism and Magnetic Materials*, *375*, pp.38-42.

[213]

[4] Agarwal, A., Aghamkar, P. and Lal, B., 2017. Structural and multiferroic properties of barium substituted bismuth ferrite nanocrystallites prepared by sol–gel method. *Journal of Magnetism and Magnetic Materials*, *426*, pp.800-805.

[5] Arora, M. and Kumar, M., 2015. Structural, magnetic and optical properties of Ce substituted BiFeO3 nanoparticles. *Ceramics International*, *41*(4), pp.5705-5712.

[6] Betancourt-Cantera, L.G., Bolarín-Miró, A.M., Cortés-Escobedo, C.A., Hernández-Cruz, L.E. and Sánchez-De Jesús, F., 2018. Structural transitions and multiferroic properties of high Ni-doped BiFeO3. *Journal of Magnetism and Magnetic Materials*, *456*, pp.381-389.

[7] Iorgu, A.I., Maxim, F., Matei, C., Ferreira, L.P., Ferreira, P., Cruz, M.M. and Berger, D., 2015. Fast synthesis of rare-earth (Pr3+, Sm3+, Eu3+ and Gd3+) doped bismuth ferrite powders with enhanced magnetic properties. *Journal of Alloys and Compounds*, *629*, pp.62-68.

[8] Philip, G.G., Senthamizhan, A., Natarajan, T.S., Chandrasekaran, G. and Therese, H.A., 2015. The effect of gadolinium doping on the structural, magnetic and photoluminescence properties of electrospun bismuth ferrite nanofibers. *Ceramics International*, *41*(10), pp.13361-13365.

[9] Agarwal, A., Aghamkar, P., Singh, V., Singh, O. and Kumar, A., 2017. Structural transitions and multiferrocity in Ba and Co substituted nanosized bismuth ferrite. *Journal of Alloys and Compounds*, *697*, pp.333-340.

[10] Singh, V., Sharma, S. and Dwivedi, R.K., 2018. Improved dielectric, magnetic and optical properties of Pr and Ti co-substituted BFO ceramics. *Journal of Alloys and Compounds*, *747*, pp.611-620.

[11] Tang, P., Kuang, D., Yang, S. and Zhang, Y., 2016. Structural, morphological and multiferroic properties of the hydrothermally grown gadolinium (Gd) and manganese (Mn) doped sub-micron bismuth ferrites. *Journal of Alloys and Compounds*, *656*, pp.912-919.

[12] Hernandez, N., Gonzalez-Gonzalez, V.A., Dzul-Bautista, I.B., Gutierrez, J., Barandiaran, J.M., De Larramendi, I.R., Cienfuegos-Pelaes, R.F. and Ortiz-Mendez, U., 2015. Nd and Sc co-doped BiFeO3 nanopowders displaying enhanced ferromagnetism at room temperature. *Journal of Alloys and Compounds*, *638*, pp.282-288.

[13] Ahmadi, P., Alamolhoda, S. and Mirkazemi, S.M., 2018. Cetyltrimethylammonium bromide (CTAB) surfactant-assisted synthesis of BiFeO 3 nanoparticles by sol-gel auto-combustion method. *Journal of Superconductivity and Novel Magnetism*, *31*, pp.3307-3314.

[14] Liu, X.M., Fu, S.Y. and Huang, C.J., 2005. Synthesis and magnetic characterization of novel CoFe2O4–BiFeO3 nanocomposites. *Materials Science and Engineering: B*, *121*(3), pp.255-260.

[15] Goswami, S., Sahoo, A., Bhattacharya, D., Karci, O. and Mohanty, P.K., 2020. Large structure-dependent room temperature exchange bias in self-assembled BiFeO3 nanoparticles. *APL Materials*, *8*(8), p.081101.

[16] Comes, R., Liu, H., Khokhlov, M., Kasica, R., Lu, J. and Wolf, S.A., 2012. Directed self-assembly of epitaxial CoFe2O4–BiFeO3 multiferroic nanocomposites. *Nano letters*, *12*(5), pp.2367-2373.

[17] Stratulat, S.M., Lu, X., Morelli, A., Hesse, D., Erfurth, W. and Alexe, M., 2013. Nucleation-induced self-assembly of multiferroic BiFeO3–CoFe2O4 nanocomposites. *Nano letters*, *13*(8), pp.3884-3889.

[18] Aimon, N.M., Kim, D.H., Sun, X. and Ross, C.A., 2015. Multiferroic behavior of templated BiFeO3–CoFe2O4 self-assembled nanocomposites. *ACS applied materials & interfaces*, *7*(4), pp.2263-2268.

[19] Kim, D.H., Sun, X., Kim, T.C., Eun, Y.J., Lee, T., Jeong, S.G. and Ross, C.A., 2016. Magnetic phase formation in self-assembled epitaxial BiFeO3–MgO and BiFeO3–MgAl2O4 nanocomposite films grown by combinatorial pulsed laser deposition. *ACS Applied Materials & Interfaces*, *8*(4), pp.2673-2679.

[20] Nie, Z., Petukhova, A. and Kumacheva, E., 2010. Properties and emerging applications of self-assembled structures made from inorganic nanoparticles. *Nature nanotechnology*, *5*(1), pp.15-25.

[21] Granados-Miralles, C., Quesada, A., Saura-Múzquiz, M., Andersen, H.L., Fernández, J.F. and Christensen, M., 2020. Expanding the tunability and applicability of exchange-coupled/decoupled magnetic nanocomposites. *Materials Chemistry Frontiers*, *4*(4), pp.1222-1230.

[22] Liu, F., Dong, Y., Yang, W., Yu, J., Xu, Z. and Hou, Y., 2014. Exchange-Coupled fct-FePd/α-Fe Nanocomposite Magnets Converted from Pd/Fe3O4 Core/Shell Nanoparticles. *Chemistry–A European Journal*, *20*(46), pp.15197-15202.

[23] Shen, B. and Sun, S., 2020. Chemical synthesis of magnetic nanoparticles for permanent magnet applications. *Chemistry–A European Journal*, *26*(30), pp.6757-6766.

[24] Jesús, S.D., Bolarín-Miró, A.M., Cortés Escobedo, C.A., Torres-Villaseñor, G. and Vera-Serna, P., 2016. Structural analysis and magnetic properties of FeCo alloys obtained by mechanical alloying. *Journal of Metallurgy*, *2016*.

[25] Noma, K., Matsuoka, M., Kanai, H., Uehara, Y., Nomura, K. and Awaji, N., 2006. Ultra-high magnetic moment films for write head. *IEEE transactions on magnetics*, *42*(2), pp.140-144.

[26] Scheunert, G., Heinonen, O., Hardeman, R., Lapicki, A., Gubbins, M. and Bowman, R.M., 2016. A review of high magnetic moment thin films for microscale and nanotechnology applications. *Applied Physics Reviews*, *3*(1), p.011301.

[27] Pervikov, A.V., 2021. Metal, metal composite, and composited nanoparticles obtained by electrical explosion of wires. *Nanobiotechnology Reports*, *16*, pp.401-420.

[28] Bai, J. and Wang, J.P., 2005. High-magnetic-moment core-shell-type FeCo–Au∕ Ag nanoparticles. *Applied Physics Letters*, *87*(15), p.152502.

[29] Bai, J., Xu, Y.H., Thomas, J. and Wang, J.P., 2007. (FeCo) 3Si–SiOx core–shell nanoparticles fabricated in the gas phase. *Nanotechnology*, *18*(6), p.065701.

[30] Rai, M., Yadav, A. and Gade, A., 2009. Silver nanoparticles as a new generation of antimicrobials. *Biotechnology advances*, *27*(1), pp.76-83.

[31] Takahashi, M., Mohan, P., Nakade, A., Higashimine, K., Mott, D., Hamada, T., Matsumura, K., Taguchi, T. and Maenosono, S., 2015. Ag/FeCo/Ag core/shell/shell magnetic nanoparticles with plasmonic imaging capability. *Langmuir*, *31*(7), pp.2228-2236.

[32] Chaturvedi, S., Sarkar, I., Shirolkar, M.M., Jeng, U., Yeh, Y.Q., Rajendra, R., Ballav, N. and Kulkarni, S., 2014. Probing bismuth ferrite nanoparticles by hard x-ray photoemission: Anomalous occurrence of metallic bismuth. *Applied Physics Letters*, *105*(10).

[33] Bag, S., Bhattacharya, S., Dinda, D., Jyothirmai, M.V., Thapa, R. and Saha, S.K., 2018. Induced ferromagnetism and metal-insulator transition due to a charge transfer effect in silver nanoparticle decorated Mo S 2. *Physical Review B*, *98*(1), p.014109.

[34] Puntes, V.F., Gorostiza, P., Aruguete, D.M., Bastus, N.G. and Alivisatos, A.P., 2004. Collective behaviour in two-dimensional cobalt nanoparticle assemblies observed by magnetic force microscopy. *Nature materials*, *3*(4), pp.263-268.

[35] Gomez, R.D., Pak, A.O., Anderson, A.J., Burke, E.R., Leyendecker, A.J. and Mayergoyz, I.D., 1998. Quantification of magnetic force microscopy images using combined electrostatic and magnetostatic imaging. *Journal of applied physics*, *83*(11), pp.6226-6228.

[36] Asenjo, A., 2019. Characterization of nanomagnets by Advanced Magnetic Force Microscopy. *Appl. Phys*, *125*, p.060901.

[37] Moldovan, A. and Dinescu, M., 2022. Single-pass magnetic force microscopy technique, with topography feedback based on scanning polarization force microscopy. *Applied Surface Science*, *597*, p.153747.

[38] Parker, A.C., Maryon, O.O., Kaffash, M.T., Jungfleisch, M.B. and Davis, P.H., 2022. Optimizing Magnetic Force Microscopy Resolution and Sensitivity to Visualize Nanoscale Magnetic Domains. *JoVE (Journal of Visualized Experiments)*, (185), p.e64180.

[39] Goswami, S., Sahoo, A., Bhattacharya, D., Karci, O. and Mohanty, P.K., 2020. Large structure-dependent room temperature exchange bias in self-assembled BiFeO3 nanoparticles. *APL Materials*, *8*(8), p.081101.

[40] Jebari, H., Tahiri, N., Boujnah, M., El Bounagui, O., Taibi, M. and Ez-Zahraouy, H., 2021. Theoretical investigation of electronic, magnetic and magnetocaloric properties of Bi25FeO40 compound. *Phase Transitions*, *94*(3-4), pp.147-158

[41] Mohapatra, S., Kumar, R.K. and Maji, T.K., 2011. Green synthesis of catalytic and ferromagnetic gold nanoparticles. *Chemical Physics Letters*, *508*(1-3), pp.76-79.

[42] Le Trong, H., Kiryukhina, K., Gougeon, M., Baco-Carles, V., Courtade, F., Dareys, S. and Tailhades, P., 2017. Paramagnetic behaviour of silver nanoparticles generated by decomposition of silver oxalate. *Solid State Sciences*, *69*, pp.44-49.

[43] Pereiro, M., Baldomir, D. and Arias, J.E., 2007. Unexpected magnetism of small silver clusters. *Physical Review A*, *75*(6), p.063204.

[44] Chen, F. and Johnston, R.L., 2008. Charge transfer driven surface segregation of gold atoms in 13-atom Au–Ag nanoalloys and its relevance to their structural, optical and electronic properties. *Acta Materialia*, *56*(10), pp.2374-2380.

[45] Luo, W., Pennycook, S.J. and Pantelides, S.T., 2007. s-Electron ferromagnetism in gold and silver nanoclusters. *Nano letters*, *7*(10), pp.3134-3137.

[46] Garitaonandia, J.S., Insausti, M., Goikolea, E., Suzuki, M., Cashion, J.D., Kawamura, N., Ohsawa, H., Gil de Muro, I., Suzuki, K., Plazaola, F. and Rojo, T., 2008. Chemically induced permanent magnetism in Au, Ag, and Cu nanoparticles: localization of the magnetism by element selective techniques. *Nano Letters*, *8*(2), pp.661-667.

[47] Suber, L., Fiorani, D., Scavia, G., Imperatori, P. and Plunkett, W.R., 2007. Permanent magnetism in dithiol-capped silver nanoparticles. *Chemistry of materials*, *19*(6), pp.1509-1517.

[48] Kunisada, Y., Escaño, M.C. and Kasai, H., 2011. Surface magnetism in O2 dissociation—from basics to application. *Journal of Physics: Condensed Matter*, *23*(39), p.394207.

[49] Marenco, A.J., Pedersen, D.B. and Trudel, S., 2017. On the origin of the ferromagnetic signature in silver nanoparticles and thin films. *Journal of Materials Chemistry C*, *5*(20), pp.4899-4908.

[217]

[50] Jaffari, Z.H., Lam, S.M., Sin, J.C. and Zeng, H., 2019. Boosting visible light photocatalytic and antibacterial performance by decoration of silver on magnetic spindle-like bismuth ferrite. *Materials Science in Semiconductor Processing*, *101*, pp.103-115.

[51] Cheng, S., Xu, Q., Hao, X., Wang, Z., Ma, N. and Du, P., 2017. Formation of nano Ag/BiFeO 3 composite thin film with extraordinary high dielectric and effective ferromagnetic properties. *Journal of Materials Science: Materials in Electronics*, *28*, pp.5652-5662.

[52] Ahmed, M.A., Mansour, S.F., El-Dek, S.I. and Abu-Abdeen, M., 2014. Conduction and magnetization improvement of BiFeO3 multiferroic nanoparticles by Ag+ doping. *Materials Research Bulletin*, *49*, pp.352-359.

[53] Karegar, M. and Khodaei, M.M., 2022. Magnetic polyindole-Ag composite for the catalytic reduction and removing of the organic pollutants. *Polymer Bulletin*, *79*(12), pp.11431-11460.

[54] Wang, Y., Wang, K., Zou, B., Gao, T., Zhang, X., Du, Z. and Zhou, S., 2013. Magnetic-based silver composite microspheres with nanosheet-assembled shell for effective SERS substrate. *Journal of Materials Chemistry C*, *1*(13), pp.2441-2447.

[55] Shi, X., Huang, C., Zheng, Z., Zhong, B., Ding, G., Li, J., You, L. and Wang, S., 2021. Preparation of magnetically recoverable MPCTP-Ag composite nanoparticles and their application as high-performance catalysts. *Langmuir*, *37*(34), pp.10249-10258.

[56] Mahmoudi, M. and Serpooshan, V., 2012. Silver-coated engineered magnetic nanoparticles are promising for the success in the fight against antibacterial resistance threat. *ACS nano*, *6*(3), pp.2656-2664.

[57] Chatterjee, T., Mukherjee, A., Pal, P., Kaushik, S., Siruguri, V., Mandal, S., Hazra, S., Bhattacharjee, S., Ghosh, C.K. and Bhattacharya, D., 2022. Nonmonotonic Magnetic Field Dependence of Remnant Ferroelectric Polarization in Reduced Graphene Oxide–BiFeO3 Nanocomposite. *physica status solidi (RRL)–Rapid Research Letters*, *16*(7), p.2200077.

[58] Hasan, M., Islam, M.F., Mahbub, R., Hossain, M.S. and Hakim, M.A., 2016. A soft chemical route to the synthesis of BiFeO3 nanoparticles with enhanced magnetization. *Materials Research Bulletin*, *73*, pp.179-186.

[59] Liu, J., Su, D., Wu, K. and Wang, J.P., 2020. High-moment magnetic nanoparticles. *Journal of Nanoparticle Research*, *22*(3), p.66.

7   Chapter

Study of magnetic and electrical properties of hydrogenated single layer graphene

7.1 <u>Introduction</u>

This chapter discuss about fabrication of single layer Graphene (SLG) flowed by its extensive hydrogenation and its oxidation back to the conducting SLG along with the study about the changes in properties.

Graphene is an exciting two-dimensional monolayer of sp^2 carbon with honey-comb like structure[1,2] having unique physical[3], mechanical and electrical properties[4,5]. In spite of chemical inertness of Graphene chemical modification of graphene can tune its material properties required for a given application[6,7,8,9,10,11]. Several types of chemical reactions have already been demonstrated on graphene[12,13,14,15]. Pure graphene is electronically half filled (one π electron per site) on a bipartite lattice. The π electrons on A and B sublattice which are responsible of high conductivity are anti-ferromagnetically correlated[16]. Pristine graphene sheets only exhibit Laudau orbital diamagnetism[17]. A long-range ferromagnetic order in graphene does not occur without exchange coupling between the local moments. Efforts have been made in introducing magnetism in Graphene. Local staggered moments were seen in zigzag edged Graphene and investigation found out that the moment was proportional to the edge length[18]. Another investigation was made using an Hartree Fock mean field theory of the Hubbard model of Graphne lattice which showed presence of other edges along with the zigzag edges that retains considerable amount of magnetization. The investigation was further enriched with the study of armchair defects along with irregular defects[19]. Spin polarized DFT calculations on structural defects of Graphene concluded that spin magnetic moment may arise in pristine Graphene due to introduction of vacancies (even mono vacancy) and adatoms[20, 21]. Chemically modified Graphene like Graphene oxide[22], hydrogenated graphene[23] also incorporate magnetism in the lattice. Hydrogenation assures no breakage of C-C bonds no disruption of doping of graphene. Hydrogenation can bond H to each C in a lattice along with inert nature due to non-polarity and

offers great application in electronic and magnetic field[24]. A number of groups have directly measured room temperature ferro-magnetism using SQUIID[25 26], MFM in single layer partially hydrogenated Graphene[27]. Gonazalez et al., used STM to calculate magnetic moments arising out of local density of states, thereby, giving experimental proof of already predicted theoretical hypothesis[28]. Along with the magnetic property hydrogenation can transform a zero-band-gap semiconductor to a wide band gap insulator[29] and depending on the extent of hydrogenation to a medium band gap semiconductor[30,31,32]. These background studies recommend us to explore the field more in respect to reversibility of hydrogenated graphene to pristine form. Previous efforts at hydrogenation of graphene[13,33] included physical techniques like exposing graphene to an atomic hydrogen plasma and also plasma hydrogenation[34]. However, these methods yields partially hydrogenated graphene having partial conductivity. A more effective and rapid route for hydrogenation of graphene is done using chemical reaction of Birch reduction where alkali metal is dissolved in liquid ammonia before adding graphene/graphite into it[35]. This is followed by addition of a proton source like tert-butanol (t-BuOH) in the reaction mixture to create highly hydrogenated graphene/graphite nanosheets. The as hydrogenated graphene sheets can be restored back using thermal annealing technique[35], however, such process are costly and also include loss of carbon atoms from the graphene lattice.

In this chapter, we report a one-step dehydrogenation of birch reduced "hydrogenated graphene" using 2,3-Dichloro-5,6-dicyano-1,4-benzoquinone (DDQ) as an oxidizing agent. A near pristine graphene comparable to the starting SLG can be obtained by this technique. The chemically de-hydrogenated graphene has been characterized extensively and it was observed that a near pristine graphene comparable to the starting SLG can be obtained by this technique.

7.2 <u>Results and discussion</u>

The detailed preparation of Single Layer Graphene (SLG), Hydrogenated Graphene (H) and De-hydrogenated Graphene (HD) are discussed in Chapter 2- section 2.3.4.1, section 2.3.4.2 and section 2.3.4.3 respectively.

The details of the Raman spectra were obtained using a RenishawInVia Reflex micro Raman spectrometer with excitation by argon ion (514 nm) laser. The laser power was kept sufficiently low to avoid heating of the samples and the spectra were collected with a resolution of 1 cm^{-1}. Multiple spectra (3–5) were obtained, normalized to the G band, and averaged to present a comprehensive overview of the material. Fourier transform infrared (FT-IR) spectra of the samples were recorded on a Perkin Elmer FTIR Spectrometer in reflectance mode. Two probe conductivity (current-voltage) measurements were taken on a Keithley 4200 SCS and performed on SLG transferred onto quartz substrate. Magnetism of the samples was studied using SQUID Magnetometer at room temperature on quartz transferred SLG.
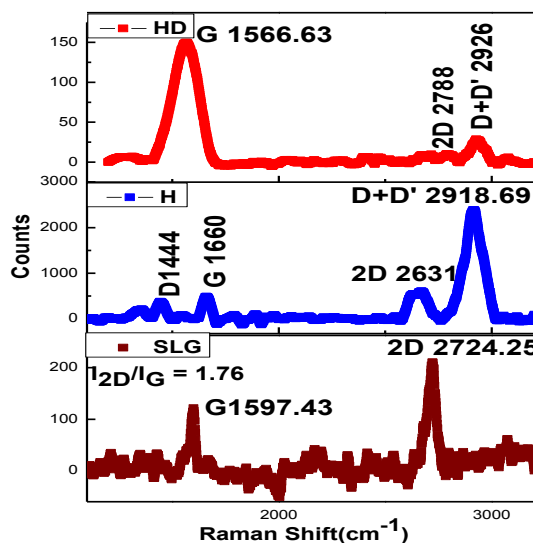
7.2.1 <u>RAMAN analysis</u>

Figure 7.1 RAMAN data plot of SLG, Hydrogenated SLG and De-hydrogenated SLG

The Raman spectra of the SLG on Cu foil, SLG transferred onto quartz substrate, hydrogenated and de-hydrogenated SLG on quartz is shown in Figure 7.1. The large 2D band observed in the SLG on copper foil and SLG transferred onto quartz substrate is indicative of high quality single layer graphene with very less defects as is observed by a very small "D" or defect band at 1320 cm^{-1}. The large D band observed at 1320 cm^{-1} is indicative of the chemical disruption of the sp^{2}-hybridized carbon network that results from the covalent attachment of hydrogen atoms[13]. In addition, a decrease and broadening of the 2D band (also called the G′ band) at 2680 cm^{-1} and an increase of the (D + D′) combination band at 2890 cm^{-1} were also observed which confirms high degree of hydrogenation[34]. The reoccurrence of the 2D band and disappearance of the D+D′ combination band (in de-hydrogeneted SLG) suggests that dehydrogenation of SLG has happened to a great extent. Table 7.1 summarize the defect concentration calculated using equation mentioned in Section 3.3.2. Analysing the data it can be easily seen that sp^{3} defects are much lower in Hydrogenated SLG wrt the D+D'. We can conclude that Hydrogenation was done 9.38×10^{23}/cm^{2}. From the inter defect length calculation it can be said that because the lattice spacing of C atoms in Graphite structure is 0.37nm, out of every 15 carbon atoms in SLG, about one carbon atom is being Hydrogenated. In the case of De-hydrogenated SLG data the L$_{D+D'}$ is 30.03 nm i.e. out of every 81 carbon atoms one carbon atom is now hydrogenated. So the dehydrogenation is done to a great extent. This also reflects the defect concentration data up to one order parameter is being lowered than in hydrogenated

[221]

SLG. Also, sp^3 defects are not noticed in De-hydrogenated SLG that ensures the perfect restoration of Graphitic 2D structure.

Table 7.1 Defect concentration summary				
	I_D/I_G	L_D^2 (nm^2)	L_D(nm)	n_D (cm^{-2})
Hydrogenated SLG	0.78	204.88	14.31	1.55×10^{23}
	$I_{D+D'}/I_G$	$L_{D+D'}^2$ (nm^2)	$L_{D+D'}$(nm)	$n_{D+D'}$ (cm^{-2})
Hydrogenated SLG	4.73	33.93	5.82	9.38×10^{23}
De-hydrogenated SLG	0.178	901.85	30.03	0.35×10^{23}

7.2.2 FTIR analysis

The FTIR spectrum of the SLG, hydrogenated SLG and de-hydrogenated SLG is shown in Figure 7.2. The hydrogenated SLG exhibits a strong peak at ~2850 cm^{-1} and ~2910 cm^{-1}, indicative of the aliphatic C−H stretching mode[34]. No peaks were observed in this region for the pristine SLG and again after dehydrogenation, the peaks almost disappear confirming the success of the dehydrogenation reaction.
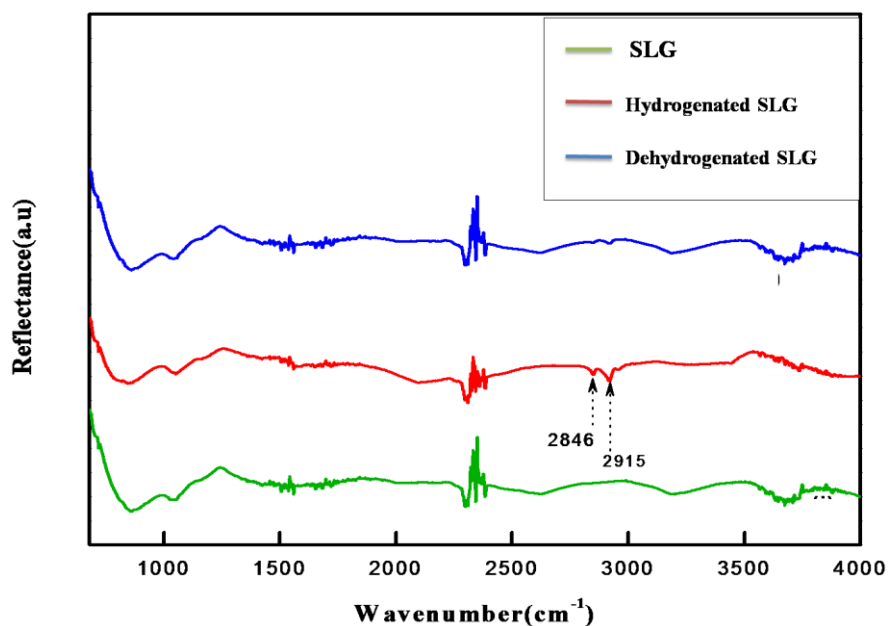

Figure 7.2 FTIR data plot of SLG, Hydrogenated SLG and De-hydrogenated SLG

7.2.3 <u>Magnetic study</u>

Magnetic moment study of the partially hydrogenated graphene shows a clear transformation from paramagnetic nature of the pristine SLG to anti-ferromagnetic behaviour as shown in Figure 7.3. Partial hydrogenation leaving the electrons in the non-hydrogenated carbon atoms localized and unpaired. The magnetic moments at these sites couple ferro-magnetically at room temperature giving rise to an infinite magnetic sheet with structural integrity and magnetic homogeneity[36]. However, with dehydrogenation such unpaired electrons and dangling bonds are removed and the extended π bonding network of the starting graphene is recovered and therefore the paramagnetic nature of the pristine SLG is revived back to a quite extent.
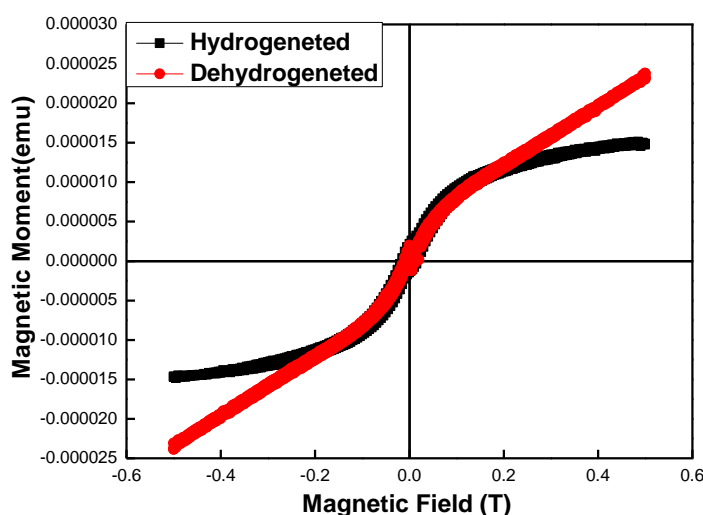

(a)
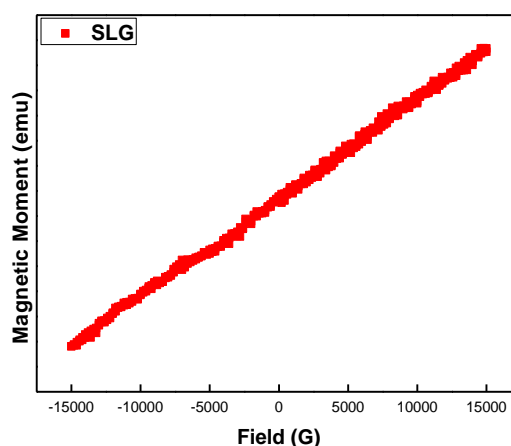
(b)

Figure 7.3 M-H Loop of Hydrogenated Graphene and De-hydrogenated Graphene (a); and SLG (b)

[223]

The Magnetization vs temperature plot is shown Figure 7.4(b) and (d) for both hydrogenated and de-hydrogenated SLG. The M-H plot at various temperatures 10K, 150K, 200K, 250K and 300K for both Hydrogenated and De-hydrogenated SLG is shown in Figure 7.4(a) & (c). The anti-ferromagneticity sustains upto a lower temperature of 30K which is observed clearly from Figure 7.4(a) and (b). This indicates a transition near to 30K. The de-hydrogenated SLG shows no such transition. This can be accounted to the resulting from the freezing of hydrogen Bonds at low temperature region.
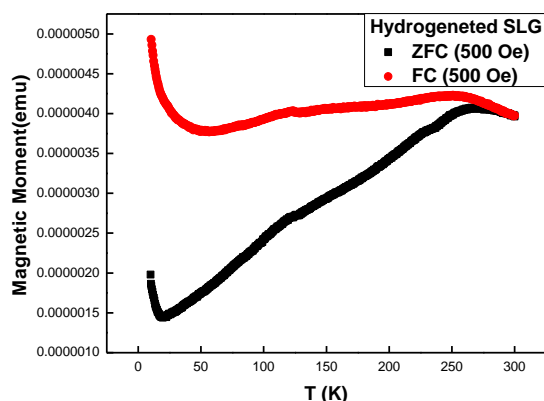
(a)
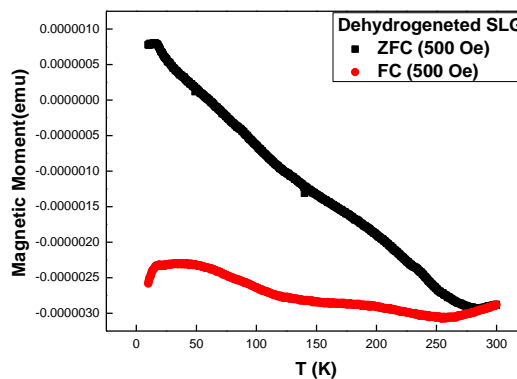
(b)
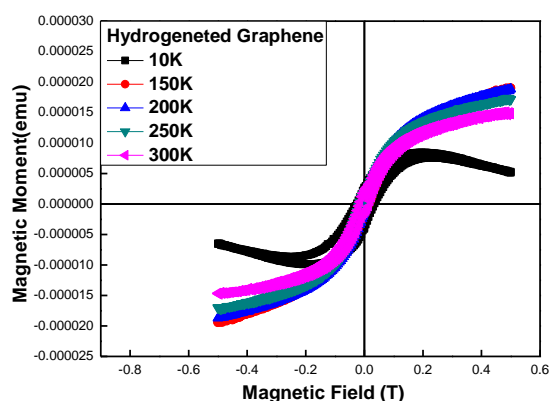
(c)
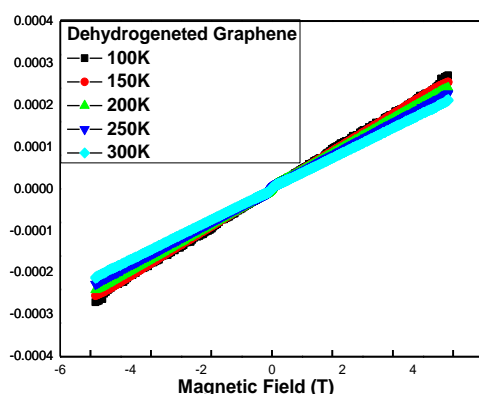
(d)

Figure 7.4 Temperature (T) vs Magnetic Moment (M) plot from 5K to 300K for Hydrogenated (a) and De-hydrogenated Graphene (b), M-H Loop at various temperature for Hydrogenated (c)and De-hydrogenated Graphene (d)

7.2.4 <u>Electrical measurement</u>

An electrical mobility study was also performed on SLG transferred onto quartz substrate using two probe I-V measurements which confirms the complete restoration of the graphitic network after dehydrogenation. Before hydrogenation, the SLG gave a sheet resistance of 0.15kΩ/square which increases to open circuit 39.70kΩ/square after

[224]

hydrogenation, also the nature of the curve changed from metallic to semiconductor with a finite band gap as is observed in Figure 7.5. However, this resistance value gets dramatically restored to 2.40kΩ/square after de-hydrogenation.

Figure 7.5 I-V measurement in top down electroding technique of SLG, hydrogenated and de-hydrogenatedGraphene

7.2.5 <u>Discussion</u>

SLG grown on copper foil was transferred onto quartz substrate for hydrogenation using lithium in liquid ammonia with methanol as the source of protons. Several analytical techniques demonstrated a very high degree of hydrogenation. Hydrogenated SLG was refluxed with DDQ in toluene at 110 °C to facilitate an easy and cost effective d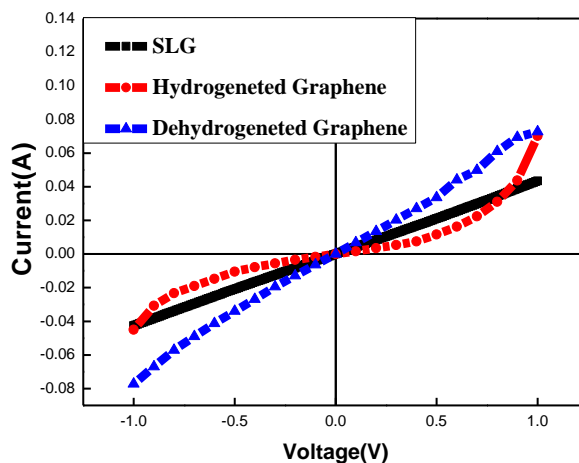ehydrogenation process. Characterization by FTIR, and Raman spectroscopy confirms the dehydrogenation process. Magnetic moment measurement studies reconfirm the reversibility of the dehydrogenation process. Of particular significance, analysis of the electronic mobility study of the de-hydrogenated graphene shows almost complete restoration of the conjugated SLG structure.

7.3 <u>Chapter summary</u>

This chapter depicts successful synthesis of ferromagnetic single layer graphene via hydrogenation reaction. The hydrogenated graphene can provide a perfect template as substrate for the growth of $BiFeO_3$ film as hydrogenated Graphene is inert in nature and will not modify with heating schedule. It was also observed here that chemically modified magnetic graphene can be converted into non-magnetic graphene. This two step reversible reaction of hydrogenation by Birch reduction followed by de-hydrogenation by oxidation incorporates switching ability of magnetic and electrical field that makes it a suitable choice for magnetic switch and sensing applications.

[225]

7.4 <u>**Bibliography**</u>

[1] Wallace, P.R., 1947. The band theory of graphite. *Physical review*, *71*(9), p.622.

[2] McClure, J.W., 1956. Diamagnetism of graphite. *Physical Review*, *104*(3), p.666.

[3] Geim, A.K. and Novoselov, K.S., 2007. The rise of graphene. *Nature materials*, *6*(3), pp.183-191.

[4] Zhang, Y.I., Zhang, L. and Zhou, C., 2013. Review of chemical vapor deposition of graphene and related applications. *Accounts of chemical research*, *46*(10), pp.2329-2339.

[5] An, C.J., Kim, S.J., Choi, H.O., Kim, D.W., Jang, S.W., Jin, M.L., Park, J.M., Choi, J.K. and Jung, H.T., 2014. Ultraclean transfer of CVD-grown graphene and its application to flexible organic photovoltaic cells. *Journal of Materials Chemistry A*, *2*(48), pp.20474-20480.

[6] Huang, X., Yin, Z., Wu, S., Qi, X., He, Q., Zhang, Q., Yan, Q., Boey, F. and Zhang, H., 2011. Graphene-based materials: synthesis, characterization, properties, and applications. *small*, *7*(14), pp.1876-1902.

[7] Zeng, Z., Yin, Z., Huang, X., Li, H., He, Q., Lu, G., Boey, F. and Zhang, H., 2011. Single-layer semiconducting nanosheets: high-yield preparation and device fabrication. *Angewandte Chemie*, *123*(47), pp.11289-11293.

[8] Huang, X., Qi, X., Boey, F. and Zhang, H., 2012. Graphene-based composites. *Chemical Society Reviews*, *41*(2), pp.666-686.

[9] Pang, S., Hernandez, Y., Feng, X. and Müllen, K., 2011. Graphene as transparent electrode material for organic electronics. *Advanced Materials*, *23*(25), pp.2779-2795.

[10] Novoselov, K.S., Geim, A.K., Morozov, S.V., Jiang, D., Katsnelson, M.I., Grigorieva, I.V., Dubonos, S. and Firsov, A., 2005. Two-dimensional gas of massless Dirac fermions in graphene. *nature*, *438*(7065), pp.197-200.

[11] Heersche, H.B., Jarillo-Herrero, P., Oostinga, J.B., Vandersypen, L.M. and Morpurgo, A.F., 2007. Bipolar supercurrent in graphene. *Nature*, *446*(7131), pp.56-59.

[12] Hirsch, A., Englert, J.M. and Hauke, F., 2013. Wet chemical functionalization of graphene. *Accounts of chemical research*, *46*(1), pp.87-96.

[13] Criado, A., Melchionna, M., Marchesan, S. and Prato, M., 2015. The covalent functionalization of graphene on substrates. *Angewandte Chemie International Edition*, *54*(37), pp.10734-10750.

[14] Zhu, J., Chen, M., He, Q., Shao, L., Wei, S. and Guo, Z., 2013. An overview of the engineered graphene nanostructures and nanocomposites. *Rsc Advances*, *3*(45), pp.22790-22824.

[15] Dreyer, Daniel R., Park, S., Bielawski, Christopher W. and Ruoff, Rodney S., 2010, The chemistry of graphene oxide. *,* *39*(1), pp. 228-240.

[16] Wang, Z., Tang, C., Sachs, R., Barlas, Y. and Shi, J., 2015. Proximity-induced ferromagnetism in graphene revealed by the anomalous Hall effect. *Physical review letters*, *114*(1), p.016603.

[17] Kumazaki, H. and S. Hirashima, D., 2008. Local magnetic moment formation on edges of graphene. *Journal of the Physical Society of Japan*, *77*(4), p.044705.

[18] Bhowmick, S. and Shenoy, V.B., 2008. Edge state magnetism of single layer graphene nanostructures. *The Journal of chemical physics*, *128*(24), p.244717.

[19] Singh, R. and Kroll, P., 2009. Magnetism in graphene due to single-atom defects: dependence on the concentration and packing geometry of defects. *Journal of Physics: Condensed Matter*, *21*(19), p.196002.

[20] Choi, S., Jeong, B.W., Kim, S. and Kim, G., 2008. Monovacancy-induced magnetism in graphene bilayers. *Journal of Physics: Condensed Matter*, *20*(23), p.235220.

[21] Zhou, J., Wang, Q., Sun, Q., Chen, X.S., Kawazoe, Y. and Jena, P., 2009. Ferromagnetism in semihydrogenated graphene sheet. *Nano letters*, *9*(11), pp.3867-3870.

[22] Whitener Jr, K.E., 2018. Hydrogenated graphene: A user's guide. *Journal of Vacuum Science & Technology A: Vacuum, Surfaces, and Films*, *36*(5), p.05G401.

[23] Xie, L., Wang, X., Lu, J., Ni, Z., Luo, Z., Mao, H., Wang, R., Wang, Y., Huang, H., Qi, D. and Liu, R., 2011. Room temperature ferromagnetism in partially hydrogenated epitaxial graphene. *Applied Physics Letters*, *98*(19), p.193113.

[24] Eng, A.Y.S., Poh, H.L., Sanek, F., Marysko, M., Matejkova, S., Sofer, Z. and Pumera, M., 2013. Searching for magnetism in hydrogenated graphene: using highly hydrogenated graphene prepared via birch reduction of graphite oxides. *Acs Nano*, *7*(7), pp.5930-5939.

[25] Lee, W.K., Whitener Jr, K.E., Robinson, J.T. and Sheehan, P.E., 2015. Patterning Magnetic Regions in Hydrogenated Graphene Via E-Beam Irradiation. *Advanced Materials*, *27*(10), pp.1774-1778.

[26] González-Herrero, H., Gómez-Rodríguez, J.M., Mallet, P., Moaied, M., Palacios, J.J., Salgado, C., Ugeda, M.M., Veuillen, J.Y., Yndurain, F. and Brihuega, I., 2016.

Atomic-scale control of graphene magnetism by using hydrogen atoms. *Science*, *352*(6284), pp.437-441.

[27] Sofo, J.O., Chaudhari, A.S. and Barber, G.D., 2007. Graphane: A two-dimensional hydrocarbon. *Physical Review B*, *75*(15), p.153401.

[28] Matis, B.R., Burgess, J.S., Bulat, F.A., Friedman, A.L., Houston, B.H. and Baldwin, J.W., 2012. Surface doping and band gap tunability in hydrogenated graphene. *ACS nano*, *6*(1), pp.17-22.

[29] Jaiswal, M., Yi Xuan Lim, C.H., Bao, Q., Toh, C.T., Loh, K.P. and Ozyilmaz, B., 2011. Controlled hydrogenation of graphene sheets and nanoribbons. *ACS nano*, *5*(2), pp.888-896.

[30] Gao, H., Wang, L., Zhao, J., Ding, F. and Lu, J., 2011. Band gap tuning of hydrogenated graphene: H coverage and configuration dependence. *The Journal of Physical Chemistry C*, *115*(8), pp.3236-3242.

[31] Whitener Jr, K.E., Lee, W.K., Campbell, P.M., Robinson, J.T. and Sheehan, P.E., 2014. Chemical hydrogenation of single-layer graphene enables completely reversible removal of electrical conductivity. *Carbon*, *72*, pp.348-353.

[32] Elias, D.C., Nair, R.R., Mohiuddin, T.M.G., Morozov, S.V., Blake, P., Halsall, M.P., Ferrari, A.C., Boukhvalov, D.W., Katsnelson, M.I., Geim, A.K. and Novoselov, K.S., 2009. Control of graphene's properties by reversible hydrogenation: evidence for graphane. *Science*, *323*(5914), pp.610-613.

[33] Yang, Z., Sun, Y., Alemany, L.B., Narayanan, T.N. and Billups, W.E., 2012. Birch reduction of graphite. Edge and interior functionalization by hydrogen. *Journal of the American Chemical Society*, *134*(45), pp.18689-18694.

8 Chapter

Summary and future projections of research work

8.1 <u>Summary</u>

The research work presented in this thesis was undertaken to explore a new type of material in the form of nano-composite or hetero-structure by combining two most commonly used systems- multiferroic $BiFeO_3$ (BFO) and graphene- who, in recent time, exhibited tremendous potential for a variety of applications in the area of spintronics. The single phase multiferroic materials are becoming popular in the field of spintronics since Allibe first introduces Giant Magneto- resistance (GMR) with the help of BFO based nano-materials. Electric field control over exchange bias in LSMO/BFO composite also becomes one of the milestones in spintronics applications. Though the search for single phase multiferroic materials suffers from multiple constraints which are already discussed in the first chapter but BFO still is the first choice because of its room temperature multiferroicity. Graphene, along with its several fascinating properties, becomes a potential candidate in spintronics because of its long spin lifetime and spin diffusion length. As we say Graphene and BFO have multifarious applications in the form of hybrid structure that we have already discussed in the historical review (section 1.8.3) while going through the literature there are a few conundrums we have addressed which inspires us to take up this research work just to explore the background physics of this new type of composite structure. We aimed to focus only on the magnetic and ferroelectric properties and to investigate its background from structural or crystallographic point of view.

Most of the literatures we have sorted out discuss the impact of magnetic and ferroelectric properties of multiferroic BFO upon Graphene but the reverse influence i.e. the impact of Graphene or its derivatives upon the structural and physical properties of BFO has not been explored so far. This was our motivation to commence this work. The questions we tried to address have been delineated in section 1.9. Neither these questions nor several possible

applications stemming from the questions have so far been taken up by the research community. There lies the uniqueness of our work.

When we started to synthesize reduced Graphene oxide/ $BiFeO_3$ (rGO/BFO) nano-composite in powder form we again had gone through various research works in past to find whether anyone have directly made any bonded composite but the answer is 'NO'.

The rGO/BFO composite were explored largely with impacts in various applications like photo-voltaic, water splitting, waste water treatment etc. Some have explored magnetism also but the origin or background physics were vaguely discussed.

In the first work included in Chapter 3 we addressed the different synthesis approaches that have taken to prepare the rGO/BFO nano-composite. Among them hydrothermally prepared nano-composite have covalent features between Fe 3d orbital of BFO and C 2p orbital of rGO. We have discussed also why hydrothermal treatment turned out to promote covalent bonding. The other composite have vdW attachment among rGO and BFO. The structural and physical properties have been compared between the two types of composites-bonded and non-bonded. We have found that covalently bonded composite proved to promote structural changes that is impactful in changing the magnetic properties and enhancing remanent ferroelectric polarization (determined by direct electrical measurements and from crystallographic details). The non-bonded composite also promotes interfacial attachments which influence ferroelectricity more than magnetism, and these features have evolved with the wt% of the rGO in the non-bonded composites.

So, from these results we may conclude that the covalent bonds across the BFO/rGO interfaces (Fe-C bonds) in the nano-composite result in important structural and physical properties than the non-bonded ones. In our second work we thoroughly have investigated rGO/BFO covalently bonded composite. All the results are discussed in Chapter 4. While discussing the synthesis part we pointed out that the rGO is acting as a positive catalyst in the preparation of nano-composite and the easiest approach and the shortest time have been reported in our work. This was not discussed by others.

The bonding percentage is also found to vary with rGO wt% and we have found a critical window of wt% for bonding to occur. This wt% variation is also advantageous to influence the magnetic properties like coercivity, saturation magnetization, remanent magnetization and exchange bias and why rGOwt% are affecting the magnetic property is discussed by calculating the magnetic anisotropy. The different features in low temperature region are also discussed. Moreover, the most important non-monotonic magnetic field dependence of ferroelectric polarization has been reported. Here, this we have observed not only from direct electrical measurements on the nano-composites but also from crystallography- by refining the neutron diffraction data recorded under different magnetic

[230]

fields. This novel property is originated from covalent bonding features of rGO/BFO nano-composite.

The non-monotonic magnetic field dependence of remanent polarization in covaletly bonded nano-composite possibly emerges from a competition between the bulk and surface magnetic anisotropy and consequently the bulk and surface magneto-striction. The magneto-striction, in turn, governs the bulk and surface magneto-electric coupling in nanoscale BFO bonded with rGO. This issue has been discussed in Chapter 4.

After investigating the bonded and non-bonded BFO/rGO nano-composites in detail, we addressed the issue whether the hetero-structure of rGO/BFO can alsogive rise to novel magneto-electric properties in order to be reckoned as a new genre of designed magneto-electric hetero-structure. We have taken the venture to make highly homogeneous film using CSD driven spin coating technique as the easiest and cheapest approach. In making BFO and rGO films there were different critical issues that were addressed in Chapter 5 in details. We have also seen the magnetic propertye changes in hetero-structure compared to BFO thin film. Various parameters in spin coating technique are tuned and their consequences are thoroughly discussed from the angle of morphology of films to ensure one protocol to obtain rGO/BFO thin film. In this work we have obtained rGO/BFO nano film of 85 nm thickness with phase purity, homogeneity and less surface roughness.

We now turn around our focus to achieve highly ferro-magnetic Graphene and BFO individually with an aim to make composite or hetero-structure of them in near future.

In this context we approach towards finding new way to make BFO nano-particle highly ferromagnetic in room temperature. In literature we have seen that magnetic saturation can be tuned in BFO nano-structure by tuning particle size, shape, adding dopants, surfactants or making composites.

The main difficulty is to achieve array of isolated nano-particles just because ferromagnetic BFO nano-particles tend to agglomerate and attachment with rGO surface cannot also help in isolating them as we have seen in our previous chapters. So, we aim to introduce silver (Ag) in BFO matrix so that it can enhance magnetic moment and also make the material bio-compatible for applications in the field of hyperthermia or radiotherapy. The overall results of BFO/Ag nano-composite are discussed in Chapter 6. Here we have found interesting results. There is an array of BFO nano-chains wrapped in Silver matrix with 20 times or an order of magnitude rise in saturation magnetisation. We have made soft ferromagnetic BFO/Ag nano-composite where charge transfer between Ag 3d state and O 2p state of BFO takes place. The magnetism has also been studied by magnetic force microscopy. This enormous rise in room temperature saturation magnetization was not even observed in bare BFO nano-particles of the same size. This work is obviously a great success towards newer applications in medical field.

[231]

We now have focussed to make graphene magnetic. For, these purposes we have now taken single layer Graphene rather than rGO. In literature numerous efforts have been discussed to make graphene magnetic like adding adatoms, adsorbates, inducing defects or edges, vacancies etc., as pristine Graphene is diamagnetic in nature. But, we want to induce magnetism chemically because adding adsorbates or other magnetic materials can tune other properties also. For this reason we choose hydrogenation of Graphene to make it ferromagnetic. Our aim was not only to make Graphene magnetic but also to chemically reverse the properties. The details of this approach have been included in Chapter 7. The result we obtained here is successfully tuning Graphene from para to anti-ferro then again para magnetic state chemically via hydrogenation and de hydrogenation.

The major aspects of our work have been thoroughly discussed throughout the chapters in this dissertation. The crucial missing link of this topic was investigated and justified in all cases. The research will hopefully shed light in various aspects of spintronics applications.

8.2 <u>Future projections</u>

[1] We have successfully found new protocols in solution chemistry route to achieve both covalent bonded, vdW attached rGO/BFO thin film. So, following the same approach other multiferroic oxides can be used instead of BFO to study newer multiferroic oxide and Graphene composite.

[2] The non-monotonic ferroelectric polarization need to be justified by carrying out more detailed Neutron diffraction experiment. The diffraction data should be taken with smaller change in magnetic field in near future.

[3] Extensive research work needed to make hetero-structure of highly magnetic BFO and highly magnetic Graphene and study their properties.

[4] The background physics of non-monotonic magneto-electric coupling and also change in magnetic and ferroelectric properties with the emergence of Fe-C covalent bonding need more substantial theoretical support via Monte Carlo simulation.

[5] The covalent bonding was calculated from XPS globally but we need to map the bonding structure locally or spatially. Additionally microscopic techniques (combined use of piezoresponse force microscopy (PFM), for example) should be used to observe the coupled magneto-electric domains across the hetero-structures or the nano-composites.

The above works mentioned under the future scopes will enrich the overall field and also pave the way for more novel applications in Spintronics.